

All-Optical and Endoscopic Photoacoustic Microscopy

by

Parsin Haji Reza

A thesis submitted in partial fulfillment of the requirements for the degree of

Doctor of Philosophy

in

Biomedical Engineering

Department of Electrical and Computer Engineering
University of Alberta

© Parsin Haji Reza, 2015

Abstract

Optical-resolution photoacoustic microscopy (OR-PAM) is a novel imaging technology providing high micron-scale lateral spatial resolution to visualize superficial structures *in vivo* with optical-absorption contrast. The term “optical resolution” is used since the lateral resolution of the system is defined by the optically-focused spot size, which is limited by the diffraction-limit of light. The axial resolution of the system is still inversely related to the bandwidth of transducer, typical of other photoacoustic microscopy (PAM) systems. Due to limitations of light transport, OR-PAM is used for imaging superficial structures to depths of about 1 mm in tissue. OR-PAM is able to image capillary networks and quantify morphological and functional parameters such as number of vessels, diameter and length of the vessels, total hemoglobin concentration and hemoglobin oxygen saturation. A tumor needs to develop angiogenesis in order to consume more oxygen and nutrients to grow. These blood vessels can provide imaging contrast for photoacoustic imaging, making OR-PAM a useful tool for tumor imaging.

However there are several limitations with current OR-PAM systems. One of the limitations is their lack of flexibility. The present OR-PAM systems are mostly mounted as a table-top device with a large footprint. In this dissertation we introduce a label free optical-resolution photoacoustic micro-endoscopy to enable access to internal body cavities and a flexible handheld probe.

Also, a multi-wavelength fiber laser with tunable repetition rates as high as 600 kHz, and high pulse-to-pulse stability is demonstrated for *in vivo* real time functional imaging. This has been done by taking advantage of stimulated Raman scattering (SRS) in a single mode fiber. This system is also modified to perform a multi-focus OR-PAM by taking advantage of chromatic aberration in the collimating/objective lens pair to refocus light from a fiber into an object so that each

wavelength is focused at a slightly different depth location. Design and fabrication of a novel Fabry-Perot etalon- based ultrasound detectors by using glancing angle deposition (GLAD) nanostructured thin-films is shown as well. Finally a novel all optical non-contact photoacoustic remote sensing (PARS) microscopy system is demonstrated with a lateral resolution as low as 2 μm . This system offers optical absorption contrast without the need of bulky ultrasound transducers or coupling medium and can provide performance comparable to previous OR-PAM systems but in a non-contact setting.

Preface

This thesis is an original work by Parsin Haji Reza. *In vivo* experiments procedures involving animals described in this dissertation followed the laboratory animal protocol approved by the University of Alberta Animal Use and Care Committee (Animal imaging protocol: AUP00001170).

Chapter 3 of this thesis has been published as P. Hajireza, W. Shi, and R. J. Zemp, "Label-free *in vivo* fiber-based optical-resolution photoacoustic microscopy," *Opt. Lett.* 36, 4107-4109 (2011) (also Vol. 6, Iss. 11 *Virtual Journal for Biomedical Optics*) (3 pages). I was responsible for the experiment design, data collection and the manuscript composition. W. Shi contributed to experiments, data analysis, and the manuscript composition and R. J. Zemp was the supervisory author and was involved with concept formation and manuscript composition.

Chapter 4 of this thesis has been published as P. Hajireza, W. Shi and R. J. Zemp, "Label-Free *in vivo* GRIN-Lens Optical Resolution Photoacoustic Micro-Endoscopy ", *Laser Phys. Lett.* 10 055603 (2013). I was responsible for the experiment design, data collection and the manuscript composition. W. Shi contributed to experiments, data analysis, and the manuscript composition and R. J. Zemp was the supervisory author and was involved with concept formation and manuscript composition.

Chapter 5 of this thesis has been published as P. Hajireza, T. Harrison, A. Forbrich and R. Zemp "Optical resolution photoacoustic microendoscopy with ultrasound-guided insertion and array system detection", *J. Biomed. Opt.* 18(9), 090502 (2013). I was responsible for the optical experiment design, data collection and the manuscript writing. T. Harrison helped with the development of the data acquisition and imaging mode, and phantom construction. A. Forbrich

aided with data collection and R. J. Zemp was the supervisory author and was involved with concept formation and manuscript composition.

Chapter 6 of this thesis has been published as P. Hajireza, W. Shi, and R. Zemp, "Real-time handheld optical-resolution photoacoustic microscopy," *Opt. Express* 19, 20097-20102 (2011) (also Vol. 6, Iss. 11 *Virtual Journal for Biomedical Optics*). I was responsible for the experiment design, data collection and the manuscript composition. W. Shi contributed to experiments, data analysis, and the manuscript composition and R. J. Zemp was the supervisory author and was involved with concept formation and manuscript composition.

Chapter 7 of this thesis has been published as P. Hajireza, A. Forbrich and R. Zemp" In-vivo functional optical-resolution photoacoustic microscopy with stimulated Raman scattering fiber-laser source" *Biomed. Opt. Express* 5, 539-546 (2014). I was responsible for the experiment design, data collection and the manuscript composition. A. Forbrich contributed to experiments, data analysis, and the software development and manuscript composition and R. J. Zemp was the supervisory author and was involved with concept formation and manuscript composition.

Chapter 8 of this thesis has been published as P. Hajireza, A. Forbrich, and Roger J. Zemp, "Multifocus optical-resolution photoacoustic microscopy using stimulated Raman scattering and chromatic aberration," *Opt. Lett.* 38, 2711-2713 (2013). I was responsible for the experiment design, data collection and the manuscript composition. A. Forbrich contributed to experiments, data analysis, and the software development and manuscript composition and R. J. Zemp was the supervisory author and was involved with concept formation and manuscript composition.

Chapter 9 of this thesis has been published as P. Hajireza, K. Krause, M. Brett, and R. Zemp, "Glancing angle deposited nanostructured film Fabry-Perot etalons for optical detection of ultrasound," *Optics Express* 21, 6391-6400 (2013) (also Vol. 8, Iss. 4 *Virtual Journal for*

Biomedical Optics). I was responsible for the experiment design, data collection, fabrication and the manuscript composition. K. Krause designed and fabricated the GLAD films. M. Brett and R. Zemp were the supervisory authors and were involved with concept formation and manuscript composition.

Chapter 10 of this thesis has been published as P. Hajireza, J. Sorge, M. Brett, and R. Zemp, "*In vivo* optical resolution photoacoustic microscopy using glancing angle-deposited nanostructured Fabry–Perot etalons," *Opt. Lett.* 40, 1350-1353 (2015). I was responsible for the experiment design, data collection, fabrication and the manuscript composition. J. Sorge designed and fabricated the GLAD films. M. Brett and R. Zemp were the supervisory authors and were involved with concept formation and manuscript composition.

Chapter 11 of this thesis has been prepared as P. Hajireza, W. Shi and R. Zemp, "Photoacoustic remote sensing (PARS)" (to be submitted, 2015)

I was responsible for the experiment design, data collection and the manuscript composition. W. Shi contributed to experiments and manuscript composition and R. J. Zemp was the supervisory author and was involved with concept formation and manuscript composition.

Acknowledgements

I would like to thank the beautiful soul of life that guides me through my journey, my amazing parents that have dedicated all their lives to my success, my beautiful sister, all my family members and all my friends. Everyone who came into my life, even though for a short period of time, and helped me to grow and learn how lovely and valuable life is... Thank you!

Very special thanks go to my supervisor Dr. Roger Zemp for all his help, support and patience. I have learned so much in both academic and personal life from him as he is one of the most knowledgeable, humble and family oriented people I have ever met. Thank you Dr. Zemp for bearing with me and my weakness and helping me to improve them.

Furthermore, I am deeply thankful to all my co-authors, Alexander Frobrich, Wei Shi, Tyler Harrison, Jason Sorge, and Kathleen Krause. I am also grateful to all my amazing colleagues at the University of Alberta for their help and support during these years. Especially, Alexander Frobrich for his constant help and Dr. Wei Shi, as the senior photoacoustic researcher in the lab.

Also, I would like to sincerely thank our collaborator and my supervisory committee members; Dr. Mike Brett, Dr. Robert Fedosejevs and Dr. Ying Tsui for their helpful suggestions and critical comments and for their great help and support on my research. I would also like to thank Dr. Michael Kolios as the external examiner of my PhD defence for providing excellent feedback.

Last but not least, I gratefully acknowledge funding from the Killam Trust for an Izaak Walton Killam Memorial Scholarship, Alberta Innovates—Technology Futures, and Alberta Enterprise and Advanced Education for a Graduate Student Scholarship, University of Alberta for

Dissertation fellowship and Andrew Stewart Awards as well as SPIE for an SPIE Scholarship in optics and photonics.

Funding for our research has been provided by a number of generous sources: Natural Sciences and Engineering Research Council of Canada (355544-2008, 375340-2009, 288338-2010 to R.E.C., STPGP 396444), Terry- Fox Foundation and the Canadian Cancer Society (TFF 019237, TFF 019240, CCS 2011-700718, 702032 to both Roger Zemp and Robert E. Campbell.), the Alberta Cancer Research Institute (ACB 23728), the Canada Foundation for Innovation, Leaders Opportunity Fund (18472), Alberta Advanced Education & Technology, Small Equipment Grants Program (URSI09007SEG), Microsystems Technology Research Initiative (MSTRI RES0003166), University of Alberta Startup Funds, Alberta Ingenuity / Alberta Innovates scholarships for graduate and undergraduate students, Canadian Federation of University Women Edmonton Margaret Brine Graduate Scholarships for Women and SPIE Optics and Photonics Education Scholarship. Dr. Lewis holds the Frank and Carla Sojonky Chair in Prostate Cancer Research supported by the Alberta Cancer Foundation.

List of Symbols

- λ : Optical wavelength
- λ_a : Acoustic wavelength.
- d_c : Characteristic dimension
- α_{th} : Thermal diffusivity
- v_s : Speed of sound
- β : Thermal coefficient
- C_p : Heat capacity
- μ_a : Optical absorption coefficient
- μ_{eff} : Effective attenuation coefficient
- μ_a : Absorption coefficient
- μ_s : Scattering coefficient
- g : Scattering anisotropy factor
- Γ : Gruneisen parameter
- T_0 : Temperature in degrees Celsius
- F : Focal length
- D : Diameter of laser beam.
- ZnS: Zinc sulfide
- Na_3AlF_6 : Sodium hexafluoroaluminate
- TiO_2 : Titanium dioxide
- I_s : Phase sensitivity
- df : optical phase
- dIR : Intensity output
- A_s : Acoustic phase sensitivity
- n : Refractive index
- l : Thickness

- E : Young's modulus
- P : Photoelastic constant
- s : Poisson's ratio
- k : Acoustic wavenumber
- $f\#$: F-number
- σ : Gaussian sigma parameter
- Pa: Pascale
- $\lambda/4$: Quarter wave plate
- R_I : Reflection coefficient
- η : Transmissivity
- Φ : Focal fluence
- η : Elasto-optic coefficient
- ρ : Mass density
- v_p : particle velocity
- ω_a : Acoustic angular frequency
- ζ : Backscattered light collection efficiency
- HbO_2 : Oxyhemoglobin
- Hb : Deoxyhemoglobin
- θ_j : Angle of incident light

Glossary of Terms

- *AL*: Aspheric lenses
- *A-line*: A 1-D image in depth (time)
- *ANSI*: American National Standards Institute
- *AOR-PAME*: Array-based optical-resolution photoacoustic micro-endoscopy
- *AR*: Anti reflection
- *BC*: Beam combiner
- *B-mode image*: 2-D image formed by collecting A-lines
- *CAM*: Chorioallantoic membrane
- *CARS*: Anti-stokes Raman spectroscopy
- *C-scan image*: A 2-D en-face image
- *CT*: Computed tomography
- *CW*: continuous wavelength
- *DOF*: Depth of focus
- *DOT*: Diffuse Optical Tomography
- *DX*: X axis mirror driver
- *DY*: Y axis mirror driver
- *ex vivo*: From latin, outside the body
- *in vivo*: From latin, inside the body
- *Exogenous*: Originating outside the body
- *FLD*: Fiber laser driver
- *F-OR-PAM*: Fiber optical resolution photoacoustic microscopy
- *FOV*: Field of view
- *FOV_x*: Field of view in X direction
- *FOV_y*: Field of view in Y direction
- *FP*: Fabry Perot
- *FPI*: Fabry Perot Interferometer

- *FWHM*: Full-width at half-maximum
- *GLAD*: Glancing angle deposition
- *GRIN*: Gradient index
- *GS*: Glass
- *HH-OR-PAM*: Handheld optical resolution photoacoustic microscopy
- *HS-DAC*: High speed data acquisition card
- *IMF*: index-matching fluid
- *LS-OR-PAM*: Laser scanning optical resolution photoacoustic microscopy
- *M*: Mirror
- *MAP*: Maximum amplitude projection
- *MF-OR-PAM*: Multi focus optical resolution photoacoustic microscopy
- *Microvasculature*: Small blood vessels; capillary networks
- *MRI*: Magnetic resonance imaging
- *MRRs*: Micro-ring resonators
- *MT*: Melanoma tumor
- *MW-OR-PAM*: Multi wavelength optical resolution photoacoustic microscopy
- *NA*: Numerical aperture
- *NDF*: natural density filter
- *NEP*: Maximum permissible exposure
- *OCT*: Optical Coherence Tomography
- *OL*: Objective lens.
- *OR-PAM*: Optical resolution photoacoustic microscopy
- *OR-PAME*: Optical resolution photoacoustic micro-endoscopy
- *OR-PARS*: Optical-Resolution Photoacoustic Remote Sensing
- *P*: prism
- *PA*: Photoacoustic microscopy
- *PAM*: Photoacoustic microscopy
- *PAT*: Photoacoustic tomography

- *PBS*: Polarized beam Splitter,
- *PD*: Photodiode
- *PDG*: Pulse delay generator
- *PET*: Positron emission tomography
- *PM-SMF*: Polarization maintaining single mode fiber
- *PRR*: Pulse repetition rate
- *PVD*: Physical vapor-deposition
- *QW*: quarter wave plate
- *Realtime*: Typically refers to video-rate (30fps) capture.
- *SEM*: Scanning electron microscope
- *SNR*: Signal-to-noise ratio, a measure of image quality
- *SRS*: Stimulated Raman Scattering
- *TiO₂*: Titanium dioxide
- *TX*: Ultrasound transducer.
- *UOT*: Ultrasound-modulated optical tomography
- *UST*: Ultrasound transducer
- *VD*: vasodilatation
- *Yb*: Ytterbium

List of Figures

Figure 1.1: Fundamental concept of photoacoustic imaging.....	24
Figure 2.1: Experimental set-up of a dark field reflection mode PAM system.....	41
Figure 2.2: (a) Structural image. (b) Vessel-by-vessel sO ₂ mapping.....	42
Figure 2.3: Schematic of the OR-PAM system.....	44
Figure 2.4: Microvasculature in a nude mouse ear. (a) <i>In vivo</i> OR-PAM image. (b) 3D pseudocolor visualization of the vasculature.....	44
Figure 2.5: Experimental setup of the second-generation optical-resolution photoacoustic microscope.....	45
Figure 2.6: <i>In vivo</i> functional optical-resolution photoacoustic microscopy of a nude mouse ear. (b) Images of the total hemoglobin concentration and (b) Images of the hemoglobin oxygen saturation (c) zoom in images of the selected area shown in (a).....	45
Figure 2.7: Longitudinal OR-PAM of developing tumor angiogenesis on (a) day 5; (b) day 7; and (c) day 9.....	47
Figure 2.8: (a) White-light photographs of a representative mouse ear (b) OR-PAM images of the tumor region [dashed boxes in (a)]. MT: melanoma tumor; VD: vasodilatation.....	47
Figure 2.9: Schematic of combined PAT, ORPAM and OCT imaging system. M1 and M2: dichroic mirrors. FPI: Fabry Perot interferometer.....	49
Figure 1.10: Left: Maximum intensity projection of an ORPAM image of a 62 μ m bore PMMA capillary tube filled with human blood.....	49
Figure 2.11: <i>In vivo</i> PAT and OCT imaging of the skin on the back of a nude mouse. (a) OCT and PAT images. (b) A close-up view of OCT and PAT image in (a) while part of the OCT data has been removed to reveal blood vessels (c) A cross-sectional image slice of the combined OCT-PAT image.....	50
Figure 2.12: (a) schematic of a Fabry-Perot polymer film ultrasound transducer. (b) FPI transfer function.....	51
Figure 2.13: (a) definition of rotation and deposition angle. (b) GLAD-capable PVD system.....	53
Figure 3.1: Simplified scanning F-OR-PAM experimental setup.....	67

Figure 3.2: F-OR-PAM images demonstrating the entire field-of-view of the image-guide. In (a) the whole aperture is covered by black tape, (b) black tape moved to cover only half of the aperture.....	69
Figure 3.3: (a) and (b) images of $\sim 7 \mu\text{m}$ carbon-fiber network. (c) Imaging of human hair with 100 μm diameter.....	70
Figure 3.4: F-OR-PAM image of the microvasculature in a Swiss Webster mouse ear <i>in vivo</i>	71
Figure 4.1: Simplified scanning GRIN-lens OR-PAME experimental setup.....	75
Figure 4.2: (a) OR-PAME image demonstrating the entire field of view of the image guide. (b) A photoacoustic image of a carbon-fiber network using the GRIN-lens OR-PAME system. Each carbon fiber is $\sim 7 \mu\text{m}$ in diameter. (c), (d) An enlarged region of (b) which shows the fine details that can be achieved using the GRIN-lens OR-PAME system.....	77
Figure 4.3: (a)–(c) GRIN-lens OR-PAME images of the microvasculature at various positions in a hairless SCID ear <i>in vivo</i>	77
Figure 5.1: Experimental setup of AOR-PAME.....	82
Figure 5.2: (a) Phantom setup with ultrasound images of (b) before, (c) during and (d) after insertion of endoscope. Figures (b-d) are rotated 90 degrees counterclockwise in comparison to figure (a).....	84
Figure 5.3: Carbon fiber images captured from $\sim 2\text{cm}$ depth in tissue-mimicking phantom, (a-b) show fiber networks, (c) shows a single carbon fiber. SNR is $\sim 40\text{dB}$, best-case resolution $\sim 9 \mu\text{m}$	84
Figure 5.4: <i>In vivo</i> AOR-PAM image of rat ear.....	84
Figure 6.1: (a) Experimental setup of our HH-OR-PAM imaging system employing a high repetition rate diode- pumped pulsed Ytterbium fiber laser with up to 600 kHz pulse repetition rate and pulse widths of 1ns.....	89
Figure 6.2: (a) and (b) network of carbon fibers with $\sim 7.5\mu\text{m}$ diameter which are as small as capillary sized blood vessels. (c) Human hair with a diameter of $\sim 100\mu\text{m}$	90
Figure 6.3: Microvasculature in the ear of a Swiss Webster mouse.....	91
Figure 6.4: FWHM due to fitting individual carbon fiber signal amplitude to a Gaussian function...	92
Figure 7.1: (a) Experimental setup of multi-wavelength OR-PAM. (b) Photograph of the generated multi-wavelength spectrum in a PM-SMF.....	97

Figure 7.2: (a) SRS peaks for 160 kHz PRR and a 15m PM-SMF. (b) Unfiltered (dashed) and filtered (solid) SRS peaks for 160 kHz PRR and a 6m PM-SMF (the input power varied between 55-100mW).....	100
Figure 7.3: C-scan images of (a) carbon fiber networks and (b) the dye-filled tubes at 3 different wavelengths for 100% red and 0% blue dyes.....	100
Figure 7.4: The average signal for selected regions within the tube shown in fig. 7.3(b). This data has been used to determine the absorption spectrum.....	101
Figure 7.5: Mock oxygen saturation estimation using mixtures of red and blue dye.....	102
Figure 7.6: Multi-wavelength <i>in vivo</i> imaging using 545nm (A) and 558nm (B) pulses. Oxygen saturation estimations are shown in (C) for the area within the dashed rectangle.....	102
Figure 8.1: Experimental setup of multi-focus OR-PAM.....	106
Figure 8.2: OR-PAM images of carbon fiber network at four different wavelengths at a fixed depth (a-d) and variable depth (e-h).....	107
Figure 8.3: Point spread functions of 532nm and combination of all the wavelengths.....	109
Figure 8.4: <i>In vivo</i> images of a Swiss Webster mouse at a) combination of all wavelengths (532, 543 and 560 nm) b) 543 nm, c) 560 nm and d) combination of all wavelengths (532, 543 and 560 nm) with the same energy level as b and c.....	110
Figure 9.1: The configuration of Fabry Perot interferometers (FPI). The thickness of each GLAD filter was 2.1 μm . The Parylene C thickness at the middle and the top layers were 23 μm and 4 μm , respectively.....	118
Figure 9.2: SEM image of first GLAD layer. Dense layers were deposited at an angle of $\alpha=60^\circ$. Sparse, columnar, layers were deposited at an angle of $\alpha=80^\circ$	118
Figure 9.3: (a) Transmission spectrum of a single GLAD film deposited on glass both simulation and experimental work. (b) Transmission spectrum of the four layer GLAD, Paralyne-C, four layer GLAD FPI showing sharp resonant peaks near the C-band (experimental). (c) Transmission spectrum of the GLAD-FPI near the excitation wavelength range (experimental). (d) Measured reflectance spectra for 1 peak (experimental).....	119
Figure 9.4: (a) The experimental setup used for testing our GLAD-FPI sensor. Two separate setups are shown. Setup 1 is used for photoacoustic imaging. Setup 2 is used to test the receive sensitivity using an external ultrasound transducer.....	122
Figure 9.5: Optical-Resolution Photoacoustic Microscopy images of carbon fiber networks with 7 μm diameter of each fiber.....	123

Figure 9.6: GLAD-FPI frequency response.....	123
Figure 10.1: Experimental setup of GLAD OR-PAM.....	128
Figure 10.2: (a) The configuration of FPI. AR (anti reflection). (b) Transmission spectrum of the GLAD FPI showing sharp resonant peaks near the C-band. (c) SEM image of first GLAD layer. Dense layers were deposited at an angle of $\alpha = 60^\circ$. Sparse, columnar, layers were deposited at an angle of $\alpha = 80^\circ$	131
Figure 10.3: GLAD OR-PAM images of carbon fiber network. Images are formed using a pulse energy of a) 30 nJ b) 1nJ.....	133
Figure 10.4: <i>in vivo</i> images of capillary beds in the CAM-membrane of 5-day chicken embryo model.....	133
Figure 11.1: Experimental setup of OR-PARS. b) Multi focus excitation and single wavelength interrogation beams.....	140
Figure 11.2: a) OR-PARS images of carbon fiber networks b) FWHM due to fitting individual carbon fiber signal amplitude to a Gaussian function. c) Resolution study using knife edge spread function d) Comparison between the reflection mode OR-PARS and a transmission mode OR-PAM using a 10 MHz unfocused transducer	141
Figure 11.3: <i>In vivo</i> PARS images of chicken embryo model. a) Multi focus images of both capillary beds and bigger blood vessels b) Zoom in image of both capillary beds and bigger blood vessels c) indicating the bleeding area in the tissue d) single wavelength (532nm) PARS images.....	142
Figure 11.4: <i>In vivo</i> en-face maximum amplitude C-Scan PARS images of microvasculature in rat's ear.....	143
Figure 11.5: (a) Experimental setup of OR-PARS using common path and Michelson interferometry setup. (b) Experimental setup of the final version of the OR-PARS.....	149
Figure 11.6: Measured photoacoustic signals from various dye concentrations.....	158
Figure 11.7: Carbon fiber images when interrogation beam is fixed.....	159
Figure 11.8: PARS photoacoustic time domain signal of an individual carbon fiber when the excitation and interrogation beams are separated by \sim (a) 0 (b) 120 and (c) 330 μ m.....	160
Figure 11.9: PARS frequency response with 10th order polynomial fit.....	160
Figure 11.10: PARS characterization for ultrasound detection.....	161

Figure 11.11: Measured signal from the water-air interface due to an immersed unfocused transducer as a function of depth.....162

Figure 11.12: Photoacoustic signal as a function of excitation energy on the sample (carbon fiber) when interrogation power is fixed at 6mW.....163

Figure 11.13: Photoacoustic signal versus interrogation power on the sample (carbon fiber) when excitation energy is fixed at 10 nJ.....164

Figure 11.14: Confocal images of chicken embryo.....165

Figure 11.15: the information acquired at each depth to form image 11.3(a).....166

List of Tables

Table 7.1: Measured power of SRS peaks generated in varying fiber lengths and at different PRR.....	99
Table 7.2: Spectral demixing of PA signals of tubes containing various concentrations dyes.....	101
Table 8.1: Results of figure 8.2.....	108

Table of Contents

Abstract.....	ii
Preface	iv
Acknowledgements	vii
List of Symbols.....	ix
Glossary of Terms	xi
Table of Contents	xx
List of Figures.....	xiv
List of Tables	xix
1. Introduction.....	1
1.1. Photoacoustic imaging.....	1
1.2. Problem statement and motivation	2
1.3. Major contributions for this dissertation	6
1.4. Organization of this dissertation.....	10
Bibliography.....	12
2. Background	16
2.1 Optical imaging	16
2.2 Principle of photoacoustic imaging.....	17
2.2.1 Physical Principles of Photoacoustic Signal Generation	19
2.3 Development of OR-PAM.....	20
2.3.1 Applications: Imaging angiogenesis.....	23
2.3.2 Combination with other optical imaging systems.....	25
2.4 Fabry Perot Interferometers for ultrasound detection.....	27
2.5 Signal to noise ratio	29
2.6 Glancing angle deposition method (GLAD)	29
2.7 Limitations.....	30
Bibliography.....	32
3. Label-free <i>in vivo</i> fiber-based optical-resolution photoacoustic microscopy	43
Bibliography.....	49

4. Label-free <i>in vivo</i> GRIN-lens optical resolution photoacoustic micro-endoscopy	50
4.1 Introduction	50
4.2 Experimental setup	51
4.3 Results and discussion	53
Bibliography	56
5. Optical-resolution photoacoustic micro-endoscopy with ultrasound-guided insertion and array system detection	57
Bibliography	63
6. Real-time handheld optical-resolution photoacoustic microscopy	64
6.1 Introduction	64
6.2 System description.....	65
6.3 Result and discussion	67
Bibliography	71
7. In-Vivo functional optical-resolution photoacoustic microscopy with stimulated Raman scattering fiber-laser source.....	72
7.1 Introduction	72
7.2 Methods	73
7.3 Result and discussion	75
Bibliography	81
8. Multi-focus optical-resolution photoacoustic microscopy using stimulated Raman scattering and chromatic aberration.....	82
Bibliography	88
9. Glancing angle deposited nanostructured film Fabry-Perot etalons for optical detection of ultrasound.....	89
9.1 Introduction	89
9.1. Fabry Perot Interferometer fabrication	92
9.2. Result and discussion	97
Bibliography	102
10. <i>In vivo</i> optical resolution photoacoustic microscopy using glancing angle deposited nanostructured Fabry-Perot etalons	104
Bibliography	112

11.	<i>In vivo</i> Optical-Resolution Photoacoustic Remote Sensing Microscopy	113
11.1.	Introductions	113
11.2.	Experimental setup	115
11.3.	Results and Discussion	118
11.3.1.	Mechanisms and Models	120
11.3.2.	Potential Advantages and Future of PARS System	122
11.4.	Methods	122
11.4.1	Multi-Wavelength Fiber Laser Source:	122
11.4.2.	System Design.....	123
11.4.3	Animal Imaging:	124
11.5	Appendix: Supplementary Information	125
1.	OR-PARS system and Methods	125
2.	OR-PARS modulation mechanisms and comparison with experiment	127
2.1.	Pressure-Induced Refractive-Index Modulation.....	128
2.2.	Thermally-Induced Refractive Index Modulation.....	130
2.3.	Surface Oscillations.....	130
2.4.	Scatterer Position Modulation Due to Confined Thermal Expansion	132
2.5.	Detected Signal.....	133
3.	Additional Experimental Results	134
3.1.	Validation of Optical Absorption Contrast.....	134
3.2.	PARS imaging with fixed detector and ultrasound time of flight study	135
3.3.	Experimental Detection of Ultrasound Signals	138
3.4.	Validation of Optical Sectioning Capabilities:.....	138
3.5.	PARS signal strength VS. Beam intensities	139
3.6.	Comparison with Fluorescence Confocal Microscopy.....	141
3.7.	Maximum amplitude projection and depth information.....	143
4.	Imaging procedures and laser safety	144
4.1.	Excitation-Beam Laser Safety	144
4.2.	Interrogation beam laser safety considerations	144

5. Laser selection.....	145
6. Photoacoustic modulation of multiply-scattered light: Beyond the Ballistic Regime	147
Bibliography.....	148
12. Conclusion and future work	151
12.1. Conclusion	151
12.2. Future	154
Bibliography.....	155

1. Introduction

1.1. Photoacoustic imaging

Photoacoustic imaging is an emerging hybrid imaging technology providing optical contrast with high spatial resolution. Figure 1.1 shows the fundamental concept of photoacoustic imaging. Photoacoustic imaging uses lasers to excite tissues. Chromophores absorb electromagnetic energy. The absorption gives rise to a local, instantaneous rise in temperature causing a thermoelastic expansion [1-3] and subsequently an emission of an acoustic pressure wave. These acoustic signals are detected and reconstructed in order to image the distribution of the optically absorbing structures in a material[2, 4]. Photoacoustic imaging is a label free technique (does not require external agents) which usually takes advantage of hemoglobin as an endogenous contrast agent. Due to its high contrast and scalable spatial resolution, as well as, the high degree of safety, photoacoustic imaging has become a popular field of research for the early diagnosis and monitoring of disease [5-7]. Photoacoustic imaging uses non-ionizing waves which have no health hazard, unlike some other techniques such as x-ray imaging [3, 5-7].



Figure 1.1: Fundamental concept of photoacoustic imaging

In conventional photoacoustic imaging (acoustic resolution), both the lateral and axial resolutions are determined by the acoustic properties of the detector. The lateral resolution is determined by the focal diameter of the transducer, while the axial spatial resolution is determined by the transducer bandwidth [5, 8-13]. On the other hand, the imaging penetration is limited by the attenuation in tissue. For instance, to obtain 5 μm lateral resolution an ultrasonic center frequency higher than 300 MHz is required. The ultrasonic attenuation in tissue at this frequency is about 80 dB/mm [9]. This limits the penetration depth to $\sim 100 \mu\text{m}$.

Optical resolution photoacoustic microscopy (OR-PAM) uses optical focusing to overcome this issue. The lateral resolution is derived from optical focusing, while the axial resolution is still determined by ultrasonic detection [9, 14]. Due to limitations of light transport, the penetration depth is limited to about 1 mm in tissue [5, 9, 15-18]. Considering other parameters such as diffraction limited performance, aberrations and poor beam quality, OR-PAM provides resolutions about 1 to 10 μm which is much higher than PAM with $>50 \mu\text{m}$ lateral resolutions (determined by ultrasound resolution) [9]. OR-PAM is capable of imaging both morphological parameters, such as the microvasculature at the capillary level, number of vessels, diameter and length of the vessels and functional parameters, such as total hemoglobin concentration and hemoglobin oxygen saturation [3, 9, 12-57]. Since cancer cells need to consume more oxygen and nutrients to grow; they invoke a range of signaling pathways to spawn new vessels in a process known as angiogenesis and therefore have plenty of contrast-providing blood vessels making OR-PAM a useful tool for tumor imaging [31, 57, 58].

1.2. Problem statement and motivation

In spite of all the great features of OR-PAM, there are still several challenges preventing its clinical applications. The limitations are limited penetration depth, long acquisition times, large footprint and lack of flexibility. Also OR-PAM as an optical imaging technique unlike other imaging techniques, suffers from its dependency to bulky ultrasound transducers and coupling medium. OR-PAM is usually used for superficial imaging to limited penetration depth. Therefore, an endoscopy version is a promising tool to expand the clinical application of OR-PAM. Realtime OR-PAM imaging can be a useful tool for clinical needs. For example the ability of monitoring the efficacy of a drug in anti-angiogenic therapies in real time can improve the accuracy and speed of pharmaceutical drug discovery. Currently, a 80 minutes acquisition time was reported for imaging a $7.8 \text{ mm} \times 10 \text{ mm}$ area with a $2.5 \mu\text{m}$ step size [25, 30].

1.2.1. Miniaturization and endoscopy system development for OR-PAM

The footprints of most OR-PAM systems are too large to permit imaging internal body structures. Furthermore, due to limited penetration depth, the current OR-PAM systems are only useful for imaging superficial structures. In order to extend the potential range of OR-PAM applications, new miniaturized optical resolution photoacoustic micro-endoscopy systems are desirable. Micro-endoscopy systems typically sacrifice wide field-of-view for high-resolution, small-footprint and flexible probes. Many types of micro-endoscopy systems have been developed including brightfield, fluorescence, confocal, and confocal fluorescence endoscopic systems [59-61]; however, these systems often require an exogenous fluorescent contrast agent to stain cells for imaging. While these systems permit “virtual biopsy” capabilities, sometimes the delivery of these agents is cumbersome and toxic, therefore, label-free imaging would be preferred. Additionally, imaging more than one species of fluorescent label usually is not trivial. Photoacoustic imaging would permit label-free imaging using a different contrast mechanism, but it has not yet been implemented in a micro-endoscopic form factor, except for some work on intravascular applications, where ultrasonic rather than optical resolution is realized in B-scan rather than C-scan format[62]. Another limitation of current OR-PAM systems is their lack of flexibility. The present OR-PAM systems are mostly mounted on a table-top device with a large footprint. A handheld and portable optical resolution photoacoustic microscope can permit imaging of different parts of body that were previously inaccessible, and will lead to many new clinical and pre-clinical applications including: functional brain mapping, cancer imaging and detection, imaging of angiogenesis to assess therapeutic efficacy, among many others.

1.2.2. Real time multi-wavelength functional optical resolution photoacoustic microscopy

Non-invasive and label-free quantification of the oxygen saturation (SO_2) in blood vessels and tissues is very important for numerous medical applications, including evaluating the effects of chemotherapy and radiotherapy on tumors [3, 31, 35, 36, 51, 63, 64], wound healing monitoring and studying gene expression [3, 57, 65]. Current techniques that show

potential for SO₂ imaging include near-infrared spectroscopy, blood-oxygen-level-dependent contrast magnetic resonance imaging, electron paramagnetic resonance imaging positron emission tomography, and single photon emission tomography[66]. However, these systems suffer from lack of either spatial resolution or sensitivity [66]. Photoacoustic imaging can provide new opportunities for functional imaging. Photoacoustic is well suited for SO₂ imaging of blood vessels, since oxyhemoglobin (HbO₂), deoxyhemoglobin (Hb) are two of the major optical absorbers in tissues[66, 67].

The optical absorption of Hb and HbO₂ varies at different wavelengths. Therefore, a multi-wavelength excitation source is necessary in order to perform photoacoustic functional imaging. Fiber and microchip lasers have recently been introduced as high-repetition-rate sources for real time photoacoustic imaging [22, 29, 44]; however, the wavelength tunability was limited. A supercontinuum source for OR-PAM has been reported by using a high-nonlinearity fiber injected with nanosecond pulses from a microchip laser [68]. The supercontinuum was filtered into bands for multi-wavelength imaging; however, energy per band was low due to broad distribution of power over such a wide spectral range. Previous microchip laser pump sources suffered from pulse-to-pulse stability, timing jitter, low repetition rates, and lack of trigger-ability. A multi-wavelength fiber laser with tunable repetition rates as high as high as 1 MHz , and high pulse-to pulse stability is desirable for *in vivo* real time functional imaging. This has been done by taking advantage of stimulated Raman scattering (SRS) in a single mode fiber.

1.2.3. Multi-focus optical resolution photoacoustic microscopy

OR-PAM takes advantage of optical focusing to achieve micrometer-scale lateral resolution [3, 9, 15, 19, 21, 37, 38, 43, 51, 52]. However, there is a trade-off between depth-of-focus and lateral resolution in OR-PAM; hence, for high-resolution systems, only a narrow depth range is in focus [3, 48, 50]. Therefore achieving a uniform energy distribution over the entire field of view with high resolution can be challenging. Mechanical scanning in the depth direction is one means of improving the depth-of-field [3, 48, 50]; however, mechanical

scanning greatly limits the speed of imaging. In order to achieve real-time imaging, a non-mechanical method to acquire information in depth is required.

1.2.4. All-optical detection of ultrasound

Ultrasound detectors are found in a range of applications from humidifiers, flow-meters, sonar, and medical imaging to non-destructive test systems. Most photoacoustic imaging techniques employ piezoelectric receivers to detect the ultrasonic signals. However, all-optical detection can become an attractive alternative in applications such as intraoperative, laparoscopic, and endoscopic ultrasound image guidance systems. In these cases, electrical interconnects must be minimized to make the imaging catheter small and flexible enough to navigate through small orifices and vessels. As well, high voltages present electrical safety hazards to patients. Additionally, legislative trends in some countries include restricting hazardous substances used in electrical and electronic equipment including lead. Hence there is significant opportunity for transducer technology which is lead-free. Finally, many invasive applications also require either sterilizable or disposable catheters. Hence the need for alternative transducer technologies for detection of ultrasound makes optical-based transducers viable candidates.

1.2.5. Remote detection of ultrasound

In most photoacoustic and ultrasound imaging systems piezoelectric transducers or optical detectors have been employed, in which an ultrasound coupling medium such as water or ultrasound gel is required. However for many clinical applications such as wound healing, burn diagnostics, surgery, and many endoscopic procedures physical contact, coupling, or immersion is undesirable or impractical. Designing a technique that doesn't require direct contact or fluid coupling, and can be used for *in vivo* studies is essential for many clinical and preclinical applications.

1.3. Major contributions for this dissertation

1.3.1 Optical resolution photoacoustic micro-endoscopy

Our work helped to pioneer the use of fiber bundles to design optical resolution photoacoustic micro-endoscopy (OR-PAME). The developed OR-PAME systems are in some ways similar to fiber-based micro-endoscopes (or endo-microscopes). Such systems also rely on image-guide fibers, miniature fiber bundles capable of transmitting images. Many such systems require the use of an exogenous fluorescent dye or contrast agent. The proposed OR-PAME system would provide the ability to image microvessels, and potentially cells and subcellular structures similar to fluorescence (confocal) micro-endoscopes, but without requiring an exogenous contrast agent. Image guide fibers are miniaturized fiber bundles with as many as 100,000 individual micrometer-sized strands in a single optical fiber with diameters ranging from 800 μm to 1.4 mm. The image guide fiber bundle can be used to transmit a focused light spot or transmit an image with minimal distortion.

Three different endoscopic systems are reported in this dissertation.

- (1) A fiber-based optical-resolution photoacoustic microscopy using image guide fibers and a unique fiber laser system for in contact applications is demonstrated. The image-guide consists of 30,000 individual fibers in a bundle 800 μm in diameter which provides transmission of a tight focused laser spot in a compact, flexible fiber. This proposed system permits label-free realtime imaging of capillary-scale biology all from the tip of a fiber-catheter. This system could have significant clinical impact for microendoscopic applications where the thin fiber can be inserted into body cavities.
- (2) A gradient index (GRIN)-lens based OR-PAM endoscopic system is demonstrated for improving the lateral resolution and depth sectioning. The proposed system, with about ~ 2 mm working distance, extends the optically focused penetration depth to ~ 1 mm, the transport-mean free path in tissue. Additionally, when focusing below the skin surface, surface fluence is significantly lower than the first version of OR-PAME, offering improved safety. The small footprint of the system, ~ 1.8 mm, gives the potential to be

useful for clinical endoscopy applications when the thin fiber is inserted into body cavities.

- (3) The third version of OR-PAME using an ultrasound linear array transducer is demonstrated. Array-based optical-resolution photoacoustic micro-endoscopy offers several advantages over previous systems. First, photoacoustic acquisition and endoscope guidance use the same ultrasound transducer, reducing the required complexity of the setup. Second, positioning of the fiber can be aided with realtime B-mode ultrasound. Finally, delay-and sum beamforming can be used to enhance the photoacoustic signals in the imaging plane by refocusing signals, meaning that fiber placement within the visual field of the array transducer does not need to be controlled precisely to capture an endoscopic image. This approach has the added benefit of being possible with a sufficiently fast ultrasound array system adapted for photoacoustic beamforming

1.3.2 Handheld optical resolution photoacoustic micro-endoscopy

We have pioneered the design of a flexible handheld optical-resolution photoacoustic microscope. The footprint of the proposed system is about 4 cm by 6 cm with weight of less than 500 g using image guide fibers and a unique fiber laser system. We anticipate that this system will open up new possibilities for clinical and pre-clinical uses, such as functional brain mapping, cancer imaging and detection, assessing completeness of melanoma resection, imaging of angiogenesis to assess therapeutic efficacy, etc. The proposed label-free system will have potential for translational research because it will be compact and potentially portable, real-time, cost-effective. It will permit clinical imaging of different parts of body that were previously inaccessible.

1.3.3 In-vivo optical-resolution photoacoustic microscopy with stimulated Raman scattering fiber-laser source

In previous SRS multi-wavelength photoacoustic imaging systems, the number of wavelength bands was limited, as was the pulse-energy. *In vivo* imaging and near-infrared wavelengths were not demonstrated. In this work we pursued two important goals:

- (1) To significantly increase the number of output wavelengths to extend to the near-infrared range, to increase energy per-band, and to ensure minimal SRS peak spectral-widths. Previous designs may not have had sufficient pulse energy to achieve *in vivo* functional imaging capabilities. Our work reports on an optimization strategy to maximize pulse energies per wavelength and is not as simple as maximizing input power. The functional imaging capabilities were assessed by determining dye concentrations in tubes and estimating the oxygen saturation levels in Swiss Webster mouse ear vasculature. Number of wavelength peaks, narrower spectral linewidths, and tunable repetition-rates are also advantages compared to previous work which may lead to many new possibilities for an all-fiber functional photoacoustic imaging source.
- (2) To perform depth scanning by wavelength tuning. We take advantage of chromatic aberration in the collimating/objective lens pair used to refocus light from a fiber into the object so that each wavelength is focused at a slightly different depth location. We use multiple wavelengths simultaneously for improved depth of field imaging. For imaging the microvasculature, wavelength-tuned depth scanning or simultaneous wavelength multifocal imaging may prove less ideal for functional imaging tasks, but may prove valuable for structural imaging of microvasculature morphology.

1.3.4 Optical resolution photoacoustic microscopy using glancing angle deposited nanostructured Fabry-Perot etalons

Previous work on optical-based ultrasound detection includes Fabry-Perot interferometer (FPI), micro-ring resonators (MRRs), and other types of interferometric sensing. Adapting these methods for reflection-mode optical-resolution photoacoustic microscopy has been challenging. Most MRRs fabricated on silicon substrates are optically opaque therefore, to

image in reflection mode, the MRR and the optical scanning area need to be physically far from each other, or the resulting PAM system could be implemented in transmission configuration, which is not practical for imaging thick biological samples. Recently a miniaturized, optically-transparent ultrasonic detector was developed. However, only phantom imaging was demonstrated. Even with such a transparent substrate, the micro-ring resonator was in a different lateral location than the optical scanning. Other interferometric sensing approaches including Fabry-Perot-based methods have yet to achieve *in vivo* reflection-mode optical-resolution imaging. In the proposed approach the effective optical sensing area on the FPI is scanned with the excitation spot as close to the source as possible. This co-scanning of excitation and probe beams can be critical for high-signal-to-noise ratio *in vivo* imaging. Challenges of all-optical PA imaging with optical resolution include damage thresholds, co-alignment of excitation and interrogation beams, and ensuring adequate *in vivo* sensitivity for low pulse energies. For the first time we have demonstrated a FPI-based ultrasound detector fabricated using glancing angle deposited (GLAD) nanostructured thin films for *in vivo* optical resolution PA imaging. The nanostructured GLAD is a single-step physical vapor-deposition (PVD) technique used to fabricate nanostructured thin films. By employing substrate motion and obliquely incident vapor flux, characteristic porous arrays of columnar structures can be produced from a range of organic, semiconductor, and dielectric materials.

1.3.5 Photoacoustic remote sensing

For the first time, we have developed a new non-contact optical bio-microscopy modality that we call Optical-Resolution Photoacoustic Remote Sensing microscopy. We optically focus a pulsed excitation laser into superficial tissues to generate very high micro-scale initial pressures. Then we harvest these large optically-focused photoacoustic signals as close to the photoacoustic source as possible. This is done by detecting photoacoustic signals using a confocal interrogation beam co-focused and co-scanned with the excitation spot. This approach may provide signal enhancement factors on the order of 10,000 or more compared to non-confocal sister techniques as discussed in chapter 11. Owing to the very large nature of these signals, we anticipate that PARS microscopy could prove a significant and important

new non-contact imaging modality similar to optical-resolution photoacoustic microscopy but without the requirement for ultrasound transducers or acoustic coupling.

1.4. Organization of this dissertation

The dissertation is organized as following:

Chapter 2 provides background information on optical imaging systems, the principle of photoacoustic imaging and literature review on the development of OR-PAM. The work presented in this dissertation can be divided into four parts. The first part (chapter 3-6) is focused on endoscopic and handheld designs. The second part (chapter 7 and 8) is focused on functional and multi-focus stimulated Raman scattering OR-PAM. The third part (chapter 9 and 10) is focused on optical detection of ultrasound and OR-PAM imaging using glancing angle deposited nanostructured thin films. The fourth part (chapter 11) is focused on the ultrasound and photoacoustic remote sensing system. Chapter 12 is a summary of contributions, offers conclusions and discusses future work. Contents of this dissertation (chapter 3 to 11) are drawn from the publications with permissions listed as following:

- [1] P. Hajireza, W. Shi, and R. J. Zemp, "Label-free *in vivo* fiber-based optical-resolution photoacoustic microscopy," *Opt. Lett.* 36, 4107-4109 (2011) (also Vol. 6, Iss. 11 *Virtual Journal for Biomedical Optics*).
- [2] P. Hajireza, W. Shi and R. J. Zemp, "Label-Free *In vivo* GRIN-Lens Optical Resolution Photoacoustic Micro-Endoscopy ", *Laser Phys. Lett.* 10 055603 (2013).
- [3] Parsin Hajireza, Tyler Harrison, Alexander Forbrich and Roger Zemp "Optical resolution photoacoustic microendoscopy with ultrasound-guided insertion and array system detection", *J. Biomed. Opt.* 18(9), 090502 (2013).
- [4] Parsin Hajireza, Wei Shi, and Roger J. Zemp, "Real-time handheld optical-resolution photoacoustic microscopy," *Opt. Express* 19, 20097-20102 (2011) (also Vol. 6, Iss. 11 *Virtual Journal for Biomedical Optics*).
- [5] Parsin Hajireza, Alexander Forbrich and Roger J. Zemp" In-vivo functional optical-resolution photoacoustic microscopy with stimulated Raman scattering fiber-laser source" *Biomed. Opt. Express* 5, 539-546 (2014).
- [6] Parsin Hajireza, Alexander Forbrich, and Roger J. Zemp, "Multifocus optical-resolution photoacoustic microscopy using stimulated Raman scattering and chromatic aberration," *Opt. Lett.* 38, 2711-2713 (2013).

- [7] Parsin Hajireza, Kathleen Krause, Michael Brett, and Roger Zemp, "Glancing angle deposited nanostructured film Fabry-Perot etalons for optical detection of ultrasound," *Optics Express* 21, 6391-6400 (2013) (also Vol. 8, Iss. 4 *Virtual Journal for Biomedical Optics*).
- [8] Parsin Hajireza, Jason Sorge, Michael Brett, and Roger Zemp, "*In vivo* optical resolution photoacoustic microscopy using glancing angle-deposited nanostructured Fabry-Perot etalons," *Opt. Lett.* 40, 1350-1353 (2015).
- [9] Parsin Hajireza, Wei Shi and Roger Zemp, "Photoacoustic remote sensing (PARS)" (submitted, 2015).

Bibliography

1. Viator, J.A., et al., *A Comparative Study of Photoacoustic and Reflectance Methods for Determination of Epidermal Melanin Content*. J Invest Dermatol, 2004. **122**(6): p. 1432-1439.
2. Wang, L.V. and H.-I. Wu, *Biomedical Optics*. 2009, Wiley-Blackwell.
3. Beard, P., *Biomedical photoacoustic imaging*. Interface Focus, 2011. **1**(4): p. 602-631.
4. Zemp, R.J., et al., *Realtime photoacoustic microscopy in vivo with a 30-MHz ultrasound array transducer*. Opt. Express, 2008. **16**(11): p. 7915.
5. Xu, M. and L.V. Wang, *Photoacoustic imaging in biomedicine*. Rev. Sci. Instrum., 2006. **77**(4): p. 041101.
6. Su, J.L., et al., *Advances in Clinical and Biomedical Applications of Photoacoustic Imaging*. Expert opinion on medical diagnostics, 2010. **4**(6): p. 497-510.
7. Yao, J. and L.V. Wang, *Breakthroughs in Photonics 2013: Photoacoustic Tomography in Biomedicine*. IEEE Photonics J., 2014. **6**(2): p. 1-6.
8. Wang, X., et al., *Noninvasive laser-induced photoacoustic tomography for structural and functional in vivo imaging of the brain*. Nature Biotechnology, 2003. **21**(7): p. 803-806.
9. Maslov, K., et al., *Optical-resolution photoacoustic microscopy for in vivo imaging of single capillaries*. Opt. Lett., 2008. **33**(9): p. 929.
10. Zhang, E.Z., et al., *In vivo high-resolution 3D photoacoustic imaging of superficial vascular anatomy*. Physics in Medicine and Biology, 2009. **54**(4): p. 1035-1046.
11. Hu, S. and L.V. Wang, *Photoacoustic imaging and characterization of the microvasculature*. J. Biomed. Opt., 2010. **15**(1): p. 011101.
12. Hajireza, P., W. Shi, and R.J. Zemp, *Real-time handheld optical-resolution photoacoustic microscopy*. Opt Express, 2011. **19**(21): p. 20097-102.
13. Hajireza, P., W. Shi, and R.J. Zemp, *Label-free in vivo fiber-based optical-resolution photoacoustic microscopy*. Opt Lett, 2011. **36**(20): p. 4107-9.
14. Xia, J., et al., *Wide-field two-dimensional multifocal optical-resolution photoacoustic computed microscopy*. Optics letters, 2013. **38**(24): p. 5236-5239.
15. Hu, S., et al., *Functional transcranial brain imaging by optical-resolution photoacoustic microscopy*. J. Biomed. Opt., 2009. **14**(4): p. 040503.
16. Xie, Z., et al., *Laser-scanning optical-resolution photoacoustic microscopy*. Opt. Lett., 2009. **34**(12): p. 1771.
17. Rao, B., et al., *Hybrid-scanning optical-resolution photoacoustic microscopy for in vivo vasculature imaging*. Opt. Lett., 2010. **35**(10): p. 1521.
18. Zhang, C., K. Maslov, and L.V. Wang, *Subwavelength-resolution label-free photoacoustic microscopy of optical absorption in vivo*. Optics letters, 2010. **35**(19): p. 3195-3197.
19. Hu, S., et al., *Intravital imaging of amyloid plaques in a transgenic mouse model using optical-resolution photoacoustic microscopy*. Opt. Lett., 2009. **34**(24): p. 3899.
20. Hu, S., K. Maslov, and L.V. Wang, *Noninvasive label-free imaging of microhemodynamics by optical-resolution photoacoustic microscopy*. Opt. Express, 2009. **17**(9): p. 7688.

21. Hu, S., K. Maslov, and L.V. Wang, *In vivo functional chronic imaging of a small animal model using optical-resolution photoacoustic microscopy*. Medical Physics, 2009. **36**(6): p. 2320.
22. Shi, W., et al., *Optical resolution photoacoustic microscopy using novel high-repetition-rate passively Q-switched microchip and fiber lasers*. J. Biomed. Opt., 2010. **15**(5): p. 056017.
23. Zhang, E.Z., et al., *Multimodal simultaneous photoacoustic tomography, optical resolution microscopy, and OCT system*, in *Photons Plus Ultrasound: Imaging and Sensing 2010*. 2010, SPIE-Intl Soc Optical Eng.
24. Wang, L., et al., *Fast voice-coil scanning optical-resolution photoacoustic microscopy*. Opt. Lett., 2011. **36**(2): p. 139.
25. Hu, S., K. Maslov, and L.V. Wang, *Second-generation optical-resolution photoacoustic microscopy with improved sensitivity and speed*. Opt. Lett., 2011. **36**(7): p. 1134.
26. Rao, B., et al., *Real-time four-dimensional optical-resolution photoacoustic microscopy with Au nanoparticle-assisted subdiffraction-limit resolution*. Opt. Lett., 2011. **36**(7): p. 1137.
27. Song, L., K. Maslov, and L.V. Wang, *Multifocal optical-resolution photoacoustic microscopy in vivo*. Opt. Lett., 2011. **36**(7): p. 1236.
28. Hu, S., K. Maslov, and L.V. Wang, *Three-dimensional Optical-resolution Photoacoustic Microscopy*. Journal of Visualized Experiments, 2011(51).
29. Shi, W., et al., *In vivo near-realtime volumetric optical-resolution photoacoustic microscopy using a high-repetition-rate nanosecond fiber-laser*. Opt Express, 2011. **19**(18): p. 17143-50.
30. Maslov, K., S. Hu, and L.V. Wang, *Second generation optical-resolution photoacoustic microscopy*, in *Photons Plus Ultrasound: Imaging and Sensing 2011*. 2011, SPIE-Intl Soc Optical Eng.
31. Yao, J., et al., *Label-free oxygen-metabolic photoacoustic microscopy in vivo*. Journal of Biomedical Optics, 2011. **16**(7): p. 076003.
32. Xing, W., et al., *Integrated optical- and acoustic-resolution photoacoustic microscopy based on an optical fiber bundle*. Opt. Lett., 2012. **38**(1): p. 52.
33. Liu, Y., C. Zhang, and L.V. Wang, *Effects of light scattering on optical-resolution photoacoustic microscopy*. J. Biomed. Opt, 2012. **17**(12): p. 126014.
34. Shao, P., et al., *Integrated micro-endoscopy system for simultaneous fluorescence and optical-resolution photoacoustic imaging*. J Biomed Opt, 2012. **17**(7): p. 076024.
35. Krumholz, A., et al., *Functional photoacoustic microscopy of diabetic vasculature*. Journal of Biomedical Optics, 2012. **17**(6): p. 060502.
36. Liao, L.-D., et al., *Transcranial imaging of functional cerebral hemodynamic changes in single blood vessels using in vivo photoacoustic microscopy*. Journal of Cerebral Blood Flow & Metabolism, 2012. **32**(6): p. 938-951.
37. Li, G., K.I. Maslov, and L.V. Wang, *Reflection-mode multifocal optical-resolution photoacoustic microscopy*. J. Biomed. Opt, 2013. **18**(3): p. 030501.
38. Liang, J., et al., *Random-access optical-resolution photoacoustic microscopy using a digital micromirror device*. Opt. Lett., 2013. **38**(15): p. 2683.

39. Hu, S. and Lihong V. Wang, *Optical-Resolution Photoacoustic Microscopy: Auscultation of Biological Systems at the Cellular Level*. Biophysical Journal, 2013. **105**(4): p. 841-847.
40. Liang, J., et al., *Cross-correlation-based transverse flow measurements using optical resolution photoacoustic microscopy with a digital micromirror device*. J. Biomed. Opt., 2013. **18**(9): p. 096004.
41. Xia, J., et al., *Wide-field two-dimensional multifocal optical-resolution photoacoustic-computed microscopy*. Opt. Lett., 2013. **38**(24): p. 5236.
42. Hajireza, P., A. Forbrich, and R.J. Zemp, *Multifocus optical-resolution photoacoustic microscopy using stimulated Raman scattering and chromatic aberration*. Opt Lett, 2013. **38**(15): p. 2711-3.
43. Hajireza, P., et al., *Glancing angle deposited nanostructured film Fabry-Perot etalons for optical detection of ultrasound*. Opt Express, 2013. **21**(5): p. 6391-400.
44. Shi, W., et al., *In vivo dynamic process imaging using real-time optical-resolution photoacoustic microscopy*. J Biomed Opt, 2013. **18**(2): p. 26001.
45. Xing, W., et al., *Integrated optical- and acoustic-resolution photoacoustic microscopy based on an optical fiber bundle*. Optics letters, 2013. **38**(1): p. 52-54.
46. Zhang, Y.S., et al., *Optical-Resolution Photoacoustic Microscopy for Volumetric and Spectral Analysis of Histological and Immunochemical Samples*. Angew. Chem. Int. Ed., 2014. **53**(31): p. 8099-8103.
47. Yang, Z., et al., *Multi-parametric quantitative microvascular imaging with optical-resolution photoacoustic microscopy in vivo*. Opt. Express, 2014. **22**(2): p. 1500.
48. Li, L., et al., *Fully motorized optical-resolution photoacoustic microscopy*. Opt. Lett., 2014. **39**(7): p. 2117.
49. Hai, P., et al., *Near-infrared optical-resolution photoacoustic microscopy*. Opt. Lett., 2014. **39**(17): p. 5192.
50. Zhu, L., et al., *Multiview optical resolution photoacoustic microscopy*. Optica, 2014. **1**(4): p. 217.
51. Hajireza, P., A. Forbrich, and R. Zemp, *In-Vivo functional optical-resolution photoacoustic microscopy with stimulated Raman scattering fiber-laser source*. Biomedical Optics Express, 2014. **5**(2): p. 539-546.
52. Liu, W., et al., *In vivo corneal neovascularization imaging by optical-resolution photoacoustic microscopy*. Photoacoustics, 2014. **2**(2): p. 81-86.
53. Rao, B., et al., *Integrated photoacoustic, confocal, and two-photon microscope*. Journal of Biomedical Optics, 2014. **19**(3): p. 036002.
54. Yang, J.-M., et al., *Optical-resolution photoacoustic endomicroscopy in vivo*. Biomed. Opt. Express, 2015. **6**(3): p. 918.
55. Kim, J.Y., et al., *Fast optical-resolution photoacoustic microscopy using a 2-axis water-proofing MEMS scanner*. Scientific Reports, 2015. **5**: p. 7932.
56. Hajireza, P., et al., *In vivo optical resolution photoacoustic microscopy using glancing angle-deposited nanostructured Fabry-Perot etalons*. Opt Lett, 2015. **40**(7): p. 1350-3.

57. Lin, R., et al., *Longitudinal label-free optical-resolution photoacoustic microscopy of tumor angiogenesis in vivo*. Quantitative Imaging in Medicine and Surgery, 2015. **5**(1): p. 23-29.
58. Liu, M., et al., *Dual modality optical coherence and whole-body photoacoustic tomography imaging of chick embryos in multiple development stages*. Biomedical Optics Express, 2014. **5**(9): p. 3150-3159.
59. Pillai, R.S., D. Lorensen, and D.D. Sampson, *Deep-tissue access with confocal fluorescence microendoscopy through hypodermic needles*. Opt. Express, 2011. **19**(8): p. 7213.
60. Jung, J.C., *In Vivo Mammalian Brain Imaging Using One- and Two-Photon Fluorescence Microendoscopy*. Journal of Neurophysiology, 2004. **92**(5): p. 3121-3133.
61. Hur, C., *High-resolution microendoscopy for esophageal cancer screening in China: A cost-effectiveness analysis*. WJG, 2015. **21**(18): p. 5513.
62. Yang, J.-M., et al., *Photoacoustic endoscopy*. Opt. Lett., 2009. **34**(10): p. 1591.
63. Rowland, K.J., et al., *Immediate Alterations in Intestinal Oxygen Saturation and Blood Flow Following Massive Small Bowel Resection As Measured By Photoacoustic Microscopy*. Journal of Pediatric Surgery, 2012. **47**(6): p. 1143-1149.
64. Wu, D., et al., *Contrast Agents for Photoacoustic and Thermoacoustic Imaging: A Review*. International Journal of Molecular Sciences, 2014. **15**(12): p. 23616-23639.
65. Paproski, R.J., et al., *Multi-wavelength photoacoustic imaging of inducible tyrosinase reporter gene expression in xenograft tumors*. Scientific Reports, 2014. **4**.
66. Wang, L.V., *Photoacoustic Imaging and Spectroscopy*, in *Optical Science and Engineering*. 2009, CRC Press.
67. Yao, L., L. Xi, and H. Jiang, *Photoacoustic computed microscopy*. Scientific Reports, 2014. **4**.
68. Billeh, Y.N., M. Liu, and T. Buma, *Spectroscopic photoacoustic microscopy using a photonic crystal fiber supercontinuum source*. Opt. Express, 2010. **18**(18): p. 18519.

2. Background

2.1 Optical imaging

Optical imaging is a non-invasive technique for imaging structural, functional and molecular details. Optical imaging methods take advantage of non-ionizing radiation, unlike other imaging methods, e.g. x-rays. Therefore, optical imaging methods may significantly reduce patient exposure to harmful radiation. They are much safer for patients, may offer high imaging speed and hence they can be used for longitudinal studies to monitor the progression of disease or the results of treatment [1-3]. There are various type of optical imaging systems including: Optical Coherence Tomography (OCT) [3-11], two photon microscopy [12-16], Diffuse Optical Tomography (DOT)[17-21], Raman Spectroscopy [22-28], Super-resolution Microscopy[29-34], and others.

OCT is a mature technology that typically takes advantage of optical scattering for obtaining sub-surface images. Commercial OCT systems are available for use in a variety of diagnostic medicine applications, including retinal and coronary artery diseases[7]. OCT is based on optical interference and inteferograms between a sample and a reference beam are mapped to a depth tomogram[10].

Two-photon microscopy is a fluorescence imaging technique that provides distinct advantages for three-dimensional imaging. Two-photon excitation can be a superior alternative to confocal microscopy systems due to its deeper tissue penetration (~1 mm) and better signal to noise ratio[12]. Two-photon microscopy has been used in different applications including, physiology, neurobiology, embryology and tissue engineering [12, 13]

DOT is a deep optical imaging technology that uses multiple source-detector pairs on the surface of a subject[1]. By solving an ill-posed inverse problem DOT reconstructs maps of optical absorption and scattering distributions. DOT enables researchers to study physiological processes including metabolism and hemodynamics and is capable of reconstructing quantitative maps of optical properties. It however, offers poor spatial resolution limited by light scattering in tissue[1].

Raman Spectroscopy relies on Raman scattering. It is widely applied to applications for identifying chemical compounds and characterizing the structure of materials and crystals[24]. Several variations of Raman spectroscopy have been developed including, surface-enhanced Raman spectroscopy[35], Stimulated Raman Microscopy[28] and coherent anti-stokes Raman spectroscopy (CARS)[36]. These microscopy techniques, however, are limited in depth to only a couple hundred microns in tissue[26].

Super-resolution Microscopy methods are capable of providing sub-diffraction limited resolution imaging of subcellular structure, at a level of detail not feasible using normal microscopy [29-32].

Each of these biomedical optical imaging modalities have respective advantages and disadvantages. Photoacoustic imaging, as the main focus of this dissertation, is an emerging hybrid biomedical optical imaging technique that offers high-resolution imaging of optical absorption, a capability not readily offered by other imaging modalities.

Photoacoustic imaging has been widely applied to pre-clinical applications in biology, vascular[37], ophthalmology[38], oncology[39], neurology[40], gastroenterology[41], dermatology[42] and etc.

2.2 Principle of photoacoustic imaging

The photoacoustic effect was first reported by Alexander Graham Bell in 1880[43]. However, in the last several years photoacoustic imaging has been developed rapidly for several biomedical applications [1, 44, 45]. Photoacoustic imaging is based on intrinsic high optical absorption contrast[44]. That means anything that absorbs light can be imaged by photoacoustic imaging [44, 46, 47]. Therefore several targets can be imaged by a photoacoustic imaging system including, oxyhemoglobin, deoxyhemoglobin, melanoma, lipids, RNA, DNA and others [1, 37, 44, 46, 47]. Optical absorption coefficients of biological tissues vary between 0.1 cm^{-1} and 100 cm^{-1} in the visible to near-infrared region [1, 37, 44, 46, 47]. Photoacoustic imaging is an important tool for functional imaging [44, 48-55] owing to blood-oxygenation-dependent optical absorption. Since optical scattering in soft tissues is two or three orders stronger than ultrasound scattering, photoacoustic imaging can offer

outstanding spatial resolution compared to other optical imaging systems in the quasi-diffusive or diffusive regime in biological tissues [1, 37, 44, 46, 47].

Photoacoustic imaging has multiple embodiments, including photoacoustic tomography (PAT) [16, 37, 40, 42, 46-48, 53, 56-64], photoacoustic microscopy (PAM) [44, 47, 49, 52, 54, 55, 65-79] and optical-resolution photoacoustic microscopy (OR-PAM) [41, 44, 50-52, 67, 71, 80-117]. In photoacoustic tomography (PAT) signals are collected from multiple transducer locations and reconstructed to form a tomographic image in a way similar to X-ray computed tomography. Typical PAM setups use loosely focused light and rely on the acoustic focal zone of the ultrasound transducer to achieve high spatial resolution [44, 46, 47]. A photoacoustic signal as a function of time (depth) is recorded for each position in a mechanically-raster-scanned trajectory to form a 3-D photoacoustic image. The maximum amplitude as a function of depth can be determined at each x-y scan position to form a maximum amplitude projection (MAP) C-scan image.

In 2005 and 2006 [54, 68] the first generation dark field reflection mode PAM system was reported (figure 2.1) using a tunable dye laser with a 10 Hz repetition rate (Q-switched pulsed Nd:YAG laser). As shown in figure 2.2 structural and functional microvasculature images of a mouse ear has been demonstrated [54, 68].

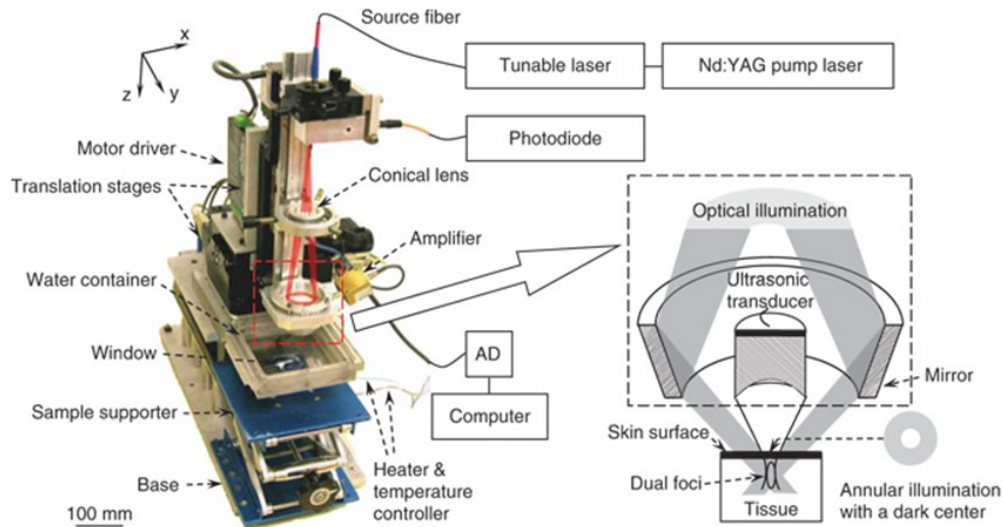


Figure 2.1: Experimental set-up of a dark field reflection mode PAM system [54]

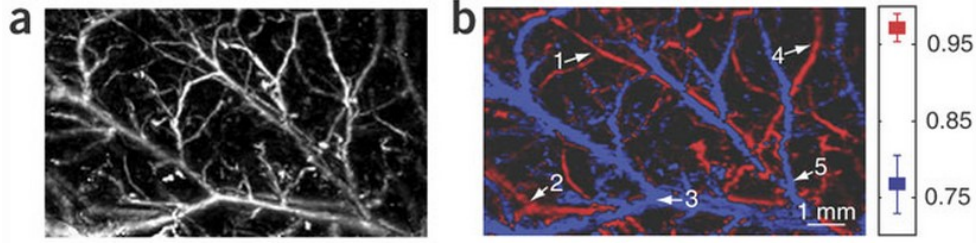


Figure 2.2: (a) Structural image. (b) Vessel-by-vessel sO₂ mapping.[54]

Later, PAM was used by different groups for imaging vascular structures from macro-vessels all the way down to micro-vessels [118-120], for functional and molecular imaging[11, 44, 48-55, 67, 70, 73, 76, 81, 121], including imaging using nanoparticle contrast agents [16, 62, 122-126] and imaging of gene expression [44, 127, 128]. Multi-wavelength photoacoustic imaging has been used for imaging of blood oxygen saturation [44, 67, 70], by using known oxy- and deoxy-hemoglobin molar extinction spectra.

2.2.1 Physical Principles of Photoacoustic Signal Generation

The efficiency of photoacoustic signals generation depends on thermal and stress confinement [1, 129]. Thermal relaxation time is characterized by the thermal diffusion of absorbed optical energy. It mathematically can be defined as $\tau_{th} = d_c^2 / \alpha_{th}$ in which d_c is the characteristic dimension, and α_{th} is the thermal diffusivity of the heated area[1, 129]. Stress relaxation time characterizes the pressure propagation. It mathematically can be defined as $\tau_s = d_c / v_s$, where v_s is the speed of sound. The local pressure induced by optical absorption via thermal expansion can be expressed as[1, 129]:

$$p_0 = \frac{\beta v_s^2}{c_p} \mu_a F = \Gamma \mu_a F \quad (1)$$

where β denotes the thermal coefficient of volume expansion in K^{-1} , C_p denotes the specific heat capacity at constant pressure in $J / (kg K)$, μ_a is the optical absorption coefficient in cm^{-1} , F is the optical fluence in J/cm^2 . $\Gamma = \frac{\beta v_s^2}{c_p}$ is the Gruneisen parameter.

The Gruneisen parameter is temperature dependent as the speed of sound and thermal coefficient of volume expansion are both temperature dependent. The following formula can be used to estimate the Gruneisen parameter for water[1, 129]:

$$\Gamma_w(T_0) = 0.0043 + 0.0053T_0 \quad (2)$$

where T_0 is the temperature in degrees Celsius. Therefore, the strength of the photoacoustic signal is proportional to the optical absorption coefficient, optical fluence, Gruneisen parameter, and is related to temperature.

OR-PAM uses scanned micron-scale focused light pulses to excite tissues and lateral spatial resolution is defined by optical rather than acoustic focusing [44, 46, 47].

2.3 Development of OR-PAM

The lateral resolution of OR-PAM is determined by the size of a focused light spot rather than the width of the ultrasonic focal zone [44, 46, 47]. The lateral resolution of OR-PAM is limited by the diffraction-limited focal spot size and derived from equation 3 where F is the focal length and D is the diameter of the laser beam. The axial resolution is still determined by time-resolved ultrasonic detection like the PAM systems. Axial resolution is inversely related to the bandwidth of transducer as defined in equation 4. Due to limitations of light transport, the penetration depth is limited to about 1 mm in tissue [1, 44].

$$\Delta R = 1.22 \frac{F}{D} \lambda \quad (3)$$

$$\text{Axial Resolution} = \frac{\text{Speed of sound in tissue}}{\text{Bandwidth}} \quad (4)$$

In 2008, Maslov et al[100] first reported OR-PAM with a micron scale lateral resolution and imaging depth of ~ 0.7 mm. Figure 2.3 and 2.4 shows the experimental setup and microvasculature images of a mouse ear respectively. Later in 2009, Xie et al.[111] developed a laser-scanning OR-PAM (LS-OR-PAM) system in which that fast-scanning

mirrors was used to scan the optical spot relative to a fixed ultrasound transducer. Many exciting OR-PAM techniques have been reported in the last few years for structural [84, 88, 89, 106-108] and functional imaging including oxygen saturation imaging[52, 67, 81, 97] and blood velocity imaging [70, 95, 130-133], amyloid plaques in a transgenic mouse model of Alzheimer’s disease[41], transcranial imaging of whole brain murine cortical capillary networks [50] and longitudinal monitoring of angiogenesis in a transgenic mouse model [97, 134, 135].

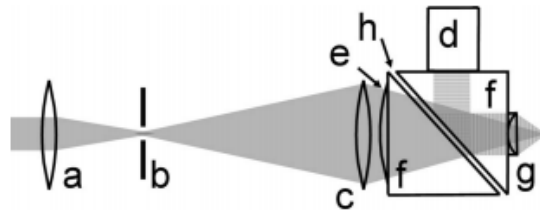


Figure 2.3: Schematic of the OR-PAM system. a: Condenser lens; b: pinhole; c: microscope objective; d: ultrasonic transducer; e: correcting lens; f: isosceles prism; g: acoustic lens; h:silicon oil.[100]

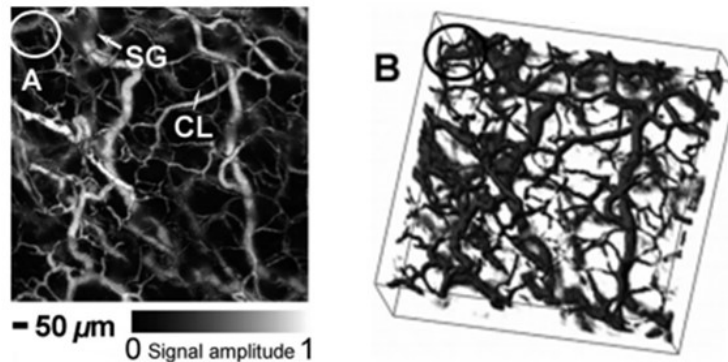


Figure 2.4: Microvasculature in a nude mouse ear. (a) In vivo OR-PAM image. (b) 3D pseudocolor visualization of the vasculature[100]

One of the most promising configurations for OR-PAM imaging is to take advantage of optical focusing for generation of photoacoustic signals and ultrasound focusing for detection as shown in 2011[88]. Figure 2.5 shows the second-generation OR-PAM with high spatial resolution (lateral: $\sim 5 \mu\text{m}$; axial: $\sim 15 \mu\text{m}$) [88, 136]. In this work, the laser pulses (with pulse energy of $\sim 100 \text{ nJ}$) pass through a $25\text{-}\mu\text{m}$ -diameter pinhole and then focused to the sample using a microscope objective lens and ultrasonic detection is achieved using a spherically focused ultrasonic transducer [88, 136].

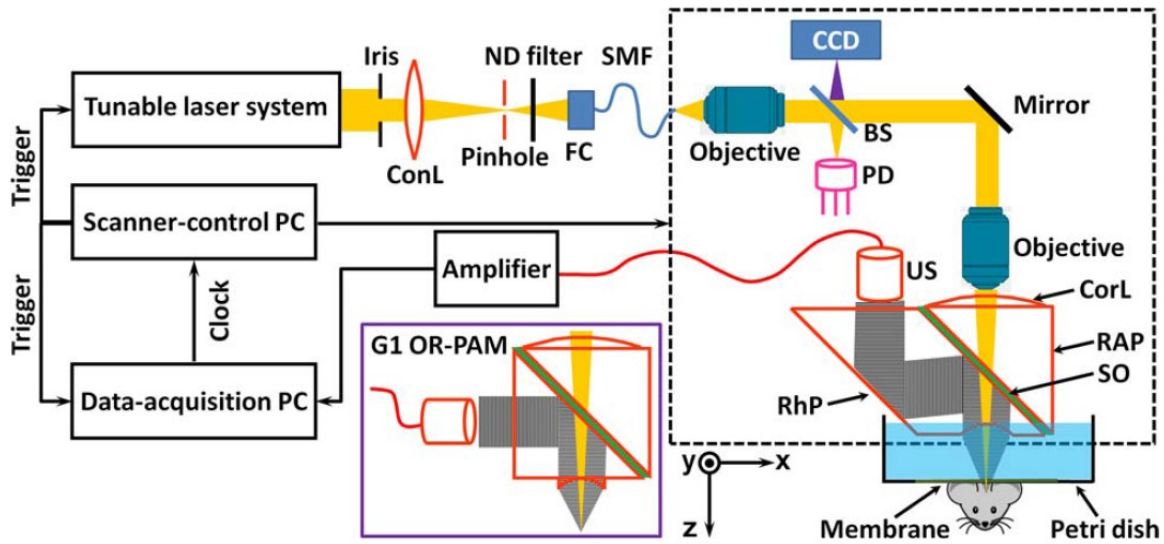


Figure 2.5: Experimental setup of the second-generation optical-resolution photoacoustic microscope.[88]

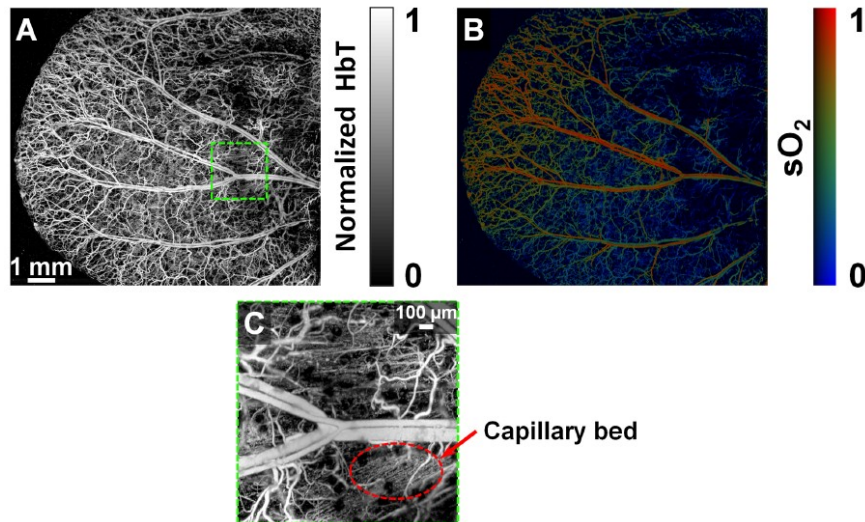


Figure 2.6: In vivo functional optical-resolution photoacoustic microscopy of a nude mouse ear. (a) Images of the total hemoglobin concentration and (b) Images of the hemoglobin oxygen saturation (c) zoom in images of the selected area shown in (a).[136]

Figure 2.6 shows the total hemoglobin concentration (figure 2.6a) and oxygen saturation (figure 2.6b) of hemoglobin in a mouse ear. The typical acquisition time to image a field of view of $10 \text{ mm} \times 10 \text{ mm}$ with a step size: $2.5 \text{ } \mu\text{m} \times 5 \text{ } \mu\text{m}$ is $\sim 80 \text{ min}$, which is 5 times speed improvement compare to the previous reported system by the same authors [88, 136].

2.3.1 Applications: Imaging angiogenesis

More than 90% of cancer death is due to metastasis [137]. A tumor in order to grow and reach to the metastatic spread phase needs to develop an independent blood network for supplying nutrients and oxygen and for removing waste products [138-147]. The growth of these abnormal blood vessels is called angiogenesis [7, 58, 70, 97, 104, 148-156]. Angiogenesis is responsible for tumor growth and metastasis [138-147]. Therefore, imaging angiogenesis to understand angiogenesis biology, and to develop anti-angiogenic pharmaceutical products are of great importance for cancer research [7, 58, 70, 97, 104, 138-164]. There are several modalities mainly used for imaging angiogenesis: x-ray computed tomography (CT) [156, 159, 161, 164, 165], magnetic resonance imaging (MRI) [19, 146, 166], positron emission tomography (PET) [151, 167, 168], ultrasound imaging [147, 157, 163, 169-171]. CT imaging usually requires large amount of “radiation dose” and does not offer enough resolution to resolve capillary networks [156, 159, 161, 164, 165]. MRI using non-ionizing radiation is capable of anatomic and functional imaging with good temporal and spatial resolution [19, 146, 166]. However, it still suffers from insufficient resolution to image smaller targets (e.g. capillaries). PET as a quantitative imaging technique offers poor spatial resolution compared to CT or MRI [151, 167, 168]. Ultrasound imaging can be used for imaging tumor vasculature [147, 157, 163, 169-171]. It can provide blood volume and perfusion information by using microbubbles as contrast agents [166].

Photoacoustic imaging offers high optical contrast between blood and tissue at significant depths unlike pure optical imaging systems due to low ultrasound scattering. The capability of imaging optical absorption based functional details down to the capillary level makes photoacoustic modalities unique for imaging angiogenesis. Photoacoustic tomography has been used for structural imaging of tumor angiogenesis in brains, and functional imaging of cerebral hemodynamic changes [57, 58, 97]. OR-PAM with micron-level lateral resolution has demonstrated its ability to image single capillaries [51, 90, 124]. In 2015, longitudinal OR-PAM of angiogenesis in a subcutaneous dorsal tumor model in mouse has been demonstrated [97]. Using OR-PAM, the most important features of tumor angiogenesis, including the change of vascular tortuosity, the dilation of vessel diameters, and the increase

of blood supply has been demonstrated [97]. Figure 2.7 shows Longitudinal OR-PAM of developing tumor angiogenesis at different days.

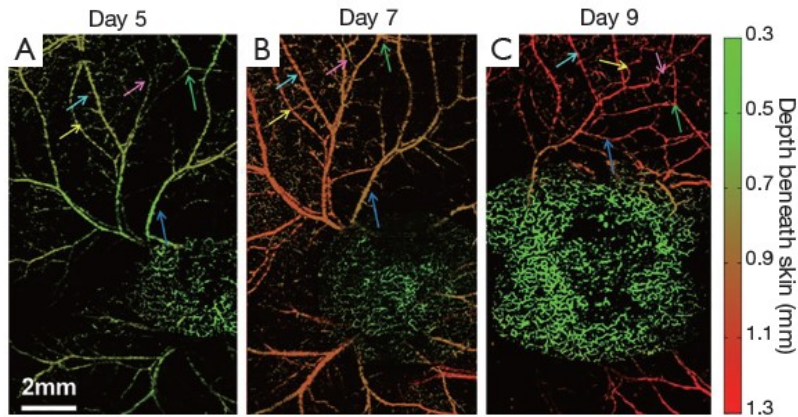


Figure 2.7: Longitudinal OR-PAM of developing tumor angiogenesis on (a) day 5; (b) day 7; and (c) day 9[97].

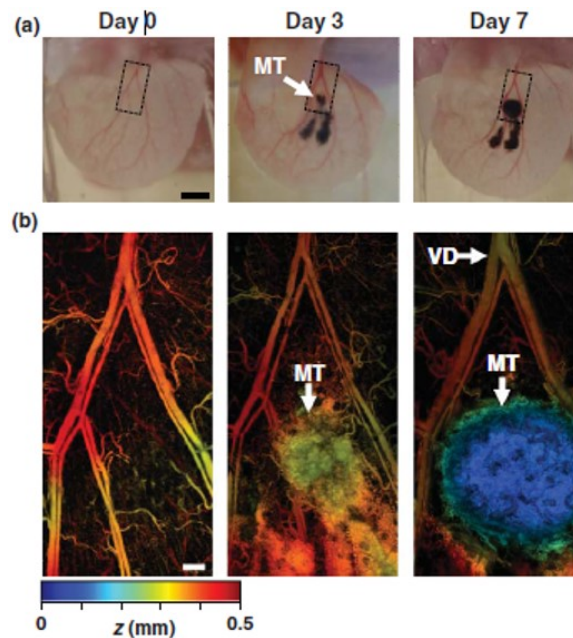


Figure 2.8: (a) White-light photographs of a representative mouse ear (b) OR-PAM images of the tumor region [dashed boxes in (a)]. MT: melanoma tumor; VD: vasodilatation.[172]

Photoacoustic imaging has also been applied for *in vivo* melanoma evaluation [42, 74, 130, 131, 173-175]. Recently OR-PAM has been applied for detection of early-stage melanoma

in vivo [172]. The hemodynamics of a mouse ear model were longitudinally monitored after the injection of melanoma cells as shown in figure 2.8.

2.3.2 Combination with other optical imaging systems

In the last several years various works have been dedicated for integration of photoacoustic imaging with other optical imaging systems including OCT [64, 176-178], Two-photon microscopy [16, 103], confocal microscopy[103] and fluorescence microscopy[104]. The combination of OR-PAM and OCT is one of the most attractive combinations. Photoacoustic tomography and OCT are capable of providing depth dependent information by taking advantage of acoustic and optical wave time-of-flight respectively [64, 176-178]. The lateral resolution of OCT is defined by the numerical aperture (NA) of the objective lens, while the axial resolution is given by the central optical wavelength and bandwidth [64, 176-178]. Integration of photoacoustic imaging and OCT is interesting as both can be label free and non-invasive. The absorption-based imaging contrast of photoacoustic imaging can be used for imaging the structure and oxygenation details of the microvasculature while the scattering based contrast of OCT can be used for imaging surrounding tissue microstructure. Although OCT has showed its ability to image blood vessel structures, the contrast is provided by the motion of red blood cells [153, 179]. Therefore, Doppler OCT cannot be used for imaging vascular occlusions due to the presence of static blood found in hemorrhages or certain microvascular pathologies [44, 64, 176, 178]. At the same time OCT unlike photoacoustic imaging is not background-free and suffers from speckle noises, polarization changes and scattering losses.

Figure 2.9 shows a multimodal simultaneous photoacoustic tomography, optical resolution microscopy and OCT system [178]. Figure 2.10 and 2.11 shows the result of OR-PAM, PET and OCT images using this multimodality imaging system [178].

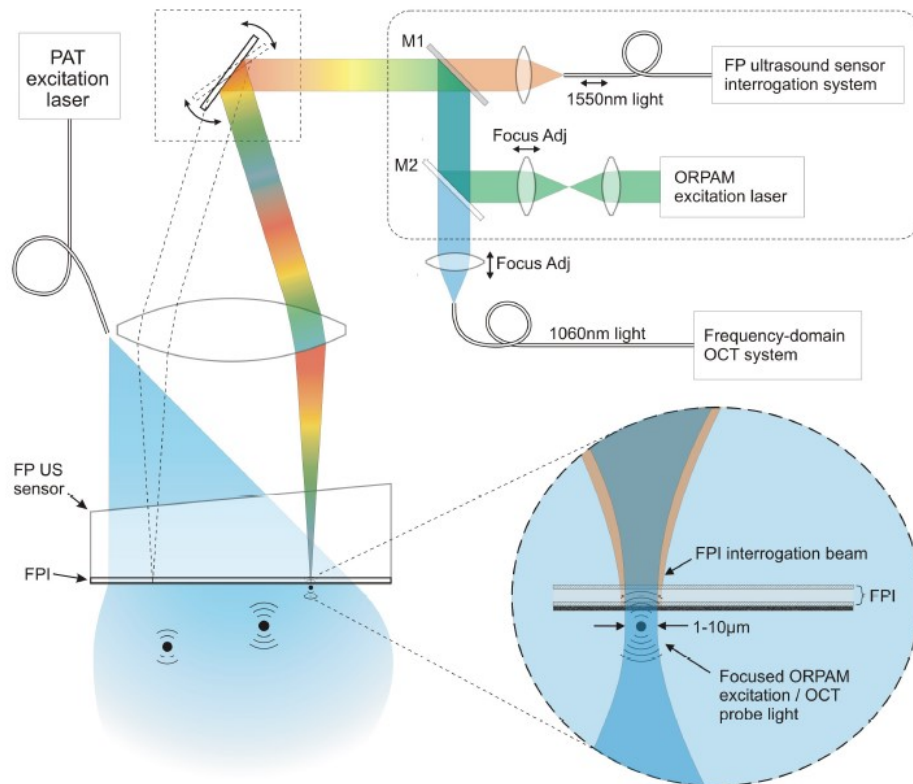


Figure 2.9: Schematic of combined PAT, ORPAM and OCT imaging system. M1 and M2: dichroic mirrors. FPI: Fabry Perot interferometer [178]

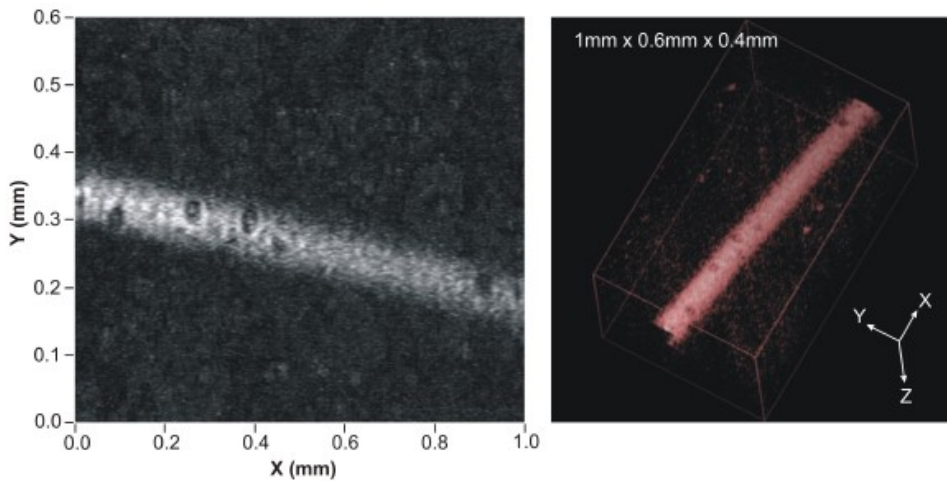


Figure 2.10: Left: Maximum intensity projection of an ORPAM image of a 62 μm bore PMMA capillary tube filled with human blood. [178]

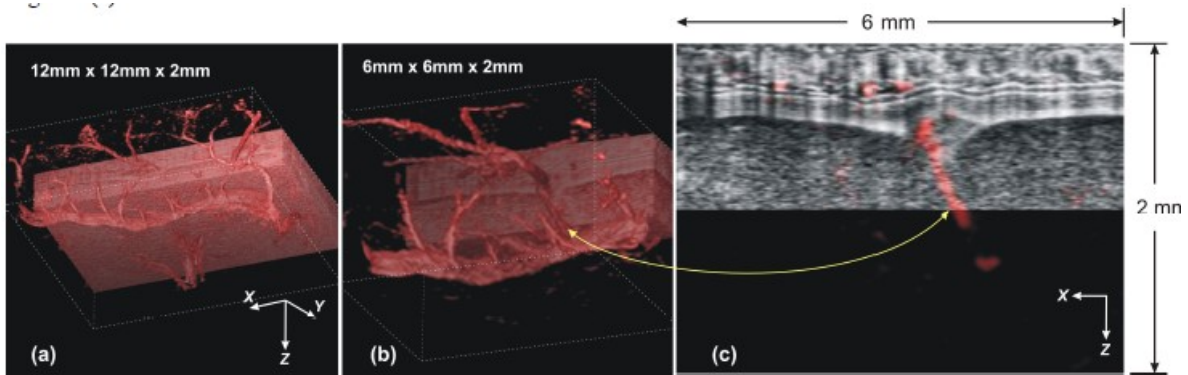


Figure 2.11: In vivo PAT and OCT imaging of the skin on the back of a nude mouse. (a) OCT and PAT images. (b) A close-up view of OCT and PAT image in (a) while part of the OCT data has been removed to reveal blood vessels (c) A cross-sectional image slice of the combined OCT-PAT image.[178]

2.4 Fabry Perot Interferometers for ultrasound detection

In most photoacoustic imaging techniques piezoelectric receivers are employed to detect the ultrasonic/acoustic signals [44, 83, 86, 180-183]. However, this suffers from several limitations. The first limitation is that using an external ultrasound transducer increase the footprint of the imaging probe [180-182]. Therefore the piezoelectric receivers particularly used for superficial imaging applications since sensitivity of piezoelectric detectors reduces with decreasing element size [180-182]. Another limitation is related to the delivery of the excitation laser beam and collection of the acoustics signals. These limitations technically prevent the extension of photoacoustic imaging applications beyond a transport mean free path (~ 1 mm in biological tissue) due to multiple scattering [1]. Therefore designing an alternative photoacoustic receiver to overcome these limitations is desirable. Different studies showed that a Fabry-Perot interferometer (FPI) can be a more sensitive receiver compared to piezoelectric receivers [44, 83, 86, 180-183]. Several teams have made considerable progress in this area, with work being done on Fabry-Perot etalons, micro-ring resonator devices, and fiber-Bragg grating approaches [180-187]. These detectors offer the high sensitivity and broad bandwidth important for photoacoustic imaging applications. For example, Xie, et al demonstrated microring resonators with sensitivity reaching 29 Pa [183]. Zhang et al has reported [181] a FPI sensor fabricated by sputtering two stacks of alternate $\lambda/4$ thick layers of ZnS and Na_3AlF_6 on to the backing stub and Parylene C polymer film

spacer with 310 Pa sensitivity over a bandwidth of 39 MHz [181]. They showed that the sensitivity of these FPI optical detectors could be significantly higher than piezoelectrics. Figure 2.12(a) shows a schematic of a Fabry-Perot polymer film ultrasound transducer[186]. The thickness of the spacing polymer film usually is in the order of 25-50 μm depending on the bandwidth required in the tens of MHz range [184-186]. The “mirrors” of the interferometer can be formed by depositing material including metallic, dielectric reflective coatings and Titanium dioxide, using different fabrication methods [83, 86, 180-182, 184-187] . The received acoustic pressure cause changes in the optical thickness of the film and then optical phase shift is converted to an intensity modulation through the intensity-phase transfer function of the interferometer as shown in figure 2.12(b) [184-186].

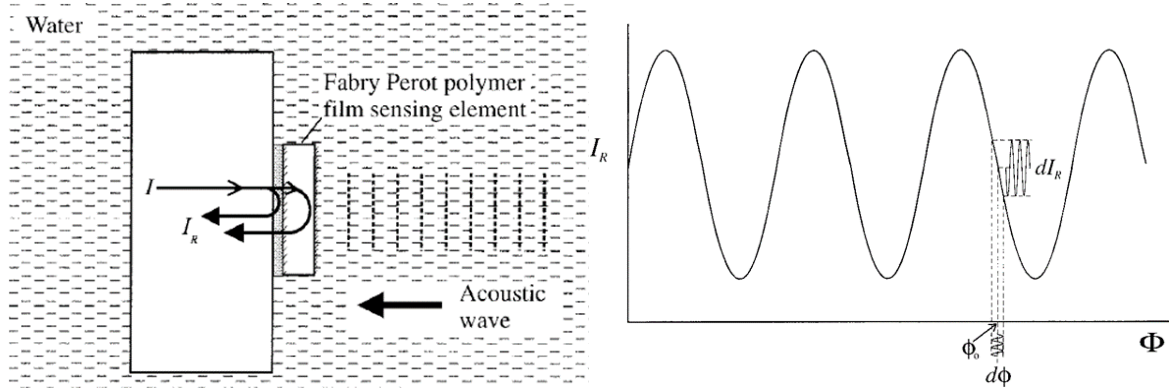


Figure 2.12: (a) schematic of a Fabry-Perot polymer film ultrasound transducer. (b) FPI transfer function.[186]

The phase sensitivity of a FPI (I_s) dependent upon the incident laser power and the reflectivity of the mirrors of the interferometer. I_s is mathematically defined by the slope efficiency of the conversion of optical phase $d\phi$ to intensity output dI_r as shown in formula 5[184,186].

$$I_s = \left[\frac{dI_r}{d\phi} \right]_{\phi_0} \quad (5)$$

The acoustic phase sensitivity (A_s) represents the conversion of detected acoustic pressure to an optical phase shift. The A_s depends upon elastic and photoelastic properties of the interferometer cavity and it is based on the acoustically-induced change in optical thickness of the FPI[184, 186].

$$A_s = \frac{d\phi}{dP} = \frac{4\pi n l}{\lambda} \frac{1}{E} \left(1 + \frac{n^2 p \sigma}{2} \right) |P_1(k)| \quad (6)$$

where n is the refractive index, l is the thickness of the film, λ the laser wavelength, E the Young's modulus, p the photoelastic constant, σ Poisson's ratio. k is the acoustic wavenumber, $k=2p/\lambda a$ where λa is the acoustic wavelength. $P_1(k)$ is a frequency-dependent modifying term representing the net stress integrated across the thickness of the sensing film. $|P(k)| \sim 2$ for a rigid backing such as glass [184]. The product of I_s and A_s gives the overall sensitivity.

2.5 Signal to noise ratio

The signal to noise ratio (SNR) is defined by the ratio of the average signal amplitude level to the background noise standard deviation on dB scale. A ratio greater than 0 dB indicates more signal than noise. In this dissertation the SNR has been calculated as:

$$\text{SNR} = 20 \log_{10} \left(\frac{S_{Ave}}{\sigma} \right) \quad (7)$$

Where S_{ave} is the average of the signal amplitude level and σ is the standard deviation of the background noise.

2.6 Glancing angle deposition (GLAD) method

GLAD is a single-step physical vapor-deposition (PVD) technique used to fabricate nanostructured thin films [188-192]. By employing substrate motion and obliquely incident vapor flux, characteristic porous arrays of columnar structures can be produced from a range of organic, semiconductor, and dielectric materials. The substrate motion can be defined by two parameters, (1) The deposition angle α and (2) Rotation angle ϕ .

The deposition angle α is defined as the angle subtended between the substrate normal and the incident vapor flux while the rotation angle ϕ is defined by rotation about the substrate as shown in figure 2.13[189].

The deposition plane is defined by plane containing the incident flux direction and the substrate normal. The GLAD apparatus as it is typically implemented in a standard PVD

system. Substrate movement is accomplished by two independent motors. The motors are computer controlled, receiving feedback from thickness monitors. Various devices such as optical filters, chromatographic plates, liquid crystal scaffolding, and solar cells have been created using the GLAD technique [188, 189]. Using materials such as titanium dioxide (TiO_2), a wide band gap and transparent semiconductor with a high refractive index ($n = 2.4$), the GLAD technique can be used to fabricate samples with tailored refractive index periodicities with a high level of control and hence provide high Q-factor reflectance spectra. By periodically altering the deposition angle, and thus the local density and refractive index of deposited columns sub-layers, GLAD photonic crystals (PCs) can be created with periodic wavelength-scale structure and resonant Bragg reflection [188, 189].

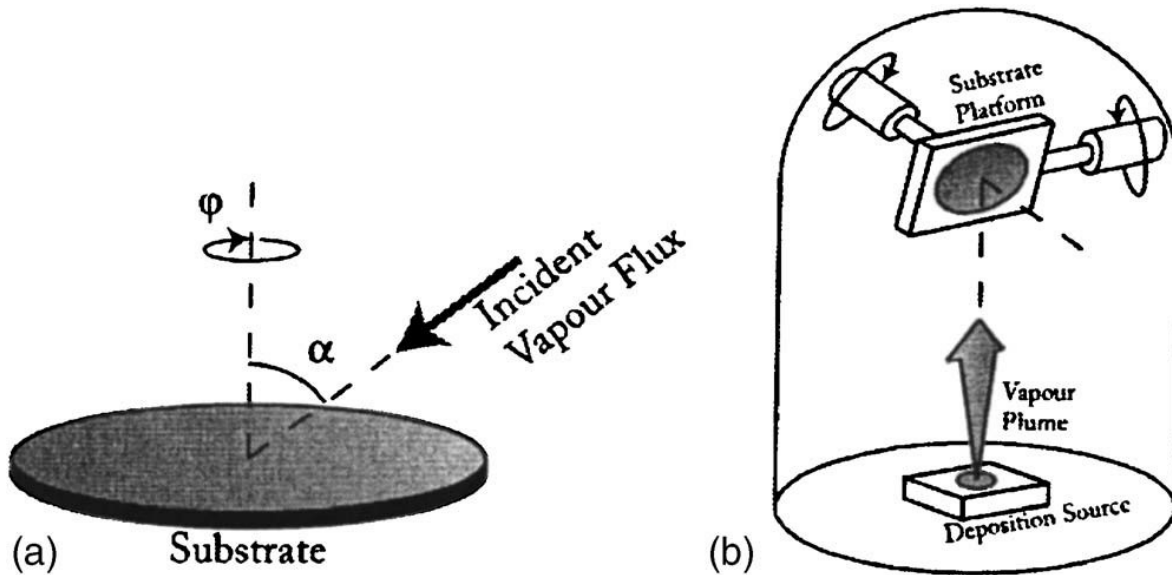


Figure 2.13: (a) definition of rotation and deposition angle. (b) GLAD-capable PVD system.[189]

2.7 Limitations

As it has been addressed in the introduction, in spite of all the great features of OR-PAM, there are still several challenges preventing its clinical applications. A design for a flexible handheld and micro-endoscopy probe was missing. Usually mechanical scanning was

utilized for depth scanning rather than a fast optical depth scanning. The sources of multi-wavelength lasers for functional imaging purposes was limited to low pulse repetition rates and hence, prevents realtime imaging. No FPI has been applied to reflection mode *in vivo* OR-PAM imaging. OR-PAM as an optical imaging technique unlike other competition is not all optical and non-contact. Most OR-PAM systems depend on bulky ultrasound transducers and ultrasound coupling medium such as water or ultrasound gel. Therefore integration of the OR-PAM systems with other optical imaging systems has been challenging. In this dissertation we have addressed many of these limitations.

Bibliography

1. Wang, L.V. and H.-I. Wu, *Biomedical Optics*. 2009, Wiley-Blackwell.
2. *Photoacoustic Imaging and Spectroscopy*, in *Optical Science and Engineering*. 2009, CRC Press.
3. Nioka, S. and Y. Chen, *Optical Tecnology Developments in Biomedicine: History, Current and Future*. Translational Medicine @ UniSa, 2011. **1**: p. 51-150.
4. Huang, D., et al., *Optical coherence tomography*. Science, 1991. **254**(5035): p. 1178-1181.
5. Lu, C.D., et al., *Handheld ultrahigh speed swept source optical coherence tomography instrument using a MEMS scanning mirror*. Biomed. Opt. Express, 2013. **5**(1): p. 293.
6. Weymouth, A., *Optical Coherence Tomography of Ocular Diseases 3 rd Edition* by Schuman JS, Puliafito CA, Fujimoto JG and Duker JS Thorofare, New Jersey, USA: Slack Inc, 2013 615 pages RRP \$358.84. Clinical and Experimental Optometry, 2014. **97**(2): p. 192-192.
7. Arevalo, J.F., et al., *Clinical applications of optical coherence tomography in the posterior pole: the 2011 José Manuel Espino Lecture – Part II*. Clinical Ophthalmology (Auckland, N.Z.), 2013. **7**: p. 2181-2206.
8. Fujimoto, J.G., et al., *Optical Coherence Tomography: An Emerging Technology for Biomedical Imaging and Optical Biopsy*. Neoplasia (New York, N.Y.), 2000. **2**(1-2): p. 9-25.
9. Gabriele, M.L., et al., *Optical Coherence Tomography: History, Current Status, and Laboratory Work*. Investigative Ophthalmology & Visual Science, 2011. **52**(5): p. 2425-2436.
10. Gutiérrez-Chico, J.L., et al., *Optical coherence tomography: from research to practice*. European heart journal cardiovascular Imaging, 2012. **13**(5): p. 370-384.
11. Hou, R., et al., *Recent advances in optical coherence tomography for the diagnoses of lung disorders*. Expert Review of Respiratory Medicine, 2011. **5**(5): p. 711-724.
12. Diaspro, A., G. Chirico, and M. Collini, *Two-photon fluorescence excitation and related techniques in biological microscopy*. Quart. Rev. Biophys., 2005. **38**(02): p. 97.
13. Helmchen, F. and W. Denk, *Deep tissue two-photon microscopy*. Nat Meth, 2005. **2**(12): p. 932-940.
14. Svoboda, K. and R. Yasuda, *Principles of Two-Photon Excitation Microscopy and Its Applications to Neuroscience*. Neuron, 2006. **50**(6): p. 823-839.
15. Crowe, S.E. and G.C.R. Ellis-Davies, *Longitudinal in vivo two-photon fluorescence imaging*. The Journal of comparative neurology, 2014. **522**(8): p. 1708-1727.
16. Zhang, Y.S., et al., *Labeling Human Mesenchymal Stem Cells with Gold Nanocages for in vitro and in vivo Tracking by Two-Photon Microscopy and Photoacoustic Microscopy*. Theranostics, 2013. **3**(8): p. 532-543.
17. Corlu, A., et al., *Three-dimensional in vivo fluorescence diffuse optical tomography of breast cancer in humans*. Opt. Express, 2007. **15**(11): p. 6696.

18. Culver, J.P., et al., *Three-dimensional diffuse optical tomography in the parallel plane transmission geometry: Evaluation of a hybrid frequency domain/continuous wave clinical system for breast imaging*. Medical Physics, 2003. **30**(2): p. 235.
19. Ntziachristos, V., et al., *Concurrent MRI and diffuse optical tomography of breast after indocyanine green enhancement*. Proceedings of the National Academy of Sciences, 2000. **97**(6): p. 2767-2772.
20. Custo, A., et al., *Anatomical Atlas-Guided Diffuse Optical Tomography of Brain Activation*. NeuroImage, 2010. **49**(1): p. 561-567.
21. Singh, H., et al., *Mapping cortical haemodynamics during neonatal seizures using diffuse optical tomography: A case study*. NeuroImage : Clinical, 2014. **5**: p. 256-265.
22. Brauchle, E. and K. Schenke-Layland, *Raman spectroscopy in biomedicine – non-invasive in vitro analysis of cells and extracellular matrix components in tissues*. Biotechnology Journal, 2013. **8**(3): p. 288-297.
23. Chen, K., et al., *Diagnosis of colorectal cancer using Raman spectroscopy of laser-trapped single living epithelial cells*. Opt. Lett., 2006. **31**(13): p. 2015.
24. Esmonde-White, K., *Raman Spectroscopy of Soft Musculoskeletal Tissues*. Applied spectroscopy, 2014. **68**(11): p. 1203-1218.
25. Jehlička, J., H.G.M. Edwards, and A. Oren, *Raman Spectroscopy of Microbial Pigments*. Applied and Environmental Microbiology, 2014. **80**(11): p. 3286-3295.
26. Li, Z., et al., *Raman Spectroscopy for In-Line Water Quality Monitoring — Instrumentation and Potential*. Sensors (Basel, Switzerland), 2014. **14**(9): p. 17275-17303.
27. Wang, Y. and J. Irudayaraj, *Surface-enhanced Raman spectroscopy at single-molecule scale and its implications in biology*. Philosophical Transactions of the Royal Society B: Biological Sciences, 2013. **368**(1611): p. 20120026.
28. Zhang, Y., H. Hong, and W. Cai, *Imaging with Raman Spectroscopy*. Current pharmaceutical biotechnology, 2010. **11**(6): p. 654-661.
29. Baddeley, D., et al., *4D Super-Resolution Microscopy with Conventional Fluorophores and Single Wavelength Excitation in Optically Thick Cells and Tissues*. PLoS ONE, 2011. **6**(5): p. e20645.
30. Galbraith, J.A. and C.G. Galbraith, *Super-resolution Microscopy for Nanosensing*. Wiley interdisciplinary reviews. Nanomedicine and nanobiotechnology, 2011. **3**(3): p. 247-255.
31. Habuchi, S., *Super-Resolution Molecular and Functional Imaging of Nanoscale Architectures in Life and Materials Science*. Frontiers in Bioengineering and Biotechnology, 2014. **2**: p. 20.
32. Huang, B., M. Bates, and X. Zhuang, *Super resolution fluorescence microscopy*. Annual review of biochemistry, 2009. **78**: p. 993-1016.
33. Lin, Y.-H. and D.P. Tsai, *Near-field scanning optical microscopy using a super-resolution cover glass slip*. Opt. Express, 2012. **20**(15): p. 16205.
34. Littleton, B., et al., *Coherent super-resolution microscopy via laterally structured illumination*. Micron, 2007. **38**(2): p. 150-157.

35. Sur, U.K., *Surface-enhanced Raman spectroscopy*. Resonance, 2010. **15**(2): p. 154-164.
36. Evans, C.L. and X.S. Xie, *Coherent Anti-Stokes Raman Scattering Microscopy: Chemical Imaging for Biology and Medicine*. Annual Review of Analytical Chemistry, 2008. **1**(1): p. 883-909.
37. Wang, L.V. and S. Hu, *Photoacoustic Tomography: In Vivo Imaging from Organelles to Organs*. Science, 2012. **335**(6075): p. 1458-1462.
38. Zhang, H.F., C.A. Puliafito, and S. Jiao, *Photoacoustic Ophthalmoscopy for In Vivo Retinal Imaging: Current Status and Prospects*. Ophthalmic Surgery, Lasers, and Imaging, 2011. **42**(4): p. S106-S115.
39. Mallidi, S., G.P. Luke, and S. Emelianov, *Photoacoustic imaging in cancer detection, diagnosis, and treatment guidance*. Trends in Biotechnology, 2011. **29**(5): p. 213-221.
40. Hu, S., *Neurovascular photoacoustic tomography*. Frontiers in Neuroenergetics, 2010.
41. Hu, S., et al., *Intravital imaging of amyloid plaques in a transgenic mouse model using optical-resolution photoacoustic microscopy*. Opt. Lett., 2009. **34**(24): p. 3899.
42. Kim, C., et al., *In Vivo Molecular Photoacoustic Tomography of Melanomas Targeted by Bioconjugated Gold Nanocages*. ACS Nano, 2010. **4**(8): p. 4559-4564.
43. Bell, A.G., *On the production and reproduction of sound by light*. American Journal of Science, 1880. **s3-20**(118): p. 305-324.
44. Beard, P., *Biomedical photoacoustic imaging*. Interface Focus, 2011. **1**(4): p. 602-631.
45. Xu, M. and L.V. Wang, *Photoacoustic imaging in biomedicine*. Rev. Sci. Instrum., 2006. **77**(4): p. 041101.
46. Jun, X. and L.V. Wang, *Small-Animal Whole-Body Photoacoustic Tomography: A Review*. IEEE Transactions on Biomedical Engineering, 2014. **61**(5): p. 1380-1389.
47. Wang, L.V. and L. Gao, *Photoacoustic Microscopy and Computed Tomography: From Bench to Bedside*. Annu. Rev. Biomed. Eng., 2014. **16**(1): p. 155-185.
48. Bai, X., et al., *Intravascular Optical-Resolution Photoacoustic Tomography with a 1.1 mm Diameter Catheter*. PLoS ONE, 2014. **9**(3): p. e92463.
49. Chatni, M.R., et al., *Functional photoacoustic microscopy of pH*. Journal of Biomedical Optics, 2011. **16**(10): p. 100503.
50. Hu, S., et al., *Functional transcranial brain imaging by optical-resolution photoacoustic microscopy*. J. Biomed. Opt., 2009. **14**(4): p. 040503.
51. Hu, S., K. Maslov, and L.V. Wang, *In vivo functional chronic imaging of a small animal model using optical-resolution photoacoustic microscopy*. Medical Physics, 2009. **36**(6): p. 2320.
52. Liao, L.-D., et al., *Transcranial imaging of functional cerebral hemodynamic changes in single blood vessels using in vivo photoacoustic microscopy*. Journal of Cerebral Blood Flow & Metabolism, 2012. **32**(6): p. 938-951.
53. Wang, X., et al., *Noninvasive laser-induced photoacoustic tomography for structural and functional in vivo imaging of the brain*. Nature Biotechnology, 2003. **21**(7): p. 803-806.

54. Zhang, H.F., et al., *Functional photoacoustic microscopy for high-resolution and noninvasive in vivo imaging*. Nat Biotechnol, 2006. **24**(7): p. 848-851.
55. Zhang, H.F., K. Maslov, and L.V. Wang, *In vivo imaging of subcutaneous structures using functional photoacoustic microscopy*. Nature Protocols, 2007. **2**(4): p. 797-804.
56. Anastasio, M., et al., *Recent advancement in transcranial brain imaging using photoacoustic computed tomography*. J. Acoust. Soc. Am., 2014. **135**(4): p. 2208-2208.
57. Ku, G., et al., *Multiple-bandwidth photoacoustic tomography*. Physics in Medicine and Biology, 2004. **49**(7): p. 1329-1338.
58. Ku, G., et al., *Imaging of tumor angiogenesis in rat brains in vivo by photoacoustic tomography*. Applied Optics, 2005. **44**(5): p. 770.
59. Xia, J., et al., *Retrospective respiration-gated whole-body photoacoustic computed tomography of mice*. J. Biomed. Opt, 2014. **19**(1): p. 016003.
60. Xiang, L., et al., *4-D Photoacoustic Tomography*. Scientific Reports, 2013. **3**.
61. Yao, J. and L.V. Wang, *Breakthroughs in Photonics 2013: Photoacoustic Tomography in Biomedicine*. IEEE Photonics J., 2014. **6**(2): p. 1-6.
62. Yao, J. and L.V. Wang, *Photoacoustic tomography: fundamentals, advances and prospects*. Contrast Media & Molecular Imaging, 2011. **6**(5): p. 332-345.
63. Zemp, R., *Quantitative Multiple-Source Photoacoustic Tomography*, in *Biomedical Optics and 3-D Imaging*. 2010, Optical Society of America (OSA).
64. Zhang, E.Z., et al., *Multimodal photoacoustic and optical coherence tomography scanner using an all optical detection scheme for 3D morphological skin imaging*. Biomed. Opt. Express, 2011. **2**(8): p. 2202.
65. Billeh, Y.N., M. Liu, and T. Buma, *Spectroscopic photoacoustic microscopy using a photonic crystal fiber supercontinuum source*. Opt. Express, 2010. **18**(18): p. 18519.
66. Favazza, C.P., et al., *In vivo photoacoustic microscopy of human cutaneous microvasculature and a nevus*. J. Biomed. Opt., 2011. **16**(1): p. 016015.
67. Krumholz, A., et al., *Functional photoacoustic microscopy of diabetic vasculature*. Journal of Biomedical Optics, 2012. **17**(6): p. 060502.
68. Maslov, K., G. Stoica, and L.V. Wang, *In vivo dark-field reflection-mode photoacoustic microscopy*. Opt. Lett., 2005. **30**(6): p. 625.
69. Matthews, T.P., et al., *Label-free photoacoustic microscopy of peripheral nerves*. J. Biomed. Opt, 2014. **19**(1): p. 016004.
70. Rowland, K.J., et al., *Immediate Alterations in Intestinal Oxygen Saturation and Blood Flow Following Massive Small Bowel Resection As Measured By Photoacoustic Microscopy*. Journal of Pediatric Surgery, 2012. **47**(6): p. 1143-1149.
71. Shi, W., et al., *In vivo dynamic process imaging using real-time optical-resolution photoacoustic microscopy*. J Biomed Opt, 2013. **18**(2): p. 26001.
72. Tang, M., et al., *Noninvasive photoacoustic microscopy of methemoglobin in vivo*. J. Biomed. Opt, 2015. **20**(3): p. 036007.
73. Wang, L., et al., *Video-rate functional photoacoustic microscopy at depths*. J. Biomed. Opt, 2012. **17**(10): p. 1060071.
74. Wang, Y., et al., *Fiber-laser-based photoacoustic microscopy and melanoma cell detection*. J. Biomed. Opt., 2011. **16**(1): p. 011014.

75. Yao, J., et al., *Photoimprint Photoacoustic Microscopy for Three-Dimensional Label-Free Subdiffraction Imaging*. Phys. Rev. Lett., 2014. **112**(1).
76. Yao, J., et al., *High-speed label-free functional photoacoustic microscopy of mouse brain in action*. Nat Meth, 2015. **12**(5): p. 407-410.
77. Yao, J. and L.V. Wang, *Sensitivity of photoacoustic microscopy*. Photoacoustics, 2014. **2**(2): p. 87-101.
78. Yao, L., L. Xi, and H. Jiang, *Photoacoustic computed microscopy*. Scientific Reports, 2014. **4**.
79. Zemp, R.J., et al., *Realtime photoacoustic microscopy in vivo with a 30-MHz ultrasound array transducer*. Opt. Express, 2008. **16**(11): p. 7915.
80. Hai, P., et al., *Near-infrared optical-resolution photoacoustic microscopy*. Opt. Lett., 2014. **39**(17): p. 5192.
81. Hajireza, P., A. Forbrich, and R. Zemp, *In-Vivo functional optical-resolution photoacoustic microscopy with stimulated Raman scattering fiber-laser source*. Biomedical Optics Express, 2014. **5**(2): p. 539-546.
82. Hajireza, P., A. Forbrich, and R.J. Zemp, *Multifocus optical-resolution photoacoustic microscopy using stimulated Raman scattering and chromatic aberration*. Opt Lett, 2013. **38**(15): p. 2711-3.
83. Hajireza, P., et al., *Glancing angle deposited nanostructured film Fabry-Perot etalons for optical detection of ultrasound*. Opt Express, 2013. **21**(5): p. 6391-400.
84. Hajireza, P., W. Shi, and R.J. Zemp, *Real-time handheld optical-resolution photoacoustic microscopy*. Opt Express, 2011. **19**(21): p. 20097-102.
85. Hajireza, P., W. Shi, and R.J. Zemp, *Label-free in vivo fiber-based optical-resolution photoacoustic microscopy*. Opt Lett, 2011. **36**(20): p. 4107-9.
86. Hajireza, P., et al., *In vivo optical resolution photoacoustic microscopy using glancing angle-deposited nanostructured Fabry-Perot etalons*. Opt Lett, 2015. **40**(7): p. 1350-3.
87. Hajireza, P., et al., *In vivo optical resolution photoacoustic microscopy using glancing angle-deposited nanostructured Fabry-Perot etalons*. Opt. Lett., 2015. **40**(7): p. 1350.
88. Hu, S., K. Maslov, and L.V. Wang, *Second-generation optical-resolution photoacoustic microscopy with improved sensitivity and speed*. Opt. Lett., 2011. **36**(7): p. 1134.
89. Hu, S., K. Maslov, and L.V. Wang, *Three-dimensional Optical-resolution Photoacoustic Microscopy*. Journal of Visualized Experiments, 2011(51).
90. Hu, S., K. Maslov, and L.V. Wang, *Noninvasive label-free imaging of microhemodynamics by optical-resolution photoacoustic microscopy*. Opt. Express, 2009. **17**(9): p. 7688.
91. Hu, S. and Lihong V. Wang, *Optical-Resolution Photoacoustic Microscopy: Auscultation of Biological Systems at the Cellular Level*. Biophysical Journal, 2013. **105**(4): p. 841-847.
92. Kim, J.Y., et al., *Fast optical-resolution photoacoustic microscopy using a 2-axis water-proofing MEMS scanner*. Scientific Reports, 2015. **5**: p. 7932.

93. Li, G., K.I. Maslov, and L.V. Wang, *Reflection-mode multifocal optical-resolution photoacoustic microscopy*. J. Biomed. Opt, 2013. **18**(3): p. 030501.
94. Li, L., et al., *Fully motorized optical-resolution photoacoustic microscopy*. Opt. Lett., 2014. **39**(7): p. 2117.
95. Liang, J., et al., *Cross-correlation-based transverse flow measurements using optical resolution photoacoustic microscopy with a digital micromirror device*. J. Biomed. Opt, 2013. **18**(9): p. 096004.
96. Liang, J., et al., *Random-access optical-resolution photoacoustic microscopy using a digital micromirror device*. Opt. Lett., 2013. **38**(15): p. 2683.
97. Lin, R., et al., *Longitudinal label-free optical-resolution photoacoustic microscopy of tumor angiogenesis in vivo*. Quantitative Imaging in Medicine and Surgery, 2015. **5**(1): p. 23-29.
98. Liu, W., et al., *In vivo corneal neovascularization imaging by optical-resolution photoacoustic microscopy*. Photoacoustics, 2014. **2**(2): p. 81-86.
99. Liu, Y., C. Zhang, and L.V. Wang, *Effects of light scattering on optical-resolution photoacoustic microscopy*. J. Biomed. Opt, 2012. **17**(12): p. 126014.
100. Maslov, K., et al., *Optical-resolution photoacoustic microscopy for in vivo imaging of single capillaries*. Opt. Lett., 2008. **33**(9): p. 929.
101. Rao, B., et al., *Hybrid-scanning optical-resolution photoacoustic microscopy for in vivo vasculature imaging*. Opt. Lett., 2010. **35**(10): p. 1521.
102. Rao, B., et al., *Real-time four-dimensional optical-resolution photoacoustic microscopy with Au nanoparticle-assisted subdiffraction-limit resolution*. Opt. Lett., 2011. **36**(7): p. 1137.
103. Rao, B., et al., *Integrated photoacoustic, confocal, and two-photon microscope*. Journal of Biomedical Optics, 2014. **19**(3): p. 036002.
104. Shao, P., et al., *Integrated micro-endoscopy system for simultaneous fluorescence and optical-resolution photoacoustic imaging*. J Biomed Opt, 2012. **17**(7): p. 076024.
105. Shi, W., et al., *In vivo near-realtime volumetric optical-resolution photoacoustic microscopy using a high-repetition-rate nanosecond fiber-laser*. Opt Express, 2011. **19**(18): p. 17143-50.
106. Shi, W., et al., *Optical resolution photoacoustic microscopy using novel high-repetition-rate passively Q-switched microchip and fiber lasers*. J. Biomed. Opt., 2010. **15**(5): p. 056017.
107. Song, L., K. Maslov, and L.V. Wang, *Multifocal optical-resolution photoacoustic microscopy in vivo*. Opt. Lett., 2011. **36**(7): p. 1236.
108. Wang, L., et al., *Fast voice-coil scanning optical-resolution photoacoustic microscopy*. Opt. Lett., 2011. **36**(2): p. 139.
109. Xia, J., et al., *Wide-field two-dimensional multifocal optical-resolution photoacoustic-computed microscopy*. Opt. Lett., 2013. **38**(24): p. 5236.
110. Xia, J., et al., *Wide-field two-dimensional multifocal optical-resolution photoacoustic computed microscopy*. Optics letters, 2013. **38**(24): p. 5236-5239.
111. Xie, Z., et al., *Laser-scanning optical-resolution photoacoustic microscopy*. Opt. Lett., 2009. **34**(12): p. 1771.

112. Xing, W., et al., *Integrated optical- and acoustic-resolution photoacoustic microscopy based on an optical fiber bundle*. Opt. Lett., 2012. **38**(1): p. 52.
113. Xing, W., et al., *Integrated optical- and acoustic-resolution photoacoustic microscopy based on an optical fiber bundle*. Optics letters, 2013. **38**(1): p. 52-54.
114. Yang, J.-M., et al., *Optical-resolution photoacoustic endomicroscopy in vivo*. Biomed. Opt. Express, 2015. **6**(3): p. 918.
115. Yang, Z., et al., *Multi-parametric quantitative microvascular imaging with optical-resolution photoacoustic microscopy in vivo*. Opt. Express, 2014. **22**(2): p. 1500.
116. Zhang, Y.S., et al., *Optical-Resolution Photoacoustic Microscopy for Volumetric and Spectral Analysis of Histological and Immunochemical Samples*. Angew. Chem. Int. Ed., 2014. **53**(31): p. 8099-8103.
117. Zhu, L., et al., *Multiview optical resolution photoacoustic microscopy*. Optica, 2014. **1**(4): p. 217.
118. Laufer, J., et al., *In vivo preclinical photoacoustic imaging of tumor vasculature development and therapy*. J. Biomed. Opt., 2012. **17**(5): p. 056016.
119. Laufer, J., et al., *In vivo photoacoustic imaging of mouse embryos*. J. Biomed. Opt., 2012. **17**(6): p. 061220.
120. Zhang, E.Z., et al., *In vivo high-resolution 3D photoacoustic imaging of superficial vascular anatomy*. Physics in Medicine and Biology, 2009. **54**(4): p. 1035-1046.
121. Yang, J.-M., et al., *Toward dual-wavelength functional photoacoustic endoscopy: laser and peripheral optical systems development*, in *Photons Plus Ultrasound: Imaging and Sensing 2012*. 2012, SPIE-Intl Soc Optical Eng.
122. Pan, D., et al., *Photoacoustic Sentinel Lymph Node Imaging with Self-Assembled Copper Neodecanoate Nanoparticles*. ACS Nano, 2012. **6**(2): p. 1260-1267.
123. Pan, D., et al., *A Brief Account of Nanoparticle Contrast Agents for Photoacoustic Imaging*. Wiley interdisciplinary reviews. Nanomedicine and nanobiotechnology, 2013. **5**(6): p. 517-543.
124. Su, J.L., et al., *Advances in Clinical and Biomedical Applications of Photoacoustic Imaging*. Expert opinion on medical diagnostics, 2010. **4**(6): p. 497-510.
125. Wei, C.-W., *Trapping and dynamic manipulation of polystyrene beads mimicking circulating tumor cells using targeted magnetic/photoacoustic contrast agents*. J. Biomed. Opt, 2012. **17**(10): p. 101517.
126. Wu, D., et al., *Contrast Agents for Photoacoustic and Thermoacoustic Imaging: A Review*. International Journal of Molecular Sciences, 2014. **15**(12): p. 23616-23639.
127. Jathoul, A.P., et al., *Deep in vivo photoacoustic imaging of mammalian tissues using a tyrosinase-based genetic reporter*. Nature Photonics, 2015.
128. Paproski, R.J., et al., *Multi-wavelength photoacoustic imaging of inducible tyrosinase reporter gene expression in xenograft tumors*. Scientific Reports, 2014. **4**.
129. Akhmanov, S.A., V.E. Gusev, and A.A. Karabutov, *Pulsed laser optoacoustics: Achievements and perspective*. Infrared Physics, 1989. **29**(2-4): p. 815-838.
130. Weight, R.M., P.S. Dale, and J.A. Viator, *Detection of circulating melanoma cells in human blood using photoacoustic flowmetry*, in *2009 Annual International Conference of the IEEE Engineering in Medicine and Biology Society*. 2009, Institute of Electrical & Electronics Engineers (IEEE).

131. Galanzha, E.I., et al., *In vivo, Noninvasive, Label-Free Detection and Eradication of Circulating Metastatic Melanoma Cells Using Two-Color Photoacoustic Flow Cytometry with a Diode Laser*. *Cancer Research*, 2009. **69**(20): p. 7926-7934.
132. Yao, J., et al., *In vivo photoacoustic imaging of transverse blood flow by using Doppler broadening of bandwidth*. *Opt. Lett.*, 2010. **35**(9): p. 1419.
133. Zackrisson, S., S. van de Ven, and S.S. Gambhir, *Light In and Sound Out: Emerging Translational Strategies for Photoacoustic Imaging*. *Cancer research*, 2014. **74**(4): p. 979-1004.
134. Oladipupo, S., et al., *VEGF is essential for hypoxia-inducible factor-mediated neovascularization but dispensable for endothelial sprouting*. *Proceedings of the National Academy of Sciences*, 2011. **108**(32): p. 13264-13269.
135. Oladipupo, S.S., et al., *Conditional HIF-1 induction produces multistage neovascularization with stage-specific sensitivity to VEGFR inhibitors and myeloid cell independence*. *Blood*, 2011. **117**(15): p. 4142-4153.
136. Maslov, K., S. Hu, and L.V. Wang, *Second generation optical-resolution photoacoustic microscopy*, in *Photons Plus Ultrasound: Imaging and Sensing 2011*. 2011, SPIE-Intl Soc Optical Eng.
137. Gupta, G.P. and J. Massagué, *Cancer Metastasis: Building a Framework*. *Cell*, 2006. **127**(4): p. 679-695.
138. Folkman, J., *Tumor Angiogenesis*, in *Advances in Cancer Research*. 1974, Elsevier BV. p. 331-358.
139. Folkman, J. and Y. Shing, *Control of Angiogenesis by Heparin and Other Sulfated Polysaccharides*, in *Heparin and Related Polysaccharides*. 1992, Springer Science + Business Media. p. 355-364.
140. Shweiki, D., et al., *Vascular endothelial growth factor induced by hypoxia may mediate hypoxia-initiated angiogenesis*. *Nature*, 1992. **359**(6398): p. 843-845.
141. Weidner, N., et al., *Tumor Angiogenesis: A New Significant and Independent Prognostic Indicator in Early-Stage Breast Carcinoma*. *JNCI Journal of the National Cancer Institute*, 1992. **84**(24): p. 1875-1887.
142. Plate, K.H., et al., *Vascular endothelial growth factor and glioma angiogenesis: Coordinate induction of VEGF receptors, distribution of VEGF protein and possible *In vivo* regulatory mechanisms*. *International Journal of Cancer*, 1994. **59**(4): p. 520-529.
143. Battagay, E.J., *Angiogenesis: mechanistic insights, neovascular diseases, and therapeutic prospects*. *J Mol Med*, 1995. **73**(7).
144. Rak, J., J. Filmus, and R.S. Kerbel, *Reciprocal paracrine interactions between tumour cells and endothelial cells: the 'angiogenesis progression' hypothesis*. *European Journal of Cancer*, 1996. **32**(14): p. 2438-2450.
145. Harris, A.L., *Antiangiogenesis for cancer therapy*. *The Lancet*, 1997. **349**: p. S13-S15.
146. Abramovitch, R., D. Frenkiel, and M. Neeman, *Analysis of subcutaneous angiogenesis by gradient echo magnetic resonance imaging*. *Magn. Reson. Med.*, 1998. **39**(5): p. 813-824.

147. Lassau, N., et al., *New Hemodynamic Approach to Angiogenesis*. Investigative Radiology, 1999. **34**(3): p. 194-198.
148. Miller, J.C., et al., *Imaging Angiogenesis: Applications and Potential for Drug Development*. JNCI Journal of the National Cancer Institute, 2005. **97**(3): p. 172-187.
149. Nishida, N., et al., *Angiogenesis in cancer*. Vascular Health and Risk Management, 2006. **2**(3): p. 213-219.
150. Provenzale, J.M., *Imaging of Angiogenesis: Clinical Techniques and Novel Imaging Methods*. American Journal of Roentgenology, 2007. **188**(1): p. 11-23.
151. Niu, G. and X. Chen, *PET Imaging of Angiogenesis*. PET Clinics, 2009. **4**(1): p. 17-38.
152. Hu, S., et al., *Label-free photoacoustic ophthalmic angiography*. Opt. Lett., 2009. **35**(1): p. 1.
153. Wang, R.K., et al., *Depth-resolved imaging of capillary networks in retina and choroid using ultrahigh sensitive optical microangiography*. Opt. Lett., 2010. **35**(9): p. 1467.
154. Carmeliet, P. and R.K. Jain, *Molecular mechanisms and clinical applications of angiogenesis*. Nature, 2011. **473**(7347): p. 298-307.
155. Pabst, A.M., et al., *Imaging angiogenesis: Perspectives and opportunities in tumour research – A method display*. Journal of Cranio-Maxillofacial Surgery, 2014. **42**(6): p. 915-923.
156. Rubin, G.D., et al., *CT Angiography after 20 Years: A Transformation in Cardiovascular Disease Characterization Continues to Advance*. Radiology, 2014. **271**(3): p. 633-652.
157. Cheng, W.-F., et al., *Vascularity index as a novel parameter for the in vivo assessment of angiogenesis in patients with cervical carcinoma*. Cancer, 1999. **85**(3): p. 651-657.
158. Li, W.W., *Tumor angiogenesis: Molecular pathology, therapeutic targeting, and imaging*. Academic Radiology, 2000. **7**(10): p. 800-811.
159. Rubin, G.D., et al., *Aorta and Iliac Arteries: Single versus Multiple Detector-Row Helical CT Angiography*. Radiology, 2000. **215**(3): p. 670-676.
160. Brasch, R.C., et al., *In vivo monitoring of tumor angiogenesis with MR imaging*. Academic Radiology, 2000. **7**(10): p. 812-823.
161. Rubin, G.D., et al., *Multi-Detector Row CT Angiography of Lower Extremity Arterial Inflow and Runoff: Initial Experience*. Radiology, 2001. **221**(1): p. 146-158.
162. Verheul, H.M.W., E.E. Voest, and R.O. Schlingemann, *Are tumours angiogenesis-dependent?* The Journal of Pathology, 2003. **202**(1): p. 5-13.
163. Zhu, Q., N. Chen, and S.H. Kurtzman, *Imaging tumor angiogenesis by use of combined near-infrared diffusive light and ultrasound*. Opt. Lett., 2003. **28**(5): p. 337.
164. Bogdan, M., *CT angiography in complex upper extremity reconstruction*. The Journal of Hand Surgery: Journal of the British Society for Surgery of the Hand, 2004. **29**(5): p. 465-469.
165. Crawford, C.R., *Computed tomography scanning with simultaneous patient translation*. Medical Physics, 1990. **17**(6): p. 967.
166. Kiessling, F., et al., *Comparing Dynamic Parameters of Tumor Vascularization in Nude Mice Revealed by Magnetic Resonance Imaging and Contrast-Enhanced*

- Intermittent Power Doppler Sonography*. Investigative Radiology, 2003. **38**(8): p. 516-524.
167. Carmeliet, P. and R.K. Jain, Nature, 2000. **407**(6801): p. 249-257.
 168. Rohren, E.M., T.G. Turkington, and R.E. Coleman, *Clinical Applications of PET in Oncology I*. Radiology, 2004. **231**(2): p. 305-332.
 169. Rebol, J., *The Vascularisation of Oral Cavity Tumours and Tumour Shell Tissue Determined by Three-Dimensional Power Doppler Sonography*. Ultrasound in Medicine & Biology, 2007. **33**(4): p. 493-499.
 170. Cheng, W.-F., et al., *Clinical application of intratumoral blood flow study in patients with endometrial carcinoma*. Cancer, 1998. **82**(10): p. 1881-1886.
 171. Rebol, J., et al., *3D Power Doppler Analysis of the Vascularisation in Tumours of the Oral Cavity*. Ultraschall Med, 2007. **28**(1): p. 40-44.
 172. Yao, J., et al., *Label-free oxygen-metabolic photoacoustic microscopy in vivo*. Journal of Biomedical Optics, 2011. **16**(7): p. 076003.
 173. Zhou, Y., et al., *Handheld photoacoustic probe to detect both melanoma depth and volume at high speed in vivo*. J. Biophoton, 2015.
 174. Schlingemann, R.O., et al., *Expression of the high molecular weight melanoma-associated antigen by pericytes during angiogenesis in tumors and in healing wounds*. Ultramicroscopy, 1989. **31**(4): p. 481.
 175. Viator, J.A., et al., *A Comparative Study of Photoacoustic and Reflectance Methods for Determination of Epidermal Melanin Content*. J Invest Dermatol, 2004. **122**(6): p. 1432-1439.
 176. Liu, M., et al., *Dual modality optical coherence and whole-body photoacoustic tomography imaging of chick embryos in multiple development stages*. Biomedical Optics Express, 2014. **5**(9): p. 3150-3159.
 177. Zhang, H. and S. Jiao, *Naturally Combined Photoacoustic Microscopy and Optical Coherence Tomography for Simultaneous Multimodal*, in *Biomedical Optics and 3-D Imaging*. 2010, Optical Society of America (OSA).
 178. Zhang, E.Z., et al., *Multimodal simultaneous photoacoustic tomography, optical resolution microscopy, and OCT system*, in *Photons Plus Ultrasound: Imaging and Sensing 2010*. 2010, SPIE-Intl Soc Optical Eng.
 179. Chinn, S.R., E.A. Swanson, and J.G. Fujimoto, *Optical coherence tomography using a frequency-tunable optical source*. Opt. Lett., 1997. **22**(5): p. 340.
 180. Cox, B.T., et al., *Fabry Perot polymer film fibre-optic hydrophones and arrays for ultrasound field characterisation*. J. Phys.: Conf. Ser., 2004. **1**: p. 32-37.
 181. Zhang, E., J. Laufer, and P. Beard, *Backward-mode multiwavelength photoacoustic scanner using a planar Fabry-Perot polymer film ultrasound sensor for high-resolution three-dimensional imaging of biological tissues*. Applied Optics, 2008. **47**(4): p. 561.
 182. Nuster, R., et al., *Downstream Fabry-Perot interferometer for acoustic wave monitoring in photoacoustic tomography*. Optics Letters, 2011. **36**(6): p. 981-983.
 183. Xie, Z., et al., *Pure optical photoacoustic microscopy*. Opt. Express, 2011. **19**(10): p. 9027.

184. Beard, P.C. and T.N. Mills, *Extrinsic optical-fiber ultrasound sensor using a thin polymer film as a low-finesse Fabry-Perot interferometer*. Applied Optics, 1996. **35**(4): p. 663.
185. Beard, P.C. and T.N. Mills, *Miniature optical fibre ultrasonic hydrophone using a Fabry-Perot polymer film interferometer*. Electron. Lett., 1997. **33**(9): p. 801.
186. Beard, P.C., F. Perennes, and T.N. Mills, *Transduction mechanisms of the Fabry-Perot polymer film sensing concept for wideband ultrasound detection*. IEEE Transactions on Ultrasonics, Ferroelectrics and Frequency Control, 1999. **46**(6): p. 1575-1582.
187. Pérennès, F., P.C. Beard, and T.N. Mills, *Analysis of a Low-Finesse Fabry-Perot Sensing Interferometer Illuminated by a Multimode Optical Fiber*. Applied Optics, 1999. **38**(34): p. 7026.
188. Hawkeye, M.M., M.T. Taschuk, and M.J. Brett, *Glancing Angle Deposition of Thin Films*. 2014, Wiley-Blackwell.
189. Hawkeye, M.M. and M.J. Brett, *Glancing angle deposition: Fabrication, properties, and applications of micro- and nanostructured thin films*. Journal of Vacuum Science & Technology A: Vacuum, Surfaces, and Films, 2007. **25**(5): p. 1317.
190. Kennedy, S.R. and M.J. Brett, *Porous Broadband Antireflection Coating by Glancing Angle Deposition*. Applied Optics, 2003. **42**(22): p. 4573.
191. Robbie, K., *Sculptured thin films and glancing angle deposition: Growth mechanics and applications*. Journal of Vacuum Science & Technology A: Vacuum, Surfaces, and Films, 1997. **15**(3): p. 1460.
192. Hawkeye, M.M., K.M. Krause, and M.J. Brett, *Ambient humidity monitoring using a 1D photonic crystal sensor fabricated with glancing angle deposition*, in *Optical Sensors 2009*. 2009, SPIE-Intl Soc Optical Eng.

3. Label-free *in vivo* fiber-based optical-resolution photoacoustic microscopy

Thus far, most OR-PAM imaging has been limited to preclinical studies with animals. Unfortunately, the footprint of most OR-PAM systems is too large to be used for anything but superficial structures on the skin [1]. Additionally, imaging frame-rates have been too slow to permit clinical applications. In this chapter, we describe a unique fiber-based OR-PAM system to address both these limitations. We demonstrate the capability of this technology by imaging ears of mice.

Microendoscopy systems typically sacrifice wide field of-view for high-resolution and small-footprint, flexible probes. Different types of microendoscopy systems including brightfield, fluorescence, confocal, and confocal fluorescence microscopy are reported [2-4]. Often an exogenous fluorescent contrast agent is required to stain cells for imaging. While these pure-optical systems permit “virtual biopsy” capabilities, sometimes the delivery of these agents is cumbersome, and label-free imaging would be preferred. Additionally, imaging more than one species of fluorescent label is not trivial.

Photoacoustic imaging would permit label-free imaging using a completely different contrast mechanism (optical absorption), but it has not yet been implemented in a microendoscopic form factor, except for some work on intravascular applications, where ultrasonic rather than optical resolution is realized in B-scan rather than C-scan format [5].

In this chapter C-scan fiber-based optical-resolution photoacoustic microscopy (F-OR-PAM) using image guide fibers and a unique fiber laser system is demonstrated. The image-guide consists of 30,000 individual fibers in a bundle 800 μm in diameter which provides transmission of a tight focused laser spot in a compact, flexible fiber. To the best of our knowledge this is the first time that the feasibility of a real-time *in-vivo* photoacoustic microendoscopic system is demonstrated. The proposed F-OR-PAM system permits label-free realtime imaging of capillary-scale biology all from the tip of a fiber-catheter. This system could have significant clinical impact for microendoscopic applications where the thin fiber can be inserted into body cavities.

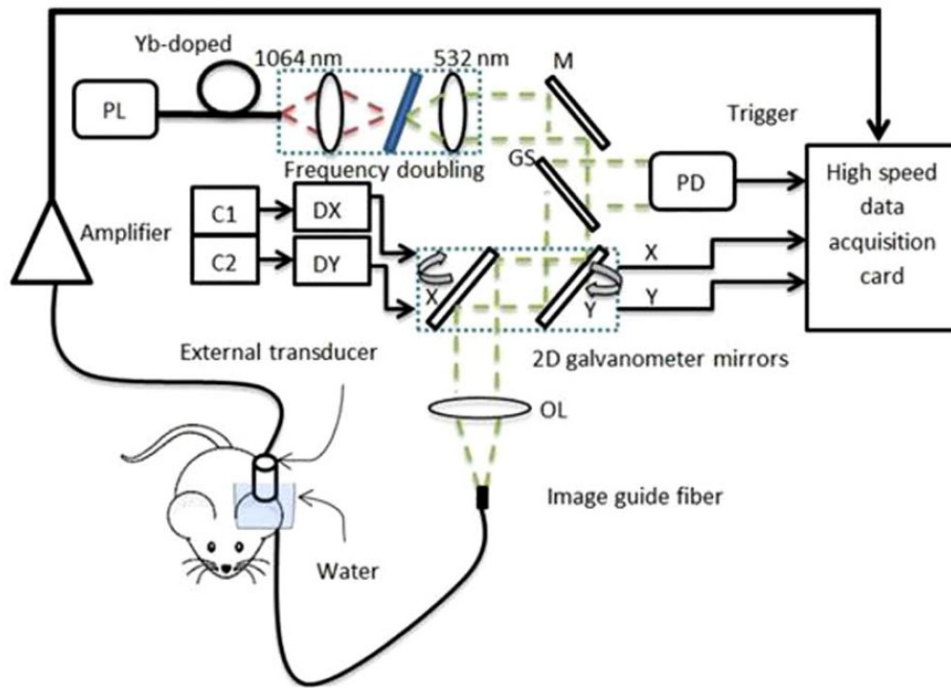


Figure 3.1: Simplified scanning F-OR-PAM experimental setup. (FLD: fiber laser driver, Yb: Ytterbium, M: mirror, GS: glass, PD: photodiode, C1: first controller, C2: second controller, DX: X axis mirror driver, DY: Y axis mirror driver, OL: objective lens.

Figure 3.1 shows a simplified scanning F-OR-PAM experimental setup. We used a diode-pumped pulsed Ytterbium fiber laser (YLP-G, IPG Photonics Corporation.) at 532 nm wavelength having ~ 1 ns pulse width, with up to $20 \mu\text{J}$ per pulse, and pulse repetition rates (PRR) of 600 kHz. A photodiode is used to trigger the data acquisition and measure the energy of each pulse.

The laser beam is directed to an x-y galvanometer scanner (6230H, Cambridge Technology Inc.). The mirrors were controlled by analog sinusoidal signals from two function generators (AFG3101, Tektronix Inc.). The frequency of the control signal determines the speed of scanning, while the peak-to-peak amplitude of the control signal is used to determine the angle of the scanning mirrors. In this experiment, the fast scanning rate of the 2D galvanometer system was fixed at 600 Hz, while slow scanning rate was fixed at 1 Hz, providing two C-scan frames per second. The light was coupled to the 1m long image-guide

fiber using an objective lens ($f = 18$ mm) focused on the fiber input and the beam was scanned across the fiber tip using the high-speed galvanometer optical scanner. We use an external 10 MHz focused ultrasound transducer (19 mm focus, 6 mm active element, $f\# = 3.17$, CD International Inc.) to receive photoacoustic signals.

For each laser pulse, photoacoustic signals were amplified and digitized using an 8-channel PCI digitizer at a sampling rate of 125 Msamples/s. X-Y galvanometer feedback signals were also digitized and used to register the position of each laser pulse. The peak-to-peak maximum amplitude from each A-scan was projected as a single pixel in a C-scan image. 2D interpolation was used to render the image on a Cartesian grid. In order to demonstrate utilization of the entire aperture of the fiber (800 μm diameter field-of-view), we used black electrical tape as the imaging target as shown in figure 3.2(a). For the next step we repeated the same procedure; however, we moved the black tape to cover only half the fiber aperture, as seen in figure 3.2(b).

We also imaged a network of carbon fibers with diameters ~ 7 μm (figures 3.3(a) and 3.3(b)) which are as small as capillary sized blood vessels. Figure 3.3(c) shows an image of a human hair with a diameter of ~ 100 μm . Fitting the carbon-fiber signal amplitudes to a Gaussian function, we determined the full-width at half-maximum (FWHM) of the signal across the fiber to be approximately 9 μm . Considering that the carbon fiber itself is ~ 7.5 μm , to find the lateral spatial resolution of the imaging system, we performed numerical convolution of a Gaussian illumination spot with a rectangular region of width 7.5 μm and found the spot-size producing the measured FWHM. Using this procedure, we estimate the lateral spatial resolution

(FWHM) as ~ 7 μm , or Gaussian sigma parameter, $\sigma = FWHM / (2\sqrt{2 \ln 2}) \sim 3$ μm . Considering the total area of the fiber bundle with 30,000 individual single-mode fibers, we obtained the diameter of each strand is ~ 4 μm which is close to measured lateral resolution. This shows that the system is almost at optimal resolution.

For *in vivo* studies, we imaged the ears of Swiss Webster mice. A custom holder was engineered to support the mouse ear on a transparent acrylic plate with an SMA-connector to hold the image-guide fiber from the bottom. The mouse ear was in direct contact with the image-guide fiber. A drop of water was placed on the top of the ear and a water tank with

transparent membrane bottom was lowered until acoustic coupling was established. A focused 10 MHz transducer (19 mm focus, 6 mm active element, $f\# = 3.17$, CD International Inc.) was positioned in the water tank facing downward and aligned by adjusting the position until signals were maximized. All experimental animal procedures were conducted in conformity with the laboratory animal protocol approved by the University of Alberta Animal Use and Care Committee. The Swiss Webster mouse was anesthetized using a breathing anesthesia system (E-Z Anesthesia, Euthanex Corp.) during image acquisition. Figure 3.4 shows an image of the microvasculature in a Swiss Webster mouse ear *in vivo* and clearly depicts a network of microvessels. A 2D Hessian-based Frangi Vesselness filter [6] was used to filter C-scan maximum amplitude projection (MAP) images to preferentially select tubular structures while rejecting noise in figures 3.3(a), 3.3(b), and 3.4. The unprecedented acquisition frame-rates for OR-PAM demonstrated here (1–2 orders of magnitude faster than previous-generation systems) are attributed to our high-repetition-rate (600 kHz PRR) fiber laser. It should be noted that the distance traveled by photoacoustic signals during the time between laser pulses at 600 kHz PRR is ~ 2.5 mm, only slightly more than the optical transport mean-free path (which defines the penetration depth of OR-PAM). Hence, repetition-rates much higher than this may be complicated by deep-tissue signals from previous pulses interfering with those due to superficial structures.

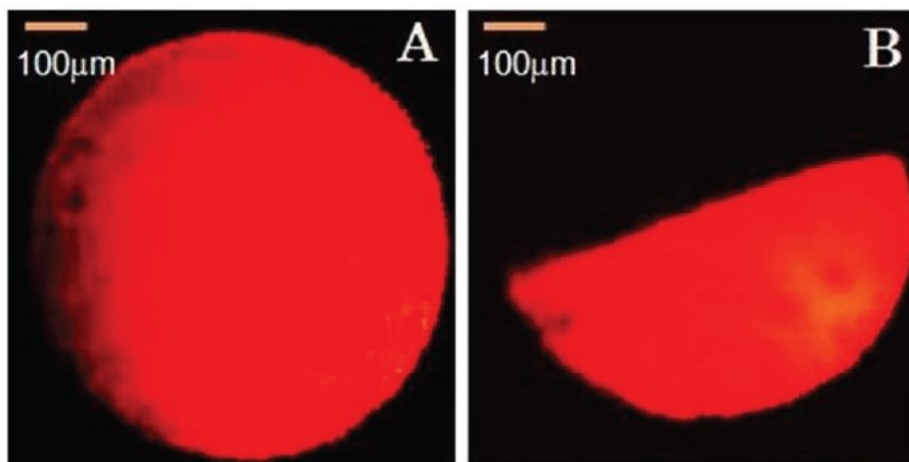


Figure 3.2: F-OR-PAM images demonstrating the entire field-of-view of the image-guide. In (a) the whole aperture is covered by black tape, (b) black tape moved to cover only half of the aperture.

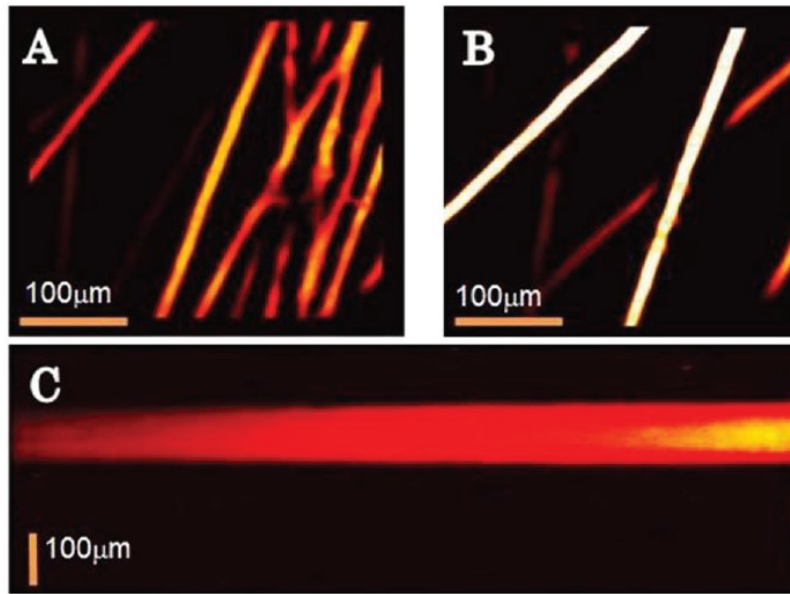


Figure 3.3: (a) and (b) images of $\sim 7 \mu\text{m}$ carbon-fiber network. (c) Imaging of human hair with $100 \mu\text{m}$ diameter.

The power at the end of the fiber is measured as $\sim 35 \text{ mW}$ with 600 kHz PRR, hence the calculated surface laser fluence is $\sim 130 \text{ mJ/cm}^2$, which is higher than the American National Standards Institute (ANSI) safety limit (20 mJ/cm^2 in the visible spectral region) [7], but typical or lower than other OR-PAM systems. With nanosecond-pulse-widths the peak power density at the tissue surface is estimated as $\sim 130 \text{ MW/cm}^2$, less than the focal fluences of 10^{10} – 10^{12} W/cm^2 typically used in 2-photon imaging. The average power across the image-guide aperture is $\sim 7 \text{ W/cm}^2$, well above the 100 mW/cm^2 ANSI-recommended exposure for CW light delivery, but comparable to or lower than other *in vivo* microscopy methods. In our experiments no tissue damage was observed, the laser power is localized to a small spot-size and future improvements in sensitivity could permit fluence reduction. Because contact-mode F-OR-PAM is demonstrated here, only superficial tissue depths may be imaged. Signal-to-noise and spatial resolution will degrade with imaging depth due to light divergence from the image guide fiber strands. Image contrast is due to optical absorption, different than reflection-mode light microscopy. Future work could involve refocusing light from the imaging tip of the image-guide fiber using gradient index (GRIN)-lenses for improved resolution and depth sectioning. Future clinical work could also use an external

ultrasound array transducer to guide catheter placement and collect the photoacoustic signals or a more integrated ultrasound detection method could be employed.

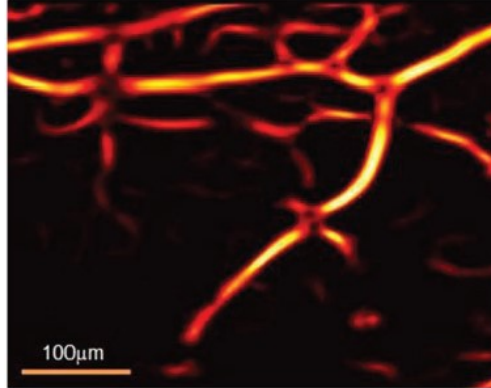


Figure 3.4: F-OR-PAM image of the microvasculature in a Swiss Webster mouse ear *in vivo*.

Despite these limitations, our present work shows that *in vivo* imaging of microvasculature with the contact-mode system is possible. Future enhancement may also include multi-wavelength capabilities for functional imaging, and optical detection of ultrasound all at the fiber tip.

In the next chapter we introduce a gradient index (GRIN)-lens OR-PAME system for improving the lateral resolution and depth sectioning. The proposed system by taking advantage of a GRIN lens with ~ 2 mm working distance extends the optically focused penetration depth to ~ 1 mm, the transport-mean free path in tissue. Additionally, when focusing below the skin surface, surface fluence is significantly lower than the reported results in this chapter, offering improved safety.

Bibliography

1. Hajireza, P., et al., *Optical-resolution photoacoustic micro-endoscopy using image-guide fibers and fiber laser technology*, in *Photons Plus Ultrasound: Imaging and Sensing 2011*. 2011, SPIE-Intl Soc Optical Eng.
2. Pillai, R.S., D. Lorensen, and D.D. Sampson, *Deep-tissue access with confocal fluorescence microendoscopy through hypodermic needles*. *Opt. Express*, 2011. **19**(8): p. 7213.
3. Jung, J.C., *In Vivo Mammalian Brain Imaging Using One- and Two-Photon Fluorescence Microendoscopy*. *Journal of Neurophysiology*, 2004. **92**(5): p. 3121-3133.
4. Spring, B.Q., et al., *Intravital fiber-optic fluorescence imaging for monitoring ovarian carcinoma progression and treatment response*, in *Photodynamic Therapy: Back to the Future*. 2009, SPIE-Intl Soc Optical Eng.
5. Yang, J.-M., et al., *Photoacoustic endoscopy*. *Opt. Lett.*, 2009. **34**(10): p. 1591.
6. Manniesing, R. and W. Niessen, *Multiscale Vessel Enhancing Diffusion in CT Angiography Noise Filtering*, in *Information Processing in Medical Imaging*. 2005, Springer Science + Business Media. p. 138-149.
7. *American National Standards Institute (ANSI) calendar*. *J. Acoust. Soc. Am.*, 2000. **107**(1): p. 13.

4. Label-free *in vivo* GRIN-lens optical resolution photoacoustic micro-endoscopy

4.1. Introduction

In 2011, for the first time, we introduced the feasibility of optical resolution photoacoustic micro-endoscopy (ORPAME) using a fiber bundle [1]. However, in the reported contact-mode operation (chapter 3), due to light divergence at the end of the image guide, the penetration depth was limited and deeper structures were not in-focus. In this chapter, we introduce a gradient index (GRIN)-lens OR-PAME system for improving the lateral resolution and depth sectioning. The proposed system, with ~ 2 mm working distance, extends the optically focused penetration depth to ~ 1 mm, the transport-mean free path in tissue. Additionally, when focusing below the skin surface, surface fluence is significantly lower than our previous contact-mode OR-PAME system, offering improved safety. The small footprint of our novel system, ~ 1.8 mm, gives this system the potential to be useful for clinical endoscopy applications when the thin fiber is inserted into body cavities.

GRIN lenses have been used in multiple modalities including two-photon microscopy, fluorescent microscopy, etc [2, 3]; however, this is the first report of a GRIN-lens-based OR-PAME system. OR-PAME is one of the few optical imaging techniques that can provide optical resolution label-free absorption-contrast images *in vivo*. Other types of micro-endoscopy systems such as fluorescence and confocal fluorescence microscopy often use exogenous dyes in order to provide labeling.

Some endoscopic systems have employed micro-motors at the distal end of the endoscopic probe to provide light scanning, which increase the size of the endoscopy probe.

In this chapter galvanometer scanning mirrors are used at the proximal end of the probes where an imaging fiber bundle is used for transferring the focused light. The image guide consists of 100,000 individual fibers in a bundle 1.4 mm in diameter which provides transmission of a scanned focused laser spot in a compact, flexible fiber.

The proposed C-scan GRIN-lens OR-PAME will bring our reported optical resolution photoacoustic micro-endoscopy (OR-PAME) system [1] one step closer to its introduction

into clinical applications which can be used in longitudinal studies to examine tumor growth, angiogenesis, and anti-angiogenic drug efficacy.

The proposed GRIN-lens OR-PAME system is a label free real-time imaging system with the capability of imaging small targets down to a capillary size. This system could have significant clinical impact for micro-endoscopic applications where the thin fiber can be inserted into body cavities. We demonstrate the capability of this technology with phantom studies and by imaging ears of hairless SCID mice.

4.2. Experimental setup

Figure 4.1 shows a simplified scanning GRIN-lens OR-PAME experimental setup. A diode-pumped pulsed ytterbium fiber laser (YLP-G, IPG Photonics Corporation) at 532 nm wavelength is used. This high pulse repetition rate (up to 600 kHz) fiber laser with ~ 1 ns pulse width and up to 20 μ J per pulse enables real-time imaging. A photodiode is used to measure the pulse energy and trigger the data acquisition card. The laser beam is directed to an x-y galvanometer scanner (6230H, Cambridge Technology Inc.). The mirrors are controlled by analog sinusoidal signals from a two channel function generator (AFG3022B, Tektronix Inc.). The speed and the angle of scanning are determined by the frequency and the peak-to-peak amplitude of the control signals respectively.

In this experiment, the fast scanning rate of the 2D galvanometer system is fixed at 400 Hz while the slow scanning rate is fixed at 1 Hz, providing 2 C-scan frames per second. The pulse repetition rate (PRR) is fixed at 160 kHz. For a 400 by 400 μ m field of view (FOV) the average step sizes for the X and Y directions are calculated as 2 and 1 μ m, respectively.

The light is coupled to the 2m long image guide fiber using an objective lens ($f = 18$ mm) focused on the fiber input and the beam is scanned by galvanometer scanning mirrors at the proximal end of the fiber. The light at the output of the fiber bundle is refocused using a 0.29 pitch GRIN lens (Thorlabs). We use an external 3.5 MHz focused ultrasound transducer to receive photoacoustic signals (19 mm focus, 6 mm active element, $f\# = 3:17$, CD International Inc.). For each laser pulse, the photoacoustic signals are amplified using a 200 MHz computer controlled pulser/receiver (5900PR, Olympus NDT Inc).

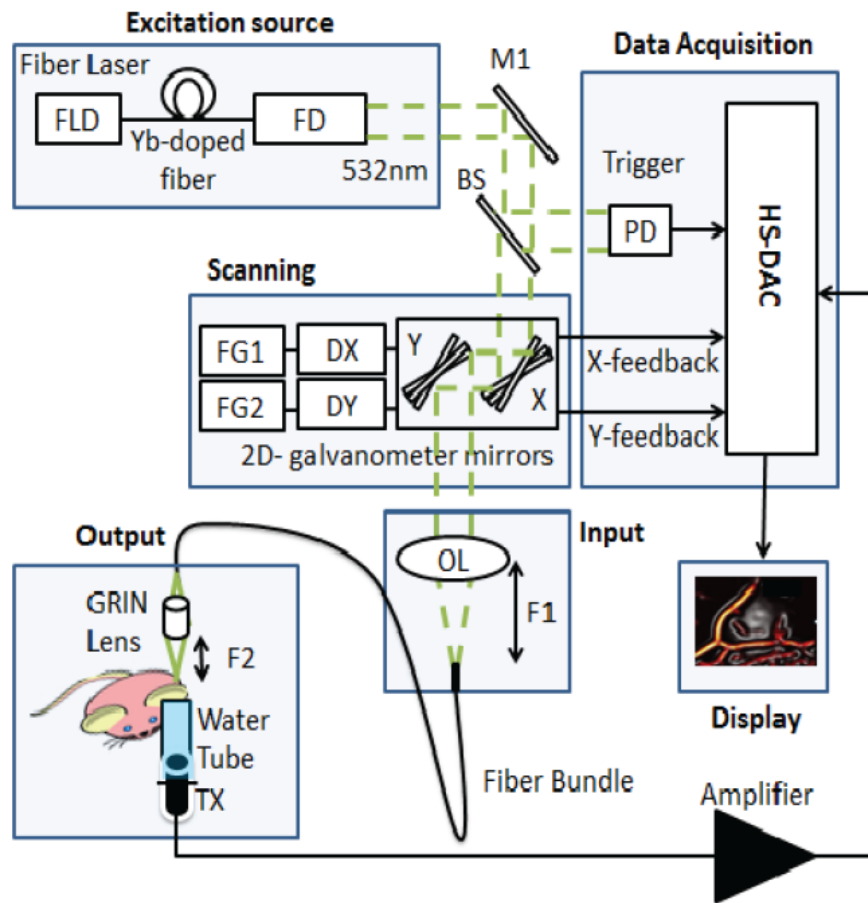


Figure 4.1: Simplified scanning GRIN-lens OR-PAME experimental setup. FLD: fiber laser driver, Yb: ytterbium, FD, frequency doubling, M: mirror, BS: beam splitter, PD: photodiode, FG1: function generator channel 1, FG2: function generator channel 2, DX: X axis mirror driver, DY: Y axis mirror driver, OL: objective lens, F1: working distance of 19 mm, F2: working distance of 1.9 mm, HS-DAC: high speed data acquisition card, TX: ultrasound transducer.

The amplified signals are then digitized using a 12-bit 8-channel PCI digitizer at a sampling rate of 125 Msamples s⁻¹ (CS8289, Gage Cobra, Gage Applied Systems, Inc.). The x–y galvanometer feedback signals are also digitized and used to locate the position of each laser pulse at the sample. The peak-to-peak maximum amplitude from each A-scan is projected as a single pixel in a C-scan image. The image on a Cartesian grid is rendered using 2D interpolation.

4.3. Results and discussion

In order to demonstrate utilization of the entire aperture of the fiber (1.4 mm diameter field of view), we used black electrical tape as the imaging target, as shown in figure 4.2(a). We also imaged a network of carbon fibers with diameters of $\sim 7 \mu\text{m}$ (figures 4.2(b)–(d)), which are as small as capillary sized blood vessels. Figure 4.2(b) shows that the entire FOV of the 1.4 mm image guide is covered by the carbon fiber network.

The full-width-half-maximum of the signal across the fiber was determined as $\sim 8.5 \mu\text{m}$ by fitting the carbon-fiber signal amplitudes to a Gaussian function. Taking into account the size of the fiber itself ($7.5 \mu\text{m}$), the lateral spatial resolution (FWHM) was estimated as $\sim 6 \mu\text{m}$ by performing numerical convolution of a Gaussian illumination spot with a rectangular region of width $7.5 \mu\text{m}$. For *in vivo* studies, we imaged the ear of hairless SCID mice. A custom holder was engineered to connect the image guide fiber and GRIN lens in the right position. A customized ultrasound transducer holder was made to keep a small amount of water at the top of the transducer. The mouse ear was positioned on a thin transparent membrane stretched over this tube, and a drop of water was added for acoustic coupling. The distance between the mouse ear and the GRIN lens was about 1.5 mm. A focused 3.5 MHz transducer was positioned at the right distance inside the holder. All experimental animal procedures were conducted in conformity with the laboratory animal protocol approved by the University of Alberta Animal Use and Care Committee.

The hairless SCID mouse was anesthetized using a breathing anesthesia system (E-Z Anesthesia, Euthanex Corp.) during image acquisition. Figure 4.3 shows different images of the microvasculature in a hairless SCID ear *in vivo*, and clearly shows a network of microvessels. Micro-endoscopy systems typically sacrifice wide field of view for high-resolution and small footprint flexible probes. A 2D-Hessian-based Frangi Vesselness filter [4] was used to filter C-scan maximum amplitude projection images to select tubular structures and reject noise. The acquisition frame rates for the GRIN-lens OR-PAME is 1–2 orders of magnitude faster than previous-generation systems thanks to our high-repetition-rate (600 kHz pulse repetition rate) fiber laser.

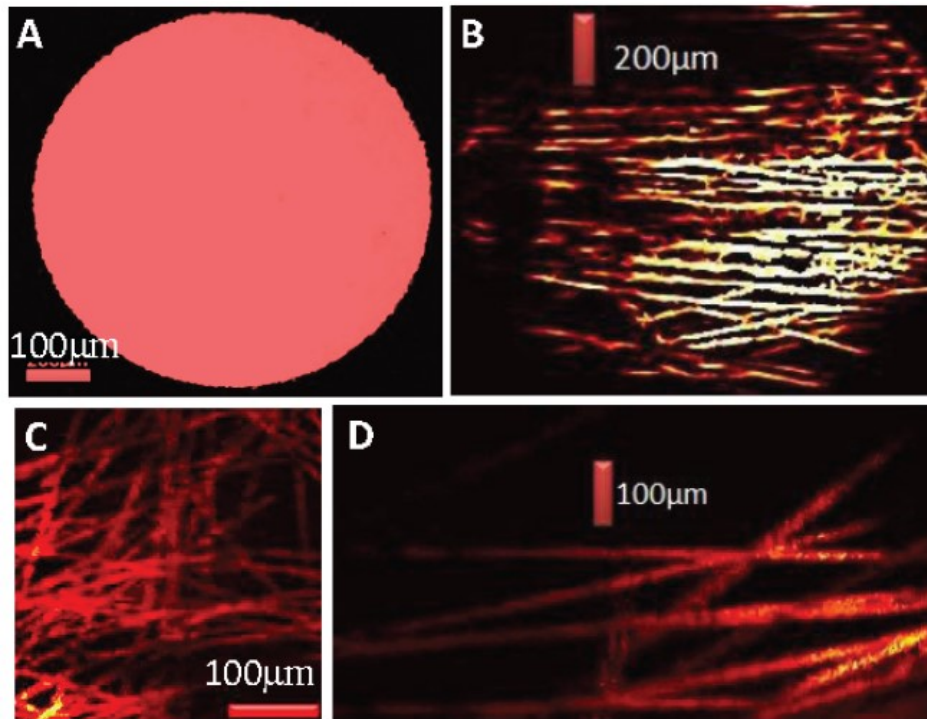


Figure 4.2: (a) OR-PAME image demonstrating the entire field of view of the image guide. (b) A photoacoustic image of a carbon-fiber network using the GRIN-lens OR-PAME system. Each carbon fiber is $\sim 7 \mu\text{m}$ in diameter. (c), (d) An enlarged region of (b) which shows the fine details that can be achieved using the GRIN-lens OR-PAME system.

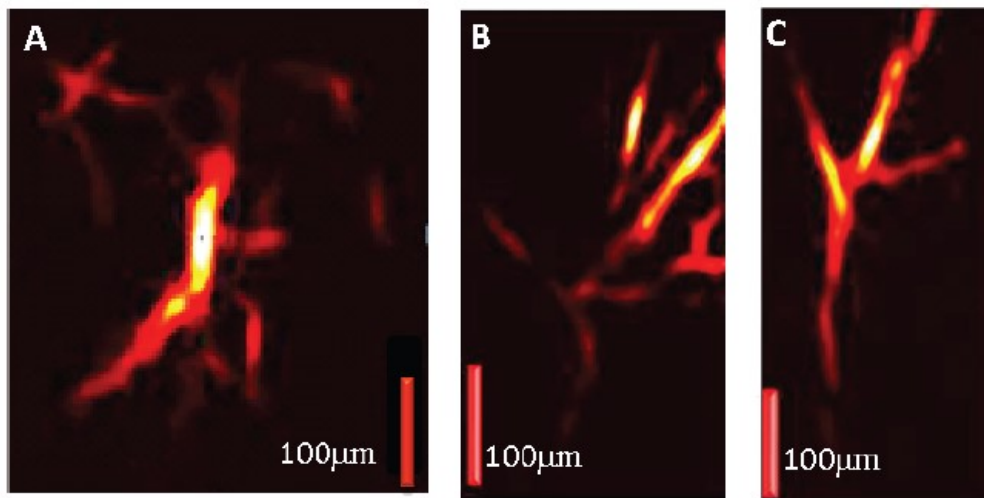


Figure 4.3: (a)–(c) GRIN-lens OR-PAME images of the microvasculature at various positions in a hairless SCID ear in vivo.

The power at the end of the fiber was measured as ~ 45 mW with 160 kHz PRR, assuming that the depth of the laser focus was >200 μm below the tissue surface and that the numerical aperture of the lens was about 0.46. The calculated surface laser fluence was less than 1 mJ cm^{-2} , which is much lower than the American National Standards Institute (ANSI) safety limit in the visible spectral region (20 mJ cm^{-2}) [5]. We did not observe any tissue damage during our experimental sessions.

In the contact-mode operation of our fiber based OR-PAM without a GRIN lens, the signal-to-noise and lateral resolution degraded with imaging depth due to the large divergence angle at the output of the image guide fiber strands. However, using the GRIN-lens OR-PAME we can overcome this limitation. Future work could involve designing an all optical photoacoustic detector at the tip of the endoscopy probe in order to eliminate any external ultrasound transducer. The use of an external transducer, however, is not unrealistic as an ultrasound system could be used to both guide the positioning of the fiber and receive OR-PAME signals. Future enhancement may also include adding multi-wavelength capabilities for functional imaging. Mosaicing may expand the field of view [6].

Extending the concept to real-world endoscopic applications using the results shown in chapter 3 and chapter 4 would be challenging due to the difficulty in positioning of the external transducer. In the next chapter, we demonstrate a new version of OR-PAME using an ultrasound linear array transducer. Using this system photoacoustic acquisition and endoscope guidance can be done by using the same ultrasound transducer with about 5 cm distance from the origin, reducing the required complexity of the setup.

Bibliography

1. Hajireza, P., W. Shi, and R.J. Zemp, *Label-free in vivo fiber-based optical-resolution photoacoustic microscopy*. Opt Lett, 2011. **36**(20): p. 4107-9.
2. Jung, W., et al., *Miniaturized probe based on a microelectromechanical system mirror for multiphoton microscopy*. Opt. Lett., 2008. **33**(12): p. 1324.
3. Wu, J., et al., *Paired-angle-rotation scanning optical coherence tomography forward-imaging probe*. Opt. Lett., 2006. **31**(9): p. 1265.
4. Manniesing, R. and W. Niessen, *Multiscale Vessel Enhancing Diffusion in CT Angiography Noise Filtering*, in *Information Processing in Medical Imaging*. 2005, Springer Science + Business Media. p. 138-149.
5. *American National Standards Institute (ANSI) calendar*. J. Acoust. Soc. Am., 2000. **107**(1): p. 13.
6. Shao, P., et al., *Mosaicing for fast wide-field-of-view optical-resolution photoacoustic microscopy*, in *Photons Plus Ultrasound: Imaging and Sensing 2012*. 2012, SPIE-Intl Soc Optical Eng.

5. Optical-resolution photoacoustic micro-endoscopy with ultrasound-guided insertion and array system detection

Endoscopic imaging has enabled physicians to visualise the interior structures of the circulatory, respiratory, and digestive systems. Recently, our group introduced the capability of a label-free optical-resolution photoacoustic microendoscopy system (OR-PAME) [1, 2]. Ultrasound acquisition and light delivery are the two primary design challenges of an endoscopic OR-PAM system. Our previous real-time OR-PAME systems take advantage of an image-guide fiber and a unique fiber laser with detection by a focused single element ultrasound transducer. Extending the concept to real-world endoscopic applications using the previously reported OR-PAME system would be very challenging due to the difficulty in positioning of the external transducer.

One potential solution for the external transducer is to use all-optical detection techniques such as Fabry-Perot interferometry (FPI) [3]. However, this solution will require another form of imaging to provide external guidance of the endoscope. In this chapter, we demonstrate a new version of OR-PAME using an ultrasound linear array transducer. Array-based optical-resolution photoacoustic micro-endoscopy (AOR-PAME) offers several advantages over previous systems. First, photoacoustic acquisition and endoscope guidance use the same ultrasound transducer, reducing the required complexity of the setup. Second, positioning of the fiber can be aided with realtime B-mode ultrasound. Finally, delay-and-sum beamforming can be used to enhance the photoacoustic signals in the imaging plane by refocusing signals, meaning that fiber placement within the visual field of the array transducer does not need to be controlled precisely to capture an endoscopic image. This approach has the added benefit of being possible with a sufficiently fast ultrasound array system adapted for photoacoustic beamforming [4].

In order to show the capabilities of AOR-PAME, imaging carbon fiber networks and the ears of rats is demonstrated. Using delay-and-sum beamforming, the images of carbon fiber networks had spatial resolution and signal-to-noise ratio (SNR), measured as the ratio of the

average signal in an area on the fiber to the standard deviation of an area off the fiber, in decibels) of 9 μm and 40 dB, respectively, taken at a depth of ~ 2 cm. From previous photoacoustic work with the Verasonics array system, detection ~ 5 cm deep within tissues is possible [5] suggesting that this detection scheme is appropriate for OR-PAME systems for many locations in the body. Additionally, we demonstrate fiber guidance and endoscopic image capture through the tissue-mimicking phantom using only hand-guidance. Thus we believe that the AOR-PAME system can be used in future clinical applications.

The basic experimental setup is shown in Figure 5.1. A 532 nm diode-pumped Ytterbium fiber laser (YPL-G, IPG Photonics Corporation) with 1 ns pulse width, up to 600 kHz pulse repetition rate, and energy up to 20 μJ is coupled into a single-mode fiber and collimated then directed into a 2D scanning mirror system (6203H, Cambridge Technology Inc.). The mirrors are controlled by a two-channel function generator (AFG3022B, Tektronix Inc.). For our experiments, a laser pulse repetition rate of 20 kHz and energy of 500 nJ is used. The frequency of the fast and slow mirrors is fixed at 5 Hz and 0.05 Hz respectively. The light from the mirrors is focused by an objective lens ($f = 4$ mm, 518125, LEICA, Germany) into the input end of the image guide fiber, consisting of 30,000 individual fibers in a 0.8 mm bundle. In order to trigger the ultrasound acquisition system, a beam splitter is used to pick off a part of the beam and redirect it into a photodiode. The photodiode signal is run through a delay generator (SRS-DG645), which is used to down sample to 1 kHz and delay the signal by almost one cycle to account for the speed constraints and triggering delay in the ultrasound acquisition system.

Ultrasound signals are collected by an L7-4 linear array transducer connected to a Verasonics VDAS ultrasound acquisition system. This captures data at a rate of 20 MSamples/sec across all 128 elements simultaneously at 1,000fps and a depth of ~ 1500 samples. Due to memory constraints, we are only capable of capturing data for 10,000 points. Data are processed post-capture on a host PC to produce focused images for each of the 10,000 points, and then a maximum amplitude projection is taken to produce a final image. Since we are using sinusoidal scanning, the image is re-interpolated on a square grid. The feedback signals used for the re-interpolation are simulated based on the function generator parameters to simplify data collection. After interpolation to the 100×100 square grid, a 3×3 Gaussian filter is

applied with $\sigma=0.5$ is applied to provide some smoothing of honeycomb noise associated with the image guide structure and laser pulse positional uncertainty, and images are shown on a linear color scale.

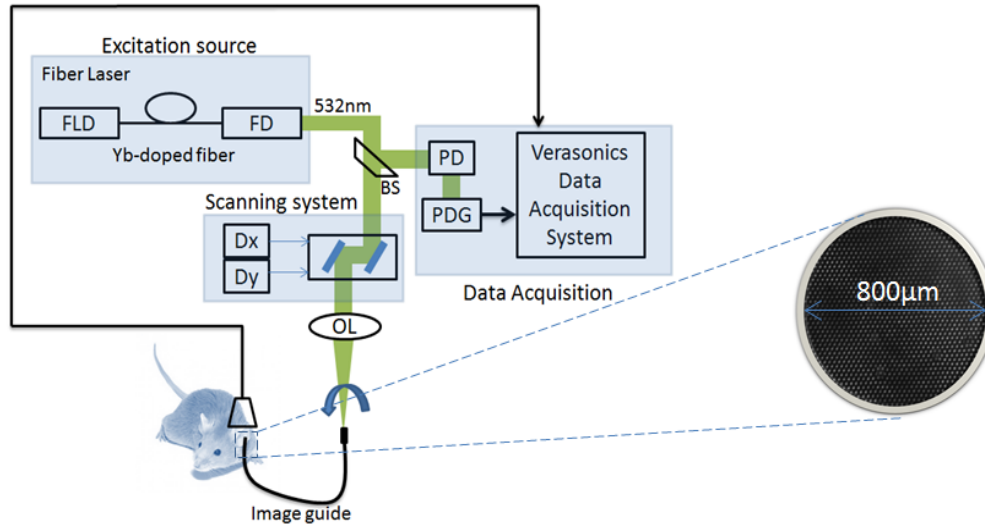


Figure 5.1: Experimental setup of AOR-PAME. FLD: fiber laser driver, Yb: ytterbium, FD: frequency doubling, BS: beam splitter, PD: photodiode, DX: X axis mirror driver, DY: Y axis mirror driver, OL: objective lens, PDG: pulse delay generator.

Tissue-mimicking phantoms were formed using 10% w/v of both porcine gelatin and corn starch. This is a tissue-mimicking phantom commonly used in photoacoustic imaging studies that provides similar optical and acoustic properties to human tissue. The phantom was formed in a mold, and a hole was formed using an appropriately-sized drill bit. Carbon fibers were pushed to the bottom of this hole, and water was used to fill the hole for acoustic coupling. The image-guide was then threaded down the hole using ultrasound imaging for guidance, and then an endoscopic image was captured. During this whole process, both the image-guide and array transducer were held by hand with no additional stabilization, unlike our previous experiments[6]. Additionally, the connector was removed from the end of the image-guide, allowing the hole that the endoscope was guided through to be much smaller than in previous experiments. This experiment shows the practicality of the proposed AOR-PAME. For *in vivo* studies, we imaged the ears of 60g rats. All the experimental procedures were carried out in conformity with the laboratory animal protocol approved by the

University of Alberta Animal Use and Care Committee. Authors are also trained and certified in order to use mice in the research work. During the imaging session the animal was anesthetized with Isoflurane using a breathing anesthesia system (E-Z Anesthesia, Euthanex Corp.).

Figure 5.2 shows the phantom imaging setup, as well as images of the tunnel as the fiber is being inserted. After the fiber was guided to the embedded carbon fibers, several images were taken as shown in Figure 5.3. SNR is measured at ~ 40 dB, in spite of the ~ 2 cm of ultrasound attenuation through the tissue phantom.

Figure 5.4 shows blood vessels of the ear of a 60g rat. The *in vivo* image of the ear was very challenging to capture due to the pressure exerted on the ear by the fiber that was necessary to ensure contact, which tended to drive blood out of the tissue. Using a GRIN lens at the tip of the fiber can solve this problem by removing the requirement for contact, with a trade-off having a larger footprint [7]. Improved means of mitigating pressure-induced flow blockage should be investigated in future work. Future clinical applications could include imaging colorectal and gastrointestinal cancers and dysplasia. *In vivo* endoscopic applications can be investigated in the future.

The full-width half-maximum (FWHM) of a single carbon fiber was measured as ~ 11 μm in Figure 5.3 which corresponds to ~ 9 μm based on convolution measurements[8]. While it is possible to form images from the raw data, there are significant advantages in terms of SNR using beamforming: our previous work has shown a 21 dB increase [9]. Currently, delay-and-sum beamforming is performed on the entire image for all 10,000 photoacoustic events (each with 128 channels and 1500 samples per channel) which takes ~ 3 minutes to complete. However, by limiting the acoustically beamformed region to an area around the fiber tip and using fixed-focus delay and sum, reconstruction could be sped up to real-time, since current reconstruction forms an entire acoustically-focused photoacoustic image for each optically-focused point. The current SNR is promising for detection deep in tissue (~ 5 cm). However, if necessary, the SNR could be improved by averaging the raw photoacoustic data of multiple images before beamforming. We believe that AOR-PAME - with capabilities of image guidance and deep capture may have a significant impact on emerging endoscopic applications.

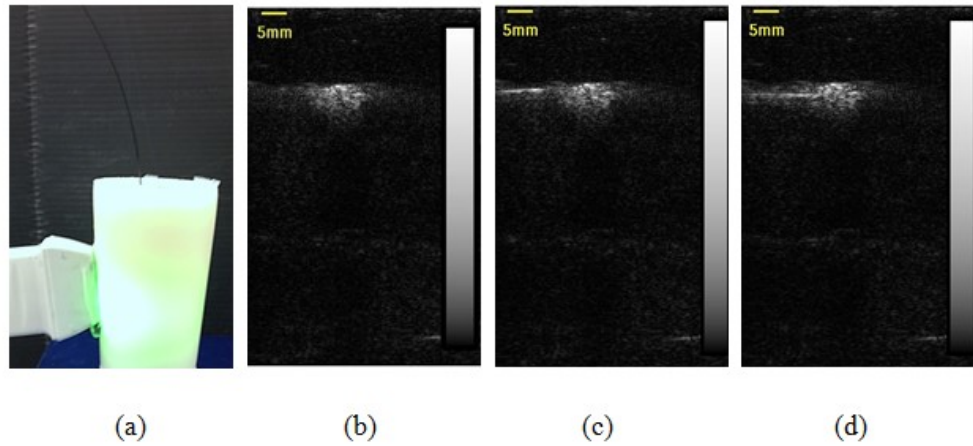


Figure 5.2: (a) Phantom setup with ultrasound images of (b) before (Video 1), (c) during (Video 1) and (d) after insertion of endoscope (Video 1). Figures (b-d) are rotated 90 degrees counterclockwise in comparison to figure (a).

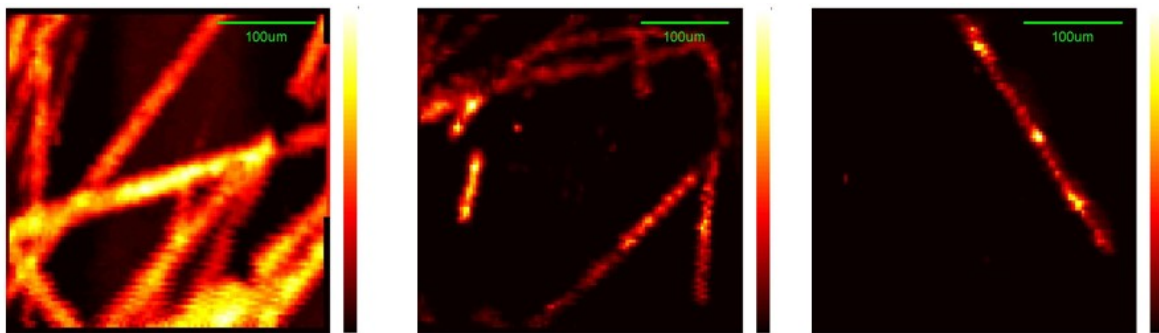


Figure 5.3: Carbon fiber images captured from ~2cm depth in tissue-mimicking phantom, (a-b) show fiber networks, (c) shows a single carbon fiber. SNR is ~40 dB, best-case resolution ~9 μm .

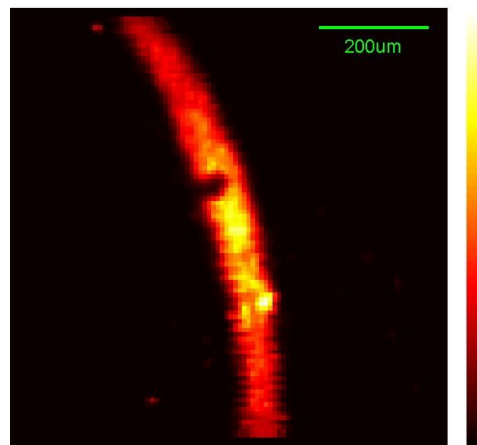


Figure 5.4: In vivo AOR-PAM image of rat ear.

In the next chapter a new generation of handheld optical-resolution photoacoustic microscopy with a wide range of potential clinical applications is demonstrated. Using fast scanning mirrors, an image guide with 30,000 fiber pixels, a refocusing lens and a unique probe we managed to reduce the footprint of an OR-PAM system from a stationary table-top system to a portable, 4 cm by 6 cm, probe weighing ~500 g tethered to a scanning unit. The compact, flexible nature of the proposed design and the small footprint of the apparatus increase the usability of OR-PAM for potential clinical applications such as in dermatology.

Bibliography

1. Hajireza, P., W. Shi, and R.J. Zemp, *Label-free in vivo fiber-based optical-resolution photoacoustic microscopy*. Opt Lett, 2011. **36**(20): p. 4107-9.
2. Hajireza, P., W. Shi, and R. Zemp, *Label-free in vivo GRIN-lens optical resolution photoacoustic micro-endoscopy*. Laser Phys. Lett., 2013. **10**(5): p. 055603.
3. Hajireza, P., et al., *Glancing angle deposited nanostructured film Fabry-Perot etalons for optical detection of ultrasound*. Opt Express, 2013. **21**(5): p. 6391-400.
4. Harrison, T. and R.J. Zemp, *The applicability of ultrasound dynamic receive beamformers to photoacoustic imaging*. IEEE Transactions on Ultrasonics, Ferroelectrics and Frequency Control, 2011. **58**(10): p. 2259-2263.
5. Harrison, T. and R.J. Zemp, *Coregistered photoacoustic-ultrasound imaging applied to brachytherapy*. J. Biomed. Opt., 2011. **16**(8): p. 080502.
6. Harrison, T., et al., *Optical-resolution photoacoustic micro-endoscopy with ultrasound array system detection*, in *Photons Plus Ultrasound: Imaging and Sensing 2013*. 2013, SPIE-Intl Soc Optical Eng.
7. Hajireza, P., W. Shi, and R. Zemp, *Label-free in vivo GRIN-lens optical resolution photoacoustic micro-endoscopy*. Laser Phys. Lett., 2013. **10**(5): p. 055603.
8. Shi, W., et al., *Optical resolution photoacoustic microscopy using novel high-repetition-rate passively Q-switched microchip and fiber lasers*. J. Biomed. Opt., 2010. **15**(5): p. 056017.
9. Harrison, T., et al., *Optical-resolution photoacoustic micro-endoscopy with ultrasound array system detection*, in *Photons Plus Ultrasound: Imaging and Sensing 2013*. 2013, SPIE-Intl Soc Optical Eng.

6. Real-time handheld optical-resolution photoacoustic microscopy

6.1. Introduction

Since cancer cells need to consume more oxygen and nutrients to grow compared to other tissues [1, 2], they signal the onset of angiogenesis and hence have plenty of contrast providing blood vessels, making OR-PAM a useful tool for tumor imaging. Real-time ORPAM may have a wide range of potential applications for clinical practice [3, 4]. Recently a real-time B-scan OR-PAM system was demonstrated [5] with scanning speed up to 40 Hz over 1-mm range or 20 Hz over 9-mm range. In order to develop a real-time OR-PAM system a high laser pulse repetition rate (PRR) and fast data acquisition and display system are required. Laser systems such as flash lamp-pumped laser systems (PRR ~up to 100 Hz) and diode-pumped solid-state Q-switched lasers (PRR ~up to few kHz) typically do not have high enough repetition rates for real-time C-scan imaging [3].

Currently laser systems with repetition rates greater than 100 kHz, adequate pulse durations, and energies for real-time OR-PAM have not yet been widely explored for photoacoustic imaging [3]. We introduce a high repetition rate, inexpensive, compact laser source for realizing high frame rate photoacoustic imaging [3, 4].

Another limitation of current OR-PAM systems is their lack of flexibility. The present OR-PAM systems are mostly mounted as a table-top device with a large footprint. However, recently we introduced label free optical-resolution photoacoustic micro-endoscopy to enable access to internal body cavities[6]. Thus far, however, an external ultrasound transducer is required. To extend the potential range of applications, for the first time, we demonstrate a handheld real-time optical-resolution photoacoustic microscope (HH-OR-PAM) with a 4 cm by 6 cm footprint and weight of less than 500 g using image guide fibers and a unique fiber laser system. Additionally, the capability of HH-OR-PAM is demonstrated by phantom and *in vivo* (microvasculature in a Swiss Webster mouse ear) studies based on a customized nanosecond-pulsed tunable fiber laser with repetition rates of up to 600kHz, enabling near real-time C-scan and volumetric imaging.

6.2. System description

Figure 6.1(a) shows the experimental setup of the laser scanning HH-OR-PAM. A pulsed fiber laser (YLP-G, IPG Photonics Corporation.) with second-harmonic wavelength of 532 nm is able to provide tunable average output power up to 13W and pulse energy up to 20 μ J. A glass slide is used to deflect a small amount of light into a photodiode. The photodiode is used to trigger the high speed data acquisition card (Gage card CS8289). The laser beam passes through a 2D galvanometer scanning mirror system (6230H, Cambridge Technology Inc.).

The mirrors are controlled by separate drivers. These drivers can run with an analog control signal or a digital waveform depending on the study requirement. In this experiment the mirrors were driven with sine waves generated by a two channel function generator (Tektronix AFG3022B). The frequency of the control signal determines the speed of scanning, while the peak-to-peak amplitude determines the angle of the scanning mirrors and eventually the field of view. In this experiment, the fast and slow scanning rates are fixed at 400 Hz and 1 Hz respectively, providing 2 C-scan frames per second. Using an objective lens ($f = 18$ mm), the scanning light via mirrors was coupled to the 1m-long image guide fiber with 30,000 individual single mode fiber elements (Sumitomo IGN-08/30). The field of view is limited by the diameter of the image guide (800 μ m). The end of the fiber is connected to the handheld probe.

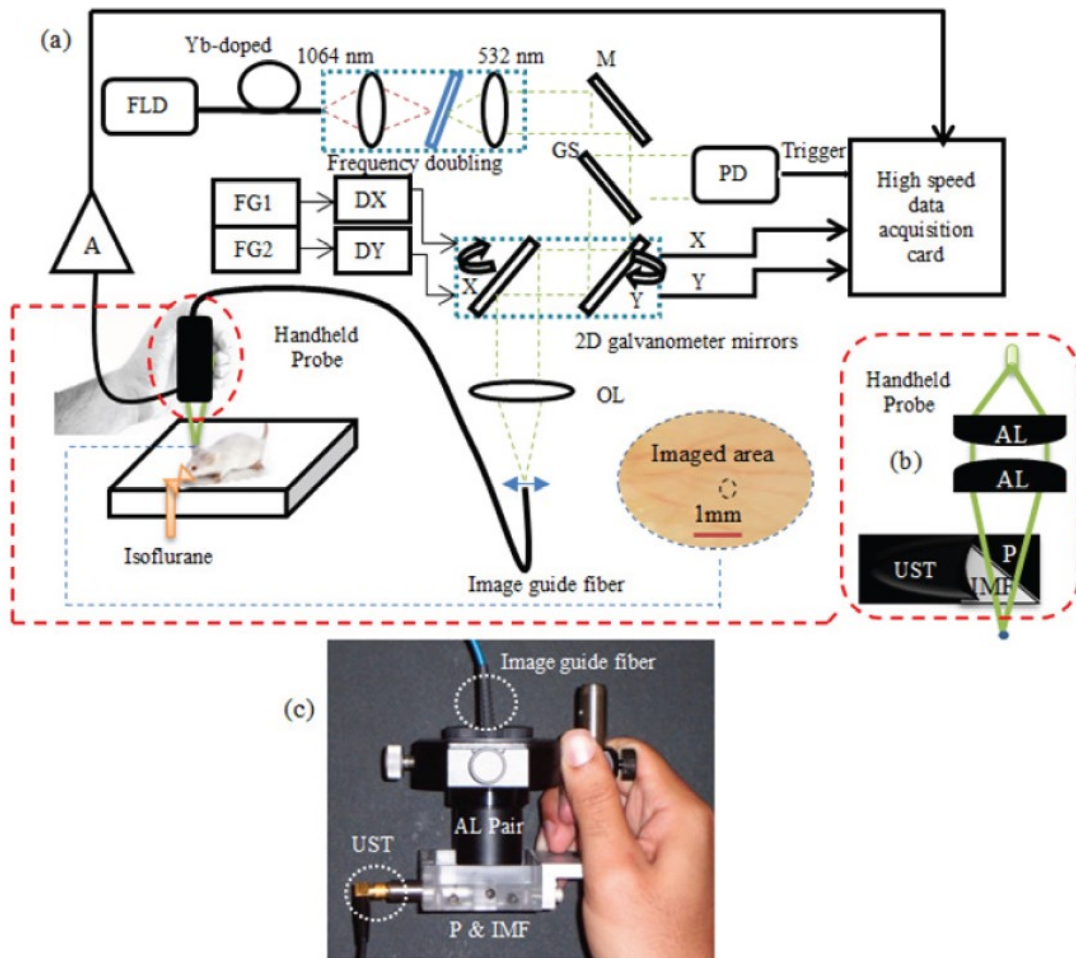


Figure 6.1: (a) Experimental setup of our HH-OR-PAM imaging system employing a high repetition rate diode-pumped pulsed Ytterbium fiber laser with up to 600 kHz pulse repetition rate and pulse widths of 1ns. FLD: fiber laser driver, Yb: Ytterbium, M: mirror, Gs: glass, PD: Photodiode, FG1: function generator channel 1, FG2: function generator channel 2, DX: X axis mirror driver, DY: Y axis mirror driver, OL: objective lens, A: amplifier (Olympus 5900PR). (b) The structure of the handheld probe. The light at the end of the fiber is refocused using a pair of glass aspheric lenses with 350 to 700 nm AR Coating. Then the light passes through an oblique 10-mm fused silica prism. The photoacoustic signals directed upward to the prism's diagonal will be deflected to a focused transducer ($f = 19$ mm). AL: glass aspheric lenses, UST: ultrasound transducer, P: prism, IMF: index-matching fluid. (c) The prototype of the handheld probe. AL: glass aspheric lenses, UST: ultrasound transducer, P: prism, IMF: index-matching fluid.

Figure 6.1(b) shows the structure of the handheld probe. The light at the end of the fiber is refocused using a pair of aspheric glass lenses with 350 to 700 nm AR Coating (Thorlabs 350260 and 352220). Then the light passes through an oblique 10-mm fused silica prism. The photoacoustic signals directed upward to the prism's diagonal will be deflected to a 10-

MHz focused ultrasound transducer (19-mm focus, 6-mm active element, $f\# = 3.17$, CD International Inc). Calculations show that most of the acoustic energy is preserved at the prism interface within 45 ± 13.4 degrees within the angular acceptance of the transducer [3]. Optical index-matching fluid is used in order to allow the top-down laser illumination to be guided to the imaging target without optical refractive path variation. Acoustic attenuation loss in index matching fluid is only slightly greater than water[7]; therefore, it is also used for ultrasonic coupling.

6.3. Result and discussion

In our experiments the fiber laser is utilized to produce 100 mW; however, considering coupling efficiency of the image guide and other optical losses, at the end of the handheld probe the power is reduced to 45 mW. The PRR is set to 160 kHz, therefore the pulse energy on the sample is calculated as $\sim 0.3 \mu\text{J}$. This power is fixed for the entire experiment. The high speed and slow speed scanning mirror are driven by 400 Hz and 1 Hz analog sine wave respectively with 400mV peak-to-peak voltage.

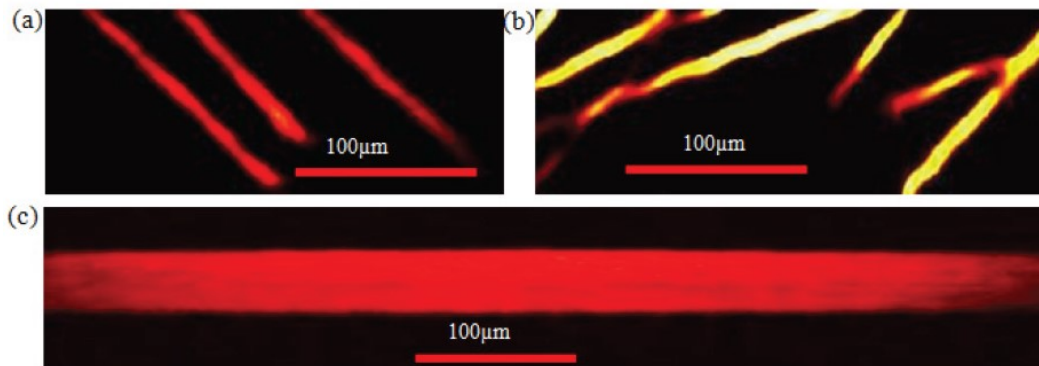


Figure 6.2: (a) and (b) network of carbon fibers with $\sim 7.5 \mu\text{m}$ diameter which are as small as capillary sized blood vessels. (c) Human hair with a diameter of $\sim 100 \mu\text{m}$.

In order to show the ability of the proposed design, different phantom targets have been imaged as shown in Figure 6.2. Figure 6.2(a) and 6.2(b) shows a network of carbon fibers with $\sim 7.5 \mu\text{m}$ diameter which are as small as capillary sized blood vessels. Figure 6.2(c) shows an image of a human hair with a diameter of $\sim 100 \mu\text{m}$. For the *in vivo* studies, we employed the HH-ORPAM to image the microvasculature in the ear of a Swiss Webster

mouse. All the experimental procedures were carried out in conformity with the laboratory animal protocol approved by the University of Alberta Animal Use and Care Committee. Authors are also trained and certified in order to use mice in the research work. During the imaging session the animal was anaesthetized using a breathing anesthesia system (E-Z Anesthesia, Euthanex Corp.). Figure 6.3 shows images of the microvasculature in the ear of a Swiss Webster mouse. A 2D Hessian-based Frangi Vesselness filter [8] was used to filter C-scan maximum amplitude projection (MAP) images to preferentially select tubular structures while rejecting noise.

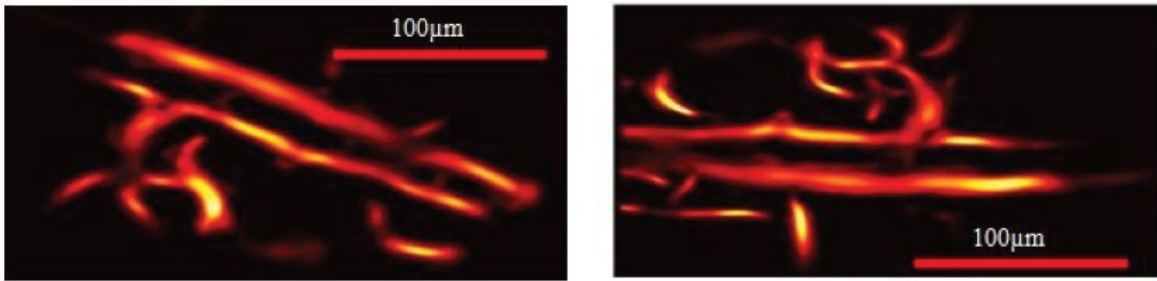


Figure 6.3: Microvasculature in the ear of a Swiss Webster mouse.

Measuring the average signal amplitude and the standard deviation of the noise, the signal to- noise ratio for the carbon fiber is calculated as ~ 22 dB. Fitting individual carbon fiber signal amplitude to a Gaussian function, the full-width-half-maximum (FWHM) is calculated approximately $8.7 \mu\text{m}$ (Figure 6.4). The measured FWHM shown in Figure 6.4 is partly due to the $7.5\text{-}\mu\text{m}$ width of the carbon fiber itself [3]. In order to measure the true optical lateral resolution, the convolution of a 2-D Gaussian beam with a carbon fiber is simulated for a range of spot sizes, and compared with measurements [3]. Using this technique, the optical lateral resolution is estimated as $7 \mu\text{m}$. As mentioned the fast and slow speed mirror scanning rates are set at 400 Hz and 1 Hz respectively, with the laser repetition-rate set at 160 kHz. This corresponds to 2 volumetric-scans (composed of 400 B-scans per volume) per second. C scans are formed from maximum-intensity projections of A-scan lines and contain 200 nonuniformly- spaced pixels in the X-direction and 400 in the Y-direction, respectively.

Higher C-scan frame rates are easily attainable; however, the field-of-view must be sacrificed if the resolution is to be maintained.

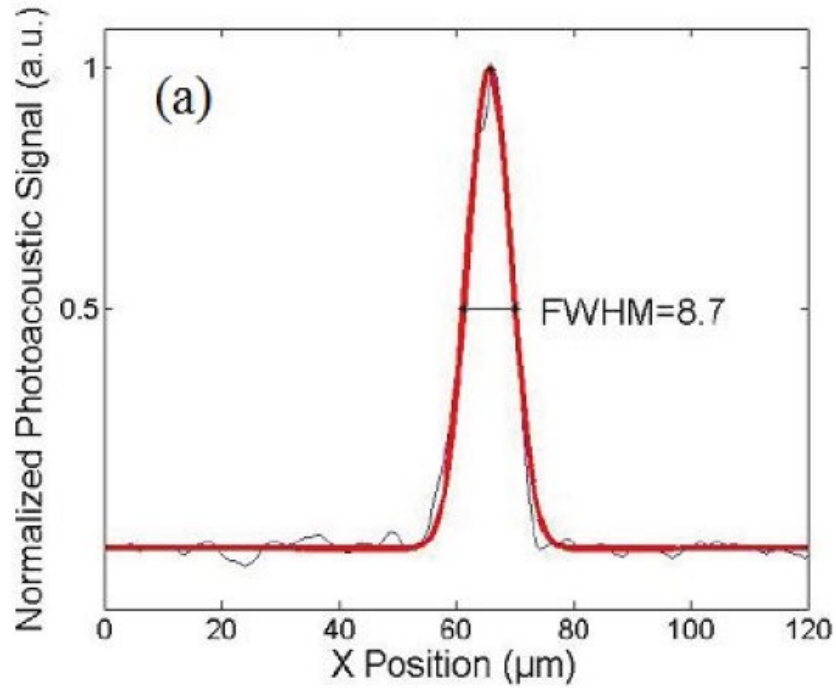


Figure 6.4: FWHM due to fitting individual carbon fiber signal amplitude to a Gaussian function.

For a 400 by 400 μm field of view (FOV) the average step size for the X and Y directions are calculated as 2 and 1 μm, respectively. Since the scanning trajectory of the laser scanning system employs sine wave driving waveforms, the step size at the middle of scanning trajectory can be larger compare to its edge. Using Eq. (1) and Eq. (2) the worst case step sizes for the X and Y directions are calculated as ~3 μm and 2 μm respectively.

$$\Delta X = FOV_x \times \pi \times FR \times PRR^{-1}, \quad (1)$$

$$\Delta Y = FOV_y \times 2 \times FR^{-1} \times SR, \quad (2)$$

where FR is Fast scanning rate, SR is slow scanning rate, FOV_x is field of view in X direction, FOV_y is field of view in Y direction and PPR is pulse repetition rate. The lateral spatial resolution (FWHM) is calculated as ~7 μm, or Gaussian sigma parameter, $\sigma = \text{FWHM} / (2\sqrt{2\ln 2}) \sim 3 \mu\text{m}$. Considering the total area of the fiber bundle with 30,000 individual single mode fibers, we obtained the diameter of each strand to be about 4 μm which is close to the

measured lateral resolution. This shows that the system is almost at optimal resolution. For the *in vivo* study, assuming that the depth of the laser focus is ~ 200 μm below the tissue surface and that the numerical aperture of the lens is about 0.16, the calculated laser surface fluence is ~ 8 mJ/cm^2 which is lower than the American National Standard Institute (ANSI) safety limit (20 mJ/cm^2) [9].

Fiber-based imaging systems have been demonstrated before [10-12]. Such systems also rely on image-guide fibers, miniature fiber bundles capable of transmitting images. Many such systems require the use of an exogenous fluorescent dye or contrast agent. HH-OR-PAM would provide the ability to image microvessels, and with improved resolution, potentially cells and subcellular structures similar to fluorescence (confocal) micro-endoscopes, but without necessarily requiring an exogenous contrast agent. We anticipate that the HH-OR-PAM system will open up new possibilities for clinical and pre-clinical uses, such as functional brain mapping, cancer imaging and detection, assessing completeness of melanoma resection, imaging of angiogenesis to assess therapeutic efficacy, etc. The proposed label-free system will have potential for translational research because it will be compact and potentially portable, real-time, cost-effective. It will permit clinical imaging of different parts of body that were previously inaccessible.

In the next chapter a multi-wavelength optical-resolution photoacoustic microscopy system using stimulated Raman scattering is demonstrated for both phantom and *in vivo* imaging. The multi-wavelength design can add functional imaging capability to the reported OR-PAM designs in the previous chapters.

Bibliography

1. Zhang, H.F., et al., *Functional photoacoustic microscopy for high-resolution and noninvasive in vivo imaging*. Nat Biotechnol, 2006. **24**(7): p. 848-851.
2. Zhang, H.F., K. Maslov, and L.V. Wang, *In vivo imaging of subcutaneous structures using functional photoacoustic microscopy*. Nature Protocols, 2007. **2**(4): p. 797-804.
3. Shi, W., et al., *Optical resolution photoacoustic microscopy using novel high-repetition-rate passively Q-switched microchip and fiber lasers*. J. Biomed. Opt., 2010. **15**(5): p. 056017.
4. Shi, W., et al., *In vivo near-realtime volumetric optical-resolution photoacoustic microscopy using a high-repetition-rate nanosecond fiber-laser*. Opt Express, 2011. **19**(18): p. 17143-50.
5. Wang, L., et al., *Fast voice-coil scanning optical-resolution photoacoustic microscopy*. Opt. Lett., 2011. **36**(2): p. 139.
6. Hajireza, P., et al., *Optical-resolution photoacoustic micro-endoscopy using image-guide fibers and fiber laser technology*, in *Photons Plus Ultrasound: Imaging and Sensing 2011*. 2011, SPIE-Intl Soc Optical Eng.
7. Ranasinghesagara, J.C., et al., *Photoacoustic technique for assessing optical scattering properties of turbid media*. J. Biomed. Opt., 2009. **14**(4): p. 040504.
8. Manniesing, R. and W. Niessen, *Multiscale Vessel Enhancing Diffusion in CT Angiography Noise Filtering*, in *Information Processing in Medical Imaging*. 2005, Springer Science + Business Media. p. 138-149.
9. *American National Standards Institute (ANSI) calendar*. J. Acoust. Soc. Am., 2000. **107**(1): p. 13.
10. Fruhwirth, G.O., et al., *Fluorescence lifetime endoscopy using TCSPC for the measurement of FRET in live cells*. Opt. Express, 2010. **18**(11): p. 11148.
11. Tang, S., et al., *Design and implementation of fiber-based multiphoton endoscopy with microelectromechanical systems scanning*. J. Biomed. Opt., 2009. **14**(3): p. 034005.
12. Sokolov, K., et al., *Endoscopic Microscopy*. Disease Markers, 2002. **18**(5-6): p. 269-291.

7. In-Vivo functional optical-resolution photoacoustic microscopy with stimulated Raman scattering fiber-laser source

7.1. Introduction

Optical-resolution photoacoustic microscopy (OR-PAM) has proven useful for quantifying functional parameters down to capillary sizes [1]. Recent OR-PAM developments include real-time systems [2, 3], small handheld systems [4, 5], endoscopy systems [6-8], and novel detection schemes [9, 10]. Fiber and microchip lasers have recently been introduced as high-repetition-rate sources for realtime OR-PAM [2, 11]; however, the wavelength tunability was limited.

Supercontinuum source for OR-PAM has been reported by using a high-nonlinearity fiber injected with nanosecond pulses from a microchip laser [12]. The supercontinuum was filtered into bands for multiwavelength imaging; however, energy per band was low due to broad distribution of power over such a wide spectral range. In 2011, Koeplinger et al. [13] demonstrated photoacoustic imaging using stimulated Raman scattering (SRS) in optical fiber. They used a 6-m polarization-maintaining fiber and a Nd:YAG microchip laser with 7.5-kHz pulse repetition rates (PRR) for generation of four wavelengths with energy exceeding 80 nJ [13]. While limited to a few discrete spectral bands, energy per band was higher than in the super-continuum case. This concept can be extended to using large-mode area photonic crystal fibers for SRS-based generation of multiple wavelength peaks [14].

Our group previously demonstrated SRS multi-wavelength generation from a fiber-laser source and used chromatic aberration advantageously to improve the depth of field of OR-PAM by focusing simultaneous discrete wavelengths at different depths [15]. This was done at the expense of optimal settings for functional imaging. In this chapter we aim to mitigate chromatic aberration and optimize outputs at each key wavelength.

In previous SRS multi-wavelength systems, the number of wavelength bands was limited, as was the pulse-energy. Near-infrared wavelengths were not demonstrated, nor were *in vivo*

imaging. Our goal was to significantly increase the number of output wavelengths to extend to the near-infrared range, to increase energy per-band, and to ensure minimal SRS peak spectral-widths. This is the first report of *in vivo* functional imaging using a multi-wavelength fiber laser source. Previous reports may not have had sufficient pulse energy to achieve functional imaging capabilities. Our work reports on an optimization strategy to maximize pulse energies per key wavelength and is not as simple as maximizing input power. The functional imaging capabilities were assessed by determining the dye concentration in tubes and estimating the oxygen saturation levels in the Swiss Webster mouse ear. Previous microchip laser pump sources suffered from pulse-to-pulse stability, timing jitter, low repetition rates, and lack of trigger-ability. These issues are now mitigated with the present fiber laser boasting trigger-ability, tunable repetition rates as high as 600 kHz, and pulse-to-pulse stability $\sim 1\%$. Number of wavelength peaks, narrower spectral linewidths, and tunable repetition-rates are also advantages compared to previous work which may lead to many new possibilities for an all-fiber functional photoacoustic imaging source.

7.2. Methods

Figure 7.1 depicts the experimental setup for generation of SRS peaks and for C-scan imaging. The output of a 1-ns pulse width, ytterbium-doped fiber laser (IPG Photonics) capable of PRR from 20-600 kHz was coupled into a 6-m polarization-maintaining single-mode fiber (PM-SMF) (HB-450, Fibercore Inc., UK) to generate SRS peaks using a fiber launch system (MBT621D/M, Thorlabs Inc.). SRS peaks are formed from inelastic nonlinear interaction between incoming photons through the fiber and the molecules in the fiber itself [16]. A fiber optic spectrometer (USB4000, Ocean Optics Inc.) measured the SRS peaks and confirmed the filtered wavelengths. The output of the PM-SMF was collimated using a collimator lens (F280APC-A, Thorlabs Inc.) and bandpass filters (FB, Thorlabs Inc.) were used to select the desired wavelength. A systematic optimization study was performed experimentally to measure the outputs from varying fiber lengths, input pulse energies, and pulse-repetition rates to maximize SRS wavelength peaks without burning the fiber. Filtered light was scanned across samples using a 2D galvanometer scanning mirror system and focused tightly using an objective lens (Leitz Wetzlar 10X/0.25 160/- EF microscope

objective, Germany). Chromatic aberration with this lens was negligible compared to the lens used in our previous work aimed at harnessing chromatic aberration for improved depth of field [15]. An unfocused ultrasound transducer (A3125-SM, 10 MHz/0.25", Olympus Inc.) was positioned beneath the sample to receive the photoacoustic signals. A customized holder was used to contain water between the target and transducer. The position feedback signals from the two mirrors and the amplified RF signals from a pulser-receiver unit (5900PR, Olympus Inc.) were collected using a data acquisition card (CS8289, Gage Applied Systems, Inc.). For maximum energy at the desired imaging wavelengths (532, 545, 558, and 590 nm), a laser PRR of 40 kHz and a 3-m fiber were used. All the experimental procedures were carried out in conformity with the laboratory animal protocol approved by the University of Alberta Animal Use and Care Committee. Authors are also trained and certified in order to use mice in the research work. During the imaging session the animal was anaesthetized using a breathing anaesthesia system (E-Z Anesthesia, Euthanex Corp.).

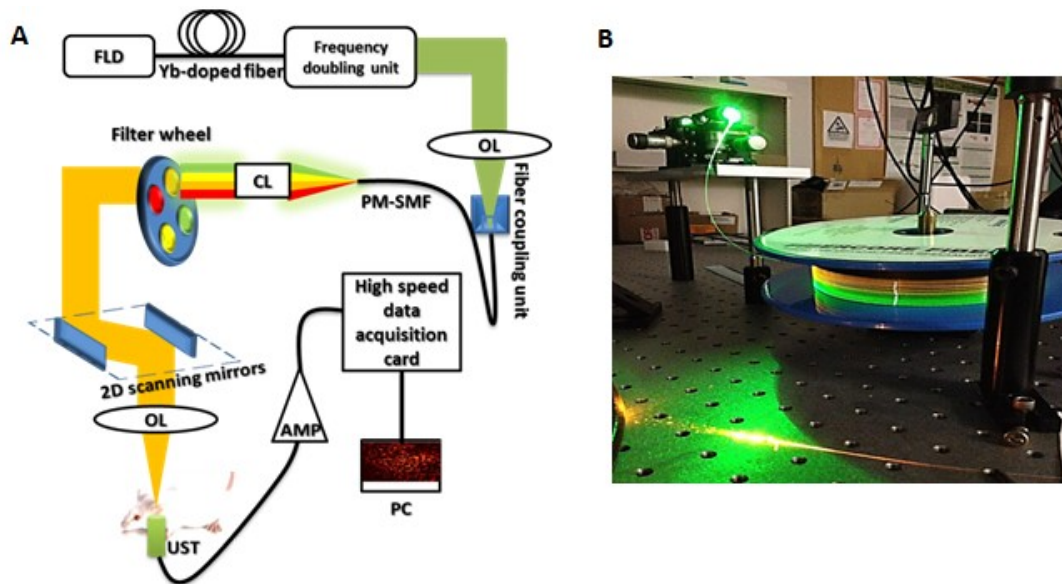


Figure 7.1: (a) Experimental setup of multi-wavelength OR-PAM. FLD: Fiber laser diode, OL: Objective lens, PM-SMF: Polarization maintaining single mode fiber, CL: Collimator lens, UST: Ultrasound transducer. (b) Photograph of the generated multi-wavelength spectrum in a PM-SMF.

7.3. Result and discussion

Table 7.1 shows the measured power at different PRR and input power level for 3-m and 6-m fiber length. The coupling efficiency for all of these experiments was $\sim 70\%$. The pulse energy of each output wavelength can be maximized by choosing a specific input power into the fiber which means, for example, in order to generate optimized pulse energies for 3 different wavelengths, 3 different input powers are necessary. While a higher input power is desirable to generate higher output power levels, input power levels will be limited due to the fiber damage threshold. In this experiment, the input power was varied between 30 mW-150 mW depending on the fiber length, the PRR, the coupling efficiency and the desired wavelength. The fiber damage was first observed at 160-kHz PRR and 150 mW average input power. The back-reflected light from the filter may also cause damage at the end of the fiber; this can be solved by introducing a small angle to the filter. Longer interaction lengths induce a wider range of wavelengths; however, for the proposed *in vivo* application the 3-m fiber length at 40-kHz PRR produced maximized pulse energies for four wavelengths under the fiber damage threshold as shown in table 7.1.

Using a 160-kHz PRR and 15-m PM-SMF, we were able to obtain SRS peaks at 489, 499, 511, 522, 532, 545, 558, 572, 587, 603, 621, 639, 656, 675, 695, 710, 740, 765 and 788 nm (figure 7.2a). The spectrometer verified that the bandpass filter accurately selected for the desired imaging wavelength (figure 7.2b). Far-red and infra-red spectral peaks have estimated pulse energies as high as $\sim 100 \pm 50$ nJ, higher than pulse energies used in previous OR-PAM experiments [4-6]. Four-wave mixing may be one source of SRS peak broadening as two or more wavelength may interact in order to produce an output at various sum or difference frequencies [16]

Broad spectral peaks could result in ambiguous oxygen saturation estimates if spectral bins are not sufficiently narrow in multi-wavelength imaging, however, this could be dealt with using narrower-line filters, at the expense of energy. For functional OR-PAM, only wavelengths of 532, 545, 558, and 580 nm were necessary to be optimized therefore to minimize four-wave mixing and for maximum energy, a 40-kHz PRR and a 3 m PM-SMF was used to generate 532, 545, and 580 nm with pulse energy between 300 and 500 nJ.

Table 7.1: Measured power of SRS peaks generated in varying fiber lengths and at different PRR

<u>3-m fiber (40kHz)</u>							
Generated Wavelength (nm)	545	550	558	570	580	590	600
Output Energy (nJ)	500	-	490	-	335	365	-
Input Energy (nJ) at 532nm to Obtain Reported Output	875	-	1250	-	1750	1875	-
<u>6-m fiber (160kHz)</u>							
Generated Wavelength (nm)	545	550	558	570	580	590	600
Output Energy (nJ)	136	76	151	121	105	213	116
Input Energy (nJ) at 532nm to Obtain Reported Output	470	500	563	625	688	813	938

- Output pulse energy below 50 nJ, Values are reported +/-10%.

Initially, carbon fiber networks and double dye experiments were conducted to assess imaging potential at each SRS peak (figure 7.3). The measured power for each filtered wavelength was set to 5 mW. Signal-to-noise ratios (SNR) for carbon fibers networks were ~ 41, 39, 43, and 42 dB and lateral resolution was 7, 7.5, 7.7, and 8 μm at 532, 545, 560, and 590 nm, respectively. The lateral resolution degrades due to spherical aberration; however this is insignificant and negligible [13]. Figure 7.3(a) shows an example of C-scan images of carbon fiber network using 560 nm wavelength at 160 kHz PRR. Double dye experiments were conducted using red dye (Fiesta Red) and blue dye (Lake Placid Blue). In this experiment the photoacoustic signals were normalized by laser fluence at each wavelength and the photoacoustic spectrum was compared to the absorption spectrum of the dyes. Using several regions within the tube from the C-scan image as shown in figure 7.3(b), spectral demixing was able to accurately estimate the concentration of blue and red dye in each tube. Figure 7.3(b) is an example of the dye-filled tubes at 3 different wavelengths at 160 kHz PRR for 100% Red and 0% Blue dyes. The demixing results of 5 different concentration of red dye are shown in Table 7.2. Figure 7.4 shows the measured absorption of figure 7.3(b) images at 3 different regions. Different regions were chosen in order to improve the accuracy of the measurement. Figure 7.5 shows

mock oxygen saturation estimation using mixtures of red and blue dye. The results show that the C-scan OR-PAM images are in good agreement with the spectrometer results.

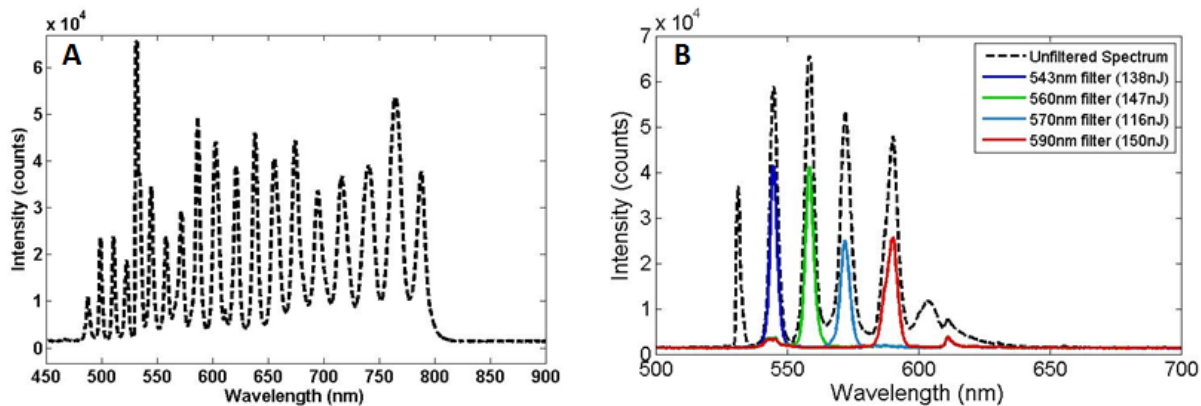


Figure 7.2: (a) SRS peaks for 160 kHz PRR and a 15m PM-SMF. (b) Unfiltered (dashed) and filtered (solid) SRS peaks for 160 kHz PRR and a 6m PM-SMF (the input power varied between 55-100 mW).

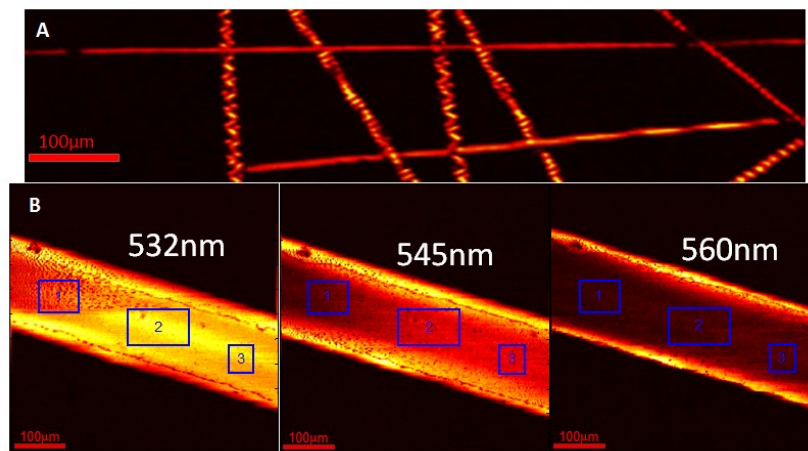


Figure 7.3: C-scan images of (a) carbon fiber networks and (b) the dye-filled tubes at 3 different wavelengths for 100% red and 0% blue dyes.

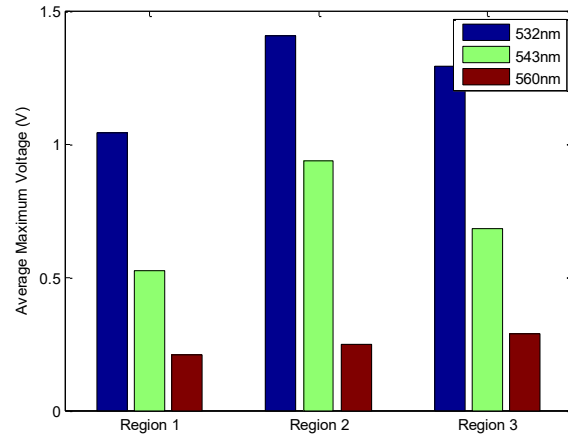


Figure 7.4: The average signal for selected regions within the tube shown in fig. 7.3(b). This data has been used to determine the absorption spectrum.

Table 7.2: Spectral demixing of PA signals of tubes containing various concentrations dyes

Relative concentration of red dye (%)	0	25	50	75	100
Estimated concentration of red dye (%)	2.1	22.7	52.0	77.6	99.9

In vivo imaging of a capillary network at 545 nm and 558 nm is shown in figure 7.6. Slight shifts between the two images were resolved with cross-correlation so that spectral demixing algorithms could be applied. Using a least squares demixing algorithm, arteries (orange in figure 7.6c) and veins (blue-violet in figure 7.6c) can be separated. The resolution of the system is measured $\sim 7 \mu\text{m}$ with $\sim 2 \mu\text{m}$ average scanning step size. The present all-fiber source is suitable for imaging at multiple wavelengths and, with minor modification to the setup, is capable of imaging at near-realtime frame rates. Our experimental work demonstrates that we can image with up to 160 kHz PRR for phantom applications and 40 kHz for *in vivo* applications and with pulse energies greater than 120 nJ – enough for typical photoacoustic imaging experiments. This system can easily be integrated with current OR-PAM table top systems, our endoscopy systems[6], and our handheld systems [4] providing

C-scan frames for each SRS peak available. This will permit quantitative estimation of blood oxygenation and saturation in capillaries, as well as, imaging other absorbing reporter molecules. Further improvements can be made by optimizing the SNR, increasing frame rates, utilizing additional SRS peaks, implementing fast electronic wavelength switching or utilizing new nonlinear fibers to generate high-order SRS peaks.

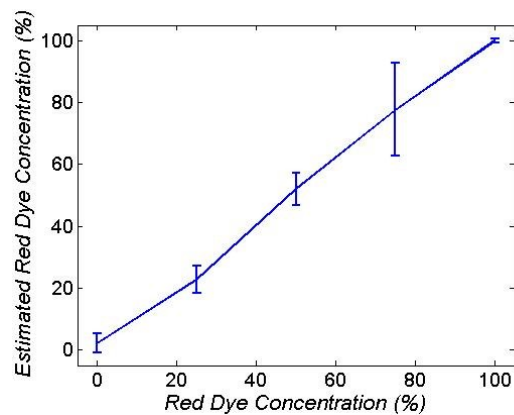


Figure 7.5: Mock oxygen saturation estimation using mixtures of red and blue dye.

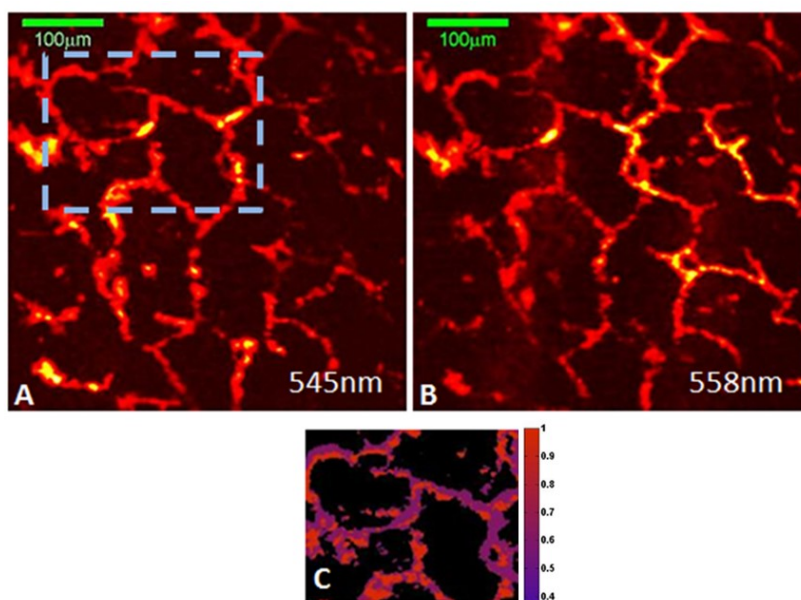


Figure 7.6: Multi-wavelength *in vivo* imaging using 545 nm (A) and 558 nm (B) pulses. Oxygen saturation estimations are shown in (C) for the area within the dashed rectangle.

In the next chapter, a multi-focus optical-resolution photoacoustic microscopy is demonstrated using wavelength tuning and chromatic aberration for depth scanning. As described in this chapter, the fiber and laser parameters were chosen to take advantage of stimulated Raman scattering (SRS) in the fiber to create a multi-wavelength output. However, rather than selecting a single wavelength, all the wavelengths have been fired simultaneously. The collimator lens and objective lens are chosen to take advantage of chromatic aberration in which each generated SRS wavelength peak focuses at a slightly different depth to improve the field of view. The maximum amplitude of photoacoustic signals is mapped to form C-scan images. The improved depth of focus could be valuable for structural imaging of microvascular morphology without the need for mechanical scanning in the depth direction.

Bibliography

1. Hu, S., et al., *Functional transcranial brain imaging by optical-resolution photoacoustic microscopy*. J. Biomed. Opt., 2009. **14**(4): p. 040503.
2. Shi, W., et al., *In vivo near-realtime volumetric optical-resolution photoacoustic microscopy using a high-repetition-rate nanosecond fiber-laser*. Opt Express, 2011. **19**(18): p. 17143-50.
3. Rao, B., et al., *Real-time four-dimensional optical-resolution photoacoustic microscopy with Au nanoparticle-assisted subdiffraction-limit resolution*. Opt. Lett., 2011. **36**(7): p. 1137.
4. Hajireza, P., W. Shi, and R.J. Zemp, *Real-time handheld optical-resolution photoacoustic microscopy*. Opt Express, 2011. **19**(21): p. 20097-102.
5. Zeng, L., et al., *Portable optical-resolution photoacoustic microscopy with a pulsed laser diode excitation*. Applied Physics Letters, 2013. **102**(5): p. 053704.
6. Hajireza, P., W. Shi, and R.J. Zemp, *Label-free in vivo fiber-based optical-resolution photoacoustic microscopy*. Opt Lett, 2011. **36**(20): p. 4107-9.
7. Hajireza, P., W. Shi, and R. Zemp, *Label-free in vivo GRIN-lens optical resolution photoacoustic micro-endoscopy*. Laser Phys. Lett., 2013. **10**(5): p. 055603.
8. Hajireza, P., et al., *Optical-resolution photoacoustic micro-endoscopy using image-guide fibers and fiber laser technology*, in *Photons Plus Ultrasound: Imaging and Sensing 2011*. 2011, SPIE-Intl Soc Optical Eng.
9. Zhang, E., J. Laufer, and P. Beard, *Backward-mode multiwavelength photoacoustic scanner using a planar Fabry-Perot polymer film ultrasound sensor for high-resolution three-dimensional imaging of biological tissues*. Applied Optics, 2008. **47**(4): p. 561.
10. Hajireza, P., et al., *Glancing angle deposited nanostructured film Fabry-Perot etalons for optical detection of ultrasound*. Opt Express, 2013. **21**(5): p. 6391-400.
11. Shi, W., et al., *In vivo dynamic process imaging using real-time optical-resolution photoacoustic microscopy*. J Biomed Opt, 2013. **18**(2): p. 26001.
12. Billeh, Y.N., M. Liu, and T. Buma, *Spectroscopic photoacoustic microscopy using a photonic crystal fiber supercontinuum source*. Opt. Express, 2010. **18**(18): p. 18519.
13. Koeplinger, D., M. Liu, and T. Buma, *Photoacoustic microscopy with a pulsed multi-color source based on stimulated Raman scattering*, in *2011 IEEE International Ultrasonics Symposium*. 2011, Institute of Electrical & Electronics Engineers (IEEE).
14. Loya, A.K., J.P. Dumas, and T. Buma, *Photoacoustic microscopy with a tunable source based on cascaded stimulated Raman scattering in a large-mode area photonic crystal fiber*, in *2012 IEEE International Ultrasonics Symposium*. 2012, Institute of Electrical & Electronics Engineers (IEEE).
15. Hajireza, P., A. Forbrich, and R.J. Zemp, *Multifocus optical-resolution photoacoustic microscopy using stimulated Raman scattering and chromatic aberration*. Opt Lett, 2013. **38**(15): p. 2711-3.
16. Agrawal, G.P., *Introduction*, in *Nonlinear Fiber Optics*. 2006, Elsevier BV. p. 1-24.

8. Multi-focus optical-resolution photoacoustic microscopy using stimulated Raman scattering and chromatic aberration

Mechanical scanning in the depth direction is one means of improving the depth of field [1]; however, mechanical scanning greatly limits the speed of imaging. In order to achieve real-time imaging, a non-mechanical method to acquire information in depth is required.

In this chapter we perform depth scanning by wavelength tuning. We take advantage of chromatic aberration in the collimating/objective lens pair used to refocus light from a fiber into the object so that each wavelength is focused at a slightly different depth location. We additionally use multiple wavelengths simultaneously for improved depth-of-field imaging. Extended depth imaging through exploitation of chromatic aberration has been reported before in confocal microscopy [2, 3] but not yet for photoacoustic imaging. For imaging the microvasculature, wavelength-tuned depth-scanning or simultaneous wavelength multi-focal imaging may prove less ideal for functional imaging tasks, but may prove valuable for structural imaging of microvasculature morphology. In order to utilize the proposed system for functional imaging an achromatic lens can be used. We take advantage of stimulated Raman scattering (SRS) in a polarization-maintaining single-mode fiber (PM-SMF) pumped by a fiber laser to produce multi-colored output. SRS peaks are formed from inelastic nonlinear interaction between incoming photons through the fiber and the molecules in the fiber itself [4]. Since discrete SRS-peaks are generated, discrete focal zones are created. The theoretical depth of field of a 532-nm beam with 7- μm beam waist full-width-half maximum (FWHM) is $\sim 100 \mu\text{m}$. We demonstrate scanning over more than 400 μm in depth using wavelength tuning and chromatic aberration.

Depth-scanning and enhanced depth of field is demonstrated in carbon fiber phantoms and *in vivo*. The experimental setup of MF-OR-PAM is depicted in figure 8.1. A 1ns pulse width, ytterbium-doped fiber laser (IPG Photonics Inc.) with a pulse repetition rate (PRR) of 40 kHz was coupled using a fiber launch system (MBT621D/M, Thorlabs Inc.) into a 3m PM-SMF (HB-450, Fibercore Inc., UK) to generate SRS peaks at 543, 560, 590, and 600 nm and pulse

energies between 300 and 500 nJ. The output of the PM-SMF was collimated (F280APC-A, Thorlabs Inc.) and scanned across the samples using a 2D galvanometer scanning mirror system (GVS012/M, Thorlabs Inc.).

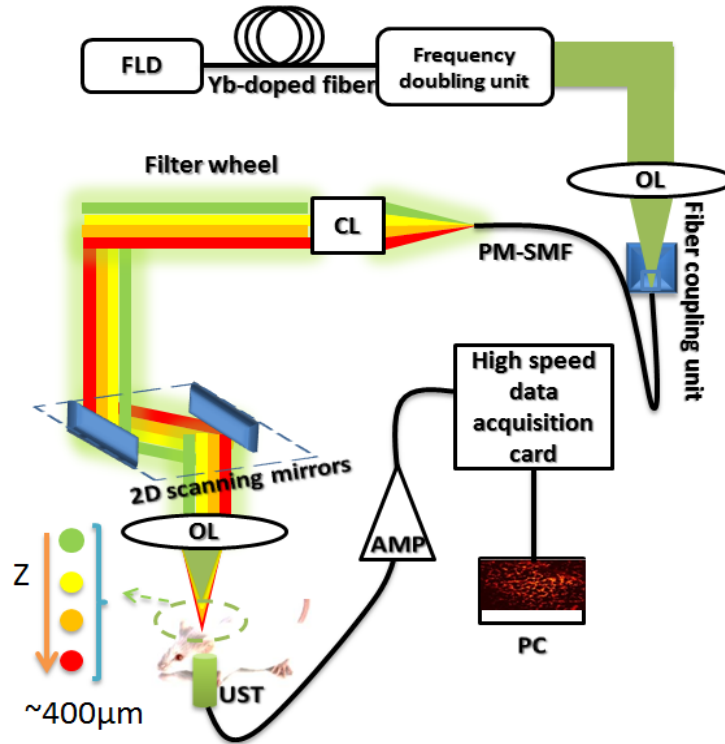


Figure 8.1. Experimental setup of multi-focus OR-PAM. FLD: Fiber laser diode, OL: Objective lens, PM-SMF: Polarization-maintaining single-mode fiber, CL: Collimator lens, UST: Ultrasound transducer

The scanning mirrors were driven by a two channel function generator. The scanning light was then focused tightly using an objective lens (Aspheric doublet lens, $f=30$ mm) which was chosen to take advantage of chromatic aberration. An unfocused ultrasound transducer (A3125-SM, 10 MHz/0.25", Olympus Inc.) in the transmission mode is used in order to receive the photoacoustic signals. The feedback signals from the 2D scanning mirror galvanometer and the amplified photoacoustic signal from a pulser-reciever unit (5900PR, Olympus Inc.) were collected using a fast data acquisition card (CS8289, Gage Applied Systems, Inc.). The maximum amplitude of photoacoustic signals is mapped to form the image.

All the experimental procedures were carried out in conformity with the laboratory animal protocols approved by the University of Alberta Animal Use and Care Committee. During the imaging session the animal was anaesthetized using a breathing anesthesia system (E-Z Anesthesia, Euthanex Corp.).

Four different wavelengths were used to image carbon fiber networks as shown in figure 8.2. Bandpass filters with 10-nm linewidths separated the generated SRS wavelength peaks. The power and pulse repetition rate were fixed at 5 mW and 40 kHz respectively for all of the carbon fiber images. Table 1 provides the measured parameters in figure 8.2.

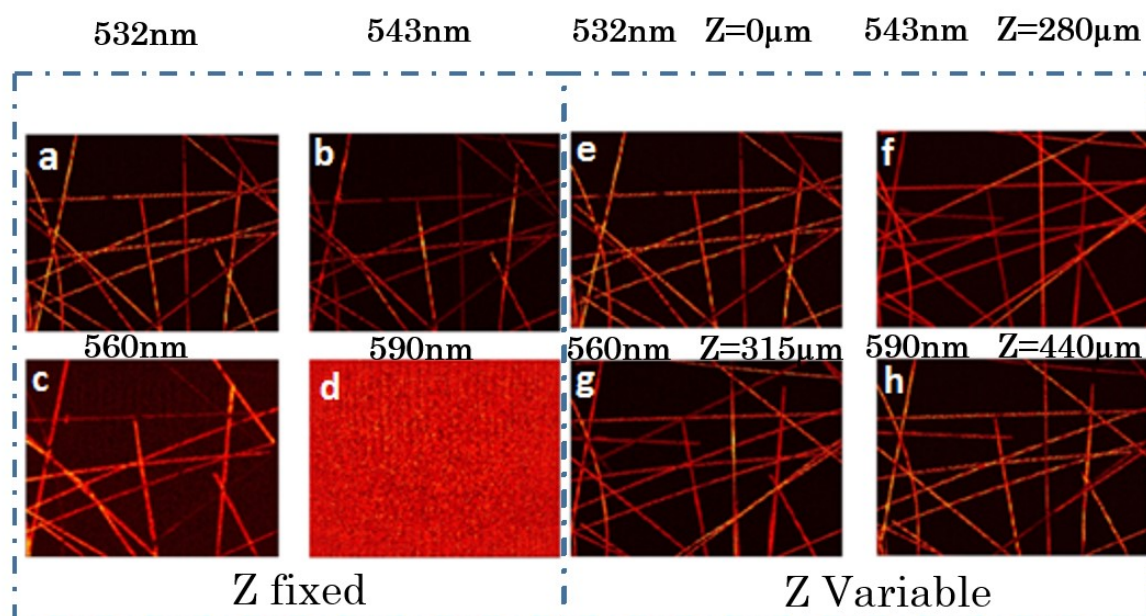


Figure 8.2: OR-PAM images of carbon fiber network at four different wavelengths at a fixed depth (a-d) and variable depth (e-h).

Figures 8.2(a-d) shows OR-PAM images of carbon fiber networks while the depth position (Z) was fixed. The full width half maximum (FWHM) of an individual carbon fiber (Table 8.1) was worse as the wavelength increased. At 590 nm the fibers were completely out of the depth of field so as to generate photoacoustic signals too weak to discern from noise. These results clearly indicate the effect of chromatic aberration in which each wavelength focuses at different depth. Targets with a narrow absorption spectrum may not be suitable for imaging

with our proposed method. However, for the task of structural imaging of blood vessels, where segmentation is performed, wavelength-dependent absorption might be tolerated.

Table 8.1: Results of figure 8.2

	a	B	c	d	e	f	g	h
$\lambda(\text{nm})$	532	543	560	590	532	543	560	590
SNR(dB)	41	30	22	-	41	39	44	42
Z(μm)	0	0	0	0	0	280	315	440
FWHM(μm)	7	13	15	N/A	7	7.5	7.7	8
DOF(μm)	-	-	-	-	104	118	120	123

Figures 8.2(e-h) show the same sample, however, the depth of the phantom has been mechanically re-positioned at each wavelength to achieve the minimum FWHM (best lateral resolution). Table 8.1 shows that at the focal plane (columns e-h) the lateral resolution as measured by the FWHM becomes slightly larger with longer wavelengths, as expected. By tuning the wavelength from 532 nm to 590 nm we achieve effective depth scanning over a distance of 440 μm , a significantly greater depth range than the single wavelength depth of field (DOF), measured to be close to the value $\sim 100 \mu\text{m}$ as shown in table 8.1. Greater depth-scanning distances could be achieved by increasing the distance between the collimating and objective lenses.

We additionally fired all wavelengths simultaneously. The rationale is that since each wavelength will focus at a different depth, structures with multiple depth layers may be visualized with improved contrast compared to a single-wavelength depth of field. To test this, we acquired signals from carbon fibers at different depth locations (0, 280, 315, and 440 μm) then added the RF signals together prior to forming C-scan images to mimic a multilayer phantom (which is difficult to construct with precise depths). Point spread functions are obtained by plotting cross-range maximum amplitude versus lateral distance (normal to the carbon fiber direction). As shown in figure 8.3, the point spread function when all wavelengths are fired simultaneously offers close to the same resolution as that of a single wavelength (532 nm), however, the mainlobe-to-sidelobe levels are degraded. This is

expected because out of focus wavelengths will add some off-target signal to the focused dominant signal.

Figure 8.4 shows *in vivo* images of a Swiss Webster mouse ear at different wavelengths. Figure 8.4(a) shows the MF-OR-PAM image with combination of four different wavelengths (532, 543, 560 and 590 nm). Figures 8.4(b) and 8.4(c) show images at 543 nm and 560 nm respectively. Figure 8.4(d) is the image with combination of four different wavelengths at the same energy level with images in figure 8.4(b) and figure 8.4(c) in order to provide a fair comparison.

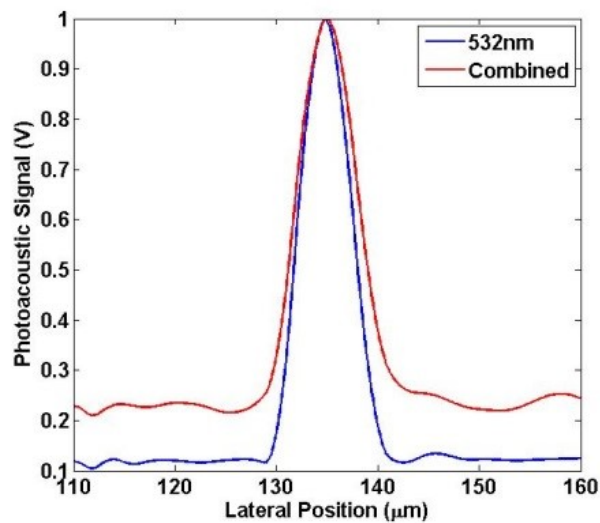


Figure 8.3: Point spread functions of 532 nm and combination of all the wavelengths.

Considering the maximum pulse energy ((for a single wavelength) of ~ 500 nJ focused to a depth of $400 \mu\text{m}$, the laser surface fluence is $\sim 7 \text{ mJ}/\text{cm}^2$ which is lower than the American National Standard Institute (ANSI) safety limit ($20 \text{ mJ}/\text{cm}^2$) [5]. The actual average pulse energy for each wavelength (532 nm, 545 nm, 560 nm and 590 nm) is $\sim 130 \pm 20$ nJ. Considering the NA of the objective lens is 0.12, if the shortest wavelength pulse is focused deeper than $150 \mu\text{m}$ into tissue the total multi-wavelength fluence is $\sim 19 \text{ mJ}/\text{cm}^2$ which is still lower than the ANSI limit.

The signal to noise ratio (SNR) of images in figure 8.4 (a-d) is measured as 51, 35, 33 and 34 dB. The yellow boxes in figure 8.4 highlight the capability of providing structural details

for each image. Figure 8.4(d) acquired with multiple simultaneous wavelengths, but with similar energy level as single-wavelength acquisitions in figure 8.4(b) and 8.4(c). Figure 8.4(d) provides more structural details due to improvement of depth of field. Figure 8.4(a) however with higher average power shows the improvement of SNR and improved depth-of-field relative to single-wavelength images.

In all of the *in vivo* images a 10-MHz unfocused transducer is used. SNR improvements could further be expected using focused transducers. In the future the sensitivity of the system can be improved using all optical detection [6].

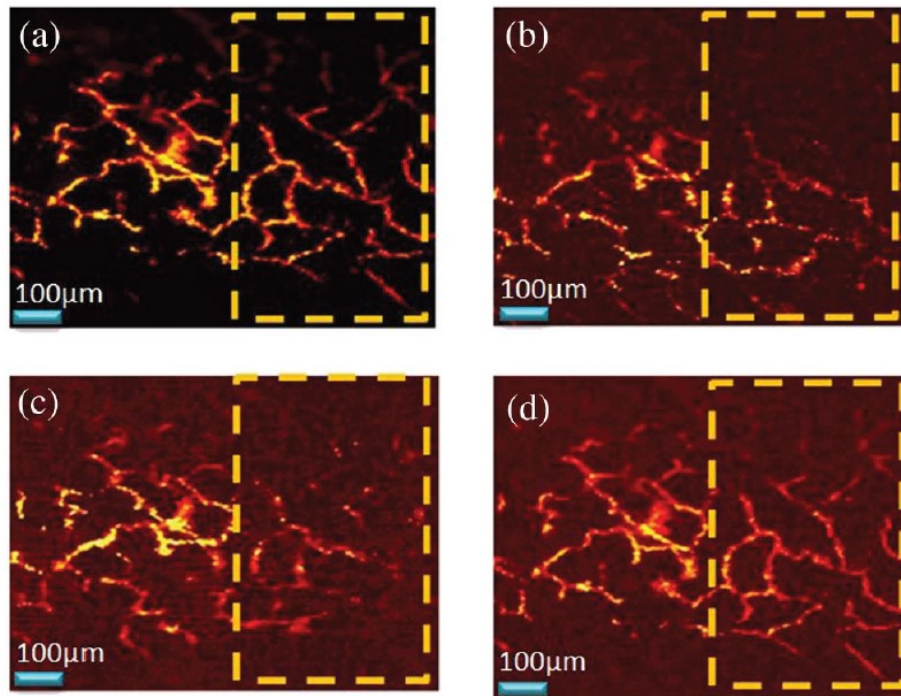


Figure 8.4: *In vivo* images of a Swiss Webster mouse at a) combination of all wavelengths (532, 543 and 560 nm) b) 543 nm, c) 560 nm and d) combination of all wavelengths (532, 543 and 560 nm) with the same energy level as b and c.

In the next chapter a new class of all optical Fabry-Perot-based ultrasound detectors using low acoustic impedance glancing angle deposited (GLAD) films is demonstrated. The GLAD Fabry Perot interferometers (FPI) are transparent to the excitation beam while providing high ultrasound sensitivity. Therefore, they can be used for designing handheld and endoscopic OR-PAM designs with much smaller footprint than reported in the chapter 3-6.

Bibliography

1. Li, G., K.I. Maslov, and L.V. Wang, *Reflection-mode multifocal optical-resolution photoacoustic microscopy*. J. Biomed. Opt, 2013. **18**(3): p. 030501.
2. Garzón, J., T. Gharbi, and J. Meneses, *Real time determination of the optical thickness and topography of tissues by chromatic confocal microscopy*. J. Opt. A: Pure Appl. Opt., 2008. **10**(10): p. 104028.
3. Olsovsky, C., et al., *Chromatic confocal microscopy for multi-depth imaging of epithelial tissue*. Biomed. Opt. Express, 2013. **4**(5): p. 732.
4. Koeplinger, D., M. Liu, and T. Buma, *Photoacoustic microscopy with a pulsed multi-color source based on stimulated Raman scattering*, in *2011 IEEE International Ultrasonics Symposium*. 2011, Institute of Electrical & Electronics Engineers (IEEE).
5. *American National Standards Institute (ANSI) calendar*. J. Acoust. Soc. Am., 2000. **107**(1): p. 13.
6. Hajireza, P., et al., *Glancing angle deposited nanostructured film Fabry-Perot etalons for optical detection of ultrasound*. Opt Express, 2013. **21**(5): p. 6391-400.

9. Glancing angle deposited nanostructured film Fabry-Perot etalons for optical detection of ultrasound

9.1. Introduction

Ultrasound detectors are found in a range of applications from humidifiers, flow-meters, sonar, and medical imaging to non-destructive test systems. Most ultrasound imaging techniques employ piezoelectric receivers to detect the ultrasonic signals. A number of optical detectors have been under investigation as alternatives to piezoelectric transducers and are beginning to offer exceptional receiver sensitivity compared to piezoelectric transducers [1]. All-optical detection can be an attractive alternative in applications such as intra-operative, laparoscopic, and endoscopic ultrasound image guidance systems. In these cases, electrical interconnects must be minimized to make the imaging catheter small and flexible enough to navigate through small orifices and vessels. As well, high voltages present electrical safety hazards to patients. Additionally, legislative trends in some countries include restricting hazardous substances used in electrical and electronic equipment including lead. Hence there is significant opportunity for transducer technology which is lead-free. Finally, many invasive applications also require either sterilizable or disposable catheters. Hence the need for alternative transducer technologies makes optical-based transducers viable candidates. Optical transducers have been under intense investigation for use in photoacoustic imaging systems where laser pulses excite tissues. In these systems, absorbed optical energy is first converted into acoustic signals by thermo-elastic expansion and then received by ultrasound transducers to be processed into final images[2]. Unlike ultrasound images, photoacoustic images provide optical contrast, enabling estimation of blood oxygen saturation, imaging of optical contrast agents, and imaging of gene expression, among other novel and promising applications [3]. Integration of optical-detectors with photoacoustic imaging is natural since the excitation source is optical as well.

Several teams have made considerable progress in this area, with work being done on Fabry-Perot etalons, micro-ring resonator devices, and fiber-Bragg grating approaches [4-7]. These detectors offer the high sensitivity and broad bandwidth important for photoacoustic imaging applications. For example, Zhang et al report a FPI sensor with 310 Pa sensitivity over a bandwidth of 39 MHz[4]. They showed that the sensitivity of these FPI optical detectors could be significantly higher than piezoelectrics. Xie, et al demonstrated microring resonators with sensitivity reaching 29 Pa[5].

Our team recently introduced an optical-resolution photoacoustic micro-endoscopy system based on a sub-mm-footprint image-guide fiber bundle [8, 9]. The system, however, required an external ultrasound transducer to detect signals from a scanned micron-sized laser spot. The present chapter was in part motivated by the need to create a photoacoustic micro-endoscope system which includes all-optical detection.

In this chapter we demonstrate a novel Fabry-Perot etalon- based ultrasound detector fabricated using GLAD nanostructured thin films. In previous studies FPI's were fabricated by sputtering two stacks of alternate $\lambda/4$ thick layers of ZnS and Na_3AlF_6 on to a PMMA backing stub and Parylene C polymer film spacer [4, 9-11]. As an alternative process to creating alternating material thin film stacks, the single-step GLAD technique can be used to create sensitive FPI-based ultrasound detectors using porous materials. As will be discussed later, the nanostructured GLAD films offer some practical and performance advantages over previous methods. GLAD is a single-step physical vapor-deposition (PVD) technique used to fabricate nanostructured thin films [12-15]. By employing substrate motion and obliquely incident vapor flux, characteristic porous arrays of columnar structures can be produced from a range of organic, semiconductor, and dielectric materials. Devices such as optical filters, chromatographic plates, liquid crystal scaffolding, and solar cells have been created using the GLAD technique [16-19]. Using materials such as titania (TiO_2), a wide band gap and transparent semiconductor with a high refractive index ($n = 2.4$), the GLAD technique can be used to fabricate samples with tailored refractive index periodicities with a high level of control and hence provide high Q-factor reflectance spectra. By periodically altering the deposition angle, and thus the local density and refractive index of deposited columns sub-layers, GLAD photonic crystals (PCs) can be created with periodic wavelength-scale

structure and resonant Bragg reflection [20-22]. Additionally, because the GLAD films are porous with a typical density of 30 to 60% of bulk, the average acoustic impedance of the films (estimated as $Z \sim 20$ MRayl in our case) can be lower than bulk materials (e.g. $Z \sim 38$ MRayl for TiO_2 , $Z \sim 24$ for ZnS) which will improve acoustic coupling to the Parylene C spacing material and to tissue, especially advantageous for high acoustic frequencies (>30 MHz) where GLAD-film thicknesses could be comparable with a significant fraction of a wavelength. Using Eq. (1) of [23] the estimated improvement in intensity transmission efficiency from water into the Paralyne C etalon with a GLAD-film interface layer ($Z \sim 20$ MRayl, thickness of $2.1 \mu\text{m}$, $c(\text{TiO}_2) = 8800 \text{m/s}$) is 12% at 15 MHz compared with bulk TiO_2 . The improvement is calculated to be hundreds of percent for frequencies above 30 MHz in future higher-bandwidth GLAD-FPI designs.

$$T = \frac{4Z_3Z_1}{(Z_1 + Z_3)^2 \cos^2\left(\frac{2\pi l}{\lambda}\right) + (Z_2 + Z_1Z_3 / Z_2)^2 \sin^2\left(\frac{2\pi l}{\lambda}\right)}. \quad (1)$$

where Z_1, Z_2, Z_3 and l corresponds to acoustic impedance of water, GLAD film, Parylene C and thickness of GLAD layer respectively. The sensitivity of the 18 MHz-bandwidth glass-backed GLAD-FPI is measured as $\sim 80 \pm 20$ Pa. Using glass as the backing material makes this sensor a suitable choice for mounting on different optical components including lenses, optical fibers, etc. Previous FPI-sensors were designed for near transparency in the 700-900 nm NIR window with high reflectivity in the C-band for optical interrogation. For many PAM and OR-PAM microvascular imaging applications visible rather than near infrared light is preferred due to the two orders of magnitude higher hemoglobin optical absorption leading to improved signal-to-noise. Non-trivially, the GLAD FPI is the first FPI sensor which is almost transparent at 532 nm, and highly reflective in the C-band. This is important since many laser systems (including frequency doubled Nd:YAG, Nd:YLF, Ytterbium-doped fiber lasers, and microchip lasers) operate in this wavelength region, and since hemoglobin absorption is high in the visible band. The GLAD FPI sensor also has high reflectivity in the C-band where a tunable 1550 nm interrogation beam can probe ultrasound-modulated etalon

reflection dynamics. Availability of low cost lasers at the C-band communication range is another advantage of this sensor.

9.2. Fabry Perot Interferometer fabrication

The first goal of this work was to create a GLAD nanostructured layer with maximum transmission in the visible spectrum near 500 nm and high reflectance in the IR near 1550 nm. For this work we selected TiO₂ as the deposition material and a simple high/low refractive index alternating stack (deposition angles $\alpha = 60^\circ$ and 80° respectively) as the components of the one-dimensional photonic crystal structure. At $\alpha = 80^\circ$ a more porous columnar structure is grown than at $\alpha = 60^\circ$, leading to a lower effective refractive index. To determine the optimal deposition parameters for the GLAD nanostructure we created a model of the optical system and iteratively adjusted the simulated thicknesses of the $\alpha = 60^\circ$ and 80° layers until the required spectrum was found. Effective refractive indices of these layers ($n_{60} = 1.93$ and $n_{80} = 1.42$) were determined from established relationships between oblique deposition angle and effective refractive index for our deposition system and through comparison of simulated (T_s) and actual transmission (T_a) spectra [24]. The expected spectrum for the GLAD thin film was created by modelling the effect of TM (p-polarization) light travelling through the multilayer structure using the characteristic matrix method [25]. The structure has N sub-layers ($j = 1 \dots N$), each described optically by a characteristic matrix (M_j) over a range of wavelengths (λ) as shown in Eq. (2).

$$M_j = \begin{vmatrix} \cos(\beta_j) & -\frac{i}{p_j} \\ -i p_j \sin(\beta_j) & \cos(\beta_j) \end{vmatrix}. \quad (2)$$

where $p_j = n_j \cos(\theta_j)$. and $\beta_j = \frac{2\pi n_j h_j \cos(\theta_j)}{\lambda}$.

h_j and n_j are the height and the refractive index of the current layer, and θ_j is the angle of incident light into the current layer (0° for light passing at normal incidence through the sample)[25, 26]. The characteristic matrix of the complete structure is then given by Eq. (3).

The transmission coefficient (t) of the entire optical system was then calculated using Eq. (4) and the transmittance spectra was found employing by Eq. (5).

$$M = \sum_{j=1}^N M_j. \quad (3)$$

$$t = \frac{2p_1}{(M_{11} + M_{12}p_N)p_1 + (M_{21} + M_{22}p_N)}. \quad (4)$$

$$T_s = \frac{p_N}{p_1} |t|^2. \quad (5)$$

Figure 9.1 shows the configuration of Fabry-Perot interferometers. The first step of the FPI fabrication process involved depositing the GLAD thin film layer which would act as the first mirror. The details of the GLAD thin film depositions carried out for the present work have been described in other work [21]. A summary of the sample preparation steps is provided here. An amorphous TiO_2 (Cerac, Inc., rutile phase 99.9% pure) structured thin film was deposited by electron-beam physical vapor evaporation (Axxis, Kurt J. Lesker Inc.) onto glass substrates (Schott B270, 1 inch² x 0.04 inch thickness, S.I. Howard Glass Co. Inc.). The GLAD films were also concurrently deposited onto cleaved p-doped (100) silicon wafer pieces (University Wafer Inc.) for scanning electron microscope (SEM) characterization. The substrates were affixed to a metal chuck which was in turn connected to two rotation motors. The deposition angle was controlled by the alpha motor, while the rotation was controlled by the phi motor. The substrates were first maintained at the oblique angle of $\alpha = 60^\circ$, while a computer-controlled motor rotated the substrates by 10 complete rotations in order to create a vertical columnar microstructure of 270 nm thickness. A flux deposition rate of 1 nm s^{-1} was maintained by manually monitoring the calibrated deposition rate returned by a quartz crystal microbalance oscillator (Maxtex, SC-105 Aluminum at 6 MHz) and adjusting the electron-beam current used to heat and evaporate the TiO_2 melt. The deposition angle was then changed to $\alpha = 80^\circ$ and another 10 rotation nanostructured layer of 170 nm were

deposited. This computer-controlled deposition process was repeated until a total four layers of dense ($t_{\alpha = 60^\circ} = 270$ nm) and porous ($t_{\alpha = 80^\circ} = 170$ nm) sub-layers, with a final dense capping layer ($t_{\alpha = 60^\circ} = 270$ nm), were fabricated. This number of layers provided a film with high transmission in the visible (95%) and good reflection (80%) in the IR. To promote TiO₂ stoichiometry, O₂ gas was introduced during deposition (pressure maintained at 3×10^{-5} Torr); after the deposition the glass samples were also annealed at 150 °C for 24 h [27, 28]. In all cases, the system base pressure was below 1×10^{-6} Torr. A 23 μ m thick Parylene-C polymer was deposited at the top of the first GLAD film by vapor deposition of the Parylene polymer Parylene-C (PDS 2010, Lab Coater 2, University of Alberta Nanofabrication Facility). Following deposition of the Parylene-C layer, samples were placed back into the Axxis vacuum system for the second GLAD deposition. Again alternating layers of $\alpha = 60^\circ$ and 80° columnar films with respective layer thicknesses of 270 nm and 170 nm were deposited. As with the first GLAD film, four sets of alternating dense and porous sub-layers, with a dense capping layer, were produced. During deposition O₂ gas was introduced (pressure maintained at 3×10^{-5} Torr). Following deposition, annealing was carried out at a lower temperature of 80°C for 24 h to promote stoichiometry while not affecting the Parylene-C layer. Figure 9.2 shows an SEM image of a GLAD film sample, with four sets of alternating dense and porous layers, and the final capping layer, visible. Top-down and side-view SEMs of the silicon witness samples were taken on a Hitachi field emission S-4800 SEM. Optical characterization was carried out on a Perkin Elmer 900 UV-VIS-NIR spectrophotometer. Transmittance was measured for normally-incident light at wavelengths from 490 to 1700 nm, in 1 nm increments.

A thin layer (4 μ m) of Parylene-C was used to encapsulate the entire sample to protect it from humidity and environmental effects known to shift resonant peaks [4, 22]. Film stress could be a major concern and a source of etalon non-uniformity should the reflective layers buckle. Etalon non-uniformity in turn will mean that each location on the etalon may have a slightly different resonant peak, resulting in the need for laser tuning at each interrogation location. Top-down SEMs were used to verify that the deposition of Parylene-C on top of a GLAD thin film or the deposition of a GLAD layer on top of Parylene-C did not result in film cracking suggesting low stress. The porous nature of the GLAD films prove

advantageous compared to bulk-materials for reducing film stress, which may in turn improve etalon uniformity but could result in unwanted optical scattering. However, the columnar features in each layer as seen in figure 9.2 are sub-wavelength, so scattering should be minimal. The structure of the GLAD films deposited on Parylene-C was as similar to the GLAD films deposited on glass as validated by SEM and optical transmission spectra

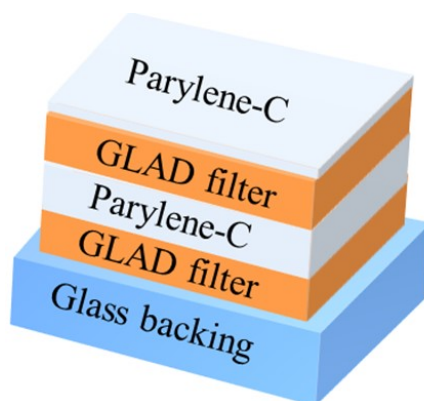


Figure 9.1: The configuration of Fabry Perot interferometers (FPI). The thickness of each GLAD filter was $2.1 \mu\text{m}$. The Parylene C thickness at the middle and the top layers were $23 \mu\text{m}$ and $4 \mu\text{m}$, respectively.

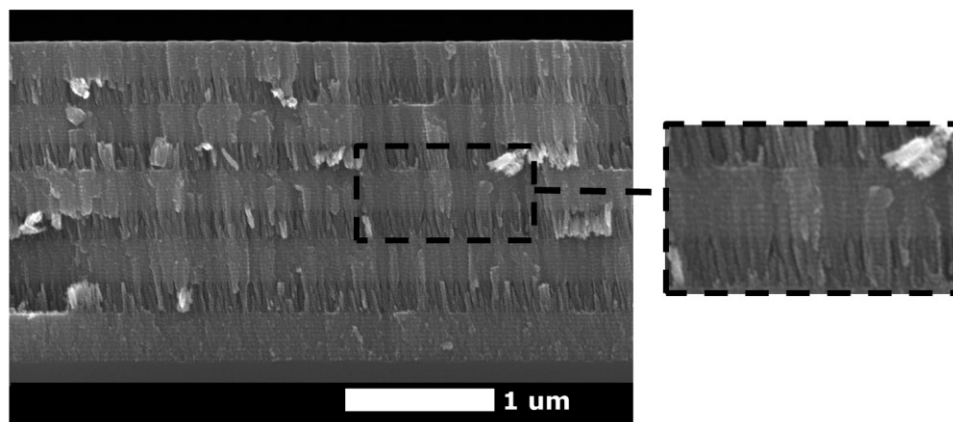


Figure 9.2: SEM image of first GLAD layer. Dense layers were deposited at an angle of $\alpha=60^\circ$. Sparse, columnar, layers were deposited at an angle of $\alpha=80^\circ$.

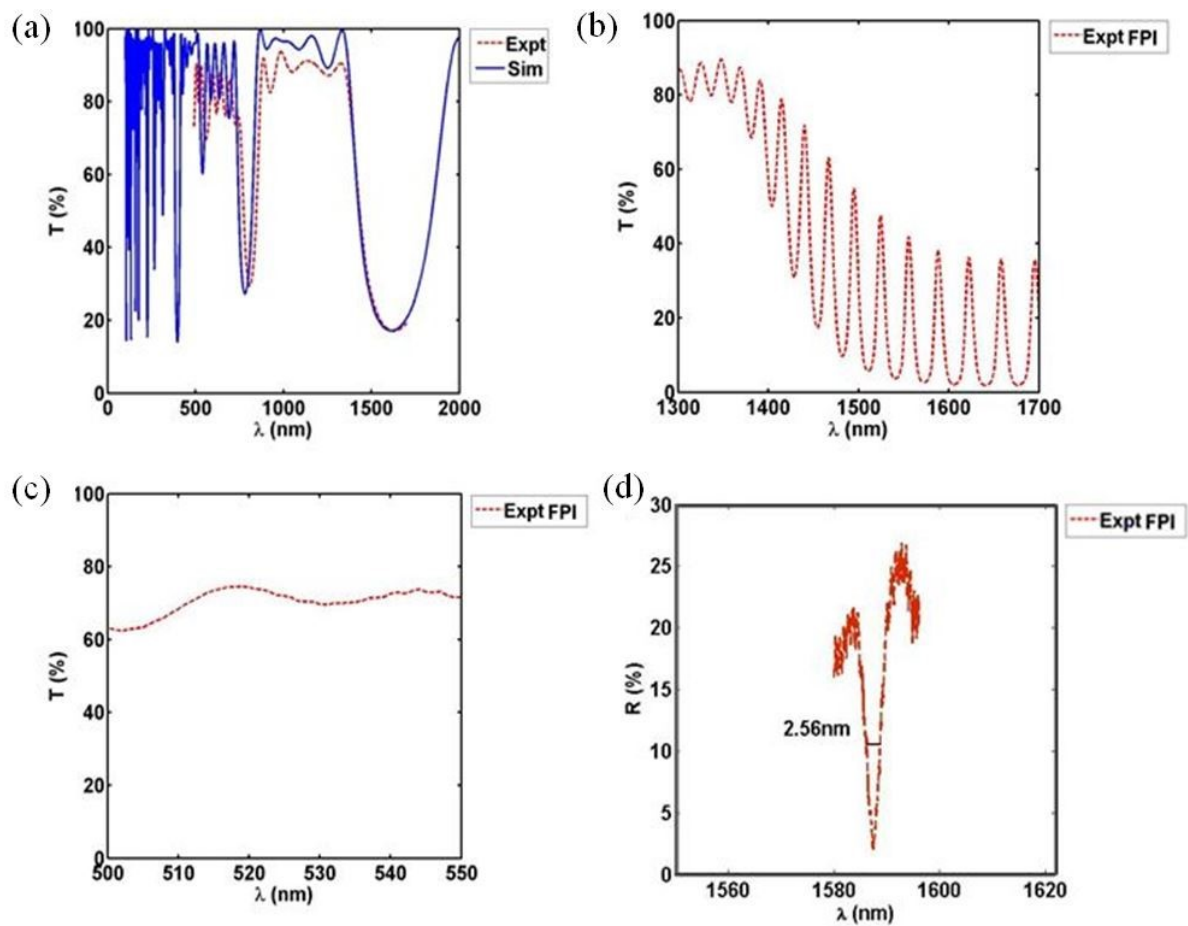


Figure 9.3: (a) Transmission spectrum of a single GLAD film deposited on glass both simulation and experimental work. (b) Transmission spectrum of the four layer GLAD, Paralyne-C, four layer GLAD FPI showing sharp resonant peaks near the C-band (experimental). (c) Transmission spectrum of the GLAD-FPI near the excitation wavelength range (experimental). (d) Measured reflectance spectra for 1 peak (experimental).

Figure 9.3(a) shows the transmission profile of a single GLAD layer filter with high transmission at 532 nm and high reflection around 1550 nm. It's shown that both simulation and experimental work are in a good agreement. Figure 9.3(b) shows experimental results of the FPI peaks formed when the Parylene-C layer is sandwiched between the two GLAD layers. The experimental result of transmission spectrum of the GLAD-FPI indicates about 70% transparency near the excitation wavelength (Figure 9.3(c)). Figure 9.3(d) shows the measured reflectance spectra for 1 peak using the optical setup (Figure 9.4). The interrogation

beam was focused tight at the surface of the FPI and the wavelengths were scanned while the reflected light was measured. The Q factor of this peak was measured as 620 considering the full width half maximum was measured ~ 2.56 nm at 1585 nm wavelength as shown in the 9.3(d).

9.3. Result and discussion

Figure 9.4(a) (setup 1) shows the experimental setup used to test the GLAD-FPI. We employed a 10 MHz unfocused transducer as a transmitter to test the receiver sensitivity. A customized holder for the transducer was engineered in order to keep the water between GLAD- FPI and the transducer. Water was used for ultrasound coupling. A tunable continuous wavelength (CW) C-band laser (TLK-L1550R, Thorlabs Inc., New Jersey) was used in order to tune the interrogation laser wavelength to the point of maximum slope on the FPI peaks. The light at the laser aperture was coupled to a single mode fiber and collimated. This collimated interrogation beam was passed through a polarized beam splitter (VBA05-1550, Thorlabs Inc., New Jersey) and $\lambda/4$ zero order wave plate (Thorlabs Inc., New Jersey), onto the sample via an focusing objective lens, and back through the wave-plate creating 90° polarization which then reflects at the polarizing beam-splitter in order to guide the maximum possible intensity of reflected light to a 150 MHz-bandwidth InGaAs photodiode (PDA10CF, Thorlabs Inc., New Jersey). An objective lens (518125, LEICA, Germany) was used in front of the photodiode in order to refocus all possible reflected interrogation light to the small photodiode element. The 30 mW interrogation beam was focused on the GLAD-FPI. The output of the photodiode was amplified (Olympus 5900PR) and digitized using an 8-channel PCI digitizer (Gage card CS8289) at a sampling rate of 125 MSamples/s. The ultrasound transducer output was calibrated using a needle hydrophone (HNP-0400, ONDA, Sunnyvale). Figure 9.4(b) shows the fabricated FPI. The minimum detectable acoustic pressure was measured as $\sim 80 \pm 20$ Pa and represents the pressure detected with a signal-to-noise ratio of 1. In order to demonstrate the capability of the sensor for 532 nm excitation optical-resolution photoacoustic microscopy (OR-PAM), we performed photoacoustic imaging on a network of 7 μm diameter carbon fibres, shown in figure 9.5 (using setup 2 of figure 9.4). Nanosecond-pulses from a Ytterbium-doped fiber laser with

repetition rates of up to 600 kHz (YLP-G, IPG Photonics Corporation) were used as the source. A beam splitter was used to deflect a small amount of light into a high speed photodiode to detect laser pulses and trigger the high speed data acquisition card. The excitation laser beam passes through a 2D galvanometer scanning mirror system (Thorlabs). The mirrors are controlled by a two channel function generator (Tektronix AFG3022B). An objective lens with 4 mm focal length was used to focus the excitation light into the target. The carbon fiber networks are located ~ 2 mm away from FPI. The optical lateral resolution was estimated ~ 7 μm as shown previously [3]. The -3 dB bandwidth was measured as 18 MHz by imaging carbon fiber network with ~ 7 μm diameter as shown in figure 9.6.

As expected, since glass (with a high acoustic impedance compared to Parylene) is the backing material, our bandwidth is about half of similar FPI sensors with a polymer (low acoustic impedance) backing and sensitivity is roughly double [29]. Polymer-backed sensors could be investigated by others, however in future work we aim to coat different glass-based optical components such as fiber optics, lenses, and prisms. To the best of our knowledge, this is the first time that a FPI fabricated using the GLAD method has been used for ultra-sensitive ultrasound detection. Other work using GLAD films predicts that ultra-high reflectivity is possible [24], which should lead to very high quality factors (Q-factors).

One of the other important factors of our design is that the interrogation wavelength and focused spot on the GLAD-FPI were fixed during the imaging session. However for a larger field of view, it may be more appropriate to scan the interrogation beam along with excitation beam. Etalon uniformity has been problematic for other FPI sensors, meaning that interrogation wavelengths must be tuned at each spatial location on the etalons. Etalon uniformity was studied by quantifying the changes in reflectivity over different spatial interrogation locations. The optimum interrogation wavelength (corresponded to the steepest slope on the reflectivity spectra) varies by only less than 1nm over a 1 mm \times 1 mm area, suggesting locally high uniformity. Over distance scales of more than 2 cm, resonant peaks were shifted several nm. We attribute the locally high etalon uniformity to the Parylene C deposition uniformity (~ 5 nm over an area of 1 cm², similar to previous work [4]) and the low-stress nature of the GLAD films. The locally high etalon uniformity means interrogation beams need not be tuned at each interrogation spot, and could eventually pave the way for

less expensive interrogation lasers with less stringent tuning requirements and for simultaneous recording of pressure signals at multiple different spatial locations with a single laser. Present work involving OR-PAM does not involve scanning the interrogation spot at all, so non-ideal etalon uniformity is well-tolerated.

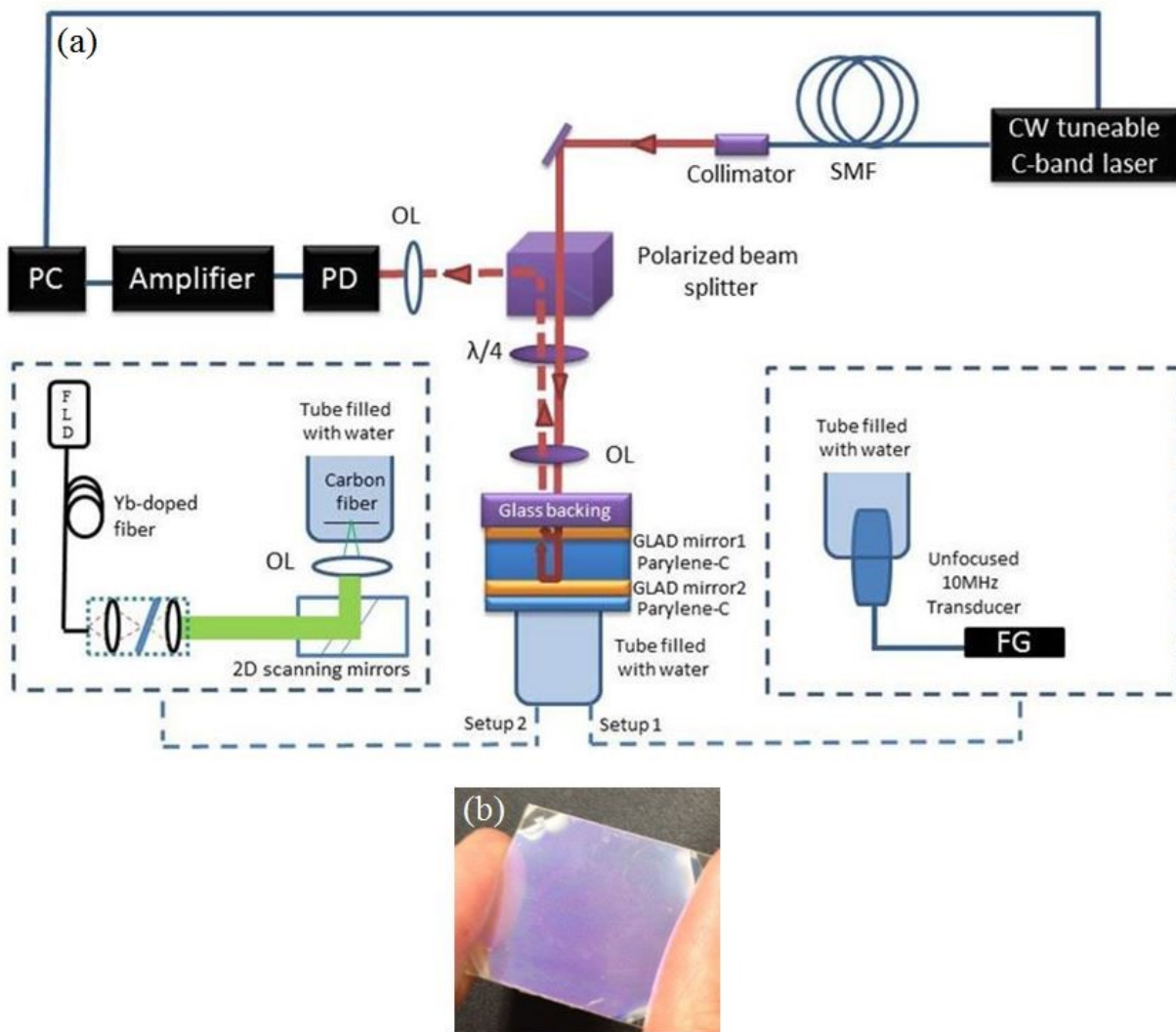


Figure 9.4: (a) The experimental setup used for testing our GLAD-FPI sensor. Two separate setups are shown. Setup 1 is used for photoacoustic imaging. Setup 2 is used to test the receive sensitivity using an external ultrasound transducer. PD: photodiode, OL: objective lens, SMF: single mode fiber, FG: function generator, FLD: Fiber Laser Driver (b) The GLAD FPI.

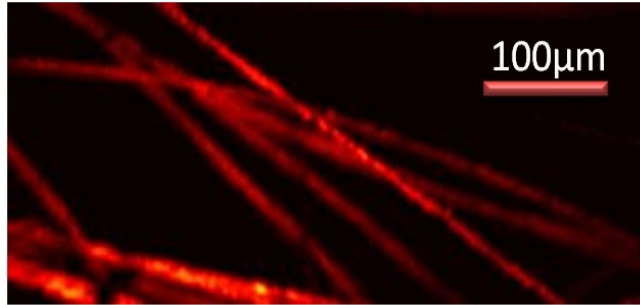


Figure 9.5: Optical-Resolution Photoacoustic Microscopy images of carbon fiber networks with 7 μm diameter of each fiber.

For future work reflection mode OR-PAM can be implemented to take advantage of high transmission GLAD filters at 532 nm wavelengths. The setup can be utilized using a beam combiner and different optical setup [11] to perform *in vivo* imaging. This ultra-sensitive sensor can be a viable alternative for piezoelectric ultrasound transducers for any techniques in which ultrasound waves need to be detected. The GLAD-FPI with high transmission at 532 nm will be a powerful and flexible technology for next-generation all-optical OR-PAM and photoacoustic micro-endoscopy systems [8,9].

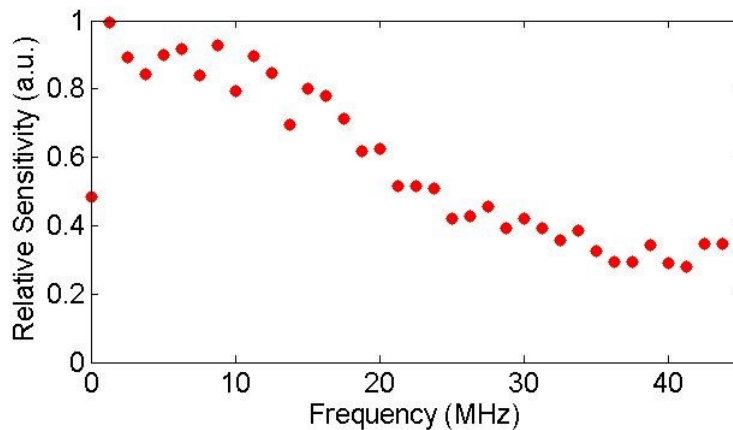


Figure 9.6: GLAD-FPI frequency response.

In the next chapter a reflection mode optical resolution photoacoustic microscopy using glancing angle deposited nanostructured Fabry-Perot interferometers for in vivo applications is reported. The sensitive GLAD FPI allows photoacoustic imaging down to a few nJ pulse energy. To the best of our knowledge, this is the first time that a FPI-based reflection mode optical resolution photoacoustic imaging technique is demonstrated for in vivo applications

Bibliography

1. Hsieh, B.-Y., et al., *All-optical scanhead for ultrasound and photoacoustic dual-modality imaging*. Opt. Express, 2012. **20**(2): p. 1588.
2. Hajireza, P., et al., *Optical-resolution photoacoustic micro-endoscopy using image-guide fibers and fiber laser technology*, in *Photons Plus Ultrasound: Imaging and Sensing 2011*. 2011, SPIE-Intl Soc Optical Eng.
3. Hajireza, P., W. Shi, and R.J. Zemp, *Real-time handheld optical-resolution photoacoustic microscopy*. Opt Express, 2011. **19**(21): p. 20097-102.
4. Zhang, E., J. Laufer, and P. Beard, *Backward-mode multiwavelength photoacoustic scanner using a planar Fabry-Perot polymer film ultrasound sensor for high-resolution three-dimensional imaging of biological tissues*. Applied Optics, 2008. **47**(4): p. 561.
5. Xie, Z., et al., *Pure optical photoacoustic microscopy*. Opt. Express, 2011. **19**(10): p. 9027.
6. Ashkenazi, S., et al., *Optoacoustic imaging using thin polymer étalon*. Applied Physics Letters, 2005. **86**(13): p. 134102.
7. Huang, S.-W., et al., *Toward fiber-based high-frequency 3D ultrasound imaging*, in *Photons Plus Ultrasound: Imaging and Sensing 2007: The Eighth Conference on Biomedical Thermoacoustics, Optoacoustics, and Acousto-optics*. 2007, SPIE-Intl Soc Optical Eng.
8. Hajireza, P., W. Shi, and R.J. Zemp, *Label-free in vivo fiber-based optical-resolution photoacoustic microscopy*. Opt Lett, 2011. **36**(20): p. 4107-9.
9. Zhang, E.Z. and P.C. Beard, *A miniature all-optical photoacoustic imaging probe*, in *Photons Plus Ultrasound: Imaging and Sensing 2011*. 2011, SPIE-Intl Soc Optical Eng.
10. Zhang, E.Z., et al., *3D photoacoustic imaging system for in vivo studies of small animal models*, in *Photons Plus Ultrasound: Imaging and Sensing 2008: The Ninth Conference on Biomedical Thermoacoustics, Optoacoustics, and Acousto-optics*. 2008, SPIE-Intl Soc Optical Eng.
11. Zhang, E.Z., et al., *Multimodal simultaneous photoacoustic tomography, optical resolution microscopy, and OCT system*, in *Photons Plus Ultrasound: Imaging and Sensing 2010*. 2010, SPIE-Intl Soc Optical Eng.
12. Robbie, K., *Sculptured thin films and glancing angle deposition: Growth mechanics and applications*. Journal of Vacuum Science & Technology A: Vacuum, Surfaces, and Films, 1997. **15**(3): p. 1460.
13. Lakhtakia, A. and R. Messier, *Sculptured Thin Films: Nanoengineered Morphology and Optics*. 2005: SPIE-Intl Soc Optical Eng.
14. Messier, R., V.C. Venugopal, and P.D. Sunal, *Origin and evolution of sculptured thin films*. Journal of Vacuum Science & Technology A: Vacuum, Surfaces, and Films, 2000. **18**(4): p. 1538.
15. Hawkeye, M.M. and M.J. Brett, *Glancing angle deposition: Fabrication, properties, and applications of micro- and nanostructured thin films*. Journal of Vacuum Science & Technology A: Vacuum, Surfaces, and Films, 2007. **25**(5): p. 1317.

16. Xi, J.Q., et al., *Optical thin-film materials with low refractive index for broadband elimination of Fresnel reflection*. Nat Photon, 2007. **1**(3): p. 176-179.
17. Jim, S.R., et al., *Engineered Anisotropic Microstructures for Ultrathin-Layer Chromatography*. Anal. Chem., 2010. **82**(12): p. 5349-5356.
18. Sit, J.C., D.J. Broer, and M.J. Brett, *Liquid Crystal Alignment and Switching in Porous Chiral Thin Films*. Adv. Mater., 2000. **12**(5): p. 371-373.
19. Yang, H.-Y., et al., *Glancing angle deposited titania films for dye-sensitized solar cells*. Thin Solid Films, 2009. **518**(5): p. 1590-1594.
20. John, S., *Strong localization of photons in certain disordered dielectric superlattices*. Phys. Rev. Lett., 1987. **58**(23): p. 2486-2489.
21. Hawkeye, M.M. and M.J. Brett, *Narrow bandpass optical filters fabricated with one-dimensionally periodic inhomogeneous thin films*. J. Appl. Phys., 2006. **100**(4): p. 044322.
22. Hawkeye, M.M., K.M. Krause, and M.J. Brett, *Ambient humidity monitoring using a 1D photonic crystal sensor fabricated with glancing angle deposition*, in *Optical Sensors 2009*. 2009, SPIE-Intl Soc Optical Eng.
23. Cobbold, R.S.C., *Foundations of Biomedical Ultrasound*. 2006.
24. Hawkeye, M.M., M.T. Taschuk, and M.J. Brett, *Glancing Angle Deposition of Thin Films*. 2014, Wiley-Blackwell.
25. Macleod, H.A., *Thin-Film Optical Filters*. 1986: Informa UK Limited.
26. Kennedy, S.R. and M.J. Brett, *Porous Broadband Antireflection Coating by Glancing Angle Deposition*. Applied Optics, 2003. **42**(22): p. 4573.
27. van Popta, A.C., J.C. Sit, and M.J. Brett, *Optical properties of porous helical thin films and the effects of post-deposition annealing*, in *Organic Optoelectronics and Photonics*. 2004, SPIE-Intl Soc Optical Eng.
28. Rao, K.N., *Influence of deposition parameters on optical properties of TiO₂ films*. Optical Engineering, 2002. **41**(9): p. 2357.
29. Cox, B.T., et al., *Fabry Perot polymer film fibre-optic hydrophones and arrays for ultrasound field characterisation*. J. Phys.: Conf. Ser., 2004. **1**: p. 32-37.

10. *In vivo* optical resolution photoacoustic microscopy using glancing angle deposited nanostructured Fabry-Perot etalons

In photoacoustic imaging (PA) systems, absorbed optical energy is converted into acoustic signals by thermo-elastic expansion and then received by ultrasound detectors to be processed into final images. PA imaging is capable of providing absorption contrast, enabling estimation of blood oxygen saturation, imaging of optical contrast agents, and imaging of gene expression, among other applications [1, 2]. Most ultrasound and PA techniques employ piezoelectric receivers to detect the ultrasonic signals. However, all-optical ultrasound detection is desirable in applications such as intraoperative, laparoscopic, and endoscopic ultrasound image guidance systems. In these applications electrical interconnects must be minimized and integration of photoacoustic imaging with existing optical methods will be facilitated. Recently optical detectors have been under intense investigation for use in PA imaging [3-10]. Previous work on optical-based ultrasound detection includes Fabry-Perot interferometer (FPI), micro-ring resonators (MRRs), and other types of interferometric sensing. Adapting these methods for reflection-mode optical-resolution photoacoustic microscopy has been challenging. Most MRRs fabricated on silicon substrates are optically opaque [4] therefore, to image in reflection mode, the MRR and the optical scanning area need to be physically far from each other, or the resulting PAM system could be implemented in transmission configuration, which is not practical for imaging thick biological samples. Recently a miniaturized, optically-transparent ultrasonic detector was developed[8]. However, only phantom imaging was demonstrated. Even with such a transparent substrate, the micro-ring resonator was in a different lateral location than the optical scanning. Other interferometric sensing approaches including Fabry-Perot-based methods have yet to achieve *in vivo* reflection-mode optical-resolution imaging. In our approach the effective optical sensing area on the FPI is scanned with the excitation spot as close to the source as possible. This co-scanning of excitation and probe beams can be critical for high-signal-to-noise ratio *in vivo* imaging. Challenges of all-optical PA imaging with optical resolution

include damage thresholds, co-alignment of excitation and interrogation beams, and ensuring adequate *in vivo* sensitivity for low pulse energies. In this chapter we demonstrate a FPI-based ultrasound detector fabricated using glancing angle deposited (GLAD) nanostructured thin films for *in vivo* optical resolution PA imaging. The nanostructured GLAD is a single-step physical vapor-deposition (PVD) technique used to fabricate nanostructured thin films [11]. By employing substrate motion and obliquely incident vapor flux, characteristic porous arrays of columnar structures can be produced from a range of organic, semiconductor, and dielectric materials.

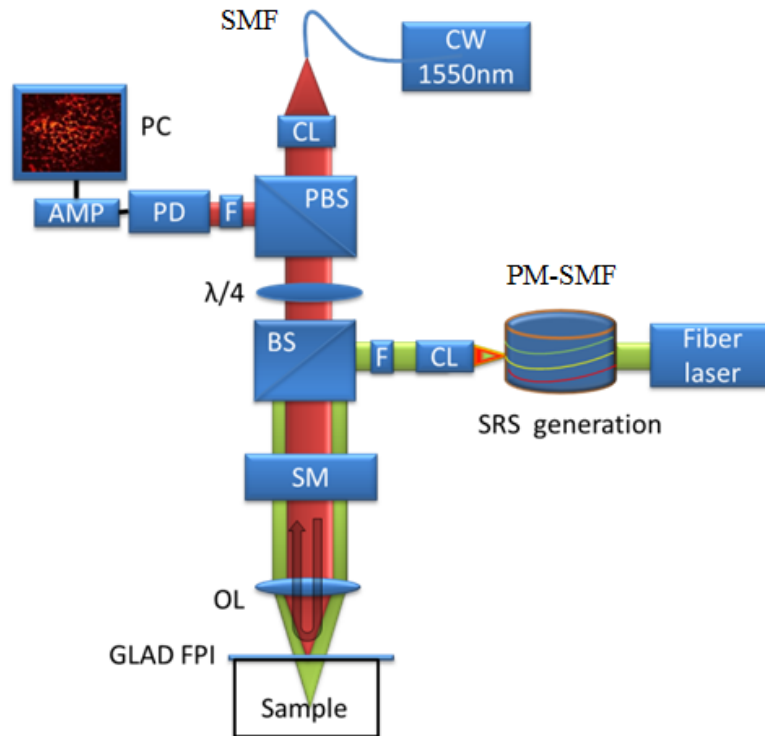


Figure 10.1: Experimental setup of GLAD OR-PAM. F: Filter, OL: Objective lens, PMf-SMF: Polarization maintaining single mode fiber, CL: Collimator lens, PBS: polarized beam splitter, BS: beam splitter, SM: 2D scanning mirrors, PD: Photodiode, AMP: Amplifier.

Using materials such as titania (TiO₂), a wide band gap and transparent semiconductor with a high refractive index ($n = 2.4$), the GLAD technique can be used to fabricate samples with tailored refractive index periodicities with a high level of control and hence provide high Q-factor reflectance spectra. Other transparent materials such as silicon dioxide and magnesium

fluoride could also be used, but FPIs fabricated with these materials would have a lower refractive index contrast due to lower bulk indexes than TiO₂. By periodically altering the deposition angle, and thus the local density and refractive index of deposited columns sublayers, GLAD photonic crystals (PCs) can be created with periodic wavelength-scale structure and resonant Bragg reflection [11] We have previously showed the first GLAD FPI for ultrasound detection for phantom imaging in transmission mode[7]. The minimum detectable acoustic pressure of this glass backing sensor was measured as 80 ± 20 Pa and the -3 dB bandwidth was measured to be 18 MHz. GLAD films offer some practical and performance advantages over previous methods for ultrasound detection as it allows low acoustic impedance FPI device fabrication for highly sensitive ultrasound detection [7]. In this chapter we report *in vivo* reflection-mode optical resolution photoacoustic microscopy (OR-PAM) with FP etalons. Reflection-mode imaging presents new challenges because (1) excitation light is optically focused through the etalon and high focal intensities can damage the etalon. (2) Ideally the excitation beam should be focused into the tissue while the probe beam should be focused into the etalon and this is not straightforward with a single objective lens for both beams. Our approach involves both optimization of the etalon and an optical design which permits scanning of both the excitation beam and interrogation beam together. This not only provides optimal sensitivity detection but also limits laser-dwell-time on any one spot to prevent etalon damage.

Figure 10.1 systematically depicts the experimental setup of GLAD OR-PAM. This system consists of two main arms, receiver and excitation arms. Both beams are co-scanned and co-focused on the sample. In the receiver arm a tunable continuous wavelength (CW) C-band laser (TLK-L1550R, Thorlabs Inc., New Jersey) was used in order to tune the interrogation laser wavelength to the point of maximum slope on the FPI peaks. The light at the laser aperture was coupled to a single mode fiber and collimated. This collimated interrogation beam was passed through a polarized beam splitter (VBA05-1550, Thorlabs Inc., New Jersey) and $\lambda/4$ zero order wave plate (Thorlabs Inc., New Jersey), onto the sample via an focusing objective lens, and back through the wave-plate creating 90° polarization which then reflects at the polarizing beam-splitter in order to guide the maximum possible intensity of reflected light to a 150 MHz-bandwidth InGaAs photodiode (PDA10CF, Thorlabs Inc.,

New Jersey). An objective lens (518125, LEICA, Germany) was used in front of the photodiode in order to refocus all possible reflected interrogation light to the small photodiode element. The 30 mW interrogation beam was focused on the GLAD-FPI. The output of the photodiode was amplified (Olympus 5900PR) and digitized using a 4-channel PCI digitizer (Gage card) at a sampling rate of 200 MSamples/s.

In the excitation arm the output of a 1ns pulse width, ytterbium-doped fiber laser (IPG Photonics) with a pulse repetition rate (PRR) of 40 kHz was initially coupled into a 6m PM-SMF to generate stimulated Raman scattering (SRS) peaks [12]. A band pass filter can be used in order to select the desired wavelength. The output of the PM-SMF was collimated using an adjustable collimator and combined by the receiver arm of the system. A 532 nm wavelength was selected for all the images shown in this manuscript. Unlike the previous design both beams are scanned across the samples using a 2D galvanometer scanning mirror system and focused tightly using an objective lens (Leitz Wetzlar 10X/0.25 160/- EF microscope objective, Germany). Also a band pass filter was used in front of the photodiode in order to reject the reflected 532 nm light.

Figure 10.2(a) shows the configuration of Fabry-Perot interferometers (FPI). The FPI was fabricated by growing multilayer optical filters using GLAD process. Figure 10.2(b) shows transmission spectrum of the GLAD FPI showing sharp resonant peaks near the C-band. Multilayer films were designed to have high transmittance at 532 nm and high reflectance at about 1550 nm. Figure 10.2(c) shows scanning electron microscope (SEM) image of the first GLAD layer. For this work, TiO₂ was used as the deposition material, due to its high refractive index and transparency at the wavelengths of interest. High reflectance was achieved through the use of high/low index stacks at deposition angles of $\alpha = 60^\circ$ and $\alpha = 80^\circ$ respectively.

At higher deposition angles, a more porous structure is grown, with a lower refractive index. When designing a reflecting medium at C-band consisting solely of quarter-wave layers, a higher order reflectance band was found to occur at 532 nm, which is undesirable. To correct this, the thicknesses of the high and low index layers were adjusted to shift the higher order reflectance band off of 532 nm, while keeping the initial reflectance band at 1550 nm intact. The effective indices of the high and low index layers were found to be $n_{60} = 1.93$ and $n_{80} =$

1.42, respectively. Half-wave plate antireflection coatings at 1550 nm were grown to increase the optical power coupled through the substrate and into the FPI.

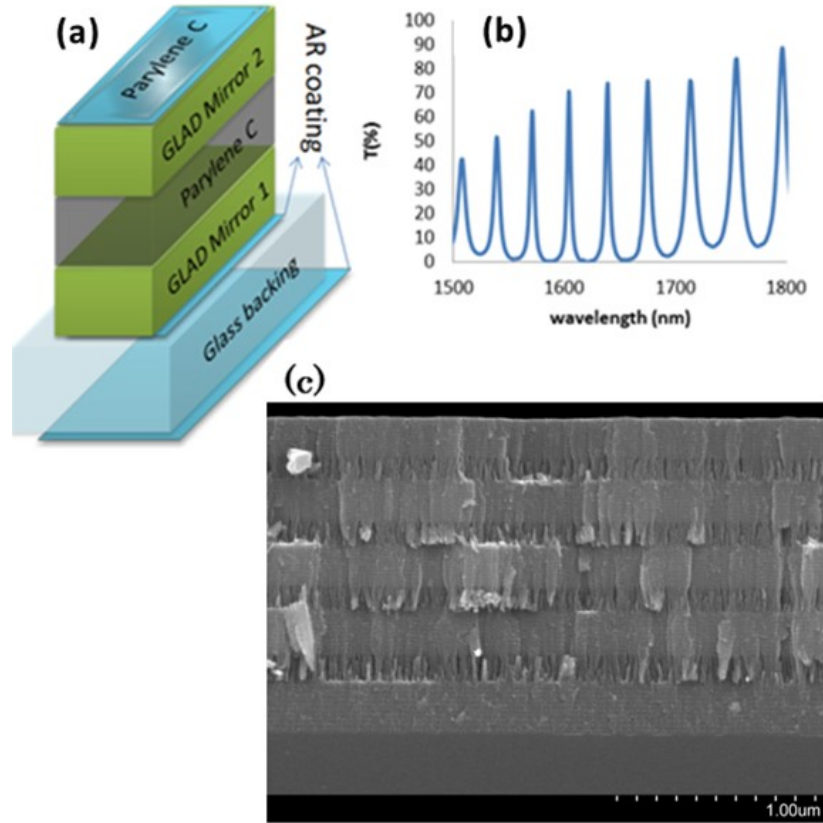


Figure 10.2: (a) The configuration of FPI. AR (anti reflection). (b) Transmission spectrum of the GLAD FPI showing sharp resonant peaks near the C-band. (c) SEM image of first GLAD layer. Dense layers were deposited at an angle of $\alpha = 60^\circ$. Sparse, columnar, layers were deposited at an angle of $\alpha = 80^\circ$.

The first step in the FPI fabrication process involved depositing a multilayer GLAD film to act as the first mirror. Electron beam evaporation (Axxis, Kurt J. Lesker Inc.) was used to deposit amorphous TiO₂ (Cerac Inc., rutile phase, 99.9% pure) onto microscope cover slips (Fisherbrand Microscope Cover Glass #1) with $\sim 250 \mu\text{m}$ thickness. The substrates were adhered to a metal substrate holder which was connected to two rotation motors. The deposition angle was controlled by one motor, while the substrate rotation was controlled by a second motor. Each high refractive index layer consisted of 10 complete substrate rotations

at a constant deposition angle of $\alpha = 60^\circ$ over a 270 nm thickness. Low index layers consisted of 10 substrate rotations at a constant deposition angle of $\alpha = 80^\circ$ over a 170 nm thickness. Each FPI mirror consisted of alternating four high and low index layers and ending with a dense layer. An extra dense layer was used to provide the best interfaces with the substrate and subsequent deposition layers. After the first multilayer film was fabricated, it was oxidized in an oven at 200 °C for 24 hours to achieve best transparency.

A 23 μm thick Parylene-C layer was deposited by vapor deposition (PDS 2010, Lab Coater 2, University of Alberta Nanofabrication Facility) on top of the first multilayer GLAD film. Following the deposition of Parylene-C, a second multilayer GLAD film was deposited in the same manner as the first. Following this deposition, the samples were oxidized in an oven at 80 °C for 120 hours, to preserve the Parylene-C layer. Afterwards, a 4 μm Parylene-C capping layer was used to encapsulate the entire sample to protect it from humidity and other environmental effects. Finally, unlike our previous approach, a half-wave layer antireflection coating consisting of a 315 nm thick layer of SiO₂ (Materion, 99.99% pure) was deposited on the backside of the substrate to improve the optical coupling to the FPI. The optimized etalon exhibited FP peaks with optical Q-factors of 870, more than 40% higher than our previous work show in chapter 9.

Figure 10.3 shows GLAD OR-PAM images of carbon fiber networks. Each individual carbon fiber has a diameter $\sim 7 \mu\text{m}$. The excitation pulse energy was set to 30 nJ and 1 nJ on figure 10.3(a) and 10.3(b) respectively. The interrogation power on the FPI was measured $\sim 10 \text{ mW}$. Detected signal levels displayed a linear relationship with pulse energy. The optical lateral resolution was estimated $\sim 7 \mu\text{m}$ [13]. Both images are formed using a 3 mm \times 3 mm FPI. The small footprint and high sensitivity of the FPI makes this system a promising method for OR-PAM handheld and endoscopy applications [14, 15]

Presently the FOV is limited to around 2 mm, where spherical aberrations of the objective lens degrade image quality far from the center axis. Also, etalon-uniformity is problematic when scanning over larger areas and would require interrogation beam wavelength-tuning. Etalon uniformity has been problematic for other reported FPI sensors. As shown before in our work [7] the optimum interrogation wavelength (corresponded to the steepest slope on the reflectivity spectra) varies by only less than 1 nm over a 1 mm \times 1 mm area, suggesting

locally high uniformity. For all the reported images in this manuscript the interrogation wavelength was fixed and need not be tuned at each interrogation spot. Larger fields-of-view could be achieved by scanning the sample.

Figure 10.4 shows *in vivo* images of a Chorioallantoic membrane (CAM) of 5-day chicken embryo model are demonstrated. The capillary beds on the surface of the model can be easily imaged. The signal to noise ratio of *in vivo* images were measured ~ 35 dB. To the best of our knowledge, this is the first time that a FPI-based reflection mode optical resolution photoacoustic imaging technique is demonstrated for *in vivo* applications.

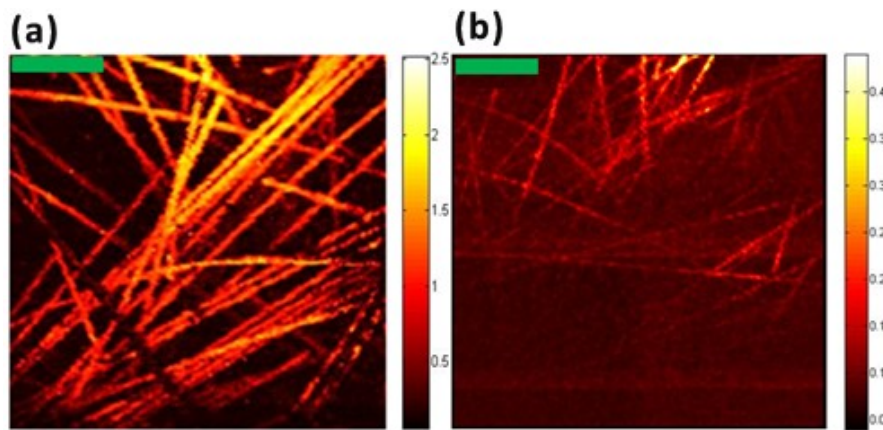


Figure 10.3: GLAD OR-PAM images of carbon fiber network. Images are formed using a pulse energy of a) 30 nJ b) 1 nJ (Scale bar: 100 μm)

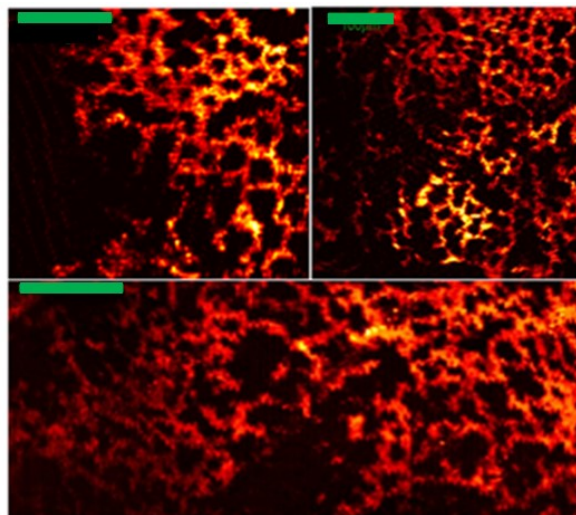


Figure 10.4: *in vivo* images of capillary beds in the CAM-membrane of 5-day chicken embryo model. (Scale bar: 100 μm)

In the next chapter a novel all-optical non-contact photoacoustic microscopy system is introduced. The system uses optically focused pulsed excitation with optical detection of photoacoustic signatures using a long-coherence interrogation beam co-focused and co-scanned with the excitation spot. The proposed system does not require any ultrasound medium or contact with the sample, unlike other all optical photoacoustic system. The proposed system can be very valuable for applications that coupling, or immersion is undesirable or impractical.

Bibliography

1. Wang, L., *Photo acoustic tomography*. Scholarpedia, 2014. **9**(2): p. 10278.
2. Wang, L.V. and S. Hu, *Photoacoustic Tomography: In Vivo Imaging from Organelles to Organs*. Science, 2012. **335**(6075): p. 1458-1462.
3. Zhang, E., J. Laufer, and P. Beard, *Backward-mode multiwavelength photoacoustic scanner using a planar Fabry-Perot polymer film ultrasound sensor for high-resolution three-dimensional imaging of biological tissues*. Applied Optics, 2008. **47**(4): p. 561.
4. Xie, Z., et al., *Pure optical photoacoustic microscopy*. Opt. Express, 2011. **19**(10): p. 9027.
5. Ashkenazi, S., et al., *Optoacoustic imaging using thin polymer étalon*. Applied Physics Letters, 2005. **86**(13): p. 134102.
6. Huang, S.-W., et al., *Toward fiber-based high-frequency 3D ultrasound imaging*, in *Photons Plus Ultrasound: Imaging and Sensing 2007: The Eighth Conference on Biomedical Thermoacoustics, Optoacoustics, and Acousto-optics*. 2007, SPIE-Intl Soc Optical Eng.
7. Hajireza, P., et al., *Glancing angle deposited nanostructured film Fabry-Perot etalons for optical detection of ultrasound*. Opt Express, 2013. **21**(5): p. 6391-400.
8. Li, H., et al., *A transparent broadband ultrasonic detector based on an optical micro-ring resonator for photoacoustic microscopy*. Scientific Reports, 2014. **4**.
9. Chen, S.-L., et al., *Miniaturized all-optical photoacoustic microscopy based on microelectromechanical systems mirror scanning*. Opt. Lett., 2012. **37**(20): p. 4263.
10. Chitnis, P.V., H. Lloyd, and R.H. Silverman, *An adaptive interferometric sensor for all-optical photoacoustic microscopy*, in *2014 IEEE International Ultrasonics Symposium*. 2014, Institute of Electrical & Electronics Engineers (IEEE).
11. Hawkeye, M.M., M.T. Taschuk, and M.J. Brett, *Glancing Angle Deposition of Thin Films*. 2014, Wiley-Blackwell.
12. Hajireza, P., A. Forbrich, and R.J. Zemp, *Multifocus optical-resolution photoacoustic microscopy using stimulated Raman scattering and chromatic aberration*. Opt Lett, 2013. **38**(15): p. 2711-3.
13. Shi, W., et al., *Optical resolution photoacoustic microscopy using novel high-repetition-rate passively Q-switched microchip and fiber lasers*. J. Biomed. Opt., 2010. **15**(5): p. 056017.
14. Hajireza, P., W. Shi, and R.J. Zemp, *Label-free in vivo fiber-based optical-resolution photoacoustic microscopy*. Opt Lett, 2011. **36**(20): p. 4107-9.
15. Hajireza, P., W. Shi, and R.J. Zemp, *Real-time handheld optical-resolution photoacoustic microscopy*. Opt Express, 2011. **19**(21): p. 20097-102.

11. *In vivo* Optical-Resolution Photoacoustic Remote Sensing Microscopy

11.1. Introductions

Optical imaging in biological specimens has provided biologists and clinicians with valuable tools for science and medicine. Many such techniques rely on fluorescence or scattering as contrast mechanisms. Optical absorption is a desirable contrast mechanism because it can potentially provide information about chemical bonds and molecular structure, blood oxygenation, and other biochemical information. While transmission-mode sensing of optical absorption is possible with thin transparent samples using ballistic imaging techniques or photothermal microscopy [1-3], reflection-mode imaging of optical absorption requires other techniques. Diffuse optical tomography is capable of estimating sub-surface absorption and scattering distributions but spatial resolution is poor and the inverse problems are ill-posed and ill-conditioned. Recently developments in optical coherence tomography (OCT) have attempted to sense absorption [4-6], however, scattering, not absorption is sensed thus absorption estimates are indirect and not yet highly quantitative.

Photoacoustic (PA) imaging has seen great success in imaging acoustic pressure distributions due to light absorption-induced thermoelastic expansion. These acoustic signals are detected and reconstructed to form images with optical absorption contrast. PA imaging has been shown to provide exquisite images of microvessels [7-10] and is capable of imaging blood oxygen saturation [11,12], gene expression[13], and contrast agents[14], among other uses. Both acoustic-resolution and optical-resolution embodiments have proved to be of considerable significance [7]. In most PA and ultrasound imaging systems piezoelectric transducers have been employed, in which an ultrasound coupling medium such as water or ultrasound gel is required. However for many clinical applications such as wound healing [15], burn diagnostics [16], surgery [17], and many endoscopic procedures [9,18,19] physical contact, coupling, or immersion is undesirable or impractical. Unlike previous non-contact photoacoustic imaging systems, in this chapter *in vivo* optical-resolution photoacoustic microscopy using non-contact optical interferometric sensing without use of any acoustic

coupling medium is demonstrated.

Optical means of detecting ultrasound and photoacoustic signals have been investigated over a number of years [20,21]; however, to date no technique has demonstrated practical non-contact *in vivo* microscopy in reflection mode with optical absorption as the contrast mechanism. Most previous approaches detected surface oscillations optically [22]. Recently a low-coherence interferometry method for sensing photoacoustic signals was proposed, resulting in 30 μ m lateral resolution [23]. However, only large surface vessels in sacrificed animals were visualized, optical-resolution focusing of the excitation spot was not demonstrated, *in vivo* measurements were lacking, and signal-to-noise ratio (SNR) was sub-optimal compared to contact-based sensing. This approach used detection of surface oscillations from subsurface photoacoustic excitations. Our approach is fundamentally different in that we aim to detect large initial pressures directly at their origin beneath the surface. Hochreiner et al. used a fiber based interferometer with optical amplification to detect photoacoustic surface signals and form images of deeper phantom structures [24], however the system offered poor SNR and designed for acoustic-resolution, not optical-resolution imaging.

Industrial laser ultrasonics has used interferometry to detect acoustic signatures due to optical excitation of inanimate objects for non-destructive testing. This approach has been adapted to detect ultrasound *ex vivo* in chicken breast and calf brain specimens [25,26], however, optical-resolution imaging, confocal scanning of pump and probe beams, and *in vivo* imaging were not examined. These approaches primarily used optical detection of surface oscillations. Present setups required \sim 1m-cavity large etendue FP interferometers to pick off modulated sidebands of optical speckles. These setups were highly sensitive to environmental perturbations and required ultra-quiet settings and vibration, unlike our approach, which additionally detects subsurface initial pressures. Laser Doppler vibrometry has been a powerful non-contact vibration sensing methodology; however, weak SNR and poor image quality have proven to be a limitation when sensing surface oscillations originating from deep tissues from broad-beam photoacoustic excitation [27]. Similarly, Mach Zehnder interferometry [28], two-wave mixing interferometry [29] have been used previously for sensing photoacoustic signals. However many such techniques still require direct contact or

fluid coupling, rely on surface oscillation-based phase-modulation and have not offered *in vivo* studies or optical resolution for phantom studies. Ultrasound-modulated optical tomography (UOT) methods are capable of detecting subsurface ultrasound-modulation of light however, because optical phase is randomized due multiple scattering, subsurface imaging relies on detection methodologies which are highly vibration-sensitive and currently signal-to-noise is poor [30,31]. Any motion including blood flow and breathing will contribute to speckle decorrelation and because of these challenges no *in vivo* imaging has yet to be demonstrated. Additionally little has been done on using UOT-based detection of photoacoustic signals and such approaches are not yet robust enough for *in vivo* imaging[30,31]. They are also not optical-resolution technologies.

We have developed a new non-contact optical bio-microscopy modality that we call Optical-Resolution Photoacoustic Remote Sensing (OR-PARS) microscopy. We optically focus a pulsed excitation laser into superficial tissues to generate very high micro-scale initial pressures. Then we harvest these large optically-focused photoacoustic signals as close to the photoacoustic source as possible. This is done by detecting photoacoustic signals using a confocal interrogation beam co-focused and co-scanned with the excitation spot. This approach offers orders of magnitude signal enhancement compared to non-confocal sister techniques as discussed in the supplementary data. Owing to the very large nature of these signals, we anticipate that PARS microscopy could prove a significant and important new non-contact imaging modality similar to optical-resolution photoacoustic microscopy but without the requirement for ultrasound transducers or acoustic coupling.

11.2. Experimental setup

A modified version of polarization sensitive Michelson interferometry has been employed to remotely record the large local initial pressures from chromophores without appreciable acoustic losses. The experimental setup of the optical-resolution photoacoustic remote sensing (OR-PARS) microscopy system is depicted in figure 11.1. The photodiode detects the interference between the signal backscattered from the sample and reference arm. Briefly, a 532-nm pulsed fiber laser is used to excite targets with a ns-pulsed optically focused spot. A 100-kHz-linewidth 1550-nm tunable laser was used to interrogate the sample with a spot co-

focused with the excitation spot. By co-focusing the excitation and probe beams we generate and detect large acoustic signals in the same micro-volume. Polarizing and non-polarizing beamsplitters are designed to recover maximum possible signal beams while providing a path-length- and intensity-controllable reference beam. Stimulated Raman Scattering in an optical fiber optionally creates other wavelengths of the pulsed excitation light (Raman peaks) for imaging with one wavelength or multiple wavelengths. When multiple wavelengths are used simultaneously chromatic aberration in the collimating and objective lens pair is harnessed to refocus light from a fiber into the object so that each wavelength is focused at a slightly different depth location. Using these wavelengths simultaneously was previously shown to improve the depth of field and SNR for structural imaging of microvasculature with OR-PAM [32]. More details about the experimental setup design and development are provided in the method section and also section 1 of the supplementary information.

Figure 11.2(a) shows OR-PARS imaging of $\sim 7\mu\text{m}$ carbon fiber networks using ~ 1 nJ excitation pulse energy and 6 mW interrogation power on the sample. SNR (defined as average of signal over the standard deviation of the noise) was quantified as 45 ± 3 dB. Figure 11.2(b) shows FWHM due to fitting individual carbon fiber (with $\sim 6\mu\text{m}$ diameter) signal amplitude to a Gaussian function. Figure 11.2(c) shows a line-spread function acquired using a knife edge experiment. The lateral resolution of the system has been measured as $\sim 3\pm 1\mu\text{m}$. Figure 11.2(d) compares the images of reflection mode OR-PARS and a transmission mode OR-PAM using a 10 MHz unfocused transducer (Olympus, V312-SM). The transmission mode OR-PAM setup was not capable of imaging with 1 nJ pulse energy. Therefore, figure 11.2(d) was formed using 50 nJ pulse energy and images were recorded simultaneously.

In all the images reported in this manuscript the X- and Y- mirror scanning rates are set at 60 Hz and 0.25 Hz respectively, with the laser repetition-rate set at 40 kHz. The PARS system is capable of being configured for imaging when both beams are scanning together (figure 11.2a) or when the interrogation beam is fixed and excitation beam is scanning as shown in figure 11.7 and figure 11.8 of supplementary information.

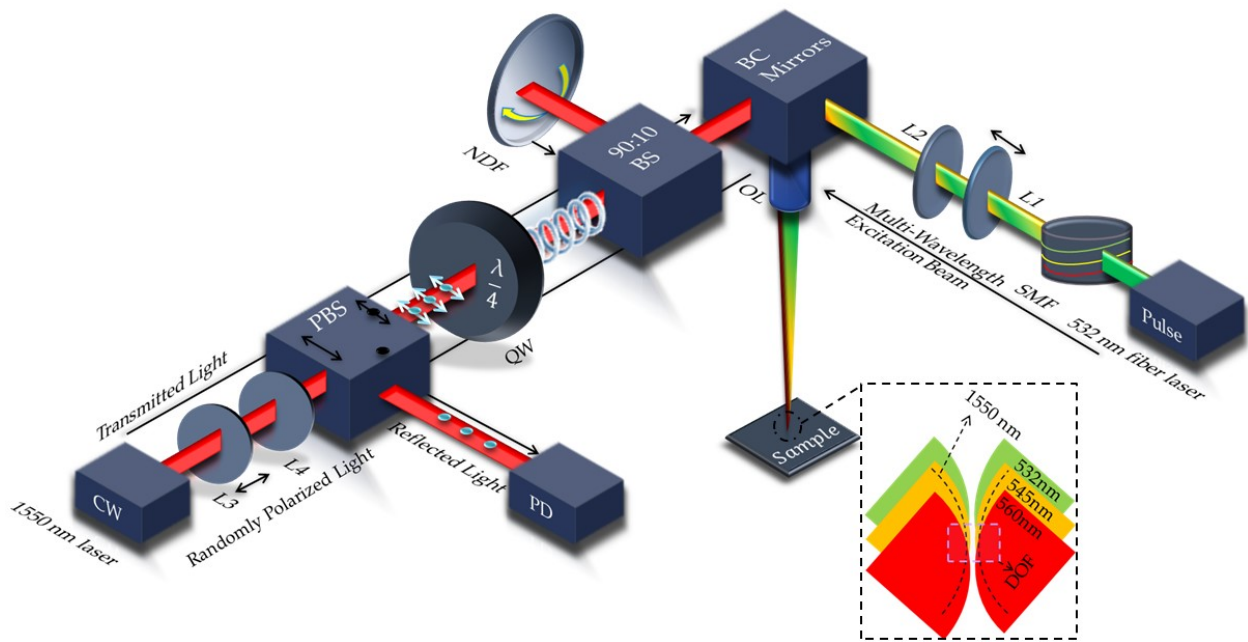


Figure 11.1: Experimental setup of OR-PARS. b) Multi focus excitation and single wavelength interrogation beams. PBS: Polarized beam Splitter, PD: photodiode, BS, Beam splitter, BC: Beam combiner, OL: Objective lens, SMF: Polarization maintaining single mode fiber, L: lens, NDF: natural density filter, CW: continuous wavelength, QW: quarter wave plate, DOF: depth of field.

Figure 11.3 shows *in vivo* images of the Chorioallantoic Membrane (CAM) of 5-day chicken embryos. Figure 11.3(a) shows PARS images revealing both capillary beds and larger blood vessels. In the chicken embryo model, bigger blood vessels usually are located deeper than capillaries. In order to see both deep- and shallow vessels simultaneously the multi-focus design is optimized to extend the depth-of-field [32]. Figure 11.3(b) shows a zoomed-in image of both capillary beds and bigger blood vessels.

11.3. Results and Discussion

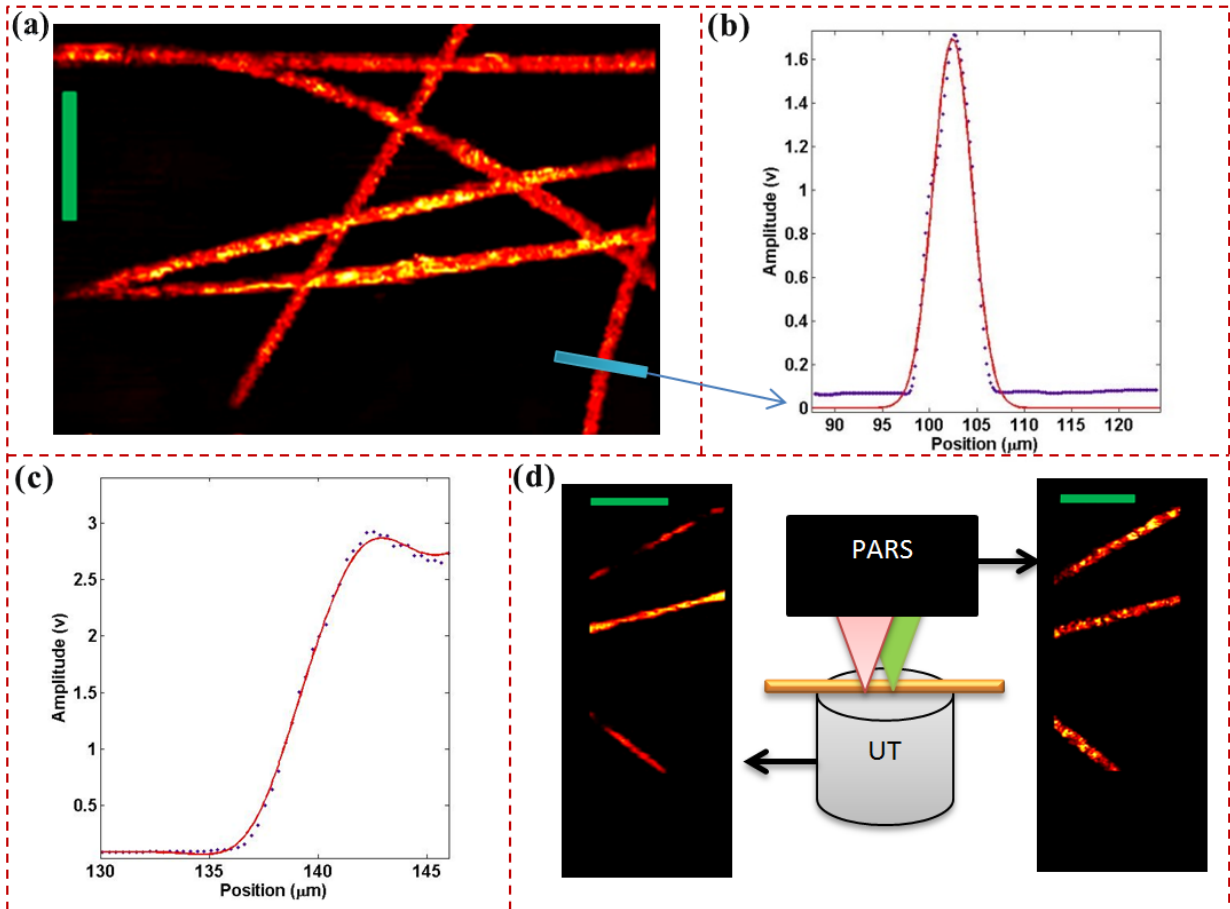


Figure 11.2: a) OR-PARS images of carbon fiber networks b) FWHM due to fitting individual carbon fiber signal amplitude to a Gaussian function. c) Resolution study using knife edge spread function d) Comparison between the reflection mode OR-PARS (with 1nJ pulse energy) and a transmission mode OR-PAM (with 50nJ pulse energy) using a 10 MHz unfocused transducer (Scale bar: 100 μm) UT: Ultrasound Transducer

Figure 11.3(c) shows that PARS is capable of indicating the bleeding area in the tissue. The bleeding area caused intentionally by using very high pulse intensity ($>5 \text{ J/cm}^2$). Figure 11.3(d) shows PARS images acquired with a single wavelength (532 nm) rather than multiple wavelengths. With a single wavelength, depth-of-focus is limited to $\sim 30 \mu\text{m}$, rather than 250 μm with the multi-focus approach. Hence single-wavelength excitation is better-suited for depth-sectioning. This is evident in figure 11.3(d), where top capillary beds are seen but not deeper large vessels. When we scan deeper with single wavelength excitation we see larger

deep vessels but not superficial capillary beds. A comparison between images in 3(a) or 3(b) with 3(d) indicate that the multi-focus design helps to improve the SNR of maximum amplitude C-scan images and improve the depth of field of the system compared to single wavelength imaging [32]. All the images shown in this manuscript are raw data and no major image processing steps are applied. The SNR and contrast to noise ratio (CNR) of the image 3(a) is measured ~ 40 dB and 15 dB respectively. The SNR and CNR of the images shown in 3(d) was measured ~ 32 dB and 12 dB respectively. The speed of image acquisition of all the images shown in this manuscript is 2s per frame.

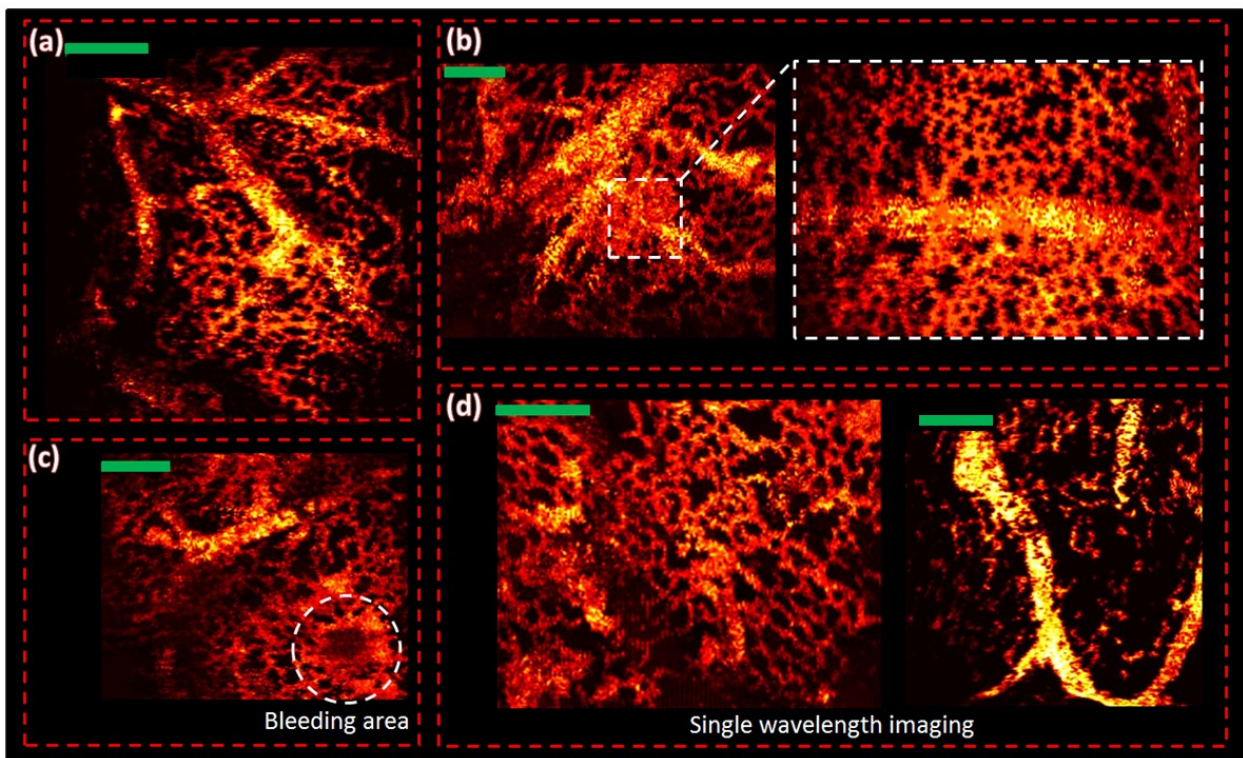


Figure 11.3: In vivo PARS images of chicken embryo model. a) Multi focus images of both capillary beds and bigger blood vessels b) Zoom in image of both capillary beds and bigger blood vessels c) indicating the bleeding area in the tissue d) single wavelength (532 nm) PARS images. Bar: 100 μ m.

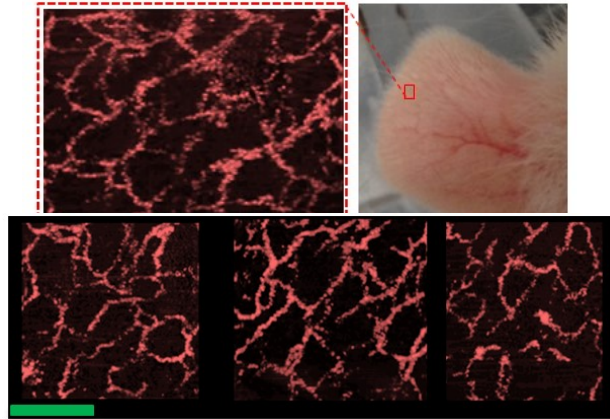


Figure 11.4: *In vivo en-face maximum amplitude C-Scan PARS images of microvasculature in rat's ear. Scale Bar: 100 μm .*

In figure 11.14 of supplementary information confocal microscopy images of the CAM membrane of the same chicken embryo has been shown and compared with PARS. Figure 11.4 shows *in vivo* PARS images of a 100g rat's ear. The capillary beds of the rat's ear is shown. In all *in vivo* images pulse energy ~ 40 nJ has been used and the interrogation power was fixed to 6 mW. The SNR of the vasculature image 4 is measured ~ 30 dB, which is still comparable to ~ 40 dB SNR reported previously by using contact or liquid-coupling second generation OR-PAM with 80 nJ pulse energy [33]. All the 2-D images shown in this manuscript is formed by the maximum amplitude projection of each A-scan as a pixel in a C-scan en-face image, similar to previous PAM approaches. Figures 11.15 of the supplementary information shows images obtained at different depths.

11.3.1. Mechanisms and Models

Some possible OR-PARS modulation mechanisms are discussed in section 2 of the supplementary information and include: (1) pressure-induced refractive-index modulation, (2) thermally-induced refractive index modulation, (3) surface oscillations and (4) scatterer position modulation due to confined thermal expansion. Our calculations indicate 0.1-1% of the light may be modulated due to these mechanisms given our experimental conditions, although thermal-induced refractive index modulation is predicted to be lower (0.0018%). Experimentally we measure $\sim 0.6\%$ of the detected light as being modulated, which agrees

with our order-of-magnitude calculations. Detection of both amplitude and phase of the probe beam are important to form PARS images. When the reference arm was removed, principally eliminating reference signals, we still detected PARS signals from absorbing targets however, signal was roughly 3x weaker. When the $\lambda/4$ -wave plate was removed, principally rejecting back-reflected horizontally-polarized light (the incident polarization), we still detected signals, $\sim 10x$ weaker than when the $\lambda/4$ -wave plate was present. Thus some incident horizontally polarized light is backscattered in alternate polarization states.

The hypothesized modulation mechanisms have a number of testable predictions. To verify that the OR-PARS signal strength is proportional to optical absorption we imaged dye phantoms with varying optical absorption coefficients, as shown in section 3.1 of the supplementary information. The PARS signals scale linearly with optical absorption as expected.

To verify that the optically detected OR-PARS signals are dominantly photoacoustic signals rather than photothermal signals, we performed experiments to demonstrate time-of-flight. Time-of-flight of signals change when optical excitation spots and detection spots are moved further apart from each-other (section 3.2 of the supplementary information). Photothermal mechanisms would observe no such time-of-flight observations. Additional evidence that detected signals are acoustic in nature is that ultrasound signals generated from a transducer can be detected by measuring surface oscillations at a water-air interface as shown in the supplementary information section 3.4. Surface oscillations are not, however, the only modulation mechanism.

To test that PARS signals are associated with more than just surface oscillations, we used a calibrated hydrophone to measure pressure signals 1mm away from a carbon fiber, measured as $\sim 250\text{KPa}$ using nJ-excitation pulses, then in a separate experimental setup, used an ultrasound transducer to transmit comparable pressure levels upwards to the water surface, validating pressure levels with a hydrophone. The PARS setup without the excitation laser produced detectable signals from this experiment, but these signals were $\sim 10x$ lower than the complementary PARS signal from a 1mm-deep carbon fiber. Additional evidence that subsurface focal initial-pressures are sensed is that a phase inversion is observed, with a positive cycle preceding a negative when the beams are confocal but the other way around

when the beams are not confocal, as discussed in section 3.2 of the supplementary information. The signal is also maximum when excitation and probe beams are co-focused. As predicted, PARS signal strength increases linearly with both signal- and reference beam intensities as shown in section 3.5 of supplementary information up to the photodiode saturation level.

11.3.2. Potential Advantages and Future of PARS System

The OR-PARS microscopy system takes advantage of optical excitation and detection which can avoid the use of coupling media and avoid bulky ultrasound transducers [7, 8] which may open up novel applications for photoacoustic imaging. This all-optical system is suitable for integrating with other optical imaging systems. Unlike previous non-contact photoacoustic imaging systems [24-29], the OR-PARS system has demonstrated high-SNR *in vivo* imaging. It takes advantage of recording large initial ultrasound pressures without appreciable acoustic losses.

Future work will focus on improving system sensitivity, extending probe-beam penetration [34, 35], expanding the field-of-view, implementing multi-spectral functional imaging, and co-integration with other optical imaging modalities.

11.4. Methods

11.4.1. Multi-Wavelength Fiber Laser Source

A multi-wavelength visible laser source using stimulated Raman scattering (SRS) [11] has been implemented to generate photoacoustic signals. A frequency doubled ytterbium-doped fiber laser (IPG Photonics Inc.) with a pulse repetition rate (PRR) of 40 kHz and 1 ns pulse width, was coupled using a fiber launch system (MBT621D/M, Thorlabs Inc.) into a 3 m polarization-maintaining single-mode fiber (PM-SMF) (HB-450, Fibercore Inc., UK) to generate SRS peaks at 543, 560, 590, and 600 nm and pulse energies up to 500 nJ [11]. The system has been optimized in order to take advantage of a multi-focus approach [32] for improving the depth-of-focus of 2D and 3D OR-PARS imaging. The output of the PM-SMF was collimated (F280APC-A, Thorlabs Inc.) and combined using a dichroic beam combiner (DBC) with the receiver arm of the system.

11.4.2. System Design

Unlike OCT, OR-PARS takes advantage of a high coherence interrogation beam. In low coherence interferometry, backscattered light is detected from a sectioned depth (via coherence gating). However in OR-PARS high-coherence signals from all depths within the optical depth of focus can be detected. Low optical noise of the interrogation beam within the passband of the RF amplifier is critical to maximize signal-to-noise. For the receiver arm a continuous wavelength (CW) C-band laser with 100-kHz linewidth (TLK-L1550R, Thorlabs Inc., New Jersey) was used. By choosing the linewidth of the interrogation beam (100 kHz) to be smaller than the passband of the photodiode and RF amplifier (1-20 MHz) we minimize such optical noise. The interrogation light at the laser aperture was coupled to a single mode fiber and collimated. The randomly polarized collimated interrogation beam was passed through a polarized beam splitter (VBA05-1550, Thorlabs Inc., New Jersey) to be linearly polarized and a $\lambda/4$ zero order wave plate (Thorlabs Inc., New Jersey) to be circularly polarized. The circularly polarized light then passes through a beam splitter (BS) with 10:90 ratio. A variable natural density filter (NDF) and then a mirror has been placed at the 10% output of the BS in order to provide the optimized reference power of the interferometry. The beam at the 90% output of the BS has been combined by the excitation arm and then scanned across the samples via a 2D galvanometer scanning mirror system (GVS012/M, Thorlabs Inc.). The scanning mirrors were driven by a two-channel function generator. The scanning light was then focused tightly using an objective lens (M Plan Apo NIR 20X, Mitutoyo, Japan). The reflected light is directed back through the wave-plate creating 90° polarization which then reflects at the polarizing beam-splitter in order to guide the maximum possible intensity of reflected light to a 150 MHz-bandwidth InGaAs photodiode (PDA10CF, Thorlabs Inc., New Jersey). A band pass filter (BPS) has been placed on the detection arm to reject the excitation beam. An objective lens (518125, LEICA, Germany) was used in front of the photodiode (not shown in the figure) in order to refocus all possible reflected interrogation light to the small photodiode aperture. The output of the photodiode was amplified using an RF amplifier (Olympus 5900PR) with a band pass filter (1 MHz-20 MHz) and 26 dB gain and then digitized using a 4-channel PCI digitizer (Gage

card) at a sampling rate of 200 MSamples/s. Also detailed discussion regarding selection of excitation and interrogation lasers are given in section 5 of the supplementary information.

11.4.3 Animal Imaging

All the experimental procedures were carried out in conformity with the laboratory animal protocol approved by the University of Alberta Animal Use and Care Committee. Authors are also trained and certified in order to use mice and rats in the research work. During the imaging session the animal was anaesthetized using a breathing anesthesia system (E-Z Anesthesia, Euthanex Corp.).

11.5. Appendix: Supplementary Information

1. OR-PARS system and Methods

A number of different OR-PARS system architectures have been considered. The first PARS system we considered had no reference-beam path. We called it a common path interferometer as shown in the setup 1 of figure 11.5 (a). A small but non-negligible back reflection light from optical components was utilized as a reference beam for interferometry. In the common path interferometer, the collimated randomly polarized interrogation beam was passed through a polarized beam splitter (VBA05-1550, Thorlabs Inc., New Jersey) to direct vertically-polarized light through a $\lambda/4$ zero order wave plate (Thorlabs Inc., New Jersey) into a beam combiner (BC) and then the beams are scanned across the samples via a 2D galvanometer scanning mirror system (GVS012/M, Thorlabs Inc.). The scanning mirrors were driven by a two-channel function generator. The scanning light was then focused tightly using an objective lens. The light reflected back through the wave-plate converts from circular to horizontal polarization which then reflects at the polarizing beam-splitter in order to guide the maximum possible intensity of reflected light to a 150 MHz-bandwidth InGaAs photodiode (PDA10CF, Thorlabs Inc., New Jersey).

A Michelson interferometer, using a non-polarized beam splitter was considered as the second configuration for PARS system as shown in the setup 2 of figure 11.5 (a). A variable neutral density filter (NDF) on a 3-axis stage has been used to tune the reference-beam power to avoid saturating the photodiode. It also provides the ability to tune the pathlength difference of the reference beam. Like the first configuration the interrogation beam was combined with the excitation beam and scanned through an objective lens on the sample. For both configurations, an objective lens (518125, LEICA, Germany) was used in front of the photodiode in order to refocus all possible reflected interrogation light to the small photodiode element. The output of the photodiode was amplified by 26-54 dB (Olympus 5900PR) and digitized using a 4-channel PCI digitizer (Gage card) at a sampling rate of 200 MSamples/s. X-Y Galvo-scanner mirror feedback signals were co-digitized to map the location of each recorded photoacoustic signal associated with each laser shot.

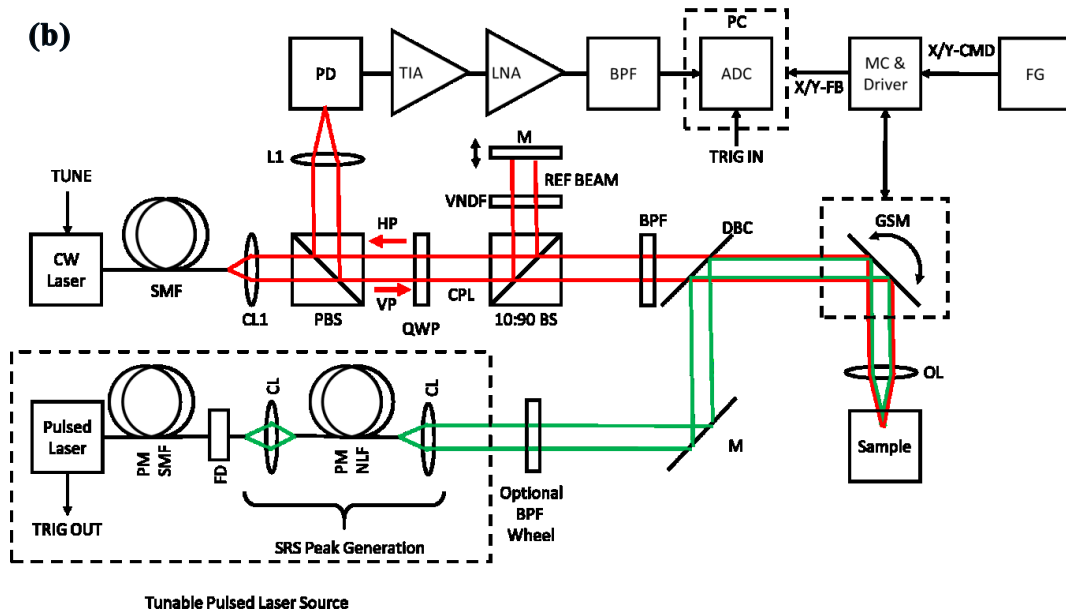
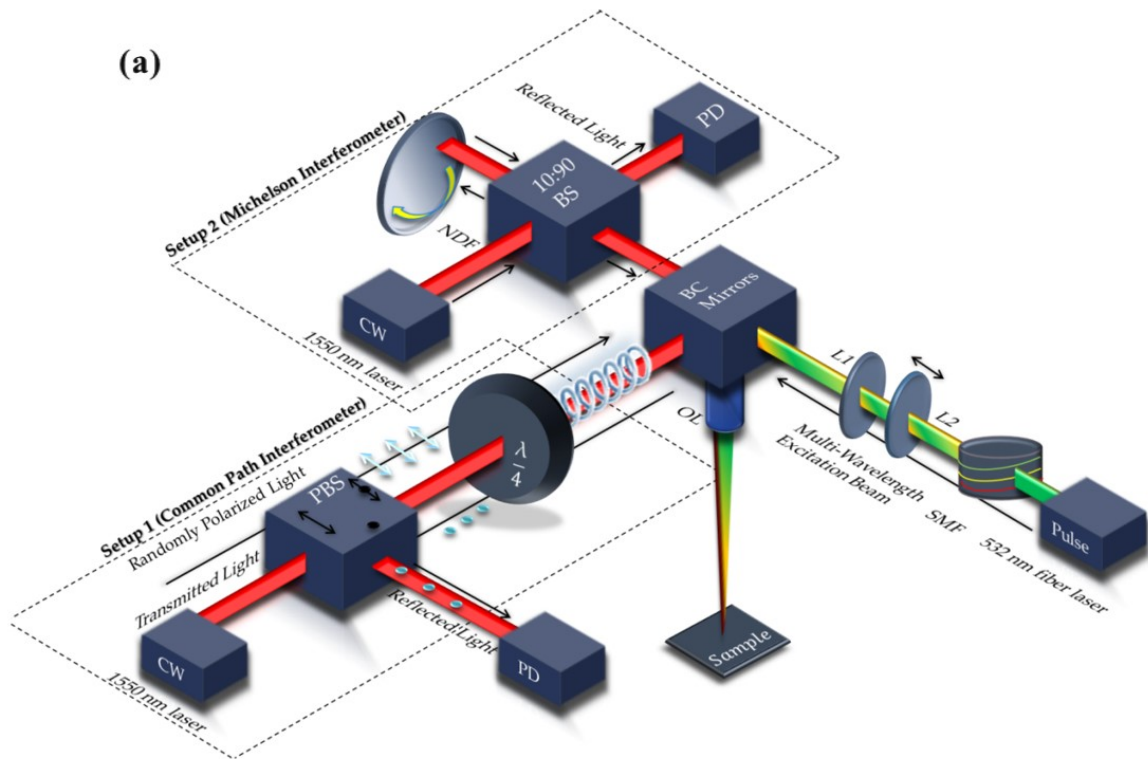


Figure 11.5: (a) Experimental setup of OR-PARS using common path and Michelson interferometry setup. (b) Experimental setup of the final version of the OR-PARS. CW: Continuous wave, PBS: Polarized beam Splitter, SMF: Polarization maintaining single

mode fiber, BS: Beam splitter, BC: beam combiner, BPS: band pass filter, DBC: choric beam combiner, GSM: galvanometer scanning mirror, QWP: quarter wave plate, CL: collimator lens, OL: Objective lens, PM-SMF: Polarization maintaining single mode fiber, L: lens, NDF: natural density filter, M: mirror, FD: frequency doubling, NLF: nonlinear fiber, PD: photodiode, TIA: Trans-impedance amplifier, LNA: Low Noise Amplifier, ADC: analog to digital convertor, FG: function generator. MC: Motor Controller, CMD: Command signals,

A 90:10 beamsplitter would allow 90% of incident light to pass to the sample then 10% of the return light (9% of the total possible light) to be directed back to the PD. A 50:50 beamsplitter would permit 25% of the light to be collected.

The final design was made based on the combination of both configurations using a polarized- and a 90:10 beamsplitter. Figure 11.5(b) shows the final design in more detail. This configuration allows $(0.9)^2 = 0.81$ of the light to be guided to the photodiode and can control the reference beam power. In our experiments we adjusted the reference beam power such that the signal beam registered 4x more photodiode DC signal when a sample of water was used as the target compared to the reference beam. The final configuration lead to roughly 3-times higher signal levels compared to the common-path configuration.

2. OR-PARS modulation mechanisms and comparison with experiment

We developed simple models to better understand signal mechanisms in PARS. The models permit us to calculate the expected fraction of light modulated and to compare this with experiment. The modulated electric field components of light due to various mechanisms will be considered. The total intensity of light incident on the photodiode is given as the ensemble average of the squared magnitude of the sample and reference beam electric fields (taking constant factors as unity for convenience):

$$I_{PD} = \langle |E_S + E_R|^2 \rangle \quad (1)$$

For the modified Michelson interferometry setup shown in figure 5, the power of light reflected from the surface of the sample then routed to the photodiode is estimated as $0.9^2 R_I I_0$ where I_0 is the incident intensity from the source, and R_I is the intensity reflection coefficient at the air-sample interface and a factor of 0.9 is included for each pass through the 10:90 beamsplitter. Likewise the reference beam power is estimated as $I_R = \langle |E_R|^2 \rangle =$

$0.1^2 \eta_{VNDf}^2 I_0$ where η_{VNDf} is the transmissivity of the variable neutral density filter (VNDf). Experimentally we fixed the VNDf such that the ratio of the sample beam detected power to reference beam detected power is 4:1 when water is used as the target. This corresponds to $\eta_{VNDf}^2 = 0.638$.

Now several potential mechanisms of signal modulation will be discussed. This is important to better understand the potential dominant sources of our signal to better optimize the system. Possible mechanisms include the following:

2.1. Pressure-Induced Refractive-Index Modulation

Refractive index changes due to temperature and pressure rises may in turn affect the scattering of light. We first consider pressure changes. Local initial pressures may be calculated as very large when optical focusing and thermal confinement conditions are applied: The initial pressure is given as $P_0 = \Gamma \Phi \mu_a$ where Γ is the Gruneisen parameter. Assuming 532nm light is focused to a micron scale spot size with a focal fluence, Φ , of $500\text{mJ}/\text{cm}^2$ (similar to OR-PAM [36]) and that this light is absorbed by oxygenated blood which has an estimated optical absorption coefficient μ_a of $0.0054 \times 43876 = 236.9\text{cm}^{-1}$ (calculated at this wavelength assuming a hemoglobin concentration of 150g/L and assuming no optical absorption saturation) the absorbed energy produces a transient temperature rise on a micro-scale as high as 30K. Using the above parameter estimates, we calculate an initial pressure as high as 118.5MPa for unity Gruneisen parameter although some tissues have a Gruneisen parameter closer to 0.2.

The optical refractive index experiences a perturbation to pressure variations estimated as

$$n(r, t) = n_0(1 + \eta n_0^2 P(r, t) / 2\rho v_a^2) \quad (2)$$

Where n_0 is the unperturbed optical refractive index, η is the elasto-optic coefficient (~ 0.32 for water), $P(r, t)$ is the pressure field, ρ is mass density and v_a is the speed of sound. The accumulated phase shift of light passing through a zone of enhanced pressure can be calculated by Raman Nath diffraction theory and will depend on the direction of the sound and the direction of the light as well as the pressure field inhomogeneity. For a light beam

incident on a plane pressure wave where both the light and sound beams are parallel the accumulated phase shift should be zero and are rather maximum when sound fields create effective diffraction gratings orthogonal to the light propagation.

Rather than calculate the phase shifts of transmitted light we are more interested in the light reflected from a refractive index mismatch. With 100MPa initial pressure a refractive index step of $\Delta n \sim 0.017$ is predicted in the confined excitation volume, which is a $\sim 1.3\%$ change. This results in an amplitude reflection coefficient of 0.006. This mechanism will contribute to both amplitude and phase variations in the probe beam.

The electric field back-reflected from the sample and incident on the photodiode is modelled as having two components, AC and DC terms

$$E_S = E_{DC,S} + E_{AC,S} \quad (3)$$

Here $E_{DC,S} = \sqrt{0.9^2 R_I I_0}$ is the electric field magnitude of light reflected from the sample surface and $E_{AC,S} = \sqrt{0.9^2 I_0 T_I^2 e^{-2\mu_{eff}d} R_{I,P}}$ is the electric field amplitude of light reflected from the excitation volume beneath the surface due to a transient pressure induced optical index step. T_I is the transmission intensity coefficient at the air-tissue interface. Here both ballistic and scattered photons are accounted for as reflecting from the index step hence $e^{-2\mu_{eff}d}$ is the effective light attenuation over depth d in a scattering medium with effective attenuation coefficient μ_{eff} . The factor of 2 accounts for a round trip. $R_{I,P}$ is the intensity reflection coefficient of the transient index-step, estimated as $\sim 4 \times 10^{-5}$. The fraction of light modulated F_P is calculated as the AC terms from the expansion of $I_{PD} = \langle |E_S + E_R|^2 \rangle$ divided by the DC terms. If the modulated light scattered from the excitation volume contains multiply scattered photons as we have assumed, then because phases of the AC component of the sample are effectively randomized the ensemble average of products of $E_{AC,S}$ with reference beam E_R or $E_{DC,S}$ will be zero, leaving the fraction of light modulated as:

$$F_P = \frac{\langle |E_{AC,S}|^2 \rangle}{\langle |E_R|^2 \rangle + \langle |E_{DC,S}|^2 \rangle} \quad (4)$$

With tissue absorption coefficient $\mu_a = 11.6\text{cm}^{-1}$, scattering coefficient $\mu_s = 32\text{cm}^{-1}$ and scattering anisotropy factor $g = 0.9$, and with a pressure-induced index step of $\Delta n \sim 0.017$, we calculate the fraction of modulated light due to pressure-induced refractive index change as $F_p \sim 0.1\%$, which is close to the 0.6% maximum fractional signal that we measure experimentally in our *in vivo* experiments.

2.2. Thermally-Induced Refractive Index Modulation

Thermal effects may also change refractive indices. At 20°C, the refractive index of water would change $\sim 0.006\% / ^\circ\text{C}$ [1], hence $\sim 0.18\%$ with a 30°C temperature rise. However, this effect would only be applicable locally at the heating zone. Thermal cooling will occur on a scale of microseconds-to-milliseconds after laser-induced heating. Given a fraction index rise $\frac{\Delta n}{n} \sim 0.0018$ due to heating in the excitation volume, the intensity reflection coefficient from the heated region is estimated as $R_{I,PT} = 4.6 \times 10^{-7}$ which is significantly lower than that predicted due to pressure rise: $R_{I,P} \sim 4 \times 10^{-5}$. Using $R_{I,PT}$ in place of $R_{I,P}$ in the calculations above we obtain the fraction of light modulated due to photothermal mechanisms as $F_{PT} \sim 1.1 \times 10^{-5}$, which is predicted as significantly less significant than pressure-induced refractive index modulation.

2.3. Surface Oscillations

Acoustic signals propagating to the surface could also result in phase modulation of the reflected light. Sound pressures decay as $1/r$ due to diffractive losses so pressure signals can be significantly weaker away from the confined heating region compared to at their source. For example, assuming an isotropic spherical heating region of diameter 5 microns (e.g. an isolated red blood cell) the sound pressure level at the boundary of the sphere is estimated as $\sim 100\text{MPa}$ but 1mm away this is predicted as only $\sim 0.25\text{MPa}$. Surface pressure modulation can cause surface oscillations and the reflection of the interrogation beam from this oscillating surface can be a source of detected signal. For a local plane wave at the tissue surface with peak pressure p the particle velocity is estimated as $v_p = \frac{p}{Z}$ where Z is the characteristic acoustic impedance. For a sinusoidal pressure field the particle/surface

displacements are thus $\Delta z \sim v_p / \omega_a$ which is a couple of nm for 10MHz ultrasound with 0.25 MPa amplitude. This is a fraction of a wavelength but still a significant source of phase modulation considering the surface reflectivity may be high and will return significant amounts of incident probe-beam light back to the detector. Notice, however, that this surface modulation has a $1/\omega_a$ dependence hence there is an inherent low-pass filtering affect that could be rejecting high-frequency components. Nevertheless such signals are readily measurable by our system, as evidenced by when we position the probe beam away from the excitation beam and can still form images when we scan the excitation spot. The surface-oscillation modulated signal to the unmodulated signal collected at photodiode (including signal from reference beam) is calculated as $\sim 0.5\%$.

If we assume that only surface oscillations are considered, the electric field phasor from the sample surface is modelled as

$$E_S = E_{S0} \cos(kz \cos(\omega_a t)) \sim E_{S0} (J_0(kz) + J_1(kz) e^{j\omega_a t} + \dots) \quad (5)$$

for a continuous wave modulation at acoustic angular frequency ω_a . Here $E_{S0} = \sqrt{0.9^2 R_I P_0}$. In this case we do not need to worry about light propagating into the sample, and the fraction of light modulated by surface oscillations is estimated as

$$F_S = \frac{2\langle E_{DC,S} E_{AC,S} \rangle + 2\langle E_R E_{AC,S} \rangle}{\langle |E_{DC,S}|^2 \rangle + \langle |E_{AC,S}|^2 \rangle + \langle |E_R|^2 \rangle + 2\langle E_R E_{DC,S} \rangle} = \frac{2E_{S0}^2 J_0(kz) J_1(kz) + 2E_{S0} E_R J_1(kz)}{E_{S0}^2 J_0^2(kz) + E_{S0}^2 J_1^2(kz) + E_R^2 + 2E_{S0} E_R J_0(kz)} \quad (6)$$

With a predicted surface oscillation of 2nm (associated with pressures 1mm from the excitation volume) we estimate $F_S \sim 0.5\%$. This could be significantly less for pulsed rather than CW oscillations.

To validate that surface modulations are indeed a mechanism contributing to our detected signal, we performed a couple of experiments: (1) we used an ultrasound transducer to generate acoustic waves detected by the PARS system focused on the surface of a water-air interface and (2) we demonstrated that we could detect signals when the excitation spot and detection spot were not confocal. In the first experiment as shown in section 3.2, we fixed the interrogation spot and scanned the excitation spot. This was achieved by introducing the

interrogation beam below the galvanometer scanning mirrors and before the imaging objective lens. With this configuration we were able to form images of carbon fiber networks but the signal-to-noise was significantly lower than when both beams were co-focused, and the field of view was more limited due to signal-to-noise dropping away from the interrogation beam location. These data suggest that acoustic waves are created at the excitation volume then propagate to the detection spot. Indeed we see time-delays associated with increasing excitation-detection spot differences.

In the next experiment (section 3.3) we used a 10MHz unfocused ultrasound transducer (Olympus, V312-SM) in immersion to create surface oscillations at the air-water interface. We adjusted the ultrasound output to be around 250KPa (with +/-20% hydrophone calibration error in pressure measurements). With this acoustic output we observed nearly 4V_{pp} of signal using our PARS system (deactivating the excitation beam), after removing the DC signal and amplifying the photodiode signal by 54 dB using an RF amplifier. The amplitude of AC components caused by surface oscillations was ~8mV_{pp} (~4 mV_p), while the reflected DC optical light without surface modulation was measured as ~4V. Therefore, the fraction of modulated light was measured as ~0.1%, which is consistent with our theoretical calculation result.

2.4.Scatterer Position Modulation Due to Confined Thermal Expansion

The volumetric thermal expansion coefficient of water is given as $\alpha_V = 207 \times 10^{-6} \text{K}^{-1}$ at 20°C. Assuming a transient temperature rise on a micro-scale as high as 30K as calculated above, a volumetric expansion $\frac{\Delta V}{V} = 207 \times 10^{-6} \text{K}^{-1} \times 30 \text{K} = 6.21 \times 10^{-3}$ is predicted. For a given temperature rise, the smaller the heated volume the larger the expansion. Now if the light is absorbed from a 3-micron spot size with a volume modelled as the 1/e penetration depth times the cross-sectional illumination area the isotropic particle motion is modelled as $(6.21 \times 10^{-3} \times \pi(r)^2 \times \text{DOF}_{ex})^{\frac{1}{3}} = 1 \mu\text{m}$ which is larger than the wavelength and a very large modulation, where r is the radius of the excitation beam spot size at focus and DOF_{ex} is the depth of field of excitation beam calculated using Gaussian beam parameters, ~27 μm . However, even though such modulation could be large, the fraction of light backscattered

from this excitation volume could be quite small, especially considering that only ballistic photons would interfere constructively with the reference beam, as multiply-scattered photons will have random phase. A rough model for the fraction of light intensity that is backscattered by the excitation volume is $F_{ev} = T_I^2 e^{-2\mu_t d} (1 - e^{-\mu_s DOF_{ex}}) \zeta$ where $\mu_t = \mu_a + \mu_s$ is the extinction coefficient corresponding the attenuation of ballistic photons, μ_s is the reduced scattering coefficient, μ_a is the absorption coefficient, d is the depth of the excitation focus, , and ζ is the backscattered light collection efficiency as a function of the numerical aperture and scattering anisotropy. Assuming a Heyney-Greenstein phase function with scattering anisotropy of $g = 0.9$, refractive index of $n=1.33$ and objective lens numerical aperture of $NA = 0.4$, we calculate $\theta = 180^\circ - \arcsin\left(\frac{NA}{n}\right) = 162^\circ$, the fraction of ballistic photons scattered within the acceptance angle of the optics as $\zeta = \int_{-1}^{\cos\theta} p(\cos\theta') d\cos\theta' = \frac{1-g^2}{2g} \left(\frac{1}{\sqrt{1+g^2-2g\cos\theta}} - \frac{1}{1+g} \right) = 6.5 \times 10^{-4}$ [1]. This light collection efficiency could be larger for more isotropically scattering tissues and approaches 0.023 in the limit of $g \rightarrow 0$. We are accounting for ballistic photons for phase-sensitive detection because multiply scattered photons will have randomized phase. Even if all the light was modulated from the sample volume, the fraction of modulated light due to scatterer position modulation is bounded by the light collection efficiency as $F_{Sp} \cong \frac{\langle |E_{AC,S}|^2 \rangle}{\langle |E_R|^2 \rangle + \langle |E_{DC,S}|^2 \rangle} \ll 0.01\%$, where $\langle |E_{AC,S}|^2 \rangle = 0.9^2 I_0 F_{ev}$. It can be orders of magnitude smaller for deeper excitation volumes, due to ballistic light attenuation. These calculations are upper bounds: the collection of scatterers within the excitation volume may move incoherently and lead to a more complicated signal model.

2.5. Detected Signal

The above calculations considered only the fraction of light which is estimated to be modulated. The actual signal level is proportional to this fraction of modulated light times the local fluence-rate or intensity of the interrogation beam which depends on excitation focusing and will additionally depend on the light collection efficiency, surface roughness and reflectivity among other factors.

3. Additional Experimental Results

We formulated a number of testable hypotheses stemming from our modeling and experimental observations: (1) observed signals are indeed photoacoustic signals, (2) surface oscillations and local pressure-induced refractive index modulation are dominant signal mechanisms, (3) PARS is capable of optical sectioning measurement, (4) The PARS signal strength increases linearly with both signal- and reference beam intensities. We performed a set of experiments to test our hypotheses.

To provide evidence that observed signals are indeed photoacoustic signals we designed experiments to test that PARS signal strength is proportional to optical absorption and incident excitation fluence, and that the PARS signals can detect time-of-flight differences associated with photoacoustic signal propagation.

3.1. Validation of Optical Absorption Contrast

We measured the photoacoustic signal generated by different dye concentrations to prove the concept of optical absorption contrast for PARS imaging. Dye imaging experiments were conducted using red dye (Fiesta Red) and blue dye (Lake Placid Blue). In these experiments the PARS photoacoustic signals were measured from 200 μm dye-filled tubes at different concentrations and the PARS photoacoustic signal was plotted against the absorption coefficient of the dyes as measured using independent spectrometer measurements. It is shown in figure 11.6 that the sample with higher absorption coefficient provides larger PARS photoacoustic signals as expected.

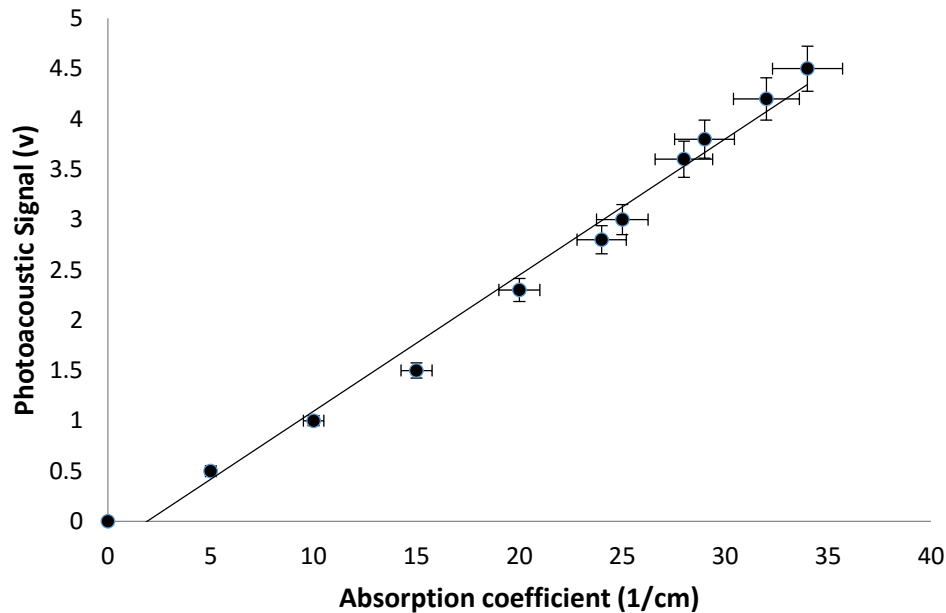


Figure 11.6: Measured photoacoustic signals from various dye concentrations.

3.2.PARS imaging with fixed detector and ultrasound time of flight study

The PARS system is capable of imaging when both beams are scanning together (figure 11.2a) or when the interrogation beam is fixed and excitation beam is scanning as shown in figure 11.7. The interrogation beam in this case was fixed by introducing the CW light between the scanning mirrors and imaging objective instead of the setup shown in figure 11.5. The field of view is limited as the generated photoacoustic signals will experience more attenuation if they are located far from the fixed interrogation beam. Figure 11.8 shows time domain photoacoustic signals from a carbon fibers network, when the interrogation and excitation beams are located at different positions. In Figure 11.8(a) both excitation and interrogation beam have been co-aligned in the x and y direction and co-focused together in the z direction. Therefore, the photoacoustic signal starts at the time zero. However this can

be changed by moving the excitation and interrogation beam apart of each other as shown in figure 11.8(b) and 8(c). In Figure 11.8(b) and 11.8(c) a time shift has been measured as the excitation and interrogation beams are separated by ~ 120 and $330 \mu\text{m}$. The results confirm the ultrasound time of flight variation by changing the location of detection spot. Signal maximization occurs when excitation and detection beams are confocal.

Interestingly there is an apparent phase shift and amplitude difference between time-zero and time-delayed measurements. Time-delayed measurements begin with a negative cycle which would correspond to a pressure wavefront inducing surface displacement in the negative z direction (with the positive z direction going down into the sample). In contrast, time-zero measurements appear to begin with a positive cycle first (which would correspond to more light being reflected at first due to initial pressure rise locally from the sample below the surface). Additionally, time-zero measurements are significantly larger. These data provide evidence that when excitation beam and interrogation beams are co-focused large initial pressure signals are measured, and that these signals originate from the excitation volume.

Figure 11.9 shows the -3 dB bandwidth was measured as ~ 10 MHz by imaging carbon fiber network. A 10th order polynomial fit was used to plot the data. The band pass response was expected as the RF amplifier was set to a band pass filter (1 MHz-20 MHz).

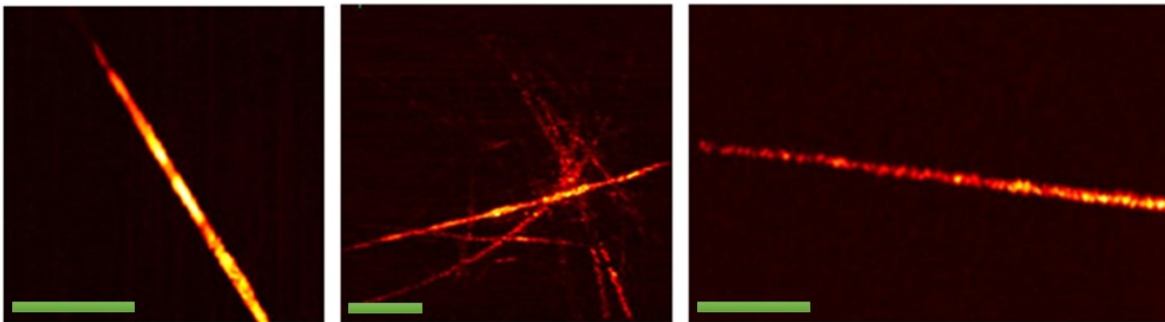


Figure 11.7: Carbon fiber images when interrogation beam is fixed. The left and right images are formed by imaging a single carbon fiber while the middle image is formed by imaging a carbon fiber networks. Bar= $100\mu\text{m}$.

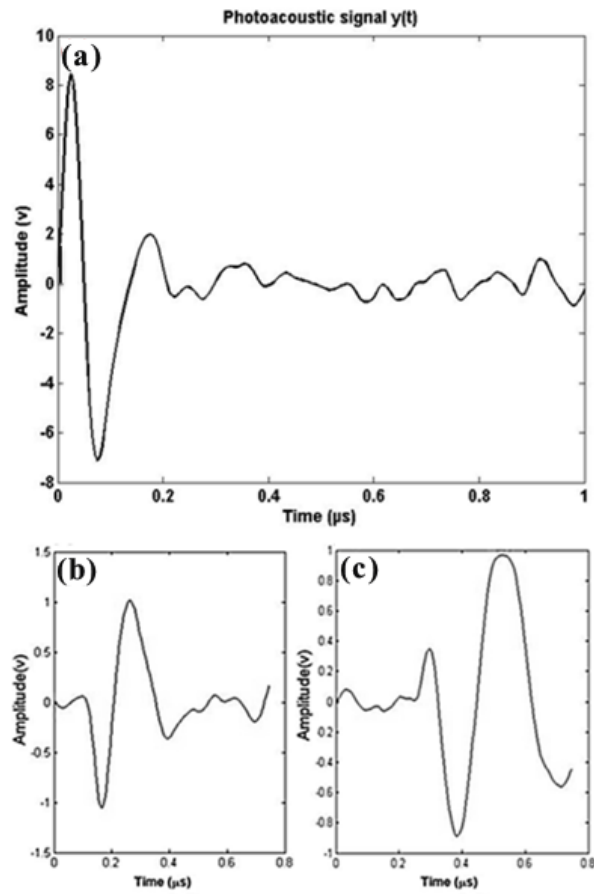


Figure 11.8: PARS photoacoustic time domain signal of an individual carbon fiber when the excitation and interrogation beams are separated by \sim (a) 0 (b) 120 and (c) 330 μm

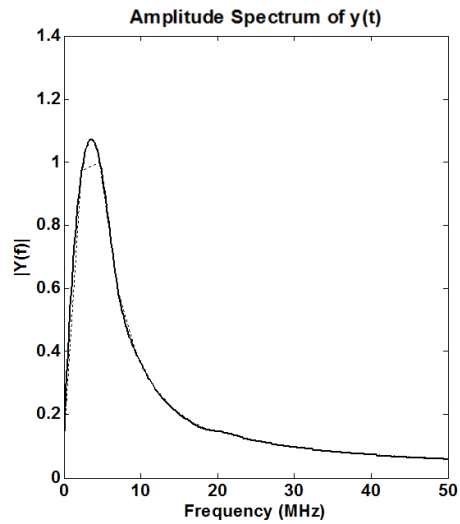


Figure 11.9: PARS frequency response with 10th order polynomial fit.

3.3. Experimental Detection of Ultrasound Signals

In order to validate that the ultrasound signals can be detected directly, the system shown in figure 11.10 has been employed to directly detect the ultrasound signals generated by an ultrasound transducer. The PARS system is also capable of detecting noncontact measurement of the displacement caused by ultrasound signals from an unfocused piezoelectric transducer (Olympus, A312-10 MHz/0.25”). A layer of water was above the transducer and the transducer was driven by a sine wave from a function generator at 10 MHz. The transducer was characterized previously by a hydrophone. The noise equivalent pressure (NEP represents the pressure detected with a signal-to-noise ratio of 1) of PARS system was measured ~ 1 kPa for detection of ultrasound generating from a transducer.

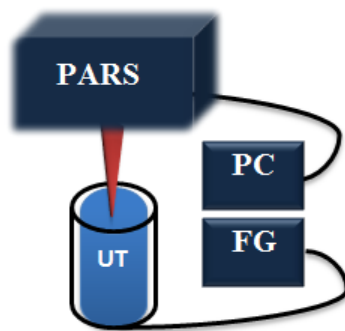


Figure 11.10: PARS characterization for ultrasound detection

3.4. Validation of Optical Sectioning Capabilities:

The system shown in figure 11.10 has been employed to measure signal from a transducer at different axial distances as shown in figure 11.11. The depth of focus of the detection beam on the sample is measured as ~ 50 μm . It shows evidence that the field of depth is determined by optics rather than acoustics and demonstrates optical sectioning capabilities.

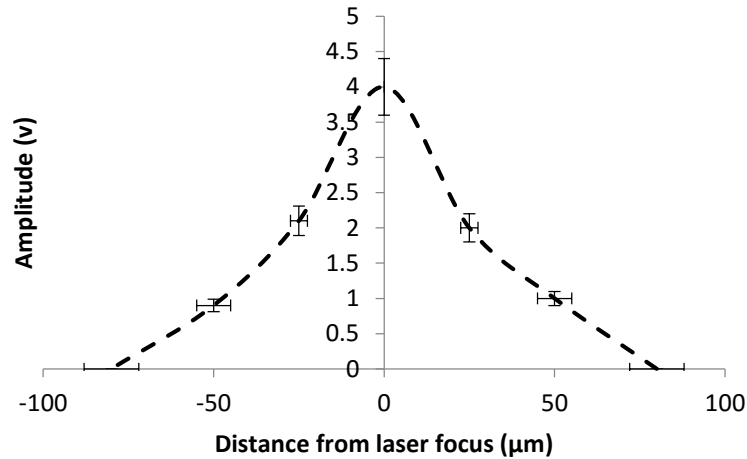


Figure 11.11: Measured signal from the water-air interface due to an immersed unfocused transducer as a function of depth.

3.5.PARS signal strength VS. Beam intensities

Figure 11.12 shows the photoacoustic signal versus energy of the excitation laser on the sample when the interrogation power is fixed at 6 mW. It shows a linear response as expected. Figure 11.13 shows the photoacoustic signal as a function of interrogation power on the sample when excitation energy is fixed at 10 nJ. It is shown that after ~11 mW the photodiode goes to its saturation region.

Given that the detected signal is linear with excitation beam pulse energy, we note that if the fluence of the excitation beam was limited to 20 mJ/cm^2 (the ANSI limit skin exposure for a non-scanned beam, as was used in previous non-contact photoacoustic papers [23][37]), we would obtain ~40 times less initial pressure than the PARS microscopy design which uses a surface fluence of $\sim 1 \text{ mJ/cm}^2$ but a focal fluence $\sim 800 \text{ mJ/cm}^2$.

Considering the fact that the detected signal is linear with the probe beam intensity (when below the photodiode saturation), we also note that if the skin surface power density of the interrogation beam was limited 100 mW/cm^2 (the ANSI limit for non-scanned probe beam, as was used in non-contact photoacoustic holography experiments [38]) we would obtain significantly less surface signal than in our PARS design. If we restricted our PARS MPE to the ANSI limit for a scanned beam, calculated below for our case as 50 W/cm^2 at the skin surface for one image frame (see Section 4.2 below), we would be 500 times more sensitive

than the non-scanned case for detecting surface oscillations. At sub-surface focal locations the scanned-beam ANSI limited probe fluence rate is calculated as $\sim 6000\text{W}/\text{cm}^2$. This fluence rate is ~ 60000 times larger than the non-scanned case.

Previous non-contact photoacoustic sensing techniques [23] focused on detection of surface oscillations. Our approach instead detects subsurface initial pressures directly at the excitation focal volume. These subsurface pressures may be orders of magnitude larger than surface pressures.

These calculations indicate that the PARS confocal scanning approach offers orders of magnitude sensitivity improvement over previous non-contact photoacoustic methods.

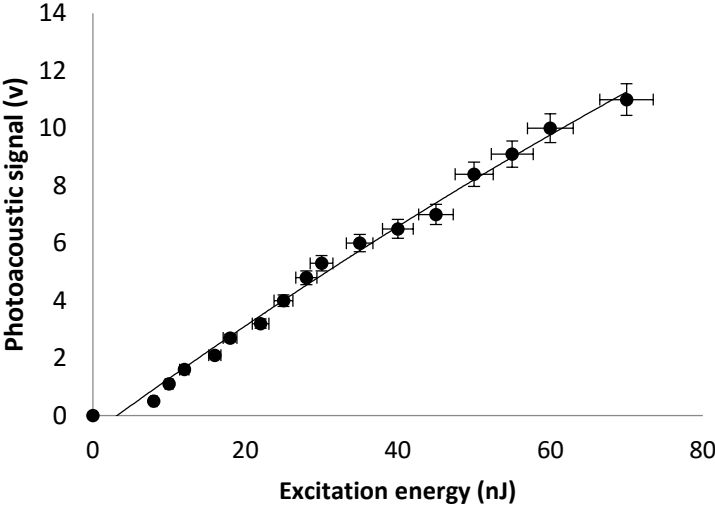


Figure 11.12: Photoacoustic signal as a function of excitation energy on the sample (carbon fiber) when interrogation power is fixed at 6 mW.

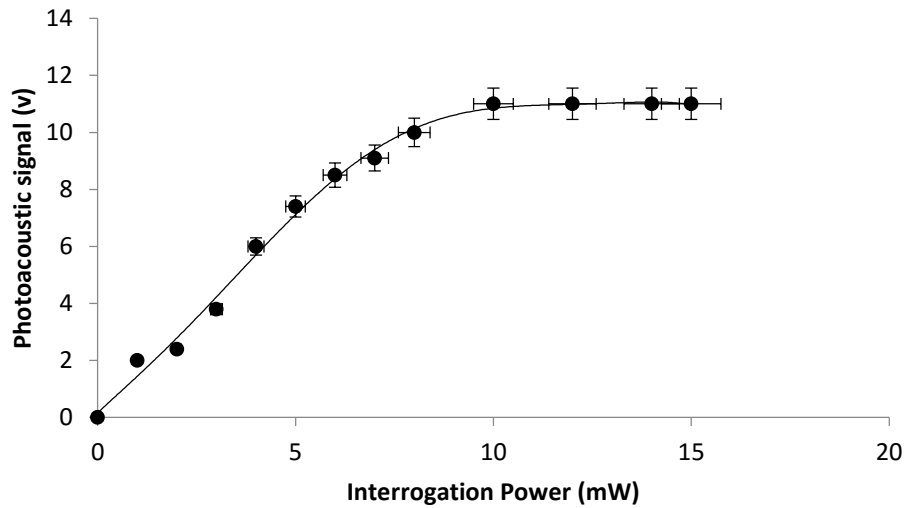


Figure 11.13: Photoacoustic signal versus interrogation power on the sample (carbon fiber) when excitation energy is fixed at 10 nJ.

3.6. Comparison with Fluorescence Confocal Microscopy

Figure 11.14 shows confocal microscopy images of the CAM membrane of a chicken embryo. Some images have extended focus to see vessels at multiple depths. The chicken embryo was injected IV with Rhodamine-conjugated lectin to stain the blood vessels. The confocal microscope used was a Zeiss AxioExaminer Z1 microscope with 6 diode lasers, a Hamamatsu ImagEM backthinned EM-CCD camera, environmental chamber and fully motorized XYZ translation built by Quorum Technologies. 496 nm laser/20x objective lens was used for image acquisition. Unlike PARS the chicken embryo had to be held stationary during the imaging section as the heartbeat of animal can cause major image defects. Unlike many other interferometric sensors PARS does not require a floating optical table. The confocal fluorescence microscopy images of the chick CAM membrane microvasculature are similar to our PARS images, validating the PARS technology, however, unlike the confocal microscopy approach, the PARS images are label free.

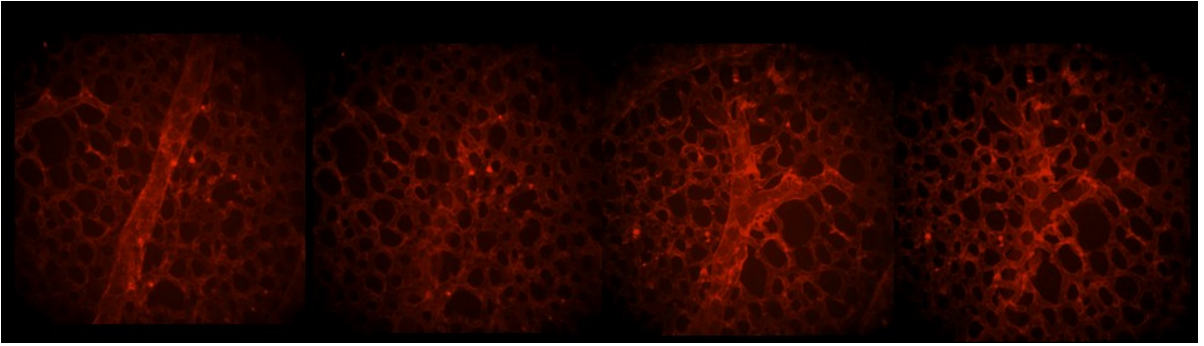


Figure 11.14: Confocal images of chicken embryo

3.7. Maximum amplitude projection and depth information

The 2D images shown in this manuscript are formed by projection of the maximum amplitude at each depth. Figure 11.15 shows the information acquired at each depth to form image 3(a). It is clearly shown that at each depth different information can be obtained.

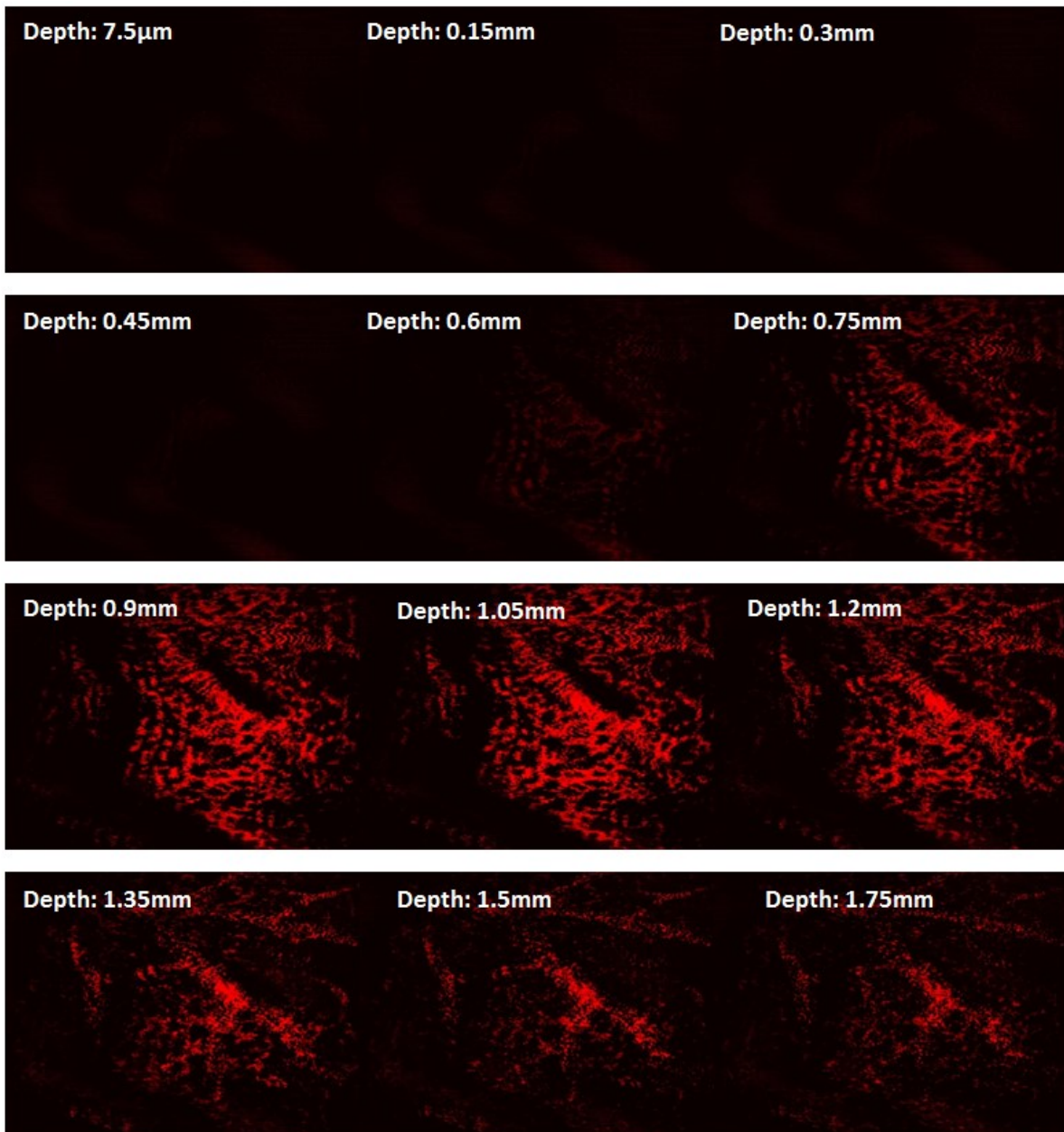


Figure 11.15: The information acquired at each depth to form image 11.3(a).

4. Imaging procedures and laser safety

4.1. Excitation-Beam Laser Safety

The pulse energy of the excitation and the power of interrogation beams for *in vivo* PARS imaging have been set as 60 nJ and 6 mW respectively. In our *in vivo* studies, given that the optical focus is $\sim 150\mu\text{m}$ beneath the tissue surface, with a focal spot of $\sim 3\mu\text{m}$ in diameter, the surface spot size is $\sim 100\mu\text{m}$ in diameter and the calculated surface laser fluence is $\sim 1\text{ mJ}/\text{cm}^2$ for excitation laser, which is below the single pulse limit of $20\text{ mJ}/\text{cm}^2$ set by the American National Standards Institute (ANSI) [37]. The spatial peak optical fluence at the focus is $\sim 800\text{ mJ}/\text{cm}^2$, which is still less than the damage threshold observed in small animals and comparable to other OR-PAM systems [7]. In our work, light delivery is confined to a localized area and no tissue damage is visible after imaging.

In addition, for an average scan-step size Δx (average distance between excitation laser shots on the sample during galvanometer scanning) of $3\mu\text{m}$, there are on average $N = 100\mu\text{m}/3\mu\text{m} \sim 33$ adjacent laser pulses overlapping on the skin surface. For 40 kHz laser PRR, the exposure time is $t \sim 0.8\text{ms}$, so the MPE for a pulse train is $MPE_{Train} = 1.1 C_A t^{0.25} = 185\text{mJ}/\text{cm}^2$, where C_A is a wavelength-correction factor equal to unity for 400-700 nm wavelengths. The average power limit set by ANSI is calculated as $MPE_{Average} = MPE_{Train}/N \sim 6\text{ mJ}/\text{cm}^2$. Thus our actual surface fluence of $\sim 1\text{ mJ}/\text{cm}^2$ is about 6 times lower than the ANSI limit. In future studies, careful selection of focusing, repetition rate, and pulse energy parameters must be considered to avoid exceeding ANSI limits. On the other hand, for some pre-clinical applications, exceeding these limits may be acceptable. One can stay below the ANSI limits by reducing the laser repetition rate at the expense of imaging frame rate.

4.2. Interrogation beam laser safety considerations

Presently we perform optical scanning on a 1 mm x 1 mm or smaller area with a laser power of 6 mW. This may naively be equivalent to an average power of $0.6\text{W}/\text{cm}^2$, which is significantly greater than the $100\text{ mW}/\text{cm}^2$ typically required by ANSI for a non-scanned CW beam. However, the exposure time associated with scanning a focused light spot is important when considering Maximum Permissible Exposure (MPE). We consider an x-galvonometer

scanning rate of 60 Hz and a y-scanning rate of 0.25 Hz (half C-scan frames per second) over 1 mm field-of-view. For CW lasers with wavelengths between 1500 and 1800 nm, and exposure times between 1ns and 10s, MPE on the skin is limited to a deposited energy density of $1\text{J}/\text{cm}^2$. If the scanning velocity is $v = 0.12\text{ m/s}$ (as is the case for a 60 kHz triangular-wave scanning trajectory over 1 mm FOV) and the 1550-nm light-spot has a radius a between $50\mu\text{m}$ and $350\mu\text{m}$ (for subsurface focal depths between $\sim 150\mu\text{m}$ and $\sim 1\text{ mm}$) on the skin surface then the exposure time $T_e = 2a/v$ associated with the scanning trajectory sweeping a path-length $2a$ will be between 0.8 and 6ms (assuming only one scan-line in a C-Scan is acquired). When acquiring one C-scan image, any given area will experience on average $N \sim 2a/\Delta y$ (N is between 25 and 175 for focal depths between $\sim 150\mu\text{m}$ and $\sim 1\text{ mm}$ respectively) passes of the probe-spot where Δy is the mean y-scanning resolution $\sim 4\mu\text{m}$. Thus the exposure time for one image is $T_{EXP} = NT_e$ and leads an ANSI-limited instantaneous surface power density of $\Phi_s = 1\text{J}/\text{cm}^2/T_{EXP}$, around $50\text{ W}/\text{cm}^2$ and $1\text{ W}/\text{cm}^2$ for focal depths between $\sim 150\mu\text{m}$ and $\sim 1\text{ mm}$ respectively. In our experiment, the fluence on skin surface can be calculated $\sim 76\text{W}/\text{cm}^2$ for a focal depth at $\sim 150\mu\text{m}$.

Considering that we need only $\sim 1\mu\text{s}$ of measurement time for each laser pulse (equivalent to $\sim 1.5\text{ mm}$ of depth), we could modulate the interrogation beam to be active only during the measurement phase to reduce the fluence rate even further. Additional improvements in signal-to-noise and detection sensitivity could also enable lower incident laser power levels. Future work will pursue such directions.

5. Laser selection

Selection of excitation laser involves a number of considerations. First, we desire conditions of stress- and thermal-confinement so that both heat- and stress- build up during the course of a laser pulse before the energy can propagate away in the form of thermal diffusion or acoustic propagation. Stress confinement is the most stringent of the two criteria. For a $3\mu\text{m}$ focused excitation spot the stress confinement requirement is that laser pulses should be shorter than $3\mu\text{m}/1500\text{ m/s} = 2\text{ ns}$. Hence we require a laser with pulse widths of a nanosecond or shorter. Second, the repetition rate of the laser will determine the imaging frame rate: the faster the repetition rate the higher. However, the repetition rate should not be

so high that signals from previous pulses overlap in time with subsequent pulses. Given that the imaging depth is not likely to be more than about a transport mean-free path (~ 1 mm in tissue) the maximum pulse-repetition rate (PRR) is on the order of 1 MHz. Pulse energy should be such that ANSI limits are met at the tissue surface, requiring sub- μJ levels of pulse energy. Finally the wavelength of the excitation source will ideally be tunable for multi-spectral imaging purposes. These requirements are similar to those for OR-PAM and we have previously demonstrated that fiber lasers can be a good choice [11]. We use a frequency doubled Ytterbium-doped fiber laser and to achieve tunable inject μJ -scale ns-pulses at 532-nm into a length of nonlinear fiber to generate Stimulated Raman Scattering peaks. We previously demonstrated that a range of wavelengths can be generated using this technique with enough pulse energy for OR-PAM [11]. Few other sources are capable of meeting this range of requirements.

The selection of the interrogation laser is also important. The linewidth of the probe laser was chosen to be significantly smaller than the acoustic frequencies to be detected otherwise significant noise power from the laser source could leach into the passband of the system even when no PA signals are present and degrade SNR. We use a laser with 100 kHz linewidth which is significantly smaller than the MHz-level frequencies to be detected. Our laser is tunable in wavelength and power but wavelength tuning is not critical. We use a wavelength of 1550 nm because it is spectrally different than our 532 nm excitation light (important so that optical filters can prevent excitation light from hitting the detector) and because it is a key band in optical communications where a plethora of components are available. Water absorption at this wavelength is higher than desirable: the $1/e$ penetration depth is a few mm. Other wavelength bands could be considered in the future to achieve higher sensitive detection. Our laser offers ~ 30 mW output power which is more than enough for good-SNR measurements and even too strong on the basis of maximum permissible exposure. A detailed discussion of laser safety considerations is discussed in section 4.

6. Photoacoustic modulation of multiply-scattered light: Beyond the Ballistic Regime

At depths beyond a transport mean-free path photoacoustic signal modulation of multiply scattered light must be given additional attention. A key difference in this regime compared to the ballistic or quasi-ballistic regime is that diffusely-scattered light may emerge incident on a detector with many statistically distinct optical speckles and ultrasound-modulated components may create speckles with modulation at the ultrasonic frequencies but with each statistically independent speckle spot having its own random phase. This can lead to parasitic reduction of signal if merely detected with a single photo-detector and the random phase-speckles can produce a source of noise. A key challenge is to detect such multiply-scattered modulated light with large-étendue and in such a way as to be immune to random phases of speckles. Several previous methods have been discussed for this purpose, including high-finesse and/or frequency stabilized Fabry-Perot etalons [20,21], CCD-based speckle contrast imaging scheme[39, 40], nonlinear crystals and spectral hole burning[41, 42].

In our approach we use optically-focused detection within ballistic or quasi-ballistic transport regimes, so while multiply scattered light may be present, we can pick out ballistic components focused with optical resolution. To further reject multiply-scattered light we could implement a pinhole as a spatial frequency filter prior to the detector which will have the effect of preserving mostly ballistic photons from the optical focus at the cost of rejecting some detected light. This approach is used in confocal microscopy. The confocal nature of our system already provides some amount of spatial filtering and we did not find it necessary to implement a pinhole or consider other large-étendue demodulators or detection systems which were previously required for detecting ultrasound-modulated light.

Bibliography

1. Wang, L.V. and H.-I. Wu, *Biomedical Optics*. 2009, Wiley-Blackwell.
2. Dunsby, C. and P.M.W. French, *Techniques for depth-resolved imaging through turbid media including coherence-gated imaging*. Journal of Physics D: Applied Physics, 2003. **36**(14): p. R207-R227.
3. Boccara, A.C., et al., *Sensitive photothermal deflection technique for measuring absorption in optically thin media*. Opt. Lett., 1980. **5**(9): p. 377.
4. Faber, D.J., et al., *Light absorption of (oxy-)hemoglobin assessed by spectroscopic optical coherence tomography*. Opt. Lett., 2003. **28**(16): p. 1436.
5. Hermann, B., et al., *Precision of extracting absorption profiles from weakly scattering media with spectroscopic time-domain optical coherence tomography*. Opt. Express, 2004. **12**(8): p. 1677.
6. Schmitt, J.M., S.H. Xiang, and K.M. Yung, *Differential absorption imaging with optical coherence tomography*. J. Opt. Soc. Am. A, 1998. **15**(9): p. 2288.
7. Wang, L.V. and L. Gao, *Photoacoustic Microscopy and Computed Tomography: From Bench to Bedside*. Annu. Rev. Biomed. Eng., 2014. **16**(1): p. 155-185.
8. Hajireza, P., W. Shi, and R.J. Zemp, *Real-time handheld optical-resolution photoacoustic microscopy*. Opt Express, 2011. **19**(21): p. 20097-102.
9. Yang, J.-M., et al., *Simultaneous functional photoacoustic and ultrasonic endoscopy of internal organs in vivo*. Nat Med, 2012. **18**(8): p. 1297-1302.
10. Wang, L.V., *Multiscale photoacoustic microscopy and computed tomography*. Nature Photonics, 2009. **3**(9): p. 503-509.
11. Hajireza, P., A. Forbrich, and R. Zemp, *In-Vivo functional optical-resolution photoacoustic microscopy with stimulated Raman scattering fiber-laser source*. Biomedical Optics Express, 2014. **5**(2): p. 539-546.
12. Zhang, H.F., et al., *Functional photoacoustic microscopy for high-resolution and noninvasive in vivo imaging*. Nat Biotechnol, 2006. **24**(7): p. 848-851.
13. Paproski, R.J., et al., *Multi-wavelength photoacoustic imaging of inducible tyrosinase reporter gene expression in xenograft tumors*. Scientific Reports, 2014. **4**.
14. Ho, C.J.H., et al., *Multifunctional Photosensitizer-Based Contrast Agents for Photoacoustic Imaging*. Scientific Reports, 2014. **4**.
15. Kavros, S.J., et al., *Expedited Wound Healing with Noncontact, Low-Frequency Ultrasound Therapy in Chronic Wounds*. Advances in Skin & Wound Care, 2008. **21**(9): p. 416-423.
16. Sy, S., et al., *Terahertz spectroscopy of liver cirrhosis: investigating the origin of contrast*. Physics in Medicine and Biology, 2010. **55**(24): p. 7587-7596.
17. Ntziachristos, V., J.S. Yoo, and G.M. van Dam, *Current concepts and future perspectives on surgical optical imaging in cancer*. J. Biomed. Opt., 2010. **15**(6): p. 066024.
18. Hajireza, P., W. Shi, and R. Zemp, *Label-free in vivo GRIN-lens optical resolution photoacoustic micro-endoscopy*. Laser Phys. Lett., 2013. **10**(5): p. 055603.
19. Hajireza, P., W. Shi, and R.J. Zemp, *Label-free in vivo fiber-based optical-resolution photoacoustic microscopy*. Opt Lett, 2011. **36**(20): p. 4107-9.

20. Zhang, E., J. Laufer, and P. Beard, *Backward-mode multiwavelength photoacoustic scanner using a planar Fabry-Perot polymer film ultrasound sensor for high-resolution three-dimensional imaging of biological tissues*. *Applied Optics*, 2008. **47**(4): p. 561.
21. Liu, M., et al., *Dual modality optical coherence and whole-body photoacoustic tomography imaging of chick embryos in multiple development stages*. *Biomedical Optics Express*, 2014. **5**(9): p. 3150-3159.
22. Carp, S.A. and V. Venugopalan, *Optoacoustic imaging based on the interferometric measurement of surface displacement*. *J. Biomed. Opt.*, 2007. **12**(6): p. 064001.
23. Wang, Y., C. Li, and R.K. Wang, *Noncontact photoacoustic imaging achieved by using a low-coherence interferometer as the acoustic detector*. *Opt. Lett.*, 2011. **36**(20): p. 3975.
24. Hochreiner, A., et al., *Non-contact photoacoustic imaging using a fiber based interferometer with optical amplification*. *Biomed. Opt. Express*, 2013. **4**(11): p. 2322.
25. Rousseau, G., A. Blouin, and J.-P. Monchalin, *Non-contact photoacoustic tomography and ultrasonography for tissue imaging*. *Biomed. Opt. Express*, 2011. **3**(1): p. 16.
26. Rousseau, G., et al., *Non-contact biomedical photoacoustic and ultrasound imaging*. *J. Biomed. Opt.*, 2012. **17**(6): p. 061217.
27. Xu, G., et al., *Non-contact photoacoustic tomography with a laser Doppler vibrometer*, in *Photons Plus Ultrasound: Imaging and Sensing 2014*. 2014, SPIE-Intl Soc Optical Eng.
28. Hochreiner, A., et al., *Fiber-based remote photoacoustic imaging utilizing a Mach Zehnder interferometer with optical amplification*, in *Photons Plus Ultrasound: Imaging and Sensing 2014*. 2014, SPIE-Intl Soc Optical Eng.
29. Berer, T., et al., *Remote photoacoustic imaging on solid material using a two-wave mixing interferometer*. *Opt. Lett.*, 2010. **35**(24): p. 4151.
30. Tay, J.W., et al., *Ultrasonically encoded wavefront shaping for focusing into random media*. *Scientific Reports*, 2014. **4**: p. 3918.
31. Wang, L.V., *Ultrasound-Mediated Biophotonic Imaging: A Review of Acousto-Optical Tomography and Photo-Acoustic Tomography*. *Disease Markers*, 2004. **19**(2-3): p. 123-138.
32. Hajireza, P., A. Forbrich, and R.J. Zemp, *Multifocus optical-resolution photoacoustic microscopy using stimulated Raman scattering and chromatic aberration*. *Opt Lett*, 2013. **38**(15): p. 2711-3.
33. Hu, S., K. Maslov, and L.V. Wang, *Second-generation optical-resolution photoacoustic microscopy with improved sensitivity and speed*. *Opt. Lett.*, 2011. **36**(7): p. 1134.
34. Kobat, D., et al., *Deep tissue multiphoton microscopy using longer wavelength excitation*. *Opt. Express*, 2009. **17**(16): p. 13354.
35. Balu, M., et al., *Effect of excitation wavelength on penetration depth in nonlinear optical microscopy of turbid media*. *J. Biomed. Opt.*, 2009. **14**(1): p. 010508.

36. Shi, W., et al., *In vivo near-realtime volumetric optical-resolution photoacoustic microscopy using a high-repetition-rate nanosecond fiber-laser*. Opt Express, 2011. **19**(18): p. 17143-50.
37. *Appendix C: American National Standards Institute (ANSI)/Electronics Industries Alliance (EIA) Standard-748, Earned Value Management Systems (EVMS) Guidelines*, in *Performance-Based Earned Value*. 2007, Institute of Electrical & Electronics Engineers (IEEE).
38. Horstmann, J. and R. Brinkmann, *Non-contact photoacoustic tomography using holographic full field detection*, in *Opto-Acoustic Methods and Applications*. 2013, SPIE-Intl Soc Optical Eng.
39. Boas, D.A. and A.K. Dunn, *Laser speckle contrast imaging in biomedical optics*. J. Biomed. Opt., 2010. **15**(1): p. 011109.
40. Humeau-Heurtier, A., G. Mahé, and P. Abraham, *Microvascular blood flow monitoring with laser speckle contrast imaging using the generalized differences algorithm*. Microvascular Research, 2015. **98**: p. 54-61.
41. Xu, X., et al., *Spectral hole burning for ultrasound-modulated optical tomography of thick tissue*. J. Biomed. Opt., 2010. **15**(6): p. 066018.
42. Devaux, F., J.-P. Huignard, and F. Ramaz, *Modelization and optimized speckle detection scheme in photorefractive self-referenced acousto-optic imaging*. Opt. Express, 2014. **22**(9): p. 10682.

12. Conclusion and future work

12.1. Conclusion

In this dissertation several improvements over previous optical-resolution photoacoustic microscopy (OR-PAM) imaging systems are reported. First, the development of an fiber-based OR-PAM (F-OR-PAM) system with a footprint size of an optical fiber is demonstrated with the aid of an image-guide. The image-guide consists of 30,000 individual fibers in an 800 μm bundle and our system provides transmission of high optical resolution images in a compact, flexible fiber bundle. Using a fiber laser we produced ~ 1 ns pulses with energy up to 20 μJ and repetition rate up to 600 kHz at a wavelength of 532 nm. The light was coupled to the 1m long fiber using an objective lens focused on the fiber input and the beam was scanned across the fiber tip using a high-speed galvanometer optical scanner. The proposed setup maintains many of the powerful properties of tabletop OR-PAM systems and adds high flexibility due to the nature of the image-guide and the sub-millimeter-scale footprint of the apparatus. Because of its flexible nature and small footprint, this system and its future modifications could have significant clinical impact for applications where thin fibers can be inserted into body cavities. Our system may find niches in nearly every application where contact- and confocal-mode microendoscopy systems are used currently and may see even more applications because imaging can be label-free.

Second, the development of a GRIN-lens OR-PAME system with a 2 mm-footprint was demonstrated with the aid of an image guide (consisting of 100 000 individual fibers in a 1.4 mm bundle). The flexible and compact fiber bundle provided transmission of high optical resolution images. A fiber laser was employed to produce ~ 1 ns pulses with energy up to 20 μJ and a repetition rate up to 600 kHz at a wavelength of 532 nm. The light was scanned using a high speed galvanometer mirror and coupled to the 2 m long fiber using an objective lens. The fiber bundle transferred the scanning focused light. The light at the output of the fiber bundle was refocused using a 0.29 pitch GRIN lens. The proposed setup maintains many of the powerful properties of bench-top OR-PAM systems and adds small footprint and high

flexibility to them. We anticipate that this system and its future modifications will have significant clinical impact for endoscopic applications.

Third, an array-based optical resolution photoacoustic micro-endoscopy with the capabilities of external guidance of the endoscope tip and data capture has been demonstrated. Both the ultrasound transducer and the endoscope were held and guided by hand. The entire footprint of the endoscopy tip was ~ 1 mm. Images of carbon fiber networks and *in vivo* imaging were demonstrated. The SNR in the phantom study was measured as ~ 40 dB through 2 cm of tissue mimicking phantom material. Based on previous work, we believe that it should be possible to push the endoscope depth to ~ 5 cm or more, though SNR may be lower which may be mitigated by averaging multiple images. Photoacoustic endoscopy has significant potential for investigating cancer and other diseases, and array-based photoacoustic detection is a simple way to minimize the footprint of the endoscope allowing for greater system flexibility.

Fourth, the development of real-time hand-held (HH-OR-PAM) system with a ~ 4 by 6-cm footprint and weight of ~ 500 g is demonstrated. The probe consists of an image-guide fiber bundle, a pair of glass aspheric lenses, a prism, index-matching fluid and a focused ultrasound transducer. The image guide is made of 30,000 individual fibers in an 800 μm bundle. A fiber laser producing ~ 1 ns pulses with tunable energy up to 20 μJ at a wavelength of 532 nm and a tunable repetition rate up to 600 kHz was coupled into the 1m-long fiber using an objective lens focused on the fiber input and the beam was scanned across the fiber tip using a high speed mirror galvanometer. Both *in vivo* and *in vitro* images were demonstrated. The resolution study shows ~ 7 μm lateral resolution. The proposed setup maintains all the powerful properties of previous OR-PAM system. Therefore, this system will improve the usability of OR-PAM and it could have clinical significance for a number of applications.

Fifth, the potential of a multi-wavelength optical-resolution photoacoustic microscopy system for *in vivo* imaging using stimulated Raman shifting has been demonstrated. The output of a ytterbium-doped fiber laser with 1ns pulse widths and laser pulse repetition rates up to 160 kHz was coupled into varying lengths of single mode polarization maintaining fiber generating wavelengths peaks out to nearly 800 nm with pulse energies of hundreds of nJ.

We anticipate that this cost effective multi-wavelength source will open up a whole range of new possibilities for functional imaging applications.

Sixth, chromatic aberrations were advantageously used in a multi-focus (MF-OR-PAM) system using Stimulated Raman Scattering (SRS) in a polarization-maintaining single-mode fiber (PM-SMF) to scan in depth optically by tuning the wavelength. Simultaneous firing of all SRS peaks was shown to improve the depth of focus of common OR-PAM systems. This technique improves the depth of focus of OR-PAM from $\sim 100 \mu\text{m}$ to more than $\sim 400 \mu\text{m}$ and provides a uniform resolution and energy distribution for the entire field of view of 3D blood vessel networks. In contrast, for a single-wavelength Gaussian beam to achieve comparable depth of field, the focal resolution would need to be $\sim 20 \mu\text{m}$ and the lateral resolution at $440 \mu\text{m}$ away from the focus would be $\sim 30 \mu\text{m}$, a factor of ~ 4 larger than our presently proposed method. The improved depth of focus could be valuable for structural imaging of microvascular morphology without the need for mechanical scanning in the depth direction. Blood-oxygen dependent contrast could be a limitation, however is not a serious one for structural imaging of microvascular morphology. In order to use the generated multi-wavelength spectrum for functional imaging, wavelength-dependent focal zones could prove problematic, but could be obviated using achromatic collimating and objective lenses.

Seventh, the process of designing an ultra-sensitive all-optical ultrasound detector using glancing angle deposition nanostructured films with glass backing is demonstrated. Glancing Angle Deposition (GLAD)-based nanostructured thin-film filters with high reflection in the C-band range and transparent in the visible range were fabricated on either side of a $23 \mu\text{m}$ Parylene C layer to form a Fabry Perot Interferometer (FPI). The GLAD method allows low acoustic impedance FPI device fabrication for highly sensitive ultrasound detection. A tunable CW C-band laser was focused at the FPI and the reflection was measured using a high speed photodiode. High uniformity of the GLAD-FP enables OR-PAM imaging using a fixed interrogation wavelength. The GLAD-FP sensor has Q-factors better than 620 and 80 ± 20 Pa sensitivity over an 18 MHz bandwidth. Utility for laser scanning optical resolution photoacoustic microscopy is demonstrated while the interrogation laser was focused and fixed at the GLAD FPI.

Eighth, a reflection mode OR-PAM system using a GLAD-FPI for *in vivo* imaging was demonstrated. The GLAD-based FPI was designed to form high quality factor peaks in the C band range and transparent in the visible range wavelengths. The GLAD method allows low acoustic impedance FPI device fabrication for highly sensitive ultrasound detection. High uniformity of the GLAD-FPI enables OR-PAM imaging using a fixed interrogation wavelength. A 532 nm excitation beam was combined by the interrogation beam and co-scanned and co-focused. Additional optimization of the focal positioning of interrogation beam into the etalon and excitation beam below the tissue surface could result in improved imaging. We anticipate that the GLAD FPI could eventually pave the way for less expensive interrogation lasers with less stringent tuning requirements and for simultaneous recording of pressure signals at multiple different spatial locations with a single laser.

Finally, a novel non-contact optical resolution photoacoustic remote sensing (PARS) microscopy system is demonstrated. The large signal-to-noise and the fine resolution of the OR-PARS system offers performance comparable to other *in vivo* optical resolution photoacoustic microscopy systems but in a non-contact reflection mode. In this method a multi-wavelength fiber laser in the visible range has been used in multi focus form to generate photoacoustic signals and the acoustic signatures have been interrogated using a long-coherence length probe beam co-focused, co-aligned and co-scanned with the excitation spots. We anticipate that OR-PARS with its confocal lateral resolution and non-contact nature may make an impact in future pre-clinical and clinical biomedical imaging applications.

12.2. Future

In future an endoscopic probe for clinical applications can be investigated. The excitation beam can take advantage of the proposed image guide fiber bundle micro endoscopy design and the detection can be handled by the transparent GLAD FPI. Also handheld PARS can be very interesting for superficial clinical applications. The handheld probe can be designed as thin as a pen. An endoscopic PARS system using single mode fibers can also open up new applications. Integration of PARS with other optical imaging system including OCT, fluorescence based microscopy designs can be very valuable.

Bibliography

Abramovitch, R., D. Frenkiel, and M. Neeman, *Analysis of subcutaneous angiogenesis by gradient echo magnetic resonance imaging*. Magn. Reson. Med., 1998. **39**(5): p. 813-824.

Agrawal, G.P., *Introduction*, in *Nonlinear Fiber Optics*. 2006, Elsevier BV. p. 1-24.

Akhmanov, S.A., V.E. Gusev, and A.A. Karabutov, *Pulsed laser optoacoustics: Achievements and perspective*. Infrared Physics, 1989. **29**(2-4): p. 815-838.

American National Standards Institute (ANSI) calendar. J. Acoust. Soc. Am., 2000. **107**(1): p. 13.

Anastasio, M., et al., *Recent advancement in transcranial brain imaging using photoacoustic computed tomography*. J. Acoust. Soc. Am., 2014. **135**(4): p. 2208-2208.

Arevalo, J.F., et al., *Clinical applications of optical coherence tomography in the posterior pole: the 2011 José Manuel Espino Lecture – Part II*. Clinical Ophthalmology (Auckland, N.Z.), 2013. **7**: p. 2181-2206.

Ashkenazi, S., et al., *Optoacoustic imaging using thin polymer étalon*. Applied Physics Letters, 2005. **86**(13): p. 134102.

Baddeley, D., et al., *4D Super-Resolution Microscopy with Conventional Fluorophores and Single Wavelength Excitation in Optically Thick Cells and Tissues*. PLoS ONE, 2011. **6**(5): p. e20645.

Bai, X., et al., *Intravascular Optical-Resolution Photoacoustic Tomography with a 1.1 mm Diameter Catheter*. PLoS ONE, 2014. **9**(3): p. e92463.

Battagay, E.J., *Angiogenesis: mechanistic insights, neovascular diseases, and therapeutic prospects*. J Mol Med, 1995. **73**(7).

Beard, P., *Biomedical photoacoustic imaging*. Interface Focus, 2011. **1**(4): p. 602-631.

Beard, P.C. and T.N. Mills, *Extrinsic optical-fiber ultrasound sensor using a thin polymer film as a low-finesse Fabry-Perot interferometer*. Applied Optics, 1996. **35**(4): p. 663.

Beard, P.C. and T.N. Mills, *Miniature optical fibre ultrasonic hydrophone using a Fabry-Perot polymer film interferometer*. Electron. Lett., 1997. **33**(9): p. 801.

Beard, P.C., F. Perennes, and T.N. Mills, *Transduction mechanisms of the Fabry-Perot polymer film sensing concept for wideband ultrasound detection*. IEEE Transactions on Ultrasonics, Ferroelectrics and Frequency Control, 1999. **46**(6): p. 1575-1582.

Bell, A.G., *On the production and reproduction of sound by light*. American Journal of Science, 1880. **s3-20**(118): p. 305-324.

Billeh, Y.N., M. Liu, and T. Buma, *Spectroscopic photoacoustic microscopy using a photonic crystal fiber supercontinuum source*. Opt. Express, 2010. **18**(18): p. 18519.

Boas, D.A. and A.K. Dunn, *Laser speckle contrast imaging in biomedical optics*. J. Biomed. Opt., 2010. **15**(1): p. 011109.

Bogdan, M., *CT angiography in complex upper extremity reconstruction*. The Journal of Hand Surgery: Journal of the British Society for Surgery of the Hand, 2004. **29**(5): p. 465-469.

Brasch, R.C., et al., *In vivo monitoring of tumor angiogenesis with MR imaging*. Academic Radiology, 2000. **7**(10): p. 812-823.

Brauchle, E. and K. Schenke-Layland, *Raman spectroscopy in biomedicine – non-invasive in vitro analysis of cells and extracellular matrix components in tissues*. Biotechnology Journal, 2013. **8**(3): p. 288-297.

Carmeliet, P. and R.K. Jain, *Molecular mechanisms and clinical applications of angiogenesis*. Nature, 2011. **473**(7347): p. 298-307.

Carmeliet, P. and R.K. Jain, Nature, 2000. **407**(6801): p. 249-257.

Chatni, M.R., et al., *Functional photoacoustic microscopy of pH*. Journal of Biomedical Optics, 2011. **16**(10): p. 100503.

Chen, J., et al., *Blind-deconvolution optical-resolution photoacoustic microscopy in vivo*. Opt. Express, 2013. **21**(6): p. 7316.

Chen, K., et al., *Diagnosis of colorectal cancer using Raman spectroscopy of laser-trapped single living epithelial cells*. Opt. Lett., 2006. **31**(13): p. 2015.

Chen, S.-L., et al., *Miniaturized all-optical photoacoustic microscopy based on microelectromechanical systems mirror scanning*. Opt. Lett., 2012. **37**(20): p. 4263.

Chen, S.-L., et al., *Photoacoustic microscopy: a potential new tool for evaluation of angiogenesis inhibitor*. Biomed. Opt. Express, 2013. **4**(11): p. 2657.

Cheng, W.-F., et al., *Clinical application of intratumoral blood flow study in patients with endometrial carcinoma*. Cancer, 1998. **82**(10): p. 1881-1886.

Cheng, W.-F., et al., *Vascularity index as a novel parameter for the in vivo assessment of angiogenesis in patients with cervical carcinoma*. Cancer, 1999. **85**(3): p. 651-657.

Chinn, S.R., E.A. Swanson, and J.G. Fujimoto, *Optical coherence tomography using a frequency-tunable optical source*. Opt. Lett., 1997. **22**(5): p. 340.

Chitnis, P.V., H. Lloyd, and R.H. Silverman, *An adaptive interferometric sensor for all-optical photoacoustic microscopy*, in *2014 IEEE International Ultrasonics Symposium*. 2014, Institute of Electrical & Electronics Engineers (IEEE).

Cobbold, R.S.C., *Foundations of Biomedical Ultrasound*. 2006.

Corlu, A., et al., *Three-dimensional in vivo fluorescence diffuse optical tomography of breast cancer in humans*. Opt. Express, 2007. **15**(11): p. 6696.

Cox, B.T., et al., *Fabry Perot polymer film fibre-optic hydrophones and arrays for ultrasound field characterisation*. J. Phys.: Conf. Ser., 2004. **1**: p. 32-37.

Crawford, C.R., *Computed tomography scanning with simultaneous patient translation*. Medical Physics, 1990. **17**(6): p. 967.

Crowe, S.E. and G.C.R. Ellis-Davies, *Longitudinal in vivo two-photon fluorescence imaging*. The Journal of comparative neurology, 2014. **522**(8): p. 1708-1727.

Culver, J.P., et al., *Three-dimensional diffuse optical tomography in the parallel plane transmission geometry: Evaluation of a hybrid frequency domain/continuous wave clinical system for breast imaging*. Medical Physics, 2003. **30**(2): p. 235.

Custo, A., et al., *Anatomical Atlas-Guided Diffuse Optical Tomography of Brain Activation*. NeuroImage, 2010. **49**(1): p. 561-567.

Devaux, F., J.-P. Huignard, and F. Ramaz, *Modelization and optimized speckle detection scheme in photorefractive self-referenced acousto-optic imaging*. Opt. Express, 2014. **22**(9): p. 10682.

Diaspro, A., G. Chirico, and M. Collini, *Two-photon fluorescence excitation and related techniques in biological microscopy*. Quart. Rev. Biophys., 2005. **38**(02): p. 97.

Esmonde-White, K., *Raman Spectroscopy of Soft Musculoskeletal Tissues*. Applied spectroscopy, 2014. **68**(11): p. 1203-1218.

Evans, C.L. and X.S. Xie, *Coherent Anti-Stokes Raman Scattering Microscopy: Chemical Imaging for Biology and Medicine*. Annual Review of Analytical Chemistry, 2008. **1**(1): p. 883-909.

Favazza, C.P., et al., *In vivo photoacoustic microscopy of human cutaneous microvasculature and a nevus*. J. Biomed. Opt., 2011. **16**(1): p. 016015.

- Folkman, J. and Y. Shing, *Control of Angiogenesis by Heparin and Other Sulfated Polysaccharides*, in *Heparin and Related Polysaccharides*. 1992, Springer Science Business Media. p. 355-364.
- Folkman, J., *Tumor Angiogenesis*, in *Advances in Cancer Research*. 1974, Elsevier BV. p. 331-358.
- Fruhworth, G.O., et al., *Fluorescence lifetime endoscopy using TCSPC for the measurement of FRET in live cells*. *Opt. Express*, 2010. **18**(11): p. 11148.
- Fujimoto, J.G., et al., *Optical Coherence Tomography: An Emerging Technology for Biomedical Imaging and Optical Biopsy*. Neoplasia (New York, N.Y.), 2000. **2**(1-2): p. 9-25.
- Gabriele, M.L., et al., *Optical Coherence Tomography: History, Current Status, and Laboratory Work*. *Investigative Ophthalmology & Visual Science*, 2011. **52**(5): p. 2425-2436.
- Galanzha, E.I., et al., *In vivo, Noninvasive, Label-Free Detection and Eradication of Circulating Metastatic Melanoma Cells Using Two-Color Photoacoustic Flow Cytometry with a Diode Laser*. *Cancer Research*, 2009. **69**(20): p. 7926-7934.
- Galbraith, J.A. and C.G. Galbraith, *Super-resolution Microscopy for Nanosensing*. Wiley interdisciplinary reviews. Nanomedicine and nanobiotechnology, 2011. **3**(3): p. 247-255.
- Garzón, J., T. Gharbi, and J. Meneses, *Real time determination of the optical thickness and topography of tissues by chromatic confocal microscopy*. *J. Opt. A: Pure Appl. Opt.*, 2008. **10**(10): p. 104028.
- Gupta, G.P. and J. Massagué, *Cancer Metastasis: Building a Framework*. *Cell*, 2006. **127**(4): p. 679-695.
- Gutiérrez-Chico, J.L., et al., *Optical coherence tomography: from research to practice*. *European heart journal cardiovascular Imaging*, 2012. **13**(5): p. 370-384.
- Habuchi, S., *Super-Resolution Molecular and Functional Imaging of Nanoscale Architectures in Life and Materials Science*. *Frontiers in Bioengineering and Biotechnology*, 2014. **2**: p. 20.
- Hai, P., et al., *Near-infrared optical-resolution photoacoustic microscopy*. *Opt. Lett.*, 2014. **39**(17): p. 5192.
- Hajireza, P., A. Forbrich, and R. Zemp, *In-Vivo functional optical-resolution photoacoustic microscopy with stimulated Raman scattering fiber-laser source*. *Biomedical Optics Express*, 2014. **5**(2): p. 539-546.

Hajireza, P., A. Forbrich, and R.J. Zemp, *Multifocus optical-resolution photoacoustic microscopy using stimulated Raman scattering and chromatic aberration*. Opt Lett, 2013. **38**(15): p. 2711-3.

Hajireza, P., et al., *Optical-resolution photoacoustic micro-endoscopy using image-guide fibers and fiber laser technology*, in *Photons Plus Ultrasound: Imaging and Sensing 2011*. 2011, SPIE-Intl Soc Optical Eng.

Hajireza, P., et al., *Glancing angle deposited nanostructured film Fabry-Perot etalons for optical detection of ultrasound*. Opt Express, 2013. **21**(5): p. 6391-400.

Hajireza, P., et al., *In vivo imaging with GRIN-lens optical resolution photoacoustic micro-endoscopy*, in *Photons Plus Ultrasound: Imaging and Sensing 2012*. 2012, SPIE-Intl Soc Optical Eng.

Hajireza, P., et al., *In vivo multi-wavelength optical-resolution photoacoustic microscopy with stimulated Raman scattering fiber-laser source*, in *Photons Plus Ultrasound: Imaging and Sensing 2013*. 2013, SPIE-Intl Soc Optical Eng.

Hajireza, P., et al., *In vivo optical resolution photoacoustic microscopy using glancing angle-deposited nanostructured Fabry-Perot etalons*. Opt Lett, 2015. **40**(7): p. 1350-3.

Hajireza, P., et al., *In vivo optical resolution photoacoustic microscopy using glancing angle-deposited nanostructured Fabry-Perot etalons*. Opt. Lett., 2015. **40**(7): p. 1350.

Hajireza, P., W. Shi, and R. Zemp, *Label-free in vivo GRIN-lens optical resolution photoacoustic micro-endoscopy*. Laser Phys. Lett., 2013. **10**(5): p. 055603.

Hajireza, P., W. Shi, and R.J. Zemp, *Label-free in vivo fiber-based optical-resolution photoacoustic microscopy*. Opt Lett, 2011. **36**(20): p. 4107-9.

Hajireza, P., W. Shi, and R.J. Zemp, *Real-time handheld optical-resolution photoacoustic microscopy*. Opt Express, 2011. **19**(21): p. 20097-102.

Harris, A.L., *Antiangiogenesis for cancer therapy*. The Lancet, 1997. **349**: p. S13-S15.

Harrison, T. and R.J. Zemp, *Coregistered photoacoustic-ultrasound imaging applied to brachytherapy*. J. Biomed. Opt., 2011. **16**(8): p. 080502.

Harrison, T. and R.J. Zemp, *The applicability of ultrasound dynamic receive beamformers to photoacoustic imaging*. IEEE Transactions on Ultrasonics, Ferroelectrics and Frequency Control, 2011. **58**(10): p. 2259-2263.

Harrison, T., et al., *Optical-resolution photoacoustic micro-endoscopy with ultrasound array system detection*, in *Photons Plus Ultrasound: Imaging and Sensing 2013*. 2013, SPIE-Intl Soc Optical Eng.

- Hawkeye, M.M. and M.J. Brett, *Glancing angle deposition: Fabrication, properties, and applications of micro- and nanostructured thin films*. Journal of Vacuum Science & Technology A: Vacuum, Surfaces, and Films, 2007. **25**(5): p. 1317.
- Hawkeye, M.M. and M.J. Brett, *Narrow bandpass optical filters fabricated with one-dimensionally periodic inhomogeneous thin films*. J. Appl. Phys., 2006. **100**(4): p. 044322.
- Hawkeye, M.M., K.M. Krause, and M.J. Brett, *Ambient humidity monitoring using a 1D photonic crystal sensor fabricated with glancing angle deposition*, in *Optical Sensors 2009*. 2009, SPIE-Intl Soc Optical Eng.
- Hawkeye, M.M., M.T. Taschuk, and M.J. Brett, *Glancing Angle Deposition of Thin Films*. 2014, Wiley-Blackwell.
- Helmchen, F. and W. Denk, *Deep tissue two-photon microscopy*. Nat Meth, 2005. **2**(12): p. 932-940.
- Hou, R., et al., *Recent advances in optical coherence tomography for the diagnoses of lung disorders*. Expert Review of Respiratory Medicine, 2011. **5**(5): p. 711-724.
- Hsieh, B.-Y., et al., *All-optical scanhead for ultrasound and photoacoustic dual-modality imaging*. Opt. Express, 2012. **20**(2): p. 1588.
- Hu, S. and L.V. Wang, *Photoacoustic imaging and characterization of the microvasculature*. J. Biomed. Opt., 2010. **15**(1): p. 011101.
- Hu, S. and Lihong V. Wang, *Optical-Resolution Photoacoustic Microscopy: Auscultation of Biological Systems at the Cellular Level*. Biophysical Journal, 2013. **105**(4): p. 841-847.
- Hu, S., et al., *Functional transcranial brain imaging by optical-resolution photoacoustic microscopy*. J. Biomed. Opt., 2009. **14**(4): p. 040503.
- Hu, S., et al., *Intravital imaging of amyloid plaques in a transgenic mouse model using optical-resolution photoacoustic microscopy*. Opt. Lett., 2009. **34**(24): p. 3899.
- Hu, S., et al., *Label-free photoacoustic ophthalmic angiography*. Opt. Lett., 2009. **35**(1): p. 1.
- Hu, S., K. Maslov, and L.V. Wang, *In vivo functional chronic imaging of a small animal model using optical-resolution photoacoustic microscopy*. Medical Physics, 2009. **36**(6): p. 2320.
- Hu, S., K. Maslov, and L.V. Wang, *Noninvasive label-free imaging of microhemodynamics by optical-resolution photoacoustic microscopy*. Opt. Express, 2009. **17**(9): p. 7688.

- Hu, S., K. Maslov, and L.V. Wang, *Second-generation optical-resolution photoacoustic microscopy with improved sensitivity and speed*. Opt. Lett., 2011. **36**(7): p. 1134.
- Hu, S., K. Maslov, and L.V. Wang, *Three-dimensional Optical-resolution Photoacoustic Microscopy*. Journal of Visualized Experiments, 2011(51).
- Hu, S., *Neurovascular photoacoustic tomography*. Frontiers in Neuroenergetics, 2010.
- Huang, B., M. Bates, and X. Zhuang, *Super resolution fluorescence microscopy*. Annual review of biochemistry, 2009. **78**: p. 993-1016.
- Huang, D., et al., *Optical coherence tomography*. Science, 1991. **254**(5035): p. 1178-1181.
- Huang, S.-W., et al., *Toward fiber-based high-frequency 3D ultrasound imaging*, in *Photons Plus Ultrasound: Imaging and Sensing 2007: The Eighth Conference on Biomedical Thermoacoustics, Optoacoustics, and Acousto-optics*. 2007, SPIE-Intl Soc Optical Eng.
- Humeau-Heurtier, A., G. Mahé, and P. Abraham, *Microvascular blood flow monitoring with laser speckle contrast imaging using the generalized differences algorithm*. Microvascular Research, 2015. **98**: p. 54-61.
- Hur, C., *High-resolution microendoscopy for esophageal cancer screening in China: A cost-effectiveness analysis*. WJG, 2015. **21**(18): p. 5513.
- Jathoul, A.P., et al., *Deep in vivo photoacoustic imaging of mammalian tissues using a tyrosinase-based genetic reporter*. Nature Photonics, 2015.
- Jehlička, J., H.G.M. Edwards, and A. Oren, *Raman Spectroscopy of Microbial Pigments*. Applied and Environmental Microbiology, 2014. **80**(11): p. 3286-3295.
- Jim, S.R., et al., *Engineered Anisotropic Microstructures for Ultrathin-Layer Chromatography*. Anal. Chem., 2010. **82**(12): p. 5349-5356.
- John, S., *Strong localization of photons in certain disordered dielectric superlattices*. Phys. Rev. Lett., 1987. **58**(23): p. 2486-2489.
- Jun, X. and L.V. Wang, *Small-Animal Whole-Body Photoacoustic Tomography: A Review*. IEEE Transactions on Biomedical Engineering, 2014. **61**(5): p. 1380-1389.
- Jung, J.C., *In vivo Mammalian Brain Imaging Using One- and Two-Photon Fluorescence Microendoscopy*. Journal of Neurophysiology, 2004. **92**(5): p. 3121-3133.
- Jung, W., et al., *Miniaturized probe based on a microelectromechanical system mirror for multiphoton microscopy*. Opt. Lett., 2008. **33**(12): p. 1324.

- Kennedy, S.R. and M.J. Brett, *Porous Broadband Antireflection Coating by Glancing Angle Deposition*. Applied Optics, 2003. **42**(22): p. 4573.
- Kiessling, F., et al., *Comparing Dynamic Parameters of Tumor Vascularization in Nude Mice Revealed by Magnetic Resonance Imaging and Contrast-Enhanced Intermittent Power Doppler Sonography*. Investigative Radiology, 2003. **38**(8): p. 516-524.
- Kim, C., et al., *In vivo Molecular Photoacoustic Tomography of Melanomas Targeted by Bioconjugated Gold Nanocages*. ACS Nano, 2010. **4**(8): p. 4559-4564.
- Kim, J.Y., et al., *Fast optical-resolution photoacoustic microscopy using a 2-axis water-proofing MEMS scanner*. Scientific Reports, 2015. **5**: p. 7932.
- Koeplinger, D., M. Liu, and T. Buma, *Photoacoustic microscopy with a pulsed multi-color source based on stimulated Raman scattering*, in *2011 IEEE International Ultrasonics Symposium*. 2011, Institute of Electrical & Electronics Engineers (IEEE).
- Krumholz, A., et al., *Functional photoacoustic microscopy of diabetic vasculature*. Journal of Biomedical Optics, 2012. **17**(6): p. 060502.
- Ku, G., et al., *Imaging of tumor angiogenesis in rat brains in vivo by photoacoustic tomography*. Applied Optics, 2005. **44**(5): p. 770.
- Ku, G., et al., *Multiple-bandwidth photoacoustic tomography*. Physics in Medicine and Biology, 2004. **49**(7): p. 1329-1338.
- Lakhtakia, A. and R. Messier, *Sculptured Thin Films: Nanoengineered Morphology and Optics*. 2005: SPIE-Intl Soc Optical Eng.
- Lassau, N., et al., *New Hemodynamic Approach to Angiogenesis*. Investigative Radiology, 1999. **34**(3): p. 194-198.
- Laufer, J., et al., *In vivo photoacoustic imaging of mouse embryos*. J. Biomed. Opt., 2012. **17**(6): p. 061220.
- Laufer, J., et al., *In vivo preclinical photoacoustic imaging of tumor vasculature development and therapy*. J. Biomed. Opt., 2012. **17**(5): p. 056016.
- Li, G., K.I. Maslov, and L.V. Wang, *Reflection-mode multifocal optical-resolution photoacoustic microscopy*. J. Biomed. Opt., 2013. **18**(3): p. 030501.
- Li, H., et al., *A transparent broadband ultrasonic detector based on an optical micro-ring resonator for photoacoustic microscopy*. Scientific Reports, 2014. **4**.
- Li, L., et al., *Fully motorized optical-resolution photoacoustic microscopy*. Opt. Lett., 2014. **39**(7): p. 2117.

- Li, W.W., *Tumor angiogenesis: Molecular pathology, therapeutic targeting, and imaging*. Academic Radiology, 2000. **7**(10): p. 800-811.
- Li, Z., et al., *Raman Spectroscopy for In-Line Water Quality Monitoring — Instrumentation and Potential*. Sensors (Basel, Switzerland), 2014. **14**(9): p. 17275-17303.
- Liang, J., et al., *Cross-correlation-based transverse flow measurements using optical resolution photoacoustic microscopy with a digital micromirror device*. J. Biomed. Opt, 2013. **18**(9): p. 096004.
- Liang, J., et al., *Random-access optical-resolution photoacoustic microscopy using a digital micromirror device*. Opt. Lett., 2013. **38**(15): p. 2683.
- Liao, L.-D., et al., *Transcranial imaging of functional cerebral hemodynamic changes in single blood vessels using in vivo photoacoustic microscopy*. Journal of Cerebral Blood Flow & Metabolism, 2012. **32**(6): p. 938-951.
- Lin, R., et al., *Longitudinal label-free optical-resolution photoacoustic microscopy of tumor angiogenesis in vivo*. Quantitative Imaging in Medicine and Surgery, 2015. **5**(1): p. 23-29.
- Lin, Y.-H. and D.P. Tsai, *Near-field scanning optical microscopy using a super-resolution cover glass slip*. Opt. Express, 2012. **20**(15): p. 16205.
- Littleton, B., et al., *Coherent super-resolution microscopy via laterally structured illumination*. Micron, 2007. **38**(2): p. 150-157.
- Liu, M., et al., *Dual modality optical coherence and whole-body photoacoustic tomography imaging of chick embryos in multiple development stages*. Biomedical Optics Express, 2014. **5**(9): p. 3150-3159.
- Liu, W., et al., *In vivo corneal neovascularization imaging by optical-resolution photoacoustic microscopy*. Photoacoustics, 2014. **2**(2): p. 81-86.
- Liu, Y., C. Zhang, and L.V. Wang, *Effects of light scattering on optical-resolution photoacoustic microscopy*. J. Biomed. Opt, 2012. **17**(12): p. 126014.
- Loya, A.K., J.P. Dumas, and T. Buma, *Photoacoustic microscopy with a tunable source based on cascaded stimulated Raman scattering in a large-mode area photonic crystal fiber*, in *2012 IEEE International Ultrasonics Symposium*. 2012, Institute of Electrical & Electronics Engineers (IEEE).
- Lu, C.D., et al., *Handheld ultrahigh speed swept source optical coherence tomography instrument using a MEMS scanning mirror*. Biomed. Opt. Express, 2013. **5**(1): p. 293.
- Macleod, H.A., *Thin-Film Optical Filters*. 1986: Informa UK Limited.

- Mallidi, S., G.P. Luke, and S. Emelianov, *Photoacoustic imaging in cancer detection, diagnosis, and treatment guidance*. Trends in Biotechnology, 2011. **29**(5): p. 213-221.
- Manniesing, R. and W. Niessen, *Multiscale Vessel Enhancing Diffusion in CT Angiography Noise Filtering*, in *Information Processing in Medical Imaging*. 2005, Springer Science + Business Media. p. 138-149.
- Maslov, K., et al., *Optical-resolution photoacoustic microscopy for in vivo imaging of single capillaries*. Opt. Lett., 2008. **33**(9): p. 929.
- Maslov, K., G. Stoica, and L.V. Wang, *In vivo dark-field reflection-mode photoacoustic microscopy*. Opt. Lett., 2005. **30**(6): p. 625.
- Maslov, K., S. Hu, and L.V. Wang, *Second generation optical-resolution photoacoustic microscopy*, in *Photons Plus Ultrasound: Imaging and Sensing 2011*. 2011, SPIE-Intl Soc Optical Eng.
- Matthews, T.P., et al., *Label-free photoacoustic microscopy of peripheral nerves*. J. Biomed. Opt, 2014. **19**(1): p. 016004.
- Messier, R., V.C. Venugopal, and P.D. Sunal, *Origin and evolution of sculptured thin films*. Journal of Vacuum Science & Technology A: Vacuum, Surfaces, and Films, 2000. **18**(4): p. 1538.
- Miller, J.C., et al., *Imaging Angiogenesis: Applications and Potential for Drug Development*. JNCI Journal of the National Cancer Institute, 2005. **97**(3): p. 172-187.
- Muldoon, T.J., et al., *Evaluation of quantitative image analysis criteria for the high-resolution microendoscopic detection of neoplasia in Barrett's esophagus*. J. Biomed. Opt., 2010. **15**(2): p. 026027.
- Nioka, S. and Y. Chen, *Optical Tecnology Developments in Biomedicine: History, Current and Future*. Translational Medicine @ UniSa, 2011. **1**: p. 51-150.
- Nishida, N., et al., *Angiogenesis in cancer*. Vascular Health and Risk Management, 2006. **2**(3): p. 213-219.
- Niu, G. and X. Chen, *PET Imaging of Angiogenesis*. PET Clinics, 2009. **4**(1): p. 17-38.
- Ntziachristos, V., et al., *Concurrent MRI and diffuse optical tomography of breast after indocyanine green enhancement*. Proceedings of the National Academy of Sciences, 2000. **97**(6): p. 2767-2772.
- Nuster, R., et al., *Downstream Fabry-Perot interferometer for acoustic wave monitoring in photoacoustic tomography*. Optics Letters, 2011. **36**(6): p. 981-983.

Oladipupo, S., et al., *VEGF is essential for hypoxia-inducible factor-mediated neovascularization but dispensable for endothelial sprouting*. Proceedings of the National Academy of Sciences, 2011. **108**(32): p. 13264-13269.

Oladipupo, S.S., et al., *Conditional HIF-1 induction produces multistage neovascularization with stage-specific sensitivity to VEGFR inhibitors and myeloid cell independence*. Blood, 2011. **117**(15): p. 4142-4153.

Olsovsky, C., et al., *Chromatic confocal microscopy for multi-depth imaging of epithelial tissue*. Biomed. Opt. Express, 2013. **4**(5): p. 732.

Pabst, A.M., et al., *Imaging angiogenesis: Perspectives and opportunities in tumour research – A method display*. Journal of Cranio-Maxillofacial Surgery, 2014. **42**(6): p. 915-923.

Pan, D., et al., *A Brief Account of Nanoparticle Contrast Agents for Photoacoustic Imaging*. Wiley interdisciplinary reviews. Nanomedicine and nanobiotechnology, 2013. **5**(6): p. 517-543.

Pan, D., et al., *Photoacoustic Sentinel Lymph Node Imaging with Self-Assembled Copper Neodecanoate Nanoparticles*. ACS Nano, 2012. **6**(2): p. 1260-1267.

Paproski, R.J., et al., *Multi-wavelength photoacoustic imaging of inducible tyrosinase reporter gene expression in xenograft tumors*. Scientific Reports, 2014. **4**.

Pérennès, F., P.C. Beard, and T.N. Mills, *Analysis of a Low-Finesse Fabry-Perot Sensing Interferometer Illuminated by a Multimode Optical Fiber*. Applied Optics, 1999. **38**(34): p. 7026.

Photoacoustic Imaging and Spectroscopy, in *Optical Science and Engineering*. 2009, CRC Press.

Pillai, R.S., D. Lorenser, and D.D. Sampson, *Deep-tissue access with confocal fluorescence microendoscopy through hypodermic needles*. Opt. Express, 2011. **19**(8): p. 7213.

Plate, K.H., et al., *Vascular endothelial growth factor and glioma angiogenesis: Coordinate induction of VEGF receptors, distribution of VEGF protein and possible *In vivo* regulatory mechanisms*. International Journal of Cancer, 1994. **59**(4): p. 520-529.

Provenzale, J.M., *Imaging of Angiogenesis: Clinical Techniques and Novel Imaging Methods*. American Journal of Roentgenology, 2007. **188**(1): p. 11-23.

Rak, J., J. Filmus, and R.S. Kerbel, *Reciprocal paracrine interactions between tumour cells and endothelial cells: the 'angiogenesis progression' hypothesis*. European Journal of Cancer, 1996. **32**(14): p. 2438-2450.

Ranasinghesagara, J.C., et al., *Photoacoustic technique for assessing optical scattering properties of turbid media*. J. Biomed. Opt., 2009. **14**(4): p. 040504.

Rao, B., et al., *Hybrid-scanning optical-resolution photoacoustic microscopy for in vivo vasculature imaging*. Opt. Lett., 2010. **35**(10): p. 1521.

Rao, B., et al., *Integrated photoacoustic, confocal, and two-photon microscope*. Journal of Biomedical Optics, 2014. **19**(3): p. 036002.

Rao, B., et al., *Real-time four-dimensional optical-resolution photoacoustic microscopy with Au nanoparticle-assisted subdiffraction-limit resolution*. Opt. Lett., 2011. **36**(7): p. 1137.

Rao, K.N., *Influence of deposition parameters on optical properties of TiO₂ films*. Optical Engineering, 2002. **41**(9): p. 2357.

Rebol, J., et al., *3D Power Doppler Analysis of the Vascularisation in Tumours of the Oral Cavity*. Ultraschall Med, 2007. **28**(1): p. 40-44.

Rebol, J., *The Vascularisation of Oral Cavity Tumours and Tumour Shell Tissue Determined by Three-Dimensional Power Doppler Sonography*. Ultrasound in Medicine & Biology, 2007. **33**(4): p. 493-499.

Robbie, K., *Sculptured thin films and glancing angle deposition: Growth mechanics and applications*. Journal of Vacuum Science & Technology A: Vacuum, Surfaces, and Films, 1997. **15**(3): p. 1460.

Rohren, E.M., T.G. Turkington, and R.E. Coleman, *Clinical Applications of PET in Oncology I*. Radiology, 2004. **231**(2): p. 305-332.

Rowland, K.J., et al., *Immediate Alterations in Intestinal Oxygen Saturation and Blood Flow Following Massive Small Bowel Resection As Measured By Photoacoustic Microscopy*. Journal of Pediatric Surgery, 2012. **47**(6): p. 1143-1149.

Rubin, G.D., et al., *Aorta and Iliac Arteries: Single versus Multiple Detector-Row Helical CT Angiography I*. Radiology, 2000. **215**(3): p. 670-676.

Rubin, G.D., et al., *CT Angiography after 20 Years: A Transformation in Cardiovascular Disease Characterization Continues to Advance*. Radiology, 2014. **271**(3): p. 633-652.

Rubin, G.D., et al., *Multi-Detector Row CT Angiography of Lower Extremity Arterial Inflow and Runoff: Initial Experience I*. Radiology, 2001. **221**(1): p. 146-158.

Schlingemann, R.O., et al., *Expression of the high molecular weight melanoma-associated antigen by pericytes during angiogenesis in tumors and in healing wounds*. Ultramicroscopy, 1989. **31**(4): p. 481.

Shao, P., et al., *Integrated micro-endoscopy system for simultaneous fluorescence and optical-resolution photoacoustic imaging*. J Biomed Opt, 2012. **17**(7): p. 076024.

Shao, P., et al., *Mosaicing for fast wide-field-of-view optical-resolution photoacoustic microscopy*, in *Photons Plus Ultrasound: Imaging and Sensing 2012*. 2012, SPIE-Intl Soc Optical Eng.

Shi, W., et al., *Real-time optical-resolution photoacoustic microscopy using fiber-laser technology*, in *Photons Plus Ultrasound: Imaging and Sensing 2011*. 2011, SPIE-Intl Soc Optical Eng.

Shi, W., et al., *In vivo dynamic process imaging using real-time optical-resolution photoacoustic microscopy*. J Biomed Opt, 2013. **18**(2): p. 26001.

Shi, W., et al., *In vivo near-realtime volumetric optical-resolution photoacoustic microscopy using a high-repetition-rate nanosecond fiber-laser*. Opt Express, 2011. **19**(18): p. 17143-50.

Shi, W., et al., *Optical resolution photoacoustic microscopy using novel high-repetition-rate passively Q-switched microchip and fiber lasers*. J. Biomed. Opt., 2010. **15**(5): p. 056017.

Shweiki, D., et al., *Vascular endothelial growth factor induced by hypoxia may mediate hypoxia-initiated angiogenesis*. Nature, 1992. **359**(6398): p. 843-845.

Singh, H., et al., *Mapping cortical haemodynamics during neonatal seizures using diffuse optical tomography: A case study*. NeuroImage : Clinical, 2014. **5**: p. 256-265.

Sit, J.C., D.J. Broer, and M.J. Brett, *Liquid Crystal Alignment and Switching in Porous Chiral Thin Films*. Adv. Mater., 2000. **12**(5): p. 371-373.

Sokolov, K., et al., *Endoscopic Microscopy*. Disease Markers, 2002. **18**(5-6): p. 269-291.

Song, L., K. Maslov, and L.V. Wang, *Multifocal optical-resolution photoacoustic microscopy in vivo*. Opt. Lett., 2011. **36**(7): p. 1236.

Spring, B.Q., et al., *Intravital fiber-optic fluorescence imaging for monitoring ovarian carcinoma progression and treatment response*, in *Photodynamic Therapy: Back to the Future*. 2009, SPIE-Intl Soc Optical Eng.

Su, J.L., et al., *Advances in Clinical and Biomedical Applications of Photoacoustic Imaging*. Expert opinion on medical diagnostics, 2010. **4**(6): p. 497-510.

Sur, U.K., *Surface-enhanced Raman spectroscopy*. Resonance, 2010. **15**(2): p. 154-164.

Svoboda, K. and R. Yasuda, *Principles of Two-Photon Excitation Microscopy and Its Applications to Neuroscience*. Neuron, 2006. **50**(6): p. 823-839.

Tang, M., et al., *Noninvasive photoacoustic microscopy of methemoglobin in vivo*. J. Biomed. Opt., 2015. **20**(3): p. 036007.

Tang, S., et al., *Design and implementation of fiber-based multiphoton endoscopy with microelectromechanical systems scanning*. J. Biomed. Opt., 2009. **14**(3): p. 034005.

van Popta, A.C., J.C. Sit, and M.J. Brett, *Optical properties of porous helical thin films and the effects of post-deposition annealing*, in *Organic Optoelectronics and Photonics*. 2004, SPIE-Intl Soc Optical Eng.

Verheul, H.M.W., E.E. Voest, and R.O. Schlingemann, *Are tumours angiogenesis-dependent?* The Journal of Pathology, 2003. **202**(1): p. 5-13.

Viator, J.A., et al., *A Comparative Study of Photoacoustic and Reflectance Methods for Determination of Epidermal Melanin Content*. J Invest Dermatol, 2004. **122**(6): p. 1432-1439.

Wang, H., et al., *Reflection-mode optical-resolution photoacoustic microscopy based on a reflective objective*. Opt. Express, 2013. **21**(20): p. 24210.

Wang, L., et al., *Fast voice-coil scanning optical-resolution photoacoustic microscopy*. Opt. Lett., 2011. **36**(2): p. 139.

Wang, L., et al., *Video-rate functional photoacoustic microscopy at depths*. J. Biomed. Opt, 2012. **17**(10): p. 1060071.

Wang, L., *Photoacoustic tomography*. Scholarpedia, 2014. **9**(2): p. 10278.

Wang, L.V. and H.-I. Wu, *Biomedical Optics*. 2009, Wiley-Blackwell.

Wang, L.V. and L. Gao, *Photoacoustic Microscopy and Computed Tomography: From Bench to Bedside*. Annu. Rev. Biomed. Eng., 2014. **16**(1): p. 155-185.

Wang, L.V. and S. Hu, *Photoacoustic Tomography: In vivo Imaging from Organelles to Organs*. Science, 2012. **335**(6075): p. 1458-1462.

Wang, L.V., *Photoacoustic Imaging and Spectroscopy*, in *Optical Science and Engineering*. 2009, CRC Press.

Wang, R.K., et al., *Depth-resolved imaging of capillary networks in retina and choroid using ultrahigh sensitive optical microangiography*. Opt. Lett., 2010. **35**(9): p. 1467.

Wang, X., et al., *Noninvasive laser-induced photoacoustic tomography for structural and functional in vivo imaging of the brain*. Nature Biotechnology, 2003. **21**(7): p. 803-806.

- Wang, Y. and J. Irudayaraj, *Surface-enhanced Raman spectroscopy at single-molecule scale and its implications in biology*. Philosophical Transactions of the Royal Society B: Biological Sciences, 2013. **368**(1611): p. 20120026.
- Wang, Y., et al., *Fiber-laser-based photoacoustic microscopy and melanoma cell detection*. J. Biomed. Opt., 2011. **16**(1): p. 011014.
- Wei, C.-W., *Trapping and dynamic manipulation of polystyrene beads mimicking circulating tumor cells using targeted magnetic/photoacoustic contrast agents*. J. Biomed. Opt, 2012. **17**(10): p. 101517.
- Weidner, N., et al., *Tumor Angiogenesis: A New Significant and Independent Prognostic Indicator in Early-Stage Breast Carcinoma*. JNCI Journal of the National Cancer Institute, 1992. **84**(24): p. 1875-1887.
- Weight, R.M., P.S. Dale, and J.A. Viator, *Detection of circulating melanoma cells in human blood using photoacoustic flowmetry*, in *2009 Annual International Conference of the IEEE Engineering in Medicine and Biology Society*. 2009, Institute of Electrical & Electronics Engineers (IEEE).
- Weymouth, A., *Optical Coherence Tomography of Ocular Diseases 3rd Edition by Schuman JS, Puliafito CA, Fujimoto JG and Duker JS Thorofare, New Jersey, USA: Slack Inc, 2013 615 pages RRP \$358.84*. Clinical and Experimental Optometry, 2014. **97**(2): p. 192-192.
- Wu, D., et al., *Contrast Agents for Photoacoustic and Thermoacoustic Imaging: A Review*. International Journal of Molecular Sciences, 2014. **15**(12): p. 23616-23639.
- Wu, J., et al., *Paired-angle-rotation scanning optical coherence tomography forward-imaging probe*. Opt. Lett., 2006. **31**(9): p. 1265.
- Xi, J.Q., et al., *Optical thin-film materials with low refractive index for broadband elimination of Fresnel reflection*. Nat Photon, 2007. **1**(3): p. 176-179.
- Xia, J., et al., *Retrospective respiration-gated whole-body photoacoustic computed tomography of mice*. J. Biomed. Opt, 2014. **19**(1): p. 016003.
- Xia, J., et al., *Wide-field two-dimensional multifocal optical-resolution photoacoustic computed microscopy*. Optics letters, 2013. **38**(24): p. 5236-5239.
- Xia, J., et al., *Wide-field two-dimensional multifocal optical-resolution photoacoustic-computed microscopy*. Opt. Lett., 2013. **38**(24): p. 5236.
- Xiang, L., et al., *4-D Photoacoustic Tomography*. Scientific Reports, 2013. **3**.
- Xie, Z., et al., *Evaluation of bladder microvasculature with high-resolution photoacoustic imaging*. Opt. Lett., 2011. **36**(24): p. 4815.

- Xie, Z., et al., *Laser-scanning optical-resolution photoacoustic microscopy*. Opt. Lett., 2009. **34**(12): p. 1771.
- Xie, Z., et al., *Pure optical photoacoustic microscopy*. Opt. Express, 2011. **19**(10): p. 9027.
- Xing, W., et al., *Integrated optical- and acoustic-resolution photoacoustic microscopy based on an optical fiber bundle*. Opt. Lett., 2012. **38**(1): p. 52.
- Xing, W., et al., *Integrated optical- and acoustic-resolution photoacoustic microscopy based on an optical fiber bundle*. Optics letters, 2013. **38**(1): p. 52-54.
- Xu, M. and L.V. Wang, *Photoacoustic imaging in biomedicine*. Rev. Sci. Instrum., 2006. **77**(4): p. 041101.
- Xu, X., et al., *Spectral hole burning for ultrasound-modulated optical tomography of thick tissue*. J. Biomed. Opt., 2010. **15**(6): p. 066018.
- Xu, X., H. Liu, and L.V. Wang, *Time-reversed ultrasonically encoded optical focusing into scattering media*. Nature Photonics, 2011. **5**(3): p. 154-157.
- Yang, H.-Y., et al., *Glancing angle deposited titania films for dye-sensitized solar cells*. Thin Solid Films, 2009. **518**(5): p. 1590-1594.
- Yang, J.-M., et al., *Optical-resolution photoacoustic endomicroscopy in vivo*. Biomed. Opt. Express, 2015. **6**(3): p. 918.
- Yang, J.-M., et al., *Photoacoustic endoscopy*. Opt. Lett., 2009. **34**(10): p. 1591.
- Yang, J.-M., et al., *Toward dual-wavelength functional photoacoustic endoscopy: laser and peripheral optical systems development*, in *Photons Plus Ultrasound: Imaging and Sensing 2012*. 2012, SPIE-Intl Soc Optical Eng.
- Yang, Z., et al., *Multi-parametric quantitative microvascular imaging with optical-resolution photoacoustic microscopy in vivo*. Opt. Express, 2014. **22**(2): p. 1500.
- Yao, J. and L.V. Wang, *Breakthroughs in Photonics 2013: Photoacoustic Tomography in Biomedicine*. IEEE Photonics J., 2014. **6**(2): p. 1-6.
- Yao, J. and L.V. Wang, *Photoacoustic tomography: fundamentals, advances and prospects*. Contrast Media & Molecular Imaging, 2011. **6**(5): p. 332-345.
- Yao, J. and L.V. Wang, *Sensitivity of photoacoustic microscopy*. Photoacoustics, 2014. **2**(2): p. 87-101.
- Yao, J., et al., *Double-illumination photoacoustic microscopy*. Opt. Lett., 2012. **37**(4): p. 659.

- Yao, J., et al., *High-speed label-free functional photoacoustic microscopy of mouse brain in action*. Nat Meth, 2015. **12**(5): p. 407-410.
- Yao, J., et al., *In vivo photoacoustic imaging of transverse blood flow by using Doppler broadening of bandwidth*. Opt. Lett., 2010. **35**(9): p. 1419.
- Yao, J., et al., *Label-free oxygen-metabolic photoacoustic microscopy in vivo*. Journal of Biomedical Optics, 2011. **16**(7): p. 076003.
- Yao, J., et al., *Photoimprint Photoacoustic Microscopy for Three-Dimensional Label-Free Subdiffraction Imaging*. Phys. Rev. Lett., 2014. **112**(1).
- Yao, L., L. Xi, and H. Jiang, *Photoacoustic computed microscopy*. Scientific Reports, 2014. **4**.
- Zackrisson, S., S. van de Ven, and S.S. Gambhir, *Light In and Sound Out: Emerging Translational Strategies for Photoacoustic Imaging*. Cancer research, 2014. **74**(4): p. 979-1004.
- Zemp, R., *Quantitative Multiple-Source Photoacoustic Tomography*, in *Biomedical Optics and 3-D Imaging*. 2010, Optical Society of America (OSA).
- Zemp, R.J., et al., *Realtime photoacoustic microscopy in vivo with a 30-MHz ultrasound array transducer*. Opt. Express, 2008. **16**(11): p. 7915.
- Zeng, L., et al., *Portable optical-resolution photoacoustic microscopy with a pulsed laser diode excitation*. Applied Physics Letters, 2013. **102**(5): p. 053704.
- Zhang, C., K. Maslov, and L.V. Wang, *Subwavelength-resolution label-free photoacoustic microscopy of optical absorption in vivo*. Optics letters, 2010. **35**(19): p. 3195-3197.
- Zhang, E., J. Laufer, and P. Beard, *Backward-mode multiwavelength photoacoustic scanner using a planar Fabry-Perot polymer film ultrasound sensor for high-resolution three-dimensional imaging of biological tissues*. Applied Optics, 2008. **47**(4): p. 561.
- Zhang, E.Z. and P.C. Beard, *A miniature all-optical photoacoustic imaging probe*, in *Photons Plus Ultrasound: Imaging and Sensing 2011*. 2011, SPIE-Intl Soc Optical Eng.
- Zhang, E.Z., et al., *3D photoacoustic imaging system for in vivo studies of small animal models*, in *Photons Plus Ultrasound: Imaging and Sensing 2008: The Ninth Conference on Biomedical Thermoacoustics, Optoacoustics, and Acousto-optics*. 2008, SPIE-Intl Soc Optical Eng.
- Zhang, E.Z., et al., *Multimodal simultaneous photoacoustic tomography, optical resolution microscopy, and OCT system*, in *Photons Plus Ultrasound: Imaging and Sensing 2010*. 2010, SPIE-Intl Soc Optical Eng.

Zhang, E.Z., et al., *In vivo high-resolution 3D photoacoustic imaging of superficial vascular anatomy*. *Physics in Medicine and Biology*, 2009. **54**(4): p. 1035-1046.

Zhang, E.Z., et al., *Multimodal photoacoustic and optical coherence tomography scanner using an all optical detection scheme for 3D morphological skin imaging*. *Biomed. Opt. Express*, 2011. **2**(8): p. 2202.

Zhang, H. and S. Jiao, *Naturally Combined Photoacoustic Microscopy and Optical Coherence Tomography for Simultaneous Multimodal*, in *Biomedical Optics and 3-D Imaging*. 2010, Optical Society of America (OSA).

Zhang, H.F., C.A. Puliafito, and S. Jiao, *Photoacoustic Ophthalmoscopy for In vivo Retinal Imaging: Current Status and Prospects*. *Ophthalmic Surgery, Lasers, and Imaging*, 2011. **42**(4): p. S106-S115.

Zhang, H.F., et al., *Functional photoacoustic microscopy for high-resolution and noninvasive in vivo imaging*. *Nat Biotechnol*, 2006. **24**(7): p. 848-851.

Zhang, H.F., K. Maslov, and L.V. Wang, *In vivo imaging of subcutaneous structures using functional photoacoustic microscopy*. *Nature Protocols*, 2007. **2**(4): p. 797-804.

Zhang, Y., H. Hong, and W. Cai, *Imaging with Raman Spectroscopy*. *Current pharmaceutical biotechnology*, 2010. **11**(6): p. 654-661.

Zhang, Y.S., et al., *Labeling Human Mesenchymal Stem Cells with Gold Nanocages for in vitro and in vivo Tracking by Two-Photon Microscopy and Photoacoustic Microscopy*. *Theranostics*, 2013. **3**(8): p. 532-543.

Zhang, Y.S., et al., *Optical-Resolution Photoacoustic Microscopy for Volumetric and Spectral Analysis of Histological and Immunochemical Samples*. *Angew. Chem. Int. Ed.*, 2014. **53**(31): p. 8099-8103.

Zhou, Y., et al., *Handheld photoacoustic probe to detect both melanoma depth and volume at high speed in vivo*. *J. Biophoton*, 2015.

Zhu, L., et al., *Multiview optical resolution photoacoustic microscopy*. *Optica*, 2014. **1**(4): p. 217.

Zhu, Q., N. Chen, and S.H. Kurtzman, *Imaging tumor angiogenesis by use of combined near-infrared diffusive light and ultrasound*. *Opt. Lett.*, 2003. **28**(5): p. 337.